I: Normal faulting on the Austroalpine 'overthrust' constrained by thermochronometry and kinematic analysis, Central Alps, Graubünden region, Switzerland

II: Clumped isotope thermometry of carbonate phases associated with the copper deposits of Kennecott, Alaska

Thesis by
Jason Brian Price

In Partial Fulfillment of the Requirements for
the degree of
Doctor of Philosophy
Geology

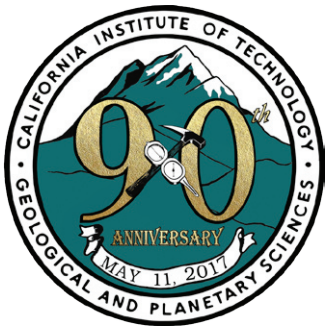

CALIFORNIA INSTITUTE OF TECHNOLOGY
Pasadena, California
2017
(defended 22 September, 2016)

Jason Brian Price
ORCID: 0000-0001-9865-603X

ACKNOWLEDGEMENTS

I thank those on my committee, Brian Wernicke, Joann Stock, John Eiler, Paul Asimow, and Ken Farley, for their help and encouragement along the way. Brian, in particular, deserves a measure of gratitude because it was he who, in 2010 when I was just starting to apply to PhD programs, told me, "If you want to get in here, you better go back and take a Differential Equations class and get an 'A' in it." Given that it had been more than 10 years since I had taken Calculus III, this was a daunting request! Nevertheless, I joined the DiffEq class at CU Denver two weeks late, worked my tail off (and got fired from my job for it), and got the requisite 'A'; Brian upheld his end of the deal, and by late July, 2011, I was collecting rock samples in the picture-perfect Swiss Alps. I also want to thank Paul and John who helped to fund this thesis work at various times along the way when the Wernicke NSF funds either had not yet materialized (2013) or had suddenly dissipated (2016), no doubt from the unfavorable exchange between the USD and CHF among other things ($29 hamburgers, etc.).

I thank my dearly beloved family, Kari, Tobin, Elias, and Whitney, for sticking with me and supporting me through these several years. I could not have done it without you! And only you really know the difficulty it was to have me traveling back and forth from Colorado to California for five years while making only a small fraction of the paycheck that I once made working in the mining industry. But we have to believe that the sacrifice will be worth it in the long run.

I thank my field assistants, in order of appearance, Bryan Palmintier, Lukas Flükiger Nibourel, Luca Malatesta, Kari Price, Brian Wernicke, Peter Nievergelt, and Dominik Letsch, for their tremendous help in acquiring rocks from all across Switzerland. This was no small task and not for the faint of heart, as I got head-to-toe soaking wet in rain storms separately with Lukas F.-N. and then Luca M. in 2013 and again with Brian W. in 2015; and, in 2011 with Bryan P., spent one of the harshest nights of my life exposed in an open bivouac at 3600 m on the west ridge of Piz Roseg on the Swiss-Italian border, sleeping on a carefully laid-out rope as insulation from the cold rocks and pressed into Bryan for warmth. We were fortunate in that the weather was as clear and as calm as could be hoped for in August at 3600 m at 46°22' North latitude. These several adversities made the 2015 field season, equipped with a Mercedes Benz station wagon and a helicopter for a one-day traverse that would have otherwise required a week's worth of hiking to complete the same sampling, feel like a piece of cake!

I thank my friends and colleagues here at Caltech, particularly my Pit mates (10 total! Packed in like sardines! Best Pit ever!): Adam Subhas, Sophie Hines, Frank Sousa (Falafel), Ted Present (Theodopolis), Vicky Stevens (shovel wrestler #1), Kirsten Siebach, Renata Cummins (with whose dad I attempted *Astroman* while she was still a 'tween'), Jen Hamon, and Luca Malatesta (my secret Swiss weapon); 310 North Mudd office mates (Go 310NM! We had so

many rocks that even the Geology Division squawked about it!): Steve Skinner (CA hybrid), Erika Swanson, Kristel Chanard (Ça roule ma poule), Jen Hamon, Daven Quinn (Creek, the master of all things Python), Baptiste Gombert, Maxime Bernaudin, Marion Barre, and Lee Saper; the Eiler group: Katie Snell, Kristin Bergmann, Nithya Thiagarajan (காபி நானை?), Max Lloyd, Daniel Stolper, Paul Magyar (how come those fashion ads don't state their location?), Brooke Dallas (you can hold your breath for how long??), Alison Piasecki (shovel wrestler #2), Nami Kitchen; and many other folks for general merry-making, in no particular order, Michael Long and little Raman (Scrubjay), François Ayoub, Naresh Satyan (the bird encyclopedia), Nick Boekelheide, Seb Kopf, Ryan McKeon (Go Broncos), Jena Johnson (saved me the best desk in the Pit!), Kat Dawson, John Magyar, James Rae and Andrea Burke, J.C. Creveling (lovin' those vitreous white baby doll heads), Kate Masiuk Present, Jeff Prancevich (we map volcanic rocks in our sleep), Sarah Slotznik (midnight chocolate), Jennifer Buz, Chris Rollins (Henry's cuz), Natalia Solomatova, Roberta Poceviciute (who kindly reminded me to do my chores), Kelly Mauser, Joel Scheingross (who let me in on a great place to live in Pasadena), Sean Symon, Maddie Lewis, Dana Anderson, Vish Ratnaswamy (whisky hour), Cheik Mbengue, Lincoln Collins (orange beemer), Mike Wong (feistiest sportsman in the division), Sally Zhang, Sean Mullin (fearless 136 TA), Lewis Ward (vest mate), Hayden Miller (Joshua Tree is the best stone ever), Stephen Perry (whose pulse rate during comps would have killed lesser men), Dan Johnson, Austin Chadwick, Alistair Hayden (brought music to our campfires), Hank Yu, Henry Ngo (the most enthusiastic IMer in existence), Jamshid Hassanzadeh, Mortaza Pirouz, Christoph Von Hagke, Dirk Scherler (let's get some fish tacos!), Sylvain Barbot, Eugénie Pérouse, June Wicks, Maggie Osburn (the fist) and Mitch Barklage (the glove), Megan Newcombe (sunniest face in the Division), Leah Sabbeth, Ryan Witkosky (is it pumpkin season yet?), Florian Hofmann (a German who doesn't drink beer? Unglaublich!), Alex Teng, Steve Kidder, Alan Chapman, Melanie Channon, Brian Kohan (master pig roaster), Elizabeth Trembath-Reichert, Clement Cid, Albert (slippery Al) Chan, Voon Hui Lai, Morgan Raven (looks like Mary Tyler Moore), Ellen Leask, Baptiste Rousset, Adam Waszczak, Jose Luis Garcia, Zach Erickson (what a pianist!), Elle Chimiak, Masha Kleshcheva, Mathieu Lapôtre (a future academic superstar), Peter Martin (Tonopah), Stefanie Wirth, Belle Philibosian, Sebastien Leprince, Daan Speth (who could give Goliath a run for his money), Uri Ryb (pro core logger), Emma Gatti (sweet VW van), Camilo Ponton, Forrest Horton, Men Meier (who smiles as he rides his bike home, even at 2 am), Adriano Gualandi (that's one mean 'fro bro), Cam Macris, MaryJo Brounce, Stephen Cox, Peter Buhler (fellow Watson fellow), Kevin Sutherland (big honky kilson rolling down the grape vine), Tristan Murphy (structural geology is *so* much better than structural engineering), Annie Ritch (the boy, the boy; he can't sleep here on the stairs), Alec Brenner (heckuva lens, son), Alice Michel, and Emilia Hernandez.

I am indebted to Mike Cosca, U.S. Geological Survey Denver, for being so helpful and

willing to do a dozen Ar/Ar analyses (a week's worth of instrument time) for this little "side project." I appreciate the directed attention of Jim Metcalf and Becky Flowers at CU Boulder who provided a ton of ZHe analyses on relatively short notice. Thanks to Mark Mercer, Petrographics Inc., for making outstanding thin sections at an affordable price.

I greatly appreciated my several conversations with the old-timers in the Division: Lee Silver, Peter Wyllie, Hugh Taylor, and Don Burnett, all of whom gave me meaningful advice and more encouragement than they realize! In particular, Hugh Taylor sharing with me his encyclopedic memory of American football (Pop Warner, Jim Thorpe and the Carlisle Indian School, Vow Boys, Wow Boys) will always be appreciated. Time spent in the field with Joann Stock, Brian Wernicke, Jason Saleeby, John Grotzinger, Woody Fischer, Paul Asimow, and Jean-Philippe Avouac has been invaluable. Joe Kirschvink deserves a 20 (troy) ounce gold medal for his persistence in leading Ge136, the single best way for Caltech students to learn the geography (and a little geology) in a 600-mile-radius around Pasadena, California. Keep it up, Joe!! I thought I knew a lot of geology when I got to Caltech, but these guys showed me that there was (and is) still much to learn. Saleeby taught me to persist in the inquisitive struggle because "the rocks don't just roll over and play dead for you;" wisdom I will not soon forget.

Conversations with George Rossman were always enjoyable, and I will forever appreciate the fact that, when I really screwed up one time in his laboratory, of all the things he justifiably could have called me (dumbass, dipshit, etc.), he called me 'sir.' Lindsey Hedges was an outstanding guide in the Farley lab and taught me so many little tricks for how to pick and pack apatite and zircon grains. I will always remember her. Chi Ma is the best electron microscopist, period. And John Bercaw, over in Chemistry, was extremely patient answering questions in my quest to purify black ATB (which was contaminated with a hydrocarbon I finally concluded, as it left a tarry residue in the petri dish upon complete evaporation of the solvent; sorry, John, it wasn't a metal after all). John Beckett is an excellent birder and perhaps an even better writer of prose, to say nothing of his science.

I want to thank the many staff members who helped me with all manner of institutional checkboxes, petty (and not so petty) cash reimbursements, checking out Division vehicles, palliating computer ills, etc.: Mark Garcia, Lisa Christiansen, Heather Steele, Kim Klotz, Dian Buchness, Leticia Calderon (no relation to Felipe), Terry Gennaro (you're like the gazelle, and the cops are like the lions waiting in the bushes...), Julia Zuckerman, Liz Boyd, Julie Lee, Marcia Hudson, Kathy Lima, Jen Schechet, Donna Mireles, Scott Dungan, Janice Grancich, and Ken Ou.

Two years of this thesis work, including salary and field and laboratory expenses, was covered by the National Science Foundation Tectonics program, grant EAR 14-51055 awarded to Brian Wernicke. For this, I was the primary beneficiary and am grateful. In addition, I received financial support from the ARCS Foundation, Los Angeles Chapter, the John and Ursula Kanel

scholarship at Caltech, and the Foster and Coco Stanback grant to attend the 2011 AGU meeting, the generosity of whom I will probably never be able to repay. THANK YOU!

Fig. 0.1. Lunch stop on the north flank of Piz Grisch (pt. 2479, Spunda da l'Iva, "Iva's armrest" in Romansh), August 13, 2015. Left to right: Peter Nievergelt (ETH Zürich), Brian Wernicke (Caltech), and Jason Price (Caltech). Bright rocks in the background comprise Triassic dolomites of the Kalkberg nappe, part of the larger Schams nappe that has been "backfolded" around the Permian Suretta Rofna porphyry on which the geologists stand.

ABSTRACT

I. A compilation of 362 cooling ages, including 52 newly reported in this study, from nine thermochronometric systems, $^{40}K/^{39}Ar$ amphibole, $^{40}K/^{39}Ar$ white mica, $^{87}Rb/^{86}Sr$ white mica, $^{40}K/^{39}Ar$ biotite, $^{87}Rb/^{86}Sr$ biotite, zircon and apatite fission track, zircon and apatite (U-Th)/He, indicate that the base of the Austroalpine allochthonous 'orogenic lid' was not in full thermal equilibrium with its Penninic substrate until at least the middle Oligocene, approximately 29-28 Ma, to allowably as late as the early Miocene, ca. 18 Ma. There is about a factor-of-five difference in cooling rates between the hanging wall (ca. 4°C/m.y.) and footwall (ca. 20°C/m.y.) during this period. In addition, there are demonstrably higher metamorphic grades, including blueschist- and eclogite-facies, in the Pennine footwall compared to lower greenschist-facies in the Austroalpine hanging wall. Together these two facts demonstrate that hot, high-pressure Penninic nappes were forced upward against the cold, low-pressure overriding Austroalpine plate in a very short time window of approximately 7-10 m.y. between the time of peak metamorphism during the Eocene and the time of thermal equilibration with the overriding plate during the Oligo-Miocene. The most likely mechanism to produce such a cold-on-hot juxtaposition is a normal fault, and therefore, we conclude that an important period of nappe emplacement in the Central Swiss Alps occurred concurrently with orogen-perpendicular normal fault motion at the base of the Austroalpine allochthon persisting well into the Oligocene and possibly into the early Miocene, post-dating the 32-30 Ma age of the Bergell intrusion.

Mesoscopic structural measurements made at the top and bottom of the Pennine zone in eastern Switzerland indicate multiple, spatially heterogeneous directions of movement. At the top, in the Oberhalbstein Valley, movement directions vary from dominantly top-east to top-south-southeast a very minor top-north component within Pennine rocks of the Martegnas shear zone and no preferred movement direction within the Austroalpine hanging wall. Near Piz Toissa, a minimum of two kilometers of nearby structural section in the Err and Platta nappes have been faulted out. At the bottom of the Pennine zone in Val Lumnezia and the Chur Rhein Valley at Trimmis, we observe top-northwest, top-north, and top-northeast movements. In Val Lumnezia, the Sub-Penninic Scopi zone (Gotthard cover rocks) shows movement in a top-northwest direction; the superjacent Peidener imbricate fault zone, a relatively thin (ca. 50 to 100 m thick) structural zone consisting of Scopi zone lithologies, shows movement in a northeasterly direction; above that, the basal Penninic Bündnerschiefer shows no dominant movement direction. To the east, in the Chur Rhine Valley, movement is well defined as exclusively top-north. Therefore, movement directions in the lower Bündnerschiefer are broadly top-north but heterogeneous in direction along strike between Val Lumnezia and Chur Rhein Valley, and, as first suggested by Weh and Frotizheim (2001), it may be erroneous to regard the basal Pennine thrust as a simple

through-going structure. In Val Lumnezia, the Scopi-Peidener-Pennine nappes resemble a "jelly sandwich" in which the thick Pennine mass utilized the Peidener zone to move in an oblique sinistral-normal slip sense past the southeast-dipping allochthonous Scopi zone and its east-dipping Gotthard "massif" substrate. If the Peidener zone continues northeastward beneath alluvial cover of the Chur Rhein Valley, it may serve as a late, NE-directed shear zone that separates the Pennine nappes from European units. If so, it would explain the apparent truncation and progressive omission of allochthonous elements of European affinity along the zone from southwest to northeast beneath alluvium of the Chur Rhein Valley. We therefore infer that the direct juxtaposition of Penninic units to the east with the Helvetic autochthon to the west at the latitude of Trimmis records an episode of top-northeast, orogen-parallel strike-slip and extensional movement.

Zircon (U-Th)/He (ZHe) cooling ages from the Oberhalbstein Valley indicate that the Austroalpine-Pennine contact was still active at ca. 27 Ma, and that the Martegnas shear zone was active, in part, between ca. 27 and 24 Ma. It is likely that the Piz Toissa klippe formed around this time during the late Oligocene. The pattern of much younger ZHe ages at the bottom of the Pennine zone is independent of any nappe boundaries, including the Peidener imbricate fault zone, but is consistent with the rise of the Aar massif during the Miocene. Tectonic movements, as recorded by the mesostructure in the Austroalpine, Penninic, and Sub-Penninic domains, and local ZHe cooling ages generally support the conclusion drawn strictly from cooling ages that the Pennine zone was emplaced *en masse* as a coherent 'piston' or 'mega-pip' during Oligocene to early Miocene time (approximately 29 to 18 Ma), well after juxtaposition of Apulia with cratonic Europe (continent-continent collision) and during the development of Alpine topography and the peripheral basins (viz. Molasse and Lombardi). Additional top-north movement and late uplift and flexure of the nappe stack, along with the Aar massif, occurred primarily in middle to upper Miocene time, following the post-collisional structural interposition of the Pennine zone between Europe and Apulia.

II. Nine carbonate phases at Kennecott, Alaska were measured for their clumped isotope (Δ_{47}) equilibration temperatures. The total range for carbonate temperatures spans 38-164°C. Premineral phases are relatively cool (43-71°C); synmineral phases are relatively warm (89-157°C); late postmineral phases are the most cool (38-59°C) but overlap some premineral phases. Zebra dolomite precipitated in the range 130-163°C. Dedolomite, a hallmark alteration feature of the mineralizing fluids, falls into a narrow range of 98-109°C, consistent with the stability field for the low-temperature chalcocite polymorph. Except for one sample, none of the synmineral calcites crystallized within the stability field of djurleite, a volumetrically significant component of the main-stage ore, which suggests that intergrown djurleite may have been a somewhat later recrystallization product of chalcocite rather than a coeval phase.

Calculated compositions for $\delta^{18}O_{water}$ vary from -4.2 to +11.0‰. The most depleted water precipitated hydrothermal baroque dolomite, whereas the most enriched water was associated with recrystallized limestone wallrock on the periphery of the orebody. Waters that precipitated calcite+copper vary from -1.1 to +9.3‰.

Intriguingly, rhythmic layering in zebra dolomite can be resolved in Δ_{47} space, and preliminary data indicate that the coarser-grained baroque dolomite bands precipitated at temperatures 5-10°C cooler than the surrounding, finer-grained dolomite wall rock bands.

The calculated values of $\delta^{18}O_{water}$ support a genetic model that invokes redox changes associated with fluid mixing as the likely mechanism responsible for copper deposition. In this model a sulfidic, basinal fluid having $\delta^{18}O$ similar to seawater mixes with a cuprous fluid having heavier $\delta^{18}O$ (5 to 8‰) which was derived from the Nikolai Greenstone during prehnite-pumpellyite-facies metamorphism.

TABLE OF CONTENTS

LIST OF FIGURES

LIST OF TABLES

Organization of the thesis

The thesis is divided into three chapters as follows:

Chapter 1 demonstrates through thermochronometry on multiple mineral systems that exhumation of the various Pennine nappes and, in particular, the establishment of the Austroalpine-Pennine contact in the Central Alps was accomplished by syn-convergent normal faulting, a novel hypothesis that will be resisted by traditional Alpine geologists. Chapter 1 has been submitted to *Tectonics* for publication.

Chapter 2 presents a series of kinematic analyses and field observations from eastern Switzerland from the top of the Pennine zone in the Martegnas shear zone of the Oberhalbstein Valley and at the bottom of the Pennine zone in the Peidener imbricate fault zone in Val Lumnezia and in the Chur Rhein Valley at Trimmis. Conclusions from the field work presented in Chapter 2 in part support the findings from Chapter 1, in that the Pennine zone likely was exhumed *en masse* as a piston or 'mega-pip' and that important ancillary features of the Alps, such as the deformation of the Helvetic nappes and the Subalpine Molasse, and the formation of the Molasse and Lombardi basins, were either caused by or, at least, initiated by this massive exhumation. Chapter 2 has been submitted to the *Journal of Structural Geology* for publication.

Chapter 3 presents measurements of clumped isotope temperatures and calculated $\delta^{18}O_{water}$ compositions from the Bonanza mine at Kennecott, Alaska which show that the copper mineralization occurred in an overall cooling regime between c. 150°C and 80°C from fluids with an isotopic composition very similar to modern seawater. Chapter 3, while not related to the Alps, is a project that grew out of my qualifying exam, an endeavor that required me to present results from two different, unrelated projects to my qualifying committee. I found this study at Kennecott to be stimulating enough to formalize it here in the thesis and, soon, for publication.

A quick primer on the Alps

From nearly the beginning of geologic inquiry, the European Alps have been the iconic place to study overthrust allochthonous rocks in a setting of continental convergence. Earliest now-celebrated field discoveries, such as that of the *Uberschiebung* at Glarus by Arnold Escher von der Linth (c. 1868), which demonstrated for the first time anywhere in the world that an older rock package (Permian Verrucano) unconformably sits on top of a younger rock package (Sardona flysch), or that by Amferer and Hammer (1911) who first recognized that missing Mesozoic rocks near Mt. Blanc had been swallowed in a *Verschlucken,* have propelled a continuous succession of field geologists (e.g., Heim, Argand, Termier, Cornelius, Oberholzer, Staub, Bearth, Tollmann, Trümpy, Gansser, Schmid, Pfiffner, Froitzheim, Mancktelow, and many others) to

refine the Alpine orogenic model. Together, these geologists have pieced together many of the important stratigraphic and structural features of the Alpine belt, some general facts of which are summarized here.

To understand the architecture of the mountain belt, one must recognize the paleogeography of the various Alpine domains or 'realms.' Upon retrodeformation, one recognizes three main realms: the former European passive margin, called 'Helvetic'; the intervening tripartite of oceanic 'Valaisan' trough plus Bahama-like 'Briançonnais' continental platform and the open 'Piemont' ocean, called 'Lower-, Middle-, and Upper-Pennine', respectively; and finally the impinging Hercynian crystalline mass of African affinity, called 'Austroalpine' and/or 'South Alpine'. Secondly, moving from north to south in Switzerland, one finds Helvetic rocks to be sitting underneath Penninic rocks to be sitting underneath Austroalpine rocks by way of nappe stacking. A nappe, according to Heim (1922), is a very ductile overthrust fold--essentially a jelly-like version of a Canadian ramp anticline (Fig. 0.2). Thirdly, "External" means more northerly in Switzerland or westerly in France and distal to peak metamorpism, whereas "internal" means more southerly in Switzerland and easterly in France and therefore proximal to peak metamorphism. Lastly, "Western Alps" is the region of eastern France and western Switzerland as far east as approximately the Simplon fault and the western margin of the Lepontine dome; "Central Alps" includes the Lepontine dome, Aar massif, and Pennine rocks easterly all the way to the Austroalpine-Pennine boundary, including the Engadine line, Engadine window, and Bergell intrusion. "Eastern Alps" comprises mostly Austroalpine rocks in eastern-most Switzerland, northeastern Italy, and much of Austria, including the Tauern window and the Adamello intrusion. "South Alps" is the area south of the important major fault at the south end of the Alps that has many local names: Canavese, Tonale, Giudicarie, Pusteria, Gailtal but which is generally called Insubric line for the area due south of the Lepontine dome or, more broadly, the Periadriatic line for the entire set of interconnected faults (Schmid et al., 1989).

The many abstruse details of Alpine geology are too cumbersome to reproduce here, even in summary, but the interested reader should consult such useful volumes as Heim (1922, two volumes in German), Trümpy (1980), Hsü (1995), and Pfiffner (2014).

Lastly, dear reader, please remember that an 'alp' is a meadow, not a rocky summit. The Alps, therefore, is an especially craggy collage of meadows.

References Cited

Heim, A., 1922. Geologie der Schweiz. Two Volumes. Leipzig: Tauchnitz.

Hsü, K.J., 1995. The geology of Switzerland: An introduction to tectonic facies, Vol. 25. Princeton, NJ: Princeton University Press.

Pfiffner, O.A., 2014. Geology of the Alps. West Sussex, U.K.: John Wiley & Sons.

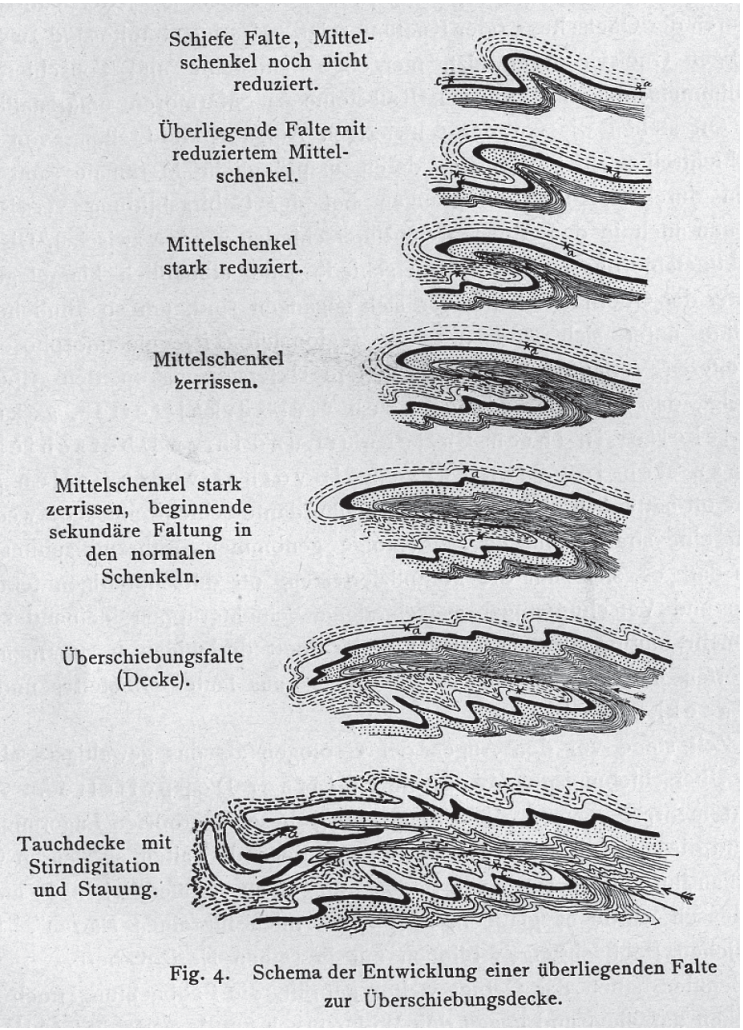

Fig. 0.2. The development of a nappe ("decke") according to Heim (1922, Vol. 1, p. 10).

Schmid, S.M., Aebli, H.R., Heller, F. and Zingg, A., 1989. The role of the Periadriatic Line in the tectonic evolution of the Alps. Geological Society, London, Special Publications, v. 45, p. 153-171.

Trümpy, R., 1980, Geology of Switzerland: An outline of the geology of Switzerland. Two Volumes. Basel: Interbook.

[This page was intentionally left blank.]

Chapter I:

Thermochronometry across the Austroalpine-Pennine boundary, Central Alps, Switzerland: Documenting normal fault slip on the world's largest 'overthrust'

A manuscript submitted to Tectonics

Abstract:

New (53 dates) and published (305 dates) thermochronometric data from the Graubünden region of the Central Alps (including seven systems with closure temperatures ranging from 450 to 70 °C) suggest that a pronounced thermal mismatch between the Austroalpine allochthon (Alpine "orogenic lid") and the Pennine Zone persisted until at least 29 Ma and, allowably, until c. 18 Ma. The observed mismatch supports previous suggestions that the famous "overthrust" between the Austroalpine allochthon and the Pennine Zone, historically regarded as primarily an Eocene top-north thrust fault, is in fact primarily an Oligocene-Miocene normal fault that has a minimum of 60 km of displacement with top-south or -southeast sense of shear. Two hallmarks of Alpine geology, deposition of the foredeep Molasse and emplacement of the Helvetic nappes, appear to be coeval, peripheral manifestations of crustal thickening via the interposition of the Pennine zone as a northward-intruding wedge between the Austroalpine "lid" and the European cratonic margin, with the Helvetic system (European margin) acting as the "floor" of the wedge. We presume the Penninic wedge is driven by the buoyant rise of subducted crust no longer able to remain attached to the descending slab. If so, emplacement of the wedge could have occurred during either convergence or divergence of Europe relative to Apulia.

1.1. Introduction

Since the advent of plate tectonics a half-century ago, there has been widespread agreement that mountain belts in the Alpine-Himalaya system formed as a consequence of convergence between continental plates, as an end-phase of oceanic subduction (e.g. McKenzie and Sclater, 1971; McKenzie, 1972). Consensus was supported by the observation that most of these orogens feature horizontal contraction along their flanks, and have thicker crust than their surrounding lowlands. More gradually, it was noted that the cores of these orogens had been affected to varying degrees by horizontal extension and vertical thinning, along presumed fossil subduction channels and within the broader collision zone (e.g. Ernst, 1975, 2005; Lister et al., 1984; Burchfiel and Royden, 1985; Selverstone, 1988; Dewey, 1988). The role such structures play in the development of mountain belts, however, remains controversial, in large measure because of uncertainties in the timing of extensional structures in relation to plate convergence, crustal thickening, and contractile structures. In the case of the Alps, for example, extensional structures have been attributed to syn-convergent thinning in the upper crust as it thickens below (e.g., Platt, 1986), episodes of plate divergence during the collision process (e.g., Beltrando et al., 2010; Malusa et al., 2011), mid-crustal, orogen-parallel spreading of an accretionary nappe stack (Schmid et al., 1996, 2004), buoyant rise of subducted crust within a subduction channel (e.g. Chemenda et al., 1995; Butler et al., 2013), and late- or post-collisional modification of the newly thickened crust, including orogen-parallel extension (e.g. Mancktelow, 1992; Selvertone, 2005). In this paper, we explore this problem by focusing on the timing of development of the complex tectonic contact zone between the "metamophic core" of the Alps (Pennine zone), a presumed fossil subduction channel of Eocene age, and the overlying "orogenic lid" (Austroalpine allochthon) where it is most extensively exposed in eastern Switzerland, traditionally referred to as the main Austroalpine overthrust. Our goal is to use thermochronometric analysis to better understand the nature and timing of this juxtaposition, and its relationship to the development of flanking belts of horizontal contraction (e.g. Helvetic nappes), thickened crust, and high topography.

Within subduction channels, the thermal inversion reequilibrates after subduction ceases, causing both footwall and hanging wall to rise in temperature on time-scales of order 10 Myr (e.g., Peacock, 1989). In continent-continent collisions, the subduction channel may be either extensionally or erosionally unroofed, either during continued subduction, or afterward. Post-kinematic unroofing histories may be rapid or shallow enough to quench and preserve late-kinematic thermal structure within the upper continental crust, or slow or deep enough such that the late-kinematic thermal structure is overprinted by a conventional geotherm during cooling (e.g., Butler et al., 2013). For example, the Pennine zone (Fig. 1.1) is widely regarded as a fossil, mid-Tertiary subduction channel complex that formed between the colliding Adriatic microplate and the European continent, and includes components ranging in metamorphic grade from sub-green-

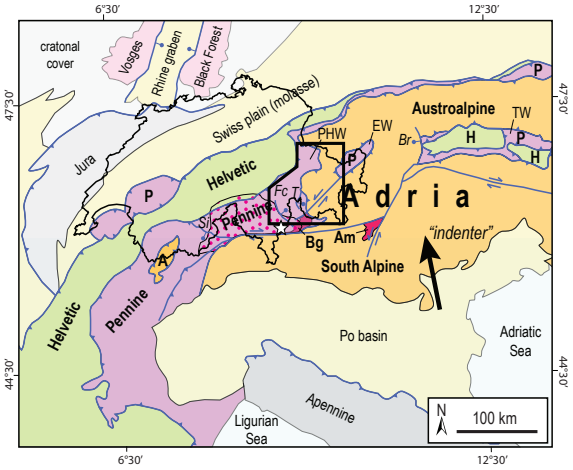

Fig. 1.1. Generalized tectonic map of Switzerland and environs. The large box outlines the study area described in this chapter. Large black arrow indicates general movement direction of the modern Adriatic sub-plate (Italy). Thrust faults are shown with teeth on the hanging wall. Several discrete normal faults are mapped: Simplon (Si), Forcola (Fc), Turba mylonite-Gurgaletsch shear zone (T-G), and Brenner fault (Br). Large windows shown are Engadine window (EW), Prättigau half-window (PHW), and Tauern window (TW). Tectonic units include Austroalpine (A), Bergell pluton (B),Helvetic nappes (H), Pennine zone (P), and South Alpine (SA). Austroalpine and South Alpine are equivalent. Modified after Pfiffner (2010).

schist to (U)HP eclogite-amphibolite facies (e.g., Wheeler et al., 2001; Chopin, 2003; Beaumont et al., 2009; Malusà et al., 2011; Angiboust et al., 2011, 2014). In the Central Alps, most of the complex is overprinted by a post-kinematic Barrovian-type metamorphism (e.g., Burg and Gerya, 2005), followed by relatively steady-state unroofing with a stable upper crustal thermal structure (Vernon et al., 2008; Bernet et al., 2009). Throughout most of the complex, low-temperature (50-300°C closure temperature (Tc)) thermochronologic transects show little relationship to structural elements of the subduction channel. Instead, for any given thermochronometer, there is a small positive correlation of age with elevation owing to rapid Neogene erosional unroofing, with most systems yielding Miocene or younger cooling ages (0-20 Ma).

In eastern Switzerland, the boundary between the Austroalpine and Pennine paleogeographic realms (main Austroalpine overthrust and associated structures) is regarded by most workers to be the top of a subduction channel which was active during mid-Tertiary continent-continent collision. Unlike the general pattern of post-subduction thermal re-equilibration observed in the Central Alps, however, marked contrasts in early- to mid-Tertiary thermal histories are recorded at different structural levels, and in at least one case, such a contrast has been reported to occur within ≤1 km of an important mylonitic shear zone associated with the top of the subduction channel (Augenstein, 2012). A similar pattern is apparent in the Tauern Window region of the Eastern Alps where Penninic and deeper structural levels with late Oligocene and Miocene cooling histories that begin above 300°C are juxtaposed beneath the Austroalpine allochthon, most of which resided at temperatures <200°C since the Late Cretaceous to Early Tertiary (Luth and Willingshofer, 2008).

Here, we report time-temperature histories from sample transects spanning the Pennine-Austroalpine boundary zone in the Central Alps of eastern Switzerland (Fig. 1.1) to help resolve the long-standing problem of the precise age and origin of Pennine nappe structure and its juxtaposition with Austroalpine units. Placing firm limits on the timing of Pennine deformation is

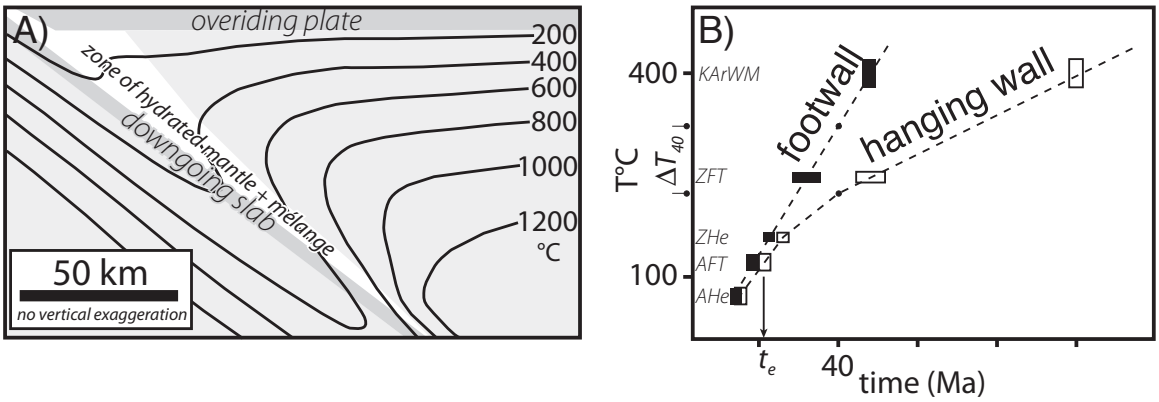

Fig. 1.2. A) Telescoped isotherms in a subduction zone indicate a very shallow thermal gradient of ~8°C/km, As a result, depths (and lithostatic pressures) a factor of four or five greater can be obtained compared to the average continental geotherm of ~25-30°C/km (modified after Gerya et al., 2002). B) Schematic temperature-time cooling paths of two rock masses with different cooling histories: quick cooling (solid boxes) at a rate of ~10°C/m.y. vs. slow cooling (open boxes) at a rate of ~3-4°C/m.y. ΔT_{40} is the difference in temperature between the two rock masses at 40 Ma, and t_e is the approximate time at which thermal equilibrium is attained. Note that because of varying thicknesses of the rock masses, differences in internal radioactive heating, and other extrinsic properties, the two rock masses, while conjoined, are never at the exact same temperature.

frustratingly elusive. The maximum age is usually based on paleontological constraints from metamorphosed, poorly-fossiliferous flysch deposits that may pre-date deformation by tens of millions of years. The minimum age is usually unconstrained by field relationships, because the Alpine orogen is virtually devoid of any pre-Quaternary sedimentary or igneous rocks that cross-cut the nappe structure. The principal existing constraints on the age of Pennine nappe movement in this area are the preservation of Lower Eocene nummulites (< c. 56 Ma) in pre-deformational sedimentary rocks (Nänny, 1948; Ziegler, 1956) and the truncation of some of the nappe boundaries and associated fabric by the c. 30 Ma Bergell pluton (Hansmann, 1996). The best hope for improving these constraints lies in identifying and dating metamorphic and/or synkinematic mineral phases that grew near or below their closure temperatures (i.e., Alpine-stage titanite at Dora Maira massif, Rubatto and Hermann, 2001; Alpine-stage zircon overgrowths at Monte Duria, Adula nappe, Hermann et al.,. 2006), or, outside of that, using a series of thermochronometers to document abrupt discontinuities in thermal history across nappe boundaries, which may yield a maximum age for the cessation of their movement (e.g., Inger et al., 1996; Campani et al., 2010; Malusà et al., 2005; Augenstein, 2012). In addition, thermal history also has the potential to constrain the minimum offsets along major structures as it often does in extensional terrains, such as the Basin and Range province of western North America (Fitzgerald et al., 1991, 2009; Reiners et al., 2000; Stöckli et al., 2005).

For problems of tectonic deformation in the low-temperature regime of subduction channels, the ideal thermochronometric tools are zircon fission track (ZFT; Tc of ~240°C) and zircon U-Th/He (ZHe; Tc of ~180°C) dating. In the Pennine zone of eastern Switzerland, the high-

pressure, hydrous inosilicate carpholite (P > c. 1 GPa) is common in even the lowest-temperature portions of the complex (e.g., Wyss and Isler, 2011). However, peak metamorphic temperatures are generally sub-greenschist facies (<400°C, e.g., Fig. 15 in Wyss and Isler, 2011; Miron et al., 2013; Schreurs, 1993; Ferriero-Mahlmann, 2001), occurring within ~200°C of ZFT and ZHe closure temperatures. In most thermomechanical models (e.g., Fig. 4 in Gerya et al., 2002; Fig. 4b in Butler et al., 2013), the temperature range 200-450°C spans the active subduction channel from depths ranging from c. 10 to 90 km (0.3 to 3 GPa), at plate convergence rates and time scales appropriate to Alpine collision zone (c. 1-3 cm/yr and 10 to 30 Myr, respectively; Fig. 1.2A). Thus, with a Tc of 350-450°C, Ar/Ar systematics in white mica are well-suited to capture the timing of peak metamorphism, including the possibility of sub-Tc grain growth (Hunziker, 1986; Schreurs, 1993). However, the Ar/Ar system in micas is generally poorly suited to record what is likely to be a protracted history of cooling and tectonism in the late stages of subduction channel evolution (Gerya et al., 2002; Beaumont et al., 2009; Butler et al., 2013, 2014). At temperatures near and below ZFT and ZHe closure, subduction channel isotherms become strongly influenced by proximity to the thermal boundary condition at the Earth's surface. For this reason, apatite thermochronometers (fission track, Tc ~110°C and U-Th/He, Tc ~70°C) tend to record processes related primarily to post-kinematic erosion and landform evolution (e.g., House et al., 1998; Bernet et al., 2001; Bernet et al., 2009). On the basis of these considerations, multi-system time-temperature cooling paths are expected to show mid-Tertiary cooling from above 400°C to less than 100°C in the footwall. In contrast, cooling through a similar temperature range in the hanging wall generally began in the Mesozoic and ended at some point in mid-Tertiary time, near the time that subduction channel activity ceased. By measuring mica, zircon, and apatite cooling ages in both hanging wall and footwall, the two cooling curves define two parameters of interest. The first is the difference in temperature between the hanging wall and footwall cooling paths, hereafter referred to as ΔT, near peak metamorphic temperatures (Fig. 1.2B). The second is the time at which the two paths merge, indicating thermal equilibrium between hanging wall and footwall, hereafter referred to as t_e.

1.2 Geologic Setting and Previous Work

The primary post-Hercynian, pre-Alpine paleogeographic elements of the Central Alps include, from north to south (Fig. 1.1), the former European continental margin (Helvetic and Ultrahelvetic domains); the tripartite Pennine zone (Valaisan marine trough, Briançonnais Rise or "continental ribbon", and Piemont Ocean); and the Adriatic microplate of north African affinity (Austroalpine and South Alpine domains). From early Jurassic through early Eocene time, Penninic strata were concordantly deposited in marine settings of variable depths that lay between Adria and the European continent. Within Adria, tectonism began in Jurassic time with the

development of a highly extended, yet magma-poor, passive margin (Beltrando et al., 2010, Mohn et al., 2010), and continued into the Cretaceous during which time there was an EoAlpine ("Trupchun phase") metamorphic and nappe-stacking event that established the major tectono-stratigraphic components of the Austroalpine allochthon (Froitzheim et al., 1994; Schmid et al., 2004; Mohn et al., 2011). By the end of the Cretaceous, all but the lowermost elements of the Austroalpine realm had stabilized into a coherent, relatively undeforming unit, at times referred to as a 'traineau écraseur' (Argand, 1916) or the 'orogenic lid' (Laubscher, 1983). Subduction initiated within the Piemont Ocean during the Late Cretaceous, and by Paleogene time Briançonnais and Valaisan elements were being subducted under and/or accreted to Adria. The Adriatic microplate began to override the European passive margin (Helvetic domain) during the Eocene (e.g. Schmid et al., 1996). The Cretaceous-Tertiary relative motions between the three domains have long been debated, but to first order, the assembly of the Western and Central Alps reflects the progressive accretion of elements of the Pennine zone to Adria along at least one (e.g., Schmid et al., 1992) or multiple (e.g., Froitzheim et al., 2008) approximately S-dipping subduction zone(s). The structural boundary between the Austroalpine and Pennine domains is preserved in an impressive fault system that can be traced continuously for >400 km along strike of the Alps. The preserved north-south structural overlap between Austroalpine and Penninic units is nearly 150 km in eastern Switzerland and western Austria (e.g. Trümpy, 1960; Schmid et al., 1996, 2004; Figure 1), and the complete mismatch between hanging wall and footwall units along the entire strike length of the fault indicates that this is a minimum amount of displacement.

Normal faulting and extension have long been understood to be integral to the evolution of the Alps, owing to the occurrence of footwall rocks of higher metamorphic grade adjacent to hanging wall rocks (e.g., Platt, 1986), and studies of the P-T-t evolution and sense-of-shear along normal fault zones, i.e., Simplon fault (Mancktelow, 1992), Brenner fault (Selverstone, 1988; Axen et al., 1995), Combin Zone (Wüst and Silverberg, 1989), Platta nappe (Bachmann et al., 2009); Bernina and Grosina detachments and Eita shear zone (Mohn et al., 2011). These extensional events occurred within a context of cyclic shortening and extension in both Cretaceous and Tertiary time (e.g. Froitzheim et al., 1994, 1996; Nievergelt et al., 1996; Weh and Froitzheim, 2001; Ciancaleoni and Marquer, 2008; Mohn et al., 2011) and multiple burial and unroofing events of (U)HP metamorphic assemblages in the Pennine Zone (e.g. Meyre et al., 1999; Beltrando et al., 2010). Since mid-Tertiary collision in the Alps, a series of tectonometamorphic events, perhaps driven by an Adriatic "indenter" (large arrow in Fig. 1.1) and opening of the Pannonian basin (directly east of the Eastern Alps) has substantially modified the system (e.g. Ratschbacher et al., 1991; Schmid et al., 1996; Scharf et al., 2013), including, (1) widespread orogen-parallel extension across the core of the Alps, (2) strike-slip faulting, especially along the southern margin of the Alps on the Periadriatic fault system, (3) folding and thrusting to the north in the Jura

Mountains, and (4) Barrovian metamorphic overprint of a large fraction of the Pennine in southern Switzerland and northernmost Italy (red dotted area in Fig. 1.1). In addition, modern GPS measurements show that the Adriatic microplate no longer functions as a cohesive whole but is breaking into a series of smaller, independent blocks (Oldow et al., 2002).

1.2.1. Austroalpine allochthon.

In map view, the trace of the base of the allochthon is sinuous, defining two re-entrants or 'half windows' (Fig. 1.1). On average, the fault zone dips gently eastward. The hanging wall is a composite of pre-Cenozoic tectonic elements, most recently defined as Lower, Middle, and Upper Austroalpine, according to their interpreted Jurassic paleogeographic position (Mohn et al., 2011). Lower Austroalpine nappes (Err-Bernina and related digitations) are exposed only in the southern half-window. The Middle and Upper units comprise the more northerly portions of the allochthon, north and east of the southern half-window (Fig. 1.3). The Austroalpine nappes generally contain Mesozoic cover sequences nonconformably resting on extensively exposed crystalline substrates. The crystalline rocks comprise voluminous silicic to intermediate orthogneisses which formed during the Late Paleozoic Hercynian (Variscan) orogeny. These sequences were dismembered by crustal-scale extensional and strike-slip faulting in the Mesozoic, which established the general architecture of the future Alpine nappes, and created dramatic juxtapositions of disparate crustal and mantle structural levels during the formation of the northwest Adriatic passive margin (Schuster and Frank, 1999; Schuster et al., 2001; Mohn et al., 2011, 2012).

Subsequent to passive margin formation, the tectonic assembly of the allochthon occurred in four main phases (D1-D3, plus "post-D3" deformation; Froitzheim et al., 1996; Handy et al., 1996; Mohn, 2011). The first and second, of mid-to Late Cretaceous age, include west-directed imbricate thrusting and folding (in several places reactivating older Jurassic normal faults), followed by extension, most profoundly along a shear zone localized near the base of the Austroalpine units ('Lunghin-Mortirolo movement zone' of Mohn et al., 2011). Below this shear zone, the Margna-Sella nappe complex and Malenco ultramafic zone, which formed along the ocean-continent transition northwest of Adria, were metamorphosed at mid-crustal pressures and exhumed along the shear zone and juxtaposed with upper crustal levels. In the third phase (D3), the entire allochthon was juxtaposed against its Penninic substrate during the Eocene. Despite the large displacements implied by the complete mismatch of hanging wall and footwall units across the base of the allochthon, deformation within the allochthon was restricted to east-trending, shallowly plunging folds. The "post-D3" phase of deformation, localized near the base of the allochthon, resulted in the development of the composite Turba, Gürgaletsch, and Martegnas shear zones (Fig. 1.3), discussed further below.

1.2.2. Penninic substrate of the allochthon.

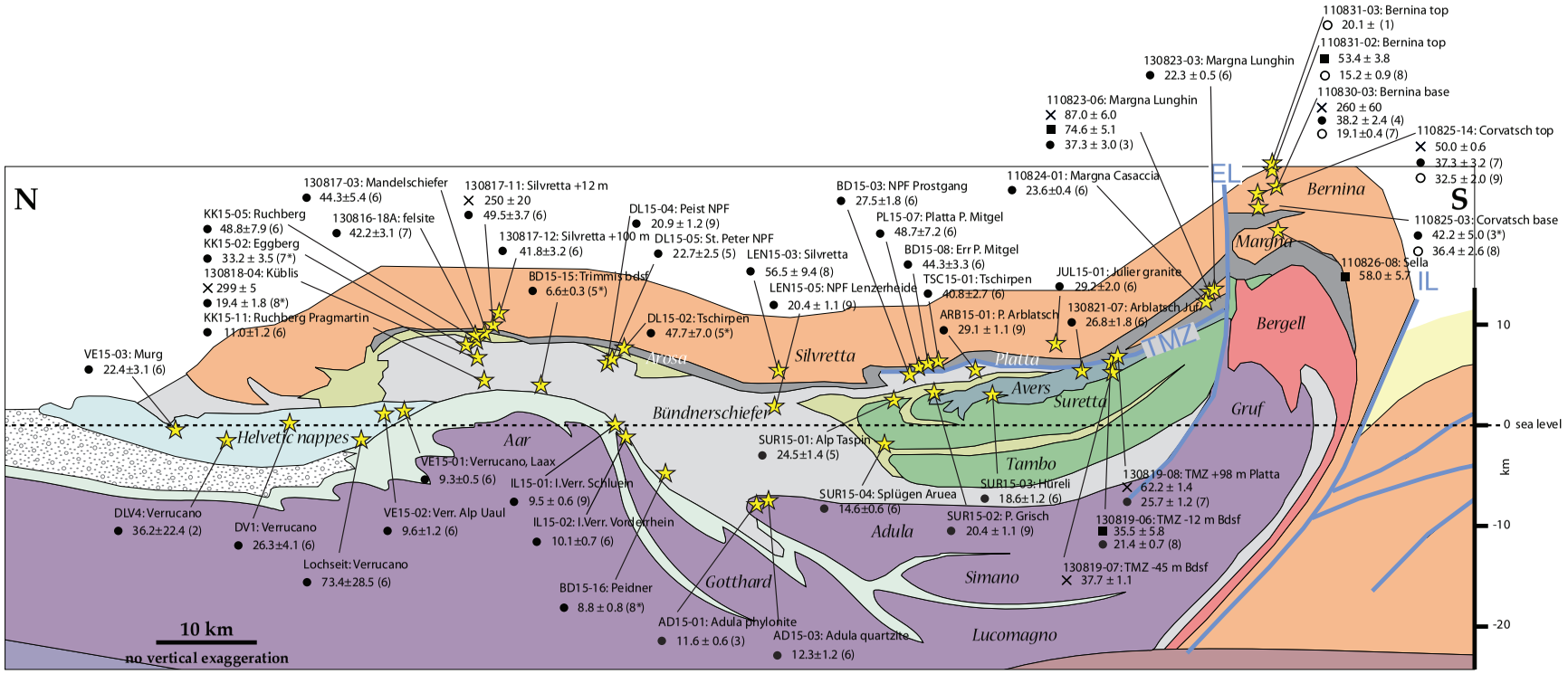

Fig. 1.3. North-south cross section through the Central Alps along easting line 755000 (1903 Swiss Grid), modified after Schmid et al., 1992. All Price (2017) age dates from Graubünden and Appenzeller are shown. Symbology follows that shown in Fig. 4.

The structure of the Penninic units in the Central Alps is dominated by a c. 20 km-thick stack of recumbent nappes with amplitudes of up to 50 km (Fig. 1.3; e.g. Milnes and Pfiffner, 1980; Schmid et al., 1996, 2004). The nappes plunge moderately to gently eastward, forming a map-view cross-section through the stack. The nappes are cored by Hercynian basement and have rounded, lobate northern cores and cuspate southern cores. Unlike the hanging wall of the allochthon, only sparing amounts of Mesozoic cover remain depositionally attached to basement. Prior to recumbent folding, the cover sequences of the basement nappes (e.g., Schams) were tectonically sheared off and 'replaced' by Mesozoic calcareous schists and sandstones, from both the Valais and Piemont oceans, collectively referred to as 'Bündnerschiefer.' In places, the ophiolitic substrates of the Bündnerschiefer are tectonically interposed within it. The two highest basement-cored nappes, Tambo and Suretta (green shading in Fig. 1.3), are most proximal to the base of the Austroalpine sheet, and their cores are generally regarded as having originally formed the basement rocks of the Briançonnais facies belt (e.g., Schmid et al., 1996). In addition to ophiolitic slices, Mesozoic Briançonnais facies cover is preserved as tectonic slices wrapped around the eastern margin of the Suretta nappe (Schams nappes) and along the base of the Austroalpine allochthon (Falknis and Sulzfluh nappes, light green shading in Fig. 1.3). The youngest sediments in the nappe pile and associated cover nappes are lower Eocene turbiditic sandstones and shales known as the Arblatsch flysch in the south and Prättigau flysch in the north, collectively called 'North Penninic flysch.' In the northern half-window, Prättigau flysch appears to grade stratigraphically downward into Bündnerschiefer from the Valais Ocean (e.g. Nänny, 1948; Trümpy, 1980; Steinmann, 1994; Weh, 1998). The large mass of tectonically interleaved Prättigau flysch and Bündnerschiefer is known as the Grava 'nappe' (Weh, 1998; Weh and Froitzheim, 2001; grey shading in Fig. 1.3 and 'Bd' in Fig. 1.4). In contrast, the Arblatsch flysch occurs as isolated, coherent lenses within the chaotically-deformed, ophiolitic Platta nappe, which generally defines the boundary zone between the Austroalpine and Penninic domains. The southern margins of the underlying Tambo and Suretta nappes are truncated by the Bergell and Novate intrusions (red shading in Fig. 1.3 and unit 'Bg' in Fig. 1.4), which have a protracted emplacement history from ca. 32 to 25 Ma (Hansmann, 1996; Liati et al., 2001; Oberli et al., 2004). These constraints have long suggested that the nappe stack was assembled entirely in Eocene time.

In Oligocene and Miocene time, rocks of the Pennine zone were juxtaposed above the Helvetic domain, coeval with the development of the northern Alpine molasse foredeep basin and with the formation of the Helvetic nappe complex (Fig. 1.1). The post-kinematic Barrovian metamorphism, mainly affecting the Lepontine dome region of the Central Alps, affected the southern part of the nappe stack, peaking at c. 18 Ma (Janots et al., 2009; Wiederkehr et al., 2008). Neogene crustal-scale dome and basin structure (i.e., Aar and Lepontine culminations, Wildstrübel and Rawil depressions) overprints the entire system, accompanied by thrust faulting,

normal faulting, and strike-slip faulting (e.g., Insubric shear zone, Simplon fault, and Engadine fault zone, respectively; Figs. 1.1, 1.3, and 1.4).

1.2.3. Position of the base of allochthon.

In the northern half-window, the Pennine-Austroalpine boundary is defined by the chaotically deformed, ophiolitic Arosa zone, which is similar lithologically to the Platta nappe that defines the boundary in the southern half-window. Although derived predominantly from oceanic domains, both Platta and Arosa appear to include tectonically interposed fragments of the Austroalpine allochthon (e.g., Tschirpen gneiss and Triassic dolomite) in its upper few hundred meters. Structural analysis of the contact between the northern part of the Austroalpine allochthon and the Arosa zone record a history of top-W to top-NW-directed shear followed by top-N shear (Ring et al., 1988; Ring et al., 1989). In contrast, detailed structural studies of the Penninic units just beneath the allochthon, one in the northern half-window and the other just north of the southern-half window (Weh and Froitzheim, 2001; Nievergelt et al., 1996, respectively; Price and Wernicke, in prep) both revealed strong extensional deformational episodes within and between Penninic units below the base of the allochthon. These include the development of a two- to three-km-thick zone of S-vergent folding that affects most of the upper boundary of the Grava nappe in the northern half-window; top-S to top-SE-directed normal simple shear along the Gürgaletsch and Martegnas shear zones between the two half-windows; and top-ENE to top-SE-directed simple shear along and below the Turba mylonite zone in the southern half-window (Nievergelt et al., 1996; Weh, 1998; Fig. 1.4). The combined Gürgaletsch-Turba fault zone is localized near the base of the chaotically dismembered Arosa zone to the north, and is depicted by Weh and Froitzheim (2001) and Nievergelt et al. (1996) to descend structurally downward to the south, such that the composite Platta and Margna-Sella nappes are in the hanging wall and the Avers Bündnerschiefer is in the footwall. Similar to the upper part of the Grava nappe, top-south shearing affects the upper half of the Suretta nappe, expressed most vividly by the backthrust "fingers" of basement gneisses preserved there (Figs. 1.3, 1.4; Niemet-Beverin fold phases of Milnes and Schmutz, 1978; Milnes and Pfiffner, 1980; Schreurs, 1993; Scheiber et al., 2012). Thus, there is abundant evidence for shearing with a strong top-S component affecting the Penninic-Austroalpine boundary along nearly its entire exposed trace from the northern margin of the Bergell intrusion in the southern half-window to the Landquart Valley in the northern half-window, a north-south distance of 70 km. According to structural reconstructions by Weh (1998), the folding of the Grava nappe during top-south deformation and the offset of North Penninic flysch across the Martegnas shear zone (Prättigau flysch in the north half-window offset to the

Fig. 1.4. Tectonic map of the study area showing nappes, cooling age samples, and cross section locations. Buffers drawn around cross sections project seven km out from the midline. Ages which fall outside of the buffer are projected to the nearest cross section. All samples on the map are listed in the data tables in Appendices 1 and 2.

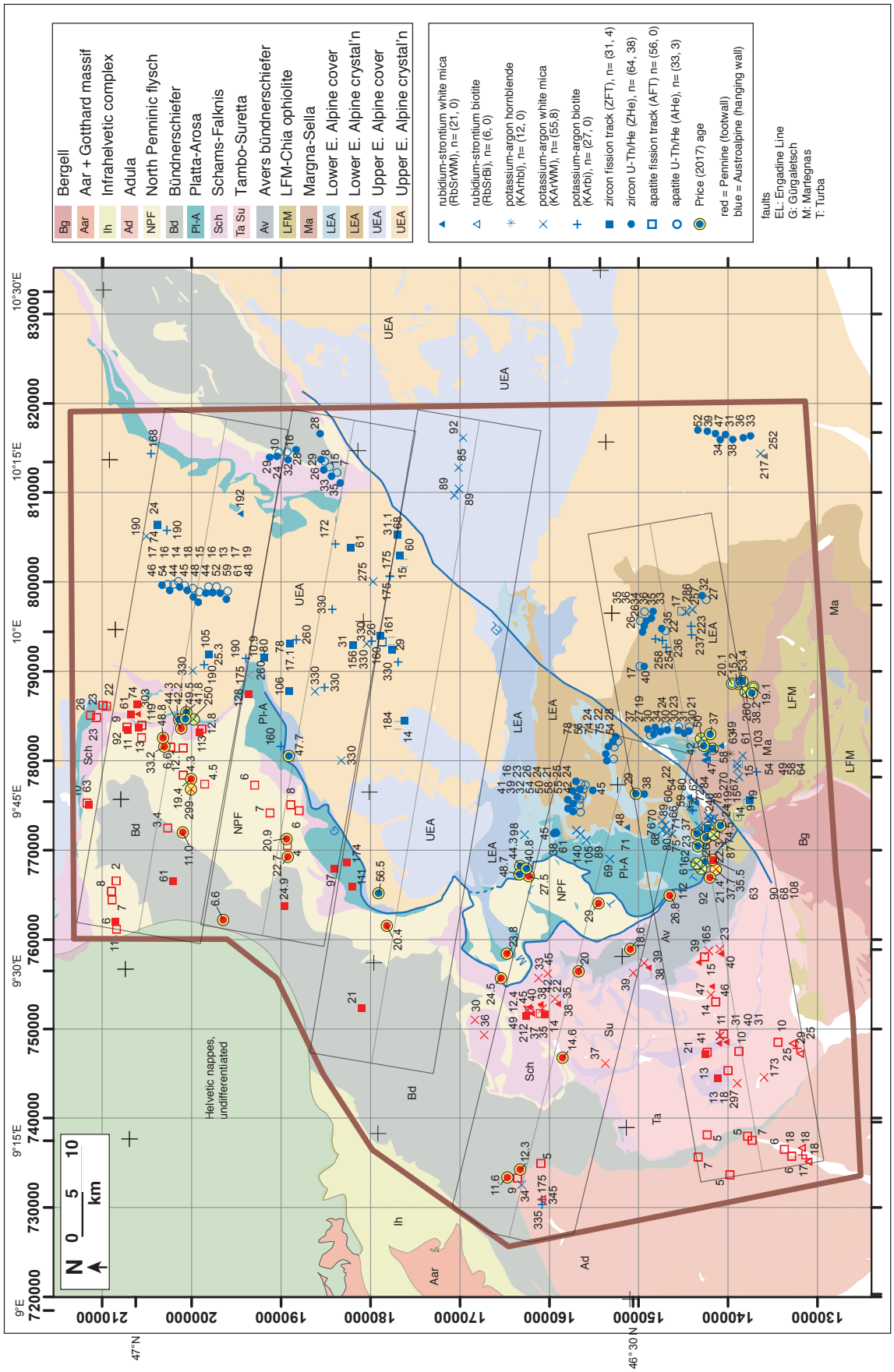
Bergell
Aar + Gotthard massif
Infrahelvetic complex
Adula
North Penninic flysch
Bündnerschiefer
Platta-Arosa
Schams-Falknis
Tambo-Suretta
Avers bündnerschiefer
LFM-Chia ophiolite
Margna-Sella
Lower E. Alpine cover
Lower E. Alpine crystal'n
Upper E. Alpine cover
Upper E. Alpine crystal'n
rubidium-strontium white mica (RbSrWM), n= (21, 0)
rubidium-strontium biotite (RbSrBi), n= (6, 0)
potassium-argon hornblende (KArhbl), n= (12, 0)
potassium-argon white mica (KArWM), n= (55,8)
potassium-argon biotite (KArbi), n= (27, 0)
zircon fission track (ZFT), n= (31, 4)
zircon U-Th/He (ZHe), n= (64, 38)
apatite fission track (AFT) n= (56, 0)
apatite U-Th/He (AHe), n= (33, 3)
Price (2017) age
red = Pennine (footwall)
blue = Austroalpine (hanging wall)
faults
EL: Engadine Line
G: Gürgaletsch
M: Martegnas
T: Turba
Helvetic nappes, undifferentiated
N
0 5 10 km
9°E
9°15'E
9°30'E
9°45'E
10°E
10°15'E
10°30'E
720000
730000
740000
750000
760000
770000
780000
790000
800000
810000
820000
830000
130000
140000
150000
160000
170000
180000
190000
200000
210000
47°N
46° 30 N

Arblatsch flysch in the southern half-window) suggest 68 km of top-south simple shear along the base of the Austroalpine allochthon (Fig. 5.12 on pg. 218 in Weh, 1998).

1.2.4. Previous thermochronology.

A wealth of thermochronologic data from across the Alps has been published over the last five decades, from recognition of metamorphic ages in certain nappes (Jäger, 1962; Steiger, 1964; Oxburgh et al., 1966), to multi-system age-elevation transects (e.g., Wagner et al., 1977), to detailed apatite fission track (AFT) and apatite (U-Th)/He (AHe) modeling of landform evolution (e.g.,. Malusà et al., 2005; Mahéo et al., 2013), periodically summarized in compendia (Hunziker et al., 1992 and Vernon et al., 2008) and regional interpretive syntheses (e.g., Hurford et al., 1989; Table 1 in Beltrando et al., 2010). Previous studies that focused on lower temperature (c. 70-240°C) thermochronometers indicate that, in regions of highest relief in the Penninic and Helvetic Alps, ages generally range from latest Oligocene to Pliocene, with age-elevation profiles that are quite steep (~1 to 4 Myr/km) and that differ in mean age by as much as 15 Myr, depending on the chronometer and location. As noted earlier, age-elevation variations, recorded by AFT and AHe systematics, tend not to correspond to specific nappe boundaries or ductile shear zones. For instance, there is very little difference in apatite ages moving northward from the central Lepontine region across the Infrahelvetic complex to the Aar massif, suggesting that these rocks record the post-kinematic descent of the 110°C and 70°C isotherms in late Miocene to Pliocene time (Rahn, 2005; Michalski and Soom, 1990; Wagner et al., 1977). The post-kinematic character of these low-temperature systems is indeed evident in the fact that a number of studies have shown that post-20 Ma cooling ages are regionally contourable and reflect patterns of broad warping across the entire Alpine orogen (e.g., Schlunegger and Willett, 1999; Luth and Willingshofer, 2008; Bernet et al., 2004, 2009; Mahéo et al., 2013; Fox et al., 2016).

In the Central and Western Alps, an important structure that affects sub-greenschist cooling histories is the Simplon low-angle normal fault, a top-southwest shear zone that juxtaposes the upper and lower parts of the Pennine nappe stack in the Valaisan Alps (Mancktelow, 1992; Campani et al., 2010). Age contrasts across the fault are greatest for systems with $Tc \geq 240°C$, with footwall white mica Ar/Ar ages c. 15 Myr younger than hanging wall ages and footwall ZFT ages 5 to 10 Myr younger than hanging wall ages. However, AFT ages across the same boundary show little, if any, contrast (Fig. 13 in Campani et al., 2010).

Other fault zones with discordant hanging wall and footwall cooling histories have been identified southwest of the Simplon low-angle normal fault. Orogen-normal AFT and ZFT transects in the Western Alps in the Aosta Valley and environs show 20 Myr age differences associated with the NE-striking, intra-Penninic Internal Houiller and Briançonnais Front fault zones (Malusà et al., 2005). In a broad region southeast of the Internal Houiller fault, ZFT and AFT

ages average c. 32 and 25 Ma, respectively, although there is much scatter in the AFT ages that may reflect age-elevation effects. To the northwest of the fault zone, ZFT and AFT ages average c. 13 and 4 Ma, respectively, with far less scatter in the AFT ages.

In the Eastern Alps in the Tauern Window, even the earliest K/Ar studies revealed dramatic cooling age contrasts between the Austroalpine allochthon and its substrate. In the hanging wall, K/Ar mica ages average 77 Ma, whereas footwall K/Ar mica ages average 22 Ma (Oxburgh et al., 1966). The cooling age data of Oxburgh et al. (1966) have been augmented by at least 27 subsequent studies (Fig. 1 in Luth and Willingshofer, 2008), which collectively indicate that thermal equilibration between the hanging wall and footwall did not occur until after 20 Ma (Figs. 4, 5 in Luth and Willingshofer, 2008).

As noted above, peak metamorphic conditions in the study area (Figs. 1.1, 1.4) are generally sub-greenschist facies; but much higher grade, upper amphibolite facies, rocks are present just to the west and south. In addition, UHP rocks are found just at Monte Duria in the southernmost part of the Adula nappe (Fig. 1; just out of view to the south of Fig. 4), which yield U/Pb ages of c. 34 to 33 Ma on zircon equilibrated with spinel peridotite, which is presumably the age of maximum burial and metamorphism for the most internal end of the Adula nappe (Hermann et al., 2006). Within the study area, sub-greenschist cooling ages (Ar in mica and ZFT) span a significant range (mostly between 35 and 15 Ma), leaving a considerable uncertainty in the timing of final nappe emplacement, and especially in the timing of juxtaposition of the Pennine and Austroalpine assemblages.

Despite the large scatter in cooling ages within the Austroalpine and Penninic realms, and a scarcity of ZFT and ZHe cooling ages near the boundary between them, existing data nonetheless define a marked regional contrast in cooling histories. It is clear that a general westward-younging of all ages in the Penninic domain is fairly continuous and is the result of structural doming and rapid erosion of the Lepontine region after 20 Ma (e.g., Wiederkehr et al., 2009; Bernet et al., 2009; Schluneggar and Willet, 1999; Fox et al., 2016). It is less clear, however, whether the contrast in pre-20 Ma ages between the Austroalpine and Pennine domains in the study area is, 1) a perpetuation of the observed younging pattern such that progressively older ages simply reflect a higher structural position along the margins of the Neogene dome (Bernet et al., 2001; Evans, 2011); or 2) the result of tectonic exhumation of the Pennine zone on faults that are along or near the main Austroalpine overthrust, at some time prior to Neogene doming (e.g., Nievergelt et al., 1996; Beltrando et al., 2010; Augenstein, 2012). Unfortunately, the current *en vogue* smooth-contouring approach of thermochronometric ages across the orogen (e.g., Bernet et al., 2001, 2004, 2009; Fox et al., 2016) cannot discriminate between the simple doming and exhumation by faulting hypotheses.

	system	published data	Price (2017) data
1	AHe	33	3
2	AFT	56	0
3	ZHe	64	38
4	ZFT	31	4
5	KArBi	27	0
6	KArWM	55	8
7	KArAm	12	0
8	RbSrBi	6	0
9	RbSrWM	21	0

Table 1.1. Summary of ages compiled for this study and plotted on the geologic map in Fig. 1.4. Published data come from Ciancaleoni (2005), Flisch (1986), Hunziker et al. (1992), Knaus (1990), Rahn (2005), Wagner et al. (1977), Weh (1998), Evans (2011), Handy et al. (1996), Hunziker (1992), Philipp (1982), Armstrong et al. (1966), Peters and Stettler (1987), Thoni (1978), Augenstein (2012), Ferriero-Mahlmann (2001), Hanson et al. (1966), Steinitz and Jager (1981), Bachmann et al. (2009), and Michalski and Soom (1990).

1.3. This Study

To help resolve this ambiguity, it is necessary to determine whether hanging wall and footwall cooling histories in samples in the immediate vicinity of the fault zone, 1) are essentially the same, as predicted by the simple doming hypothesis, or 2) contrast strongly, as predicted by the tectonic juxtaposition hypothesis. As noted above, if the Pennine zone represents a subduction channel complex, its thermal history will be best defined by ZFT and ZHe thermochronometry. However, in the published data set, there are remarkably few ages for these mineral systems in the vicinity of the fault zone, making it difficult to resolve whether the cooling histories conform to one or the other of these predictions. Therefore, the goals of this study include, 1) creating a database of all published thermochronometric data in the region, 2) collecting and analyzing samples, particularly ZHe and ZFT, that are complimentary to this database, and 3) estimating the vertical structural position of all samples relative to the main Austroalpine thrust and other potentially important structures adjacent to it.

1.3.1. Published data compilation

Three-hundred-five published age dates from eastern Switzerland, northern Italy, and western Austria were compiled in a database (Tables 1, 2; sourced from: Ciancaleoni, 2005; Flisch, 1986; Hunziker et al. 1992; Knaus, 1990; Rahn, 2005; Wagner et al., 1977; Weh, 1998; Evans, 2011; Hunziker, 1992; Handy et al., 1996; Philipp, 1982; Armstrong et al., 1966; Peters and Stettler, 1987; Thoni, 1978; Augenstein, 2012; Ferriero-Mahlmann, 2001; Hanson et al., 1966;

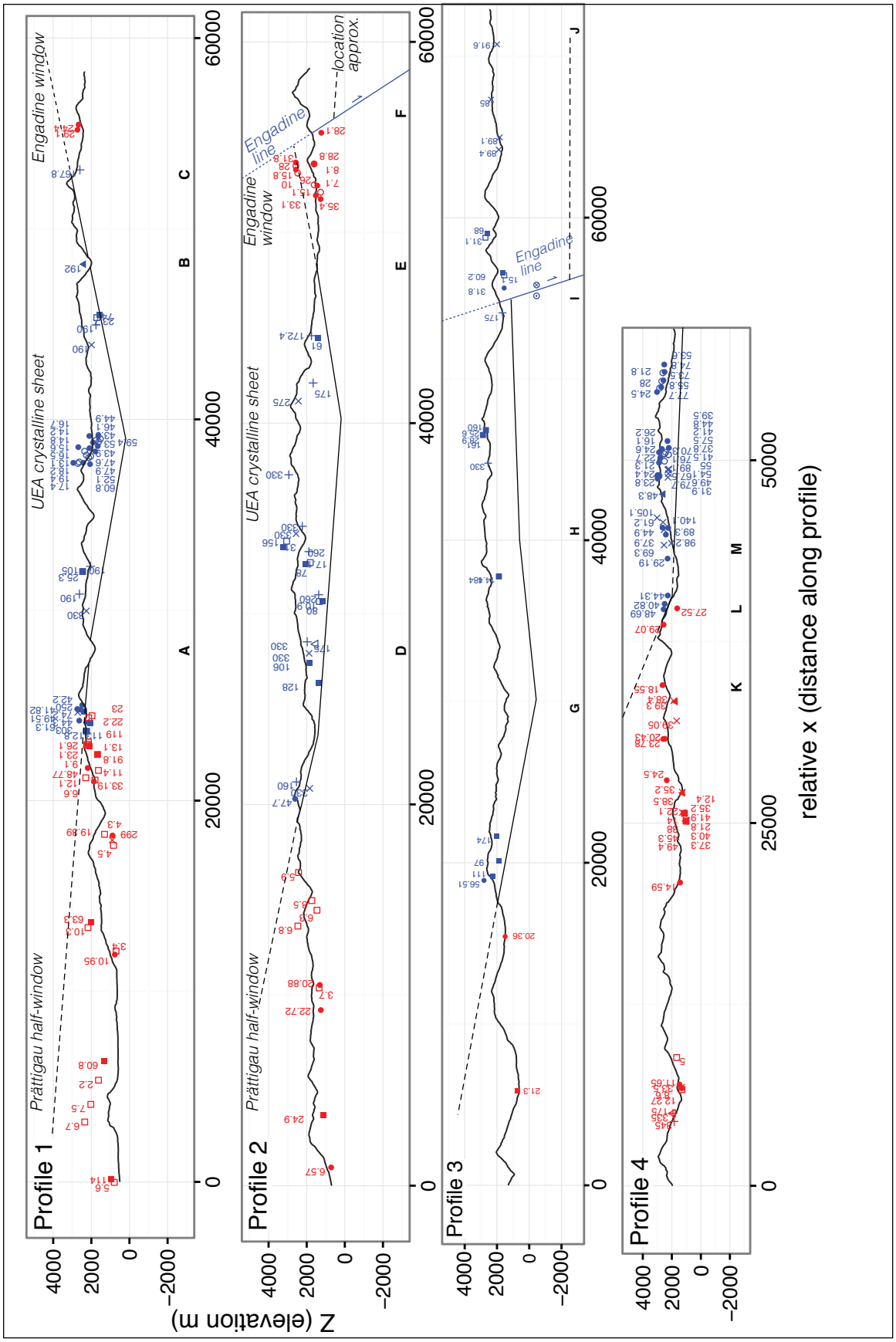
Profile 1
Profile 2
Profile 3
Profile 4
Prättigau half-window
UEA crystalline sheet
Engadine window
Engadine line
location approx.
A
B
C
D
E
F
G
H
I
J
K
L
M
Z (elevation m)
relative x (distance along profile)
4000
2000
0
−2000
0
20000
40000
60000
25000
50000

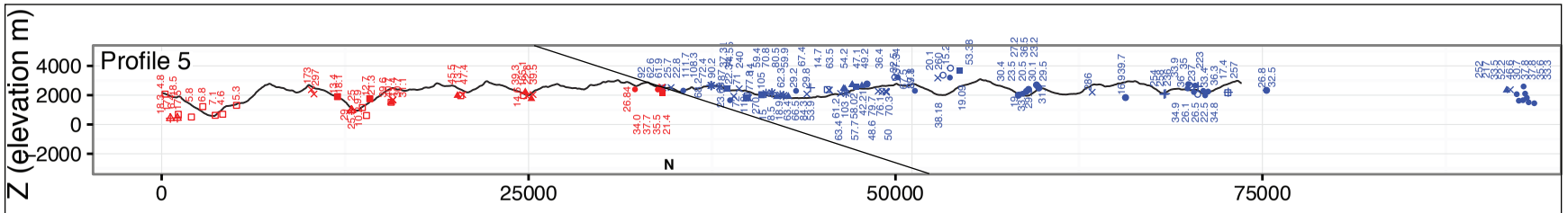

A: Gargellen window
B: Jamtal window
C: three point problem, 12° west
D: Austroalpine contact at Klosters at 1600 m elev.
requires contact east of Davos to be above 1000 m elev., possibly as high as 1500 m elev.
E: three point problem, 10° west
F: apparent dip of Engadine normal fault is 57°SE, evident in Google Earth and
on 1:25,000-scale geologic maps
G: base of crystalline sheet in Schmid et al. (1996)
H: crystalline sheet approx. 2 km thick in Schmid et al. (1996)
I: apparent dip on Engadine scissor fault 75°SE from Schmid et al. (1996)
J: 5+ km thick sheet to base of Margna from Schmid et al. (1996)
K: 22° dip on Turba mylonite zone north end near Bivio from Nievergelt et al. (1996)
L: dip slope of Piz Arblatsch
M: three point problem, 5° east
N: Turba mylonite zone, 18° apparent dip in plane of section from Nievergelt et al. (1996)

Fig. 1.5. Profiles 1-5 as shown on the geologic map (Fig. 4) with all samples projected into the sections according to their structural position. Structural-Z was measured orthogonally to the zero-datum shown in each profile. Constraints on the location and orientation of zero datum are listed and shown on profiles with bold capital letters underneath the location of the constraint. Hanging wall samples are shown in blue; footwall samples in red. Symbology is same as in Fig. 4.

Steinitz and Jager, 1981; Bachmann et al., 2009; Steinitz and Jager 1981; Michalski and Soom, 1990; Schreurs, 1993). A total of nine cooling age mineral systems are included: K/Ar amphibole, K/Ar white mica, K/Ar biotite, Rb/Sr white mica, Rb/Sr biotite, zircon- and apatite fission track, and zircon- and apatite U/Th-He. For this study, K/Ar and Ar/Ar ages are considered to be equivalent. The K/Ar-white mica category includes muscovite, phengite, illite, and "white mica". The K/Ar-amphibole category includes hornblende, glaucophane, riebeckite, and richterite. The K/Ar-biotite category includes biotite, biotite-chlorite, and phlogopite, but excludes chlorite. Ages were included in the database without filtering for grain size, i.e., white mica size fractions of >6 μm, 6-2 μm, and <2 μm were all included; generally the coarsest size fraction yielded the oldest age. We exclude four ZHe ages from the Evans (2011) dataset: One was an outlier young age from the Engadine Valley adjacent to the Engadine fault from a lone rock sample of uncertain origin; three were outlier old ages from the Err nappe on Piz Nair which overlap Ar/Ar white mica ages reported in Handy et al. (1996).

1.3.2. Sample collection and analysis

Forty-two rock samples were collected along the Austroalpine-Pennine boundary in both the hanging wall and footwall over a strike length of approximately 70 km. All samples were collected by the authors from surface outcrops and roadcuts. Means of access included car, ski lift, gondola, helicopter, hiking trail, glacier traverse, and technical mountaineering routes. From these forty-two samples, we report fifty-three new thermochronometric ages from $^{40}Ar/^{39}Ar$-white mica, zircon fission track, and zircon- and apatite U-Th/He systems (Table 1).

1.3.3. Determination of vertical structural position

Samples were projected onto five vertical WNW-ESE or ENE-WSW cross-sections (Figs. 1.4, 1.5), which were oriented to be approximately perpendicular to the strike of the Austroalpine-Pennine contact. Orientations of cross sections were rotated to account for slight changes in strike of the crystalline sheet. Attitudes of the contact were constrained using a variety of methods, including 1) solving three point problems in several locations on the west and east sides of the crystalline sheet, 2) exploiting structural windows to determine position within the allochthon, 3) projecting locations of the contact from neighboring transects, 4) using the axial surfaces of recumbent folds coring the major Pennine nappes (e.g., Niemet-Beverin fold) to constrain the orientation of the structural datum, and 5) making primary observations in the field. In addition, insofar as possible, our structural contacts conform to those found in the down-plunge projections of cross sections published by Schmid and Froitzheim (1993), Schmid et al. (1996), Scheiber et al. (2013), Milnes and Schmutz (1978), Schreurs (1993), Weh (1998), and Weh and Froitzheim (2001).

From north to south, Profile 1 is in the northern part of the northern half-window (Landquart Valley-Madrisahorn area) and contains samples from the northernmost exposures of the Pennine zone; its easternmost part includes rocks from the Engadine Window. Profile 2 includes samples from the southern part of the northern half-window, generally between the towns of Chur and Davos. Profile 3 lies along the boundary between the northern and southern half-windows, between the towns of Lenzerheide to the west and the Zernez area of the Engadine Valley to the east. Profiles 4 and 5 transect the southern half-window with Profile 4 trending WNW, parallel to Profiles 1-3, and Profile 5, trending ENE, intersects Profile 4 near its eastern terminus at St. Moritz and ends near Passo del Bernina. A group of seven samples lie in the area between Profiles 3 and 4. These samples were included in Profile 4, but their vertical position was determined by the local exposure of the base of the Austroalpine allochthon rather than its projected position from the center of Profile 4, c. 8 km to the south, which is substantially different.

In the cross sections, the zero ($z = 0$) structural datum is consistently defined at the bottom of the Arosa-Platta ophiolitic unit (or its local equivalent), generally corresponding to the Turba-Gürgaletsch fault zones as described above. Accordingly, the Schams-Falknis and Suretta nappes, Prättigau and Arblatsch flysch, North Penninic Bündnerschiefer, and Avers Bündnerschiefer represent the Pennine footwall, and the Arosa-Platta ophiolite, Tschirpen gneiss, and East Alpine crystalline nappes (Margna, Sella, Err, Corvatsch, Bernina, Julier, Silvretta, Campo, Grosina) and their respective Mesozoic cover, represent the Austroalpine hanging wall.

The along-strike width of the zone of projection for each section is approximately 7 km (a few samples lie slightly outside of this), estimated to be small enough to avoid introducing significant errors (c. 1 kilometer scale) in structural-Z (rectangular boxes in Fig. 1.4). Sample positions were projected onto cross sections according to their true elevations (m a.s.l.). In some cases (<15% of the database), owing to structural complexity, the projected structural position lay in a different structural unit on the section than its mapped position in the field. For these samples, structural-Z was adjusted up or down by a few tens to a few hundred of meters, as required to place the sample in the proper tectonic unit. Sample elevations were generally not provided in the original references and thus were assigned to every sample in the published dataset using the ASTER Global Digital Elevation Model, which has errors in elevation of approximately 10 to 25 m. By assigning every published sample an elevation-Z coordinate from this single data source, a consistent elevation is applied across the dataset. Samples from this study (Price, 2017) were assigned an elevation according to the x, y position as defined on 1:25,000-scale topographic maps published by SwissTopo (Landeskarte der Schweiz). On Profile 1, in the northern half-window, the strike of the base of the allochthon changes from north to northwest, requiring a cluster of ages from Weh (1998) to be elevated 500 m to be situated in their correct structural-Z position. Likewise, near the eastern terminus of Profile 4 due to non-planarity of the base of the alloch-

thon, a cluster of ages near Piz d'Err from Evans (2011) were adjusted downward about 800 m in structural-Z.

In addition to errors introduced by projecting perpendicular to the profiles, samples at the extreme east and west ends of the profiles with large values of structural-Z (either positive or negative) have relatively uncertain vertical position. For example, a cluster of samples (Campo-Grosina samples; Evans, 2011) that lie east of Profile 5 are too far from exposures of the base of the allochthon or any other structural datum to be assigned a credible structural-Z by projection (Fig. 1.4). Thus, they were assigned a moderate structural-Z of about 5.5 km, which is approximately equal to that of the Bernina nappe.

The structurally lowest samples in the dataset come from the Adula nappe at the western terminus of Profile 4, and the structurally highest samples come from the Bernina nappe at the eastern terminus of Profile 5, yielding a total vertical structural relief of approximately 22 km. This structural thickness is similar to values depicted in regional cross sections painstakingly constructed by down-plunge projection of the Pennine nappe stack (e.g., Milnes and Pfiffner, 1980; Schreurs, 1993; Schmid et al., 1996).

1.3.4. Methods

1.3.4.1. Mineral Separation

Mineral separates were made using the conventional steps of pulverization, washing, and sieving, followed by magnetic and heavy-liquid separation. For apatite and zircon, separates were concentrated prior to magnetic separation using a gold panning technique. Because separates obtained using this technique included a large fraction of 20 μm (length) grains, the recovery of the coarser grains in the separate used for analysis was likely >90%. The gold panning step reduced sample volume to < 20 mL, greatly expediting magnetic and heavy-liquid separation. For white mica separates, multiple steps at progressively higher amperage were used for magnetic separation. Grains which adhered to coarse paper ("paper shake" method) were sieved at -250, -180, and -125 μm and then hand-picked under a 50x binocular microscope. All samples analyzed for $^{40}Ar/^{39}Ar$ were -250/+125 μm in size, and preference was given to the coarsest size fraction that was also optically free from inclusions and defects.

1.3.4.2. Analytical Methods

The $^{40}Ar/^{39}Ar$ analyses were performed at the U.S. Geological Survey (USGS) in Denver, Colorado. Together with grains of the $^{40}Ar/^{39}Ar$ standard Fish Canyon sanidine, samples were irradiated for 7 MWH in the central thimble position of the USGS TRIGA reactor (Dalrymple et al., 1981), while also being rotated at 1 rpm. Cadmium foil was used during the irradiation to prevent unwanted ^{40}Ar produced from ^{40}K. Following irradiation, the samples and standards

were loaded with tweezers to a stainless steel sample holder and then placed into a laser chamber with an externally pumped ZnSe window. The reported incremental heating data represent results from 1-3 individual mineral grains. The volume of the mostly stainless steel vacuum extraction line, including a cryogenic trap operated at -130°C and two SAES™ GP50 getters (one operated at room temperature (0 A), one operated at 2.2 A), is estimated to be 450 cc. A combination of turbo molecular pumps and ion pumps maintain steady pressures within the extraction line of < 1.33 x 10-7 Pa. Samples were incrementally heated in steps of 90 seconds, by controlled power output of a 50W CO_2 laser equipped with a beam homogenizing lens resulting in uniform energy over the entire sample surface. During laser heating any sample gas released was exposed to the cryogenic trap and was further purified for an additional 120 seconds by exposure to both the cryogenic trap and the SAES™ getters. The sample gas was expanded into a Thermo Scientific ARGUS VI™ mass spectrometer, and argon isotopes were analyzed simultaneously using 4 Faraday detectors (^{40}Ar, ^{39}Ar, ^{38}Ar, ^{37}Ar) and one ion counter (^{36}Ar). Following data acquisition of 10 minutes, time zero intercepts were fit to the data (using parabolic and/or linear best fits) and corrected for backgrounds, detector inter-calibrations, and nucleogenic interferences. The *Masspec* computer program written by A. Deino of the Berkeley Geochronology Center was used for data acquisition, age calculations, and plotting. All $^{40}Ar/^{39}Ar$ ages reported in Table 2 and the Appendix are referenced to an age of 28.201±0.046 Ma for the Fish Canyon sanidine (Kuiper et al., 2008), the decay constants of Min et al. (2000), and an atmospheric $^{40}Ar/^{36}Ar$ ratio of 298.56±0.31 (Lee et al., 2010). Laser fusion of >10 individual Fish Canyon Tuff sanidine crystals at each closely monitored position within the irradiation package resulted in neutron flux ratios reproducible to ≤ 0.25% (2σ). Isotopic production ratios were determined from irradiated CaF_2 and KCl salts, and for this study the following values were measured: $(^{36}Ar/^{37}Ar)Ca$ = (2.48±0.10) x10-4; $(^{39}Ar/^{37}Ar)Ca$ = (1.22±0.10) x10-3; and $(^{38}Ar/^{39}Ar)K$ = (1.29±0.03) x10-2. Cadmium shielding during irradiation prevented the formation of any measurable $(^{40}Ar/^{39}Ar)K$. $^{40}Ar/^{39}Ar$ plateau ages (and uncertainties) are considered the best estimate of the cooling age of the minerals and were calculated from samples if three or more consecutive heating steps released ≥ 50% of the total ^{39}Ar and also had statistically (2σ) indistinguishable $^{40}Ar/^{39}Ar$ ages. Any use of trade, product, or firm names is for descriptive purposes only and does not imply endorsement by the U.S. Government.

Zircon fission track analyses were performed by Apatite to Zircon, Inc. Zircon grains from the Fish Canyon Tuff (Naeser locality) U-FT and U-Pb age standard, and zircon grains from the unknown samples, were mounted in FEP Teflon, polished to expose internal grain surfaces at a minimum depth of about 20 μm, and etched for 36-72 hours in a eutectic melt of NaOH-KOH to expose natural fission tracks for viewing using an optical microscope. Etched zircon grains were viewed using a Nikon Optiphot2 optical microscope affixed with a 100X dry objective and

AUSTROALPINE						
system	sample	nappe	lithology	structuralZ (km)	age (Ma)	err (1SE)
AHe	110830-03	Bernina	quartz diorite	6.6	19.09	2.32
AHe	110831-02	Bernina	quartz diorite	7.4	15.22	1.84
AHe	110831-03	Bernina	quartz diorite	6.65	20.1	1
KArWM	110825-14	Corvatsch	S-C mylonite, augen gneiss	4.9	50	0.6
KArWM	110830-03	Bernina	quartz diorite	6.6	260	60
KArWM	130817-11	Silvretta	gneissic granite	0.23	250	20
KArWM	130819-08	Platta	spilite	0.1	61.9	1.7
KArWM	130819-08b	Platta	spilite	0.1	62.6	1.2
KArWM	130823-03	Margna	augen gneiss	1.26	87	6
ZFT	110823-06	Margna	augen gneiss	1.28	74.55	10.21
ZFT	110826-08	Sella	orthogneiss	4	58.02	11.43
ZFT	110831-02	Bernina	quartz diorite	7.4	53.38	7.53
ZHe	110824-01	Margna	white mica schist	0.55	23.63	0.35
ZHe	110825-03	Corvatsch	S-C mylonite	4.2	42.21	10.2
ZHe	110825-14	Corvatsch	S-C mylonite, augen gneiss	4.9	37.34	3.2
ZHe	110830-03	Bernina	quartz diorite	6.6	38.18	2.4
ZHe	130816-18A	Tschirpen	felsite	0.22	42.17	3.08
ZHe	130817-03	Falknis	"Mandelschiefer" flysch	0.1	44.26	5.39
ZHe	130817-11	Silvretta	gneissic granite	0.23	49.51	3.74
ZHe	130817-12	Silvretta	gneissic granite	0.26	41.82	3.17
ZHe	130819-08	Platta	spilite	0.1	25.69	1.23
ZHe	130819-09	Platta	spilite	0.22	22.79	1.61
ZHe	130823-03	Margna	augen gneiss	1.27	22.34	0.54
ZHe	BD15-08	Err	metapsammite	0.33	44.31	3.31
ZHe	DL15-02	Tschirpen	greenschist granitoid	0.32	47.72	6.99
ZHe	JUL15-01	Julier	Julier granodiorite	1.9	29.19	1.95
ZHe	JUL15-01	Julier	Julier granodiorite	1.9	29.19	1.95
ZHe	LEN15-03	Silvretta	augen gneiss	1.1	56.51	9.38
ZHe	PL15-07	Platta	metadiorite	0.05	48.69	7.22
ZHe	TSC15-01	Tschirpen	greenschist granitoid	0.06	40.82	2.68
PENNINE						
KArWM	130818-04	Prättigau	Gyrenspitz, grey psammite	-2.45	299	5
KArWM	130819-07	Avers	grey metapelite	-0.05	37.7	1.1
ZFT	130819-06	Avers	grey metapelite	-0.05	35.5	11.7
ZHe	130818-04	Prättigau	Gyrenspitz, grey psammite	-2.45	19.39	1.84
ZHe	130819-06	Avers	phyllite	-0.05	21.36	0.74
ZHe	130821-07	Arblatsch	Val Gronda phyllite	-0.78	26.84	1.79
ZHe	AD15-01	Adula	white mica schist	-13.58	11.65	0.62
ZHe	AD15-03	Adula	white mica schist	-13.7	12.27	1.17
ZHe	ARB15-01	Arblatsch	coarse-grained psammite	-0.2	29.07	1.11
ZHe	BD15-03	Arblatsch	sandstone	-0.55	27.52	1.84
ZHe	BD15-07	Bündnerschiefer	phyllite	-3.3	23.78	1.56
ZHe	BD15-15	Bündnerschiefer	metapelite	-5.85	6.57	0.35
ZHe	DL15-04	Prättigau	sandstone	-3.2	20.88	1.17
ZHe	DL15-05	Prättigau	sandstone	-3.48	22.72	2.48
ZHe	KK15-02	Prättigau	Eggberg Series, gritstone	-1.1	33.19	3.54
ZHe	KK15-05	Prättigau	Ruchberg Series, gritstone	-0.65	48.77	7.92
ZHe	KK15-11	Prättigau	Pfavigrat Series, psammite	-3.4	10.95	1.2
ZHe	LEN15-05	Tomül	Ruchberg Series, sandstone	-0.65	20.36	1.08
ZHe	SUR15-01	Suretta	quartz eye porphyry	-4.5	24.5	1.36
ZHe	SUR15-02	Suretta	gneissose granitoid	-3.22	20.43	1.14
ZHe	SUR15-03	Suretta	gneissose granitoid	-1.7	18.55	1.17
ZHe	SUR15-04	Tambo-Aruea	orthogneiss	-8.08	14.59	0.58

Table 1.2. New Ar/Ar, fission track, and (U-Th)/He cooling ages presented in this study. ZHe and AHe ages are mean ages of a population of single grain ages. ZFT ages are pooled-ages. 40/39Ar ages (KARWM) are integrated ages. Errors are standard error of the mean for ZHe and AHe and 95% confidence interval for ZFT and $^{40}Ar/^{39}Ar$.

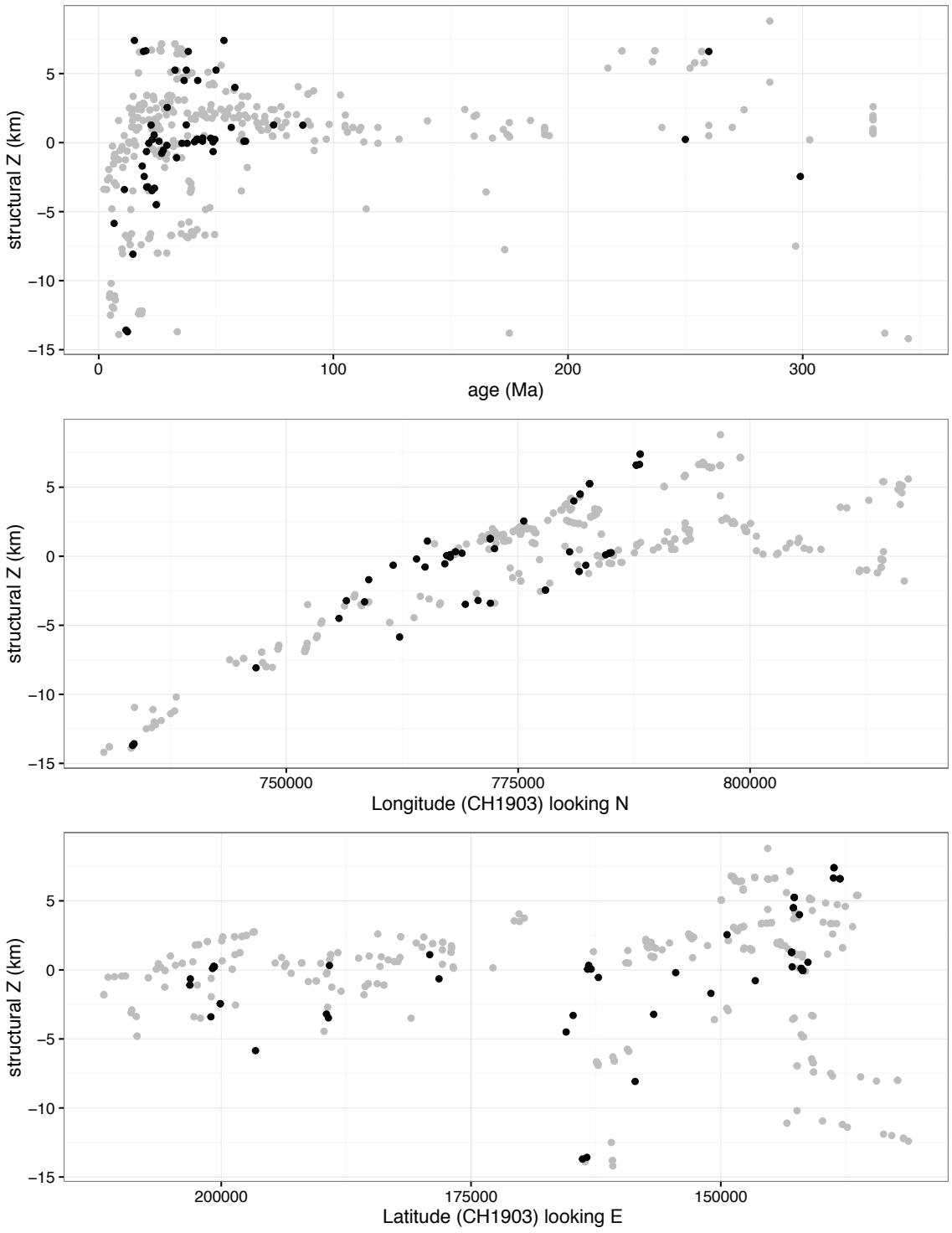

Fig. 1.6. Structural-Z vs. age, longitude, and latitude. New data are colored black; published data are grey. Locations where black dots do not overlap grey dots are unique sample locations from this study.

a Lumenara Infinity 2 1600 x 1200 pixel color digital camera, aided by an Applied Scientific Instrumentation MS-2000 XY stage and Applied Scientific Instrumentation Z-Axis drive. Fission track counting was done after LA-ICP-MS, by R. Donelick, on a computer display screen, using previously collected image stacks, and in the vicinity of the laser ablation pit, a view of which was visible during counting (Donelick et al., 2005). Zircon grains selected for fission track age dating, including Fish Canyon Tuff zircon for fission track age calibration, were analyzed by laser ablation-inductively coupled plasma mass spectrometry during two sessions (ZFTUPb_13_06_08 - sample 1292-2 and ZFTUPb_13_06_20 - samples 1292-3, 4, 8, 10, 11, 14) to determine uranium concentrations for fission track age calculation and U-Pb ages for selected areas for which fission tracks were counted.

U-Th/He analyses on apatite were completed at the California Institute of Technology. ^{4}He was measured on a Pfeiffer Prisma quadrupole mass spectrometer using isotope dilution methods referenced to calibrated quantities of ^{3}He (Farley, 2002). Concentrations of U and Th were measured on an Agilent 7500 inductively coupled plasma mass spectrometer.

One round of U-Th/He zircon analyses were split such that ^{4}He concentrations were measured on a quadrupole mass spectrometer at Caltech (same as for apatite U-Th/He above), and U, Th, Sm concentrations were measured at the University of Colorado Boulder in the CU TRaIL facility. This "split" analysis affected three grains in the current study (110830-03, 110825-03, 110825-14). The rest of the U-Th/He zircon analyses were done completely at the University of Colorado Boulder using the following method: Individual mineral grains were handpicked using a Leica M165 binocular microscope equipped with a calibrated digital camera and capable of both reflected and transmitted, polarized light. We select grains >60 µm in width and with various morphologies and/or clarities to improve the likelihood of selecting grains with a variety of effective uranium (eU) concentrations. Individual grains are measured twice for length and width, the dimensions of which define the 'spherical equivalent radius', packed into Nb tubes, and loaded into an ASI Alphachron He extraction and measurement line. The packet is placed in the UHV extraction line (~$3x10^{-8}$ torr) and heated with a 25W diode laser to ~800-1100°C for 5 to 10 minutes to extract radiogenic ^{4}He. The degassed ^{4}He is then spiked with approximately 13 ncc of pure ^{3}He, cleaned via interaction with two SAES getters, and analyzed on a Balzers PrismaPlus QME 220 quadrupole mass spectrometer. This procedure is repeated at least once to ensure complete mineral degassing. Degassed grains are then removed from the line, and taken to a Class 10 clean lab for dissolution. Zircon is dissolved using Parr large-capacity dissolution vessels in a multi-step acid-vapor dissolution process. Grains (including the Nb tube) are placed in Ludwig-style Savillex vials, spiked with a ^{235}U-^{230}Th tracer, and mixed with 200 µl of Optima grade HF. The vials are capped, stacked in a 125 mL Teflon liner, placed in a Parr dissolution vessel, and baked at 220°C for 72 hours. After cooling, the vials are uncapped and dried down on a 90°C hot

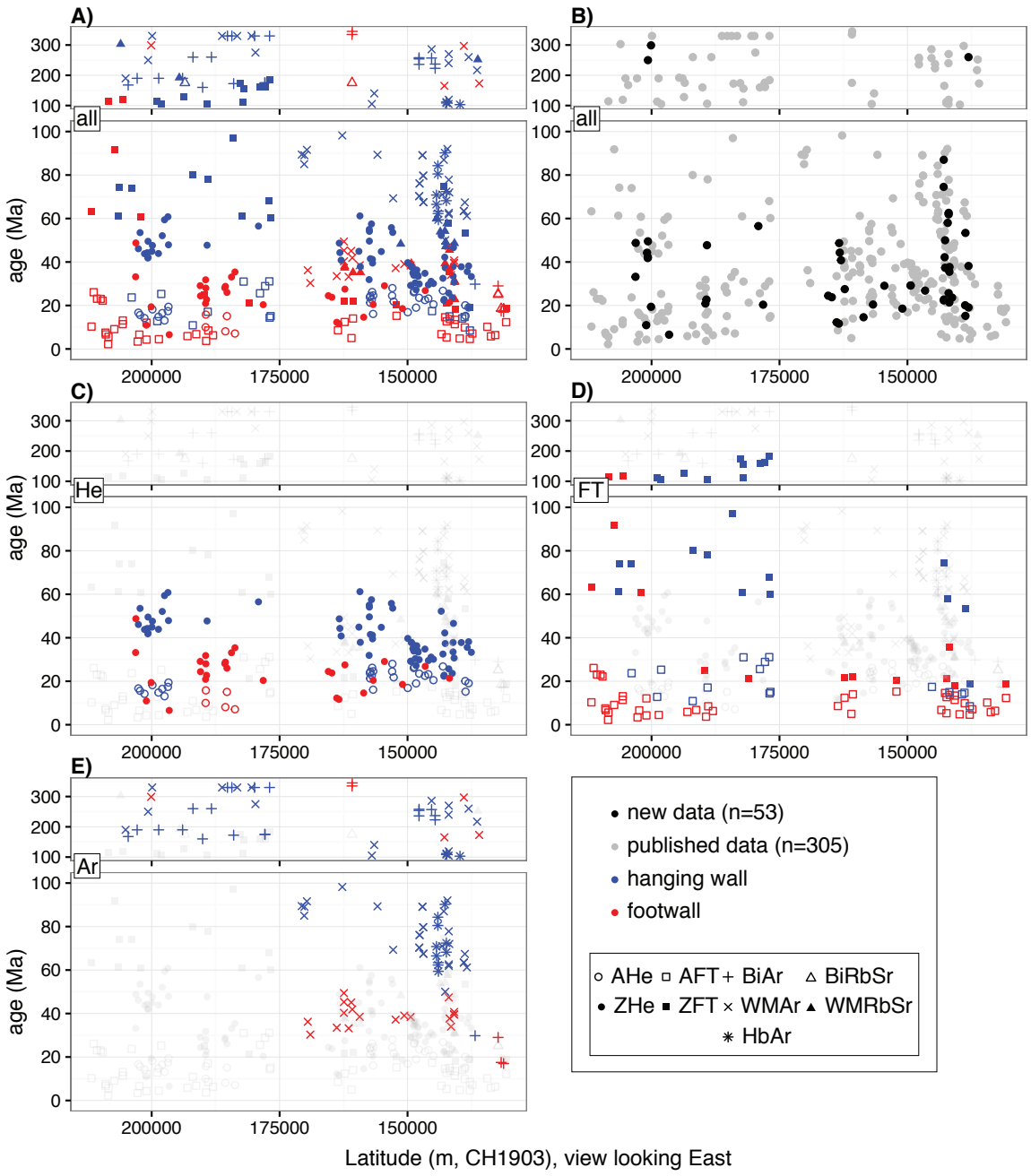

Fig. 1.7. Age vs. latitude plots for all data compiled for this study (n=358). Table of data supporting these plots is found in Appendix 1.

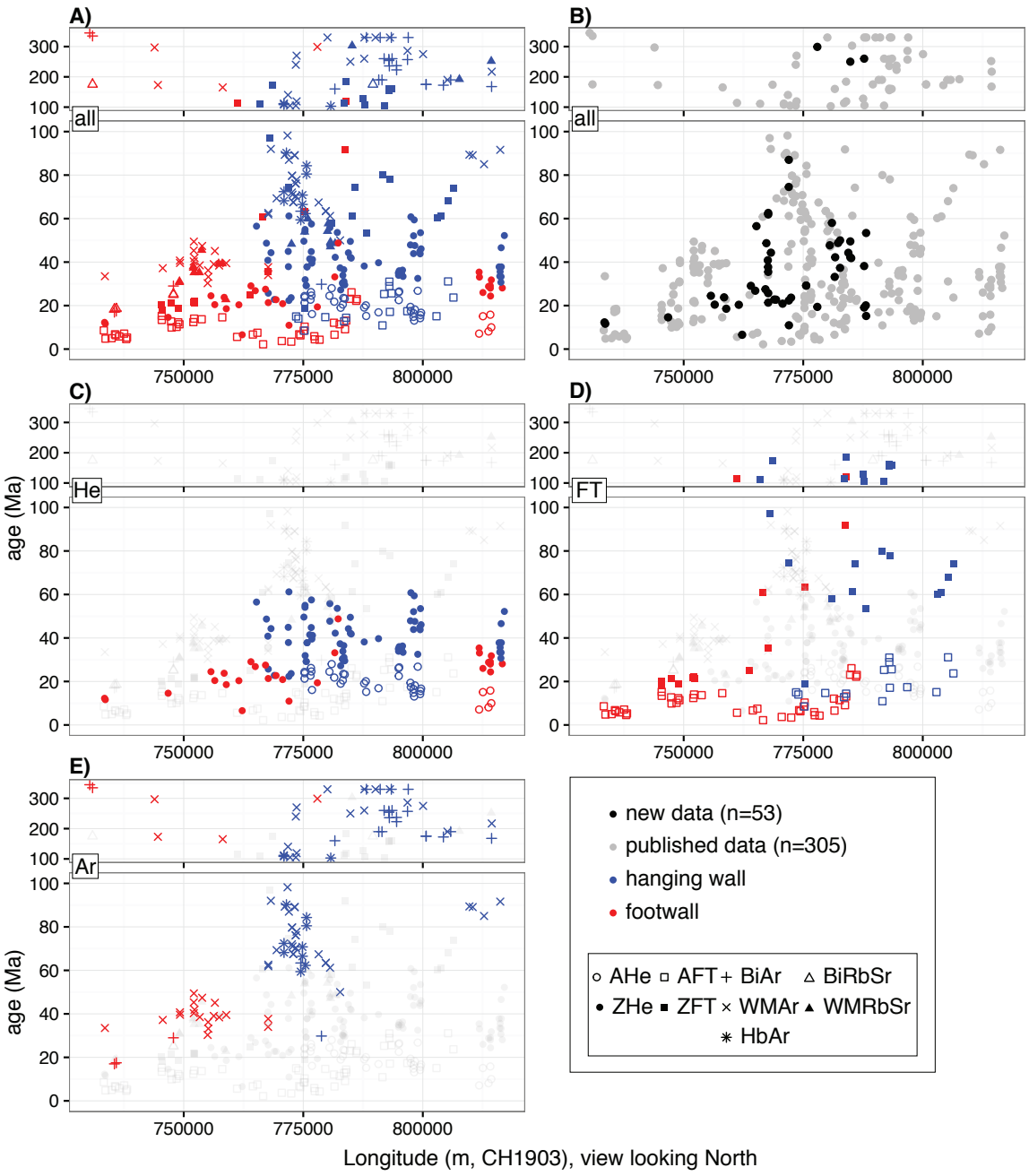

Fig. 1.8. Age vs. longitude plots for all data compiled for this study (n=358). Table of data supporting these plots is found in Appendix 1.

plate until dry. The vials then undergo a second round of acid-vapor dissolution, this time with 200 µl of Optima grade HCl in each vial that is baked at 200°C for 24 hours. Vials are dried down a second time on a hot plate. Once dry, 200 µl of a 7:1 HNO_3:HF mixture is added to each vial, the vial is capped, and heated on the hot plate at 90°C for four hours. Final solutions are diluted with 1 to 3 mL of doubly-deionized water, and taken to the ICP-MS lab for analysis. Sample solutions, along with normal solutions and blanks, are analyzed for U, Th, and Sm content using a Thermo Element 2 magnetic sector mass spectrometer equipped with a Teflon spray chamber and platinum cones. Once the U, Th, and Sm concentrations have been measured, He age dates and all associated data are calculated using the methods described in Ketcham et al., (2011). Every batch of samples includes standards run sporadically throughout the process to monitor procedures and maintain consistency from run to run. Long term averages of Fish Canyon Tuff zircons and Durango Fluorapatites run in the CU TRaIL facility are 28.7 ± 1.8 Ma (n=150) and 31.1 ± 2.1 (n=85), respectively.

1.3.5. Data

The thermochronological results from this study (Table 2) broadly overlap previously published ages when plotted as a function of structural position vs. age (Fig. 1.6). Both datasets define a sideways "L"-shape, where the short limb represents a narrow range of relatively young (Tertiary) ages in the Pennine footwall, and the long limb represents a broad span of older (Late Paleozoic to mid Tertiary) ages in the Austroalpine hanging wall. As a rule, the new ages reported in Table 1.2 for any given mineral system confirm previous constraints on the thermal histories of both the hanging wall and footwall, but, critically, they extend these constraints to a structural position much closer to their respective boundaries, facilitating an assessment of whether thermal histories adjacent to the fault are similar or different to one another, and similar or different to the thermal histories in the respective structural cores of the Penninic and Austroalpine realms. We present the data in three basic forms: 1) simple plots of age vs. geographic coordinates (easting, northing), 2) age vs. our estimates of relative structural position (structural-Z), and 3) subsets of ages from key mineral systems in hanging wall and footwall that are closest to the base of the Austroalpine allochthon ("pincher" plots).

We plot age versus geographic coordinate according to the 1903 Swiss Grid (Figs. 1.7 and 1.8 for north-south and east-west cross sectional views) following the convention in Fig. 1.4 and used in all subsequent plots (fission track ages are squares; U/Th-He ages are circles; closed for zircon, open for apatite; Rb-Sr ages are triangles, open for biotite, closed for white mica; Ar ages are asterisks (amphibole), 'X's (white mica), and plus symbols (biotite), colored red for footwall and blue for hanging wall). The plots in Figs. 1.7 and 1.8 include a composite showing data for all mineral systems (frame A), a plot discriminating previously published ages from the new ages

presented here (frame B), and plots showing subsets of data according to U-Th/He, fission track, and Ar systems (frames C, D, and E, respectively).

A few general trends are evident in the data. The first is that, in the U/Th-He plot looking east (Fig. 1.7C), the hanging wall and footwall ZHe ages are separable into older and younger populations by an approximately linear boundary with a slope of 0.22 m.y./km. This line is mainly defined by a northern cluster of hanging wall ages of ≥40 Ma at 200,000N (latitude in middle of Prättigau half-window), a southern cluster of hanging wall ages of ≥29 Ma at 149,000N (latitude of St. Moritz), and the broad distribution of footwall ages between 180,000N and 140,000N that lie below the line. Out of a population of 102 ages total, only one footwall ZHe age plots above the line, at the far northern end of the study area (at the latitude of the Madrisahorn), and two hanging wall ZHe ages plot below the line at the southern end of the study area (at the latitude of Maloja Pass). Across the entire width of the U/Th-He plot (Fig. 1.7C), footwall ZHe ages persistently overlap hanging wall AHe ages.

A second noteworthy trend is observed in the fission track data (Fig. 1.7D), in which an array of the youngest hanging wall ZFT ages, ranging from 61 Ma in the north to 53 Ma in the south, define a line of slope 0.12 m.y./km. Across the southern three-quarters of the study area, a line of similar slope of 0.14 m.y./km is defined by an array of six footwall ZFT ages ranging from 18 to 25 Ma. There is one outlier to this trend with an age of 36 +/- 12 Ma at the southern end of the section, which in any event has error nearly an order of magnitude greater than any point in the trend. In the northern one-quarter of the section (at the latitude of the northern half-window), footwall ZFT ages are much older and concordant with the hanging wall ZFT ages, ranging from 61-119 Ma. Between the two trends, there is a temporal gap between footwall and (minimum) hanging wall ZFT age of 36 m.y. that persists for at least 60 km across orogenic strike.

A third trend is observed in the Ar mica ages (Fig. 1.7E) in which the population of ages younger than 100 Ma are strongly bi-modal, with one mode ranging from 60-98 Ma corresponding to the hanging wall and a second mode ranging from 18-49 Ma corresponding to the footwall. With one notable exception, there is an absence of Ar-mica ages between 50 and 60 Ma. The range of hanging wall ages dramatically expands from north to south. Ages in the north are consistently Jurassic or older (150-330 Ma), whereas ages in the central part of the section are as young as 80 Ma and, in the southern-most part of the section, as young as 60 Ma. In addition to these patterns, the total age population in the footwall is strongly split between the Tertiary population and a smaller population that ranges from Paleozoic to Jurassic. There is a complete absence of <50 Ma Ar ages north of 170,000N (latitude of Tiefencastel). In the hanging wall, with one notable exception, there are no K/Ar ages younger than 60 Ma north of 138,000N.

The systematic geographical trends apparent in the north-south latitudinal section are not apparent in the east-west longitudinal section (Fig. 1.8) indicating that most of the variation in

cooling ages occurs across, rather than along, orogenic strike. However, there does appear to be, both in individual mineral systems and in the dataset as a whole, a westward younging trend in footwall ages in the western one-third of the dataset. For instance, near 750,000E, Ar-biotite, ZHe, and AFT ages are 30, 20, and 12 Ma, respectively, whereas near 730,000E, the same three systems record ages of 18, 12, and 5 Ma, respectively. As discussed above, the relatively strong variation in the western-most ages likely reflects the occurrence and subsequent cooling after the c. 18 Ma Lepontine Barrovian metamorphism (Wiederkehr et al., 2009). In this projection, there is significant overlap between ZHe ages in hanging wall and footwall with no overall trend otherwise apparent in either population, with the exception of westward-younging of footwall ZHe ages as just discussed.

Because we are fundamentally interested in the relationship of cooling history with respect to the base of the Austroalpine allochthon, we plot age against structural-Z. We assume that the post-Cretaceous cooling history of the hanging wall was almost exclusively the product of erosional unroofing but leave open the possibility that footwall cooling resulted from both tectonic and erosional unroofing. For erosion rates of c. 1 mm/yr or more, the rate of upward

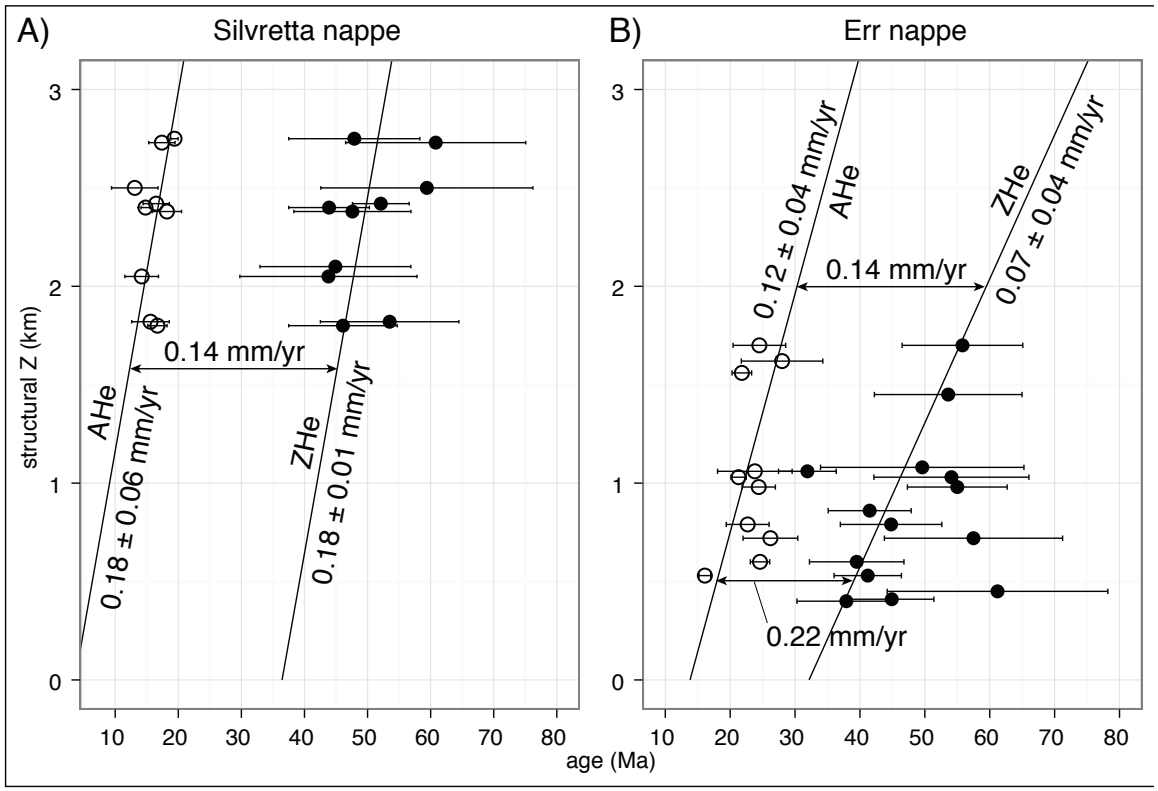

Fig. 1.9. Structural Z vs. age for (A) Silvretta and (B) Err nappes using AHe and ZHe data from Evans (2011) fit with a weighted regression (York et al., 2004) that accounts for error in age (standard deviation of a population of single grain ages in a sample) and structural-Z (±0.2 km constant). Both datasets indicate slow cooling and erosion rates of order 0.1-0.2 mm/yr through most of the Tertiary for large crystalline units of the Austroalpine allochthon, which is in general agreement with estimates made by Hurford et al. (1989) and Evans (2011).

advection of heat becomes significant relative to conductive cooling (Péclet number > 1; e.g., Fig. 2.25 in Allen and Allen, 2006). For rates of c. 0.5 mm/yr or less, advection is negligible, and hence the age gradient with structural depth is a reasonable estimate of the erosion rate. For any given mineral system, cooling ages will ideally young with structural depth. With age-structural-Z data on multiple mineral systems, there are two quasi-independent methods to estimate the rate of descent of isotherms through the crust. The first is simply age variation with depth; the second are differences in age between mineral systems in samples at the same depth. In the latter case, the change in temperature with time can be converted to change in depth with time if a geothermal gradient is assumed.

Linear regression (York et al., 2004) of depth profiles for ZHe and AHe ages from two crystalline nappes in the hanging wall, Silvretta and Err (Fig. 1.9; ages and locations shown in Figs. 1.4 and 1.5) yield slopes of 0.18 +/- 0.33 mm/yr for Silvretta-ZHe, 0.18 +/- 0.06 mm/yr for Silvretta-AHe, 0.07 +/- 0.03 mm/yr for Err-ZHe, 0.12 +/- 0.03 mm/yr for Err-AHe. For weighting purposes, error in the ordinate is qualitatively estimated to be 0.2 km for structural-Z, whereas error in the abscissa is the standard deviation (1σ) of the population of single grain ages for a given sample. For Silvretta (Fig. 1.9A), the difference in ZHe and AHe age as a function of depth is essentially invariant and yields a gradient dZ/dt of 0.14 mm/yr, assuming a 25°C/km geothermal gradient. In contrast, for Err (Fig. 1.9B), the ZHe and AHe gradients vary in age as a function of depth and decrease proportional to structural-Z, yielding an approximate dZ/dt of 0.16 mm/yr at 2 km structural-Z and 0.22 mm/yr at 0.5 km structural-Z. We interpret the regressions from Err and Silvretta ZHe and AHe data to be representative of the Austroalpine hanging wall as a whole and posit that the sheet has an average long-term exhumation rate of c. 0.1-0.2 mm/yr from Paleogene to Neogene time. Our estimate is consistent with estimates made for the Silvretta nappe by Hurford et al. (1989) using AFT ages, for the Err nappe by Evans (2011) using HeMP modeling of ZHe and AHe ages, and for the Silvretta nappe by Evans (2011) using raw thermochronometric ages.

In contrast to the broad spectrum of ages and discernable positive age-elevation slopes in some subsets of data in the hanging wall, ages in the footwall are both more tightly clustered and show comparatively little variation in age with structural depth. For example, for subsets of data with a reasonably large depth range, ages do not vary by more than 10 m.y. over nearly 10 km of total structural depth, yielding slopes corresponding to exhumation rates $\geq$1.0 mm/yr. HeMP modeling of Pennine footwall ages from the Engadine window yielded an exhumation rate of c. 1.7 mm/yr during the time period 52-38 Ma (Evans, 2011).

As presented in the format of Figures 1.7 and 1.8, relationships between structural features and cooling ages are not obvious, except as might be suggested by gross differences in age between hanging wall and footwall samples. To quantitatively address these differences, we present

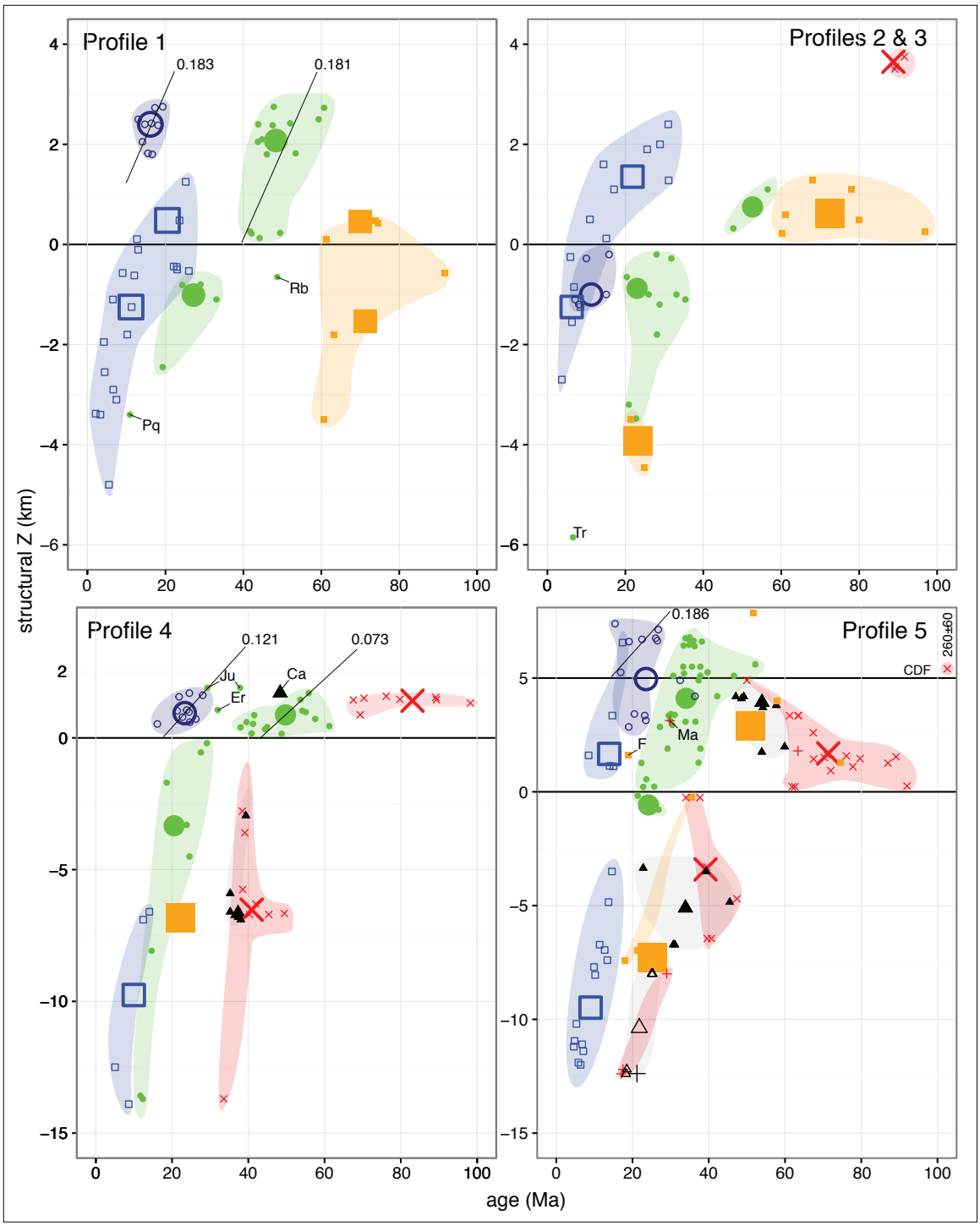

Fig. 1.10. Structural-Z vs. age plots from the five profiles defined in this study. Raw data are shown as points. Shaded regions are grouped by cooling system, and the same color is used in hanging wall and footwall. Profiles two and three have been combined since they cover similar geologic terrain and have a paucity of data in certain key cooling systems. Best fit weighted regression lines (viz. Fig. 9) are shown for certain hanging wall nappes. Outliers to the general trends are labeled: Ca: Carungas, F: Forno, Ju: Julier, Ma: Margna, Pq: Pragmartin quarry (Bündnerschiefer), Rb: Ruchberg (Prättigau flysch). Corvatsch detachment fault (CDF) shown at +5 km structural-Z in Profile 5.

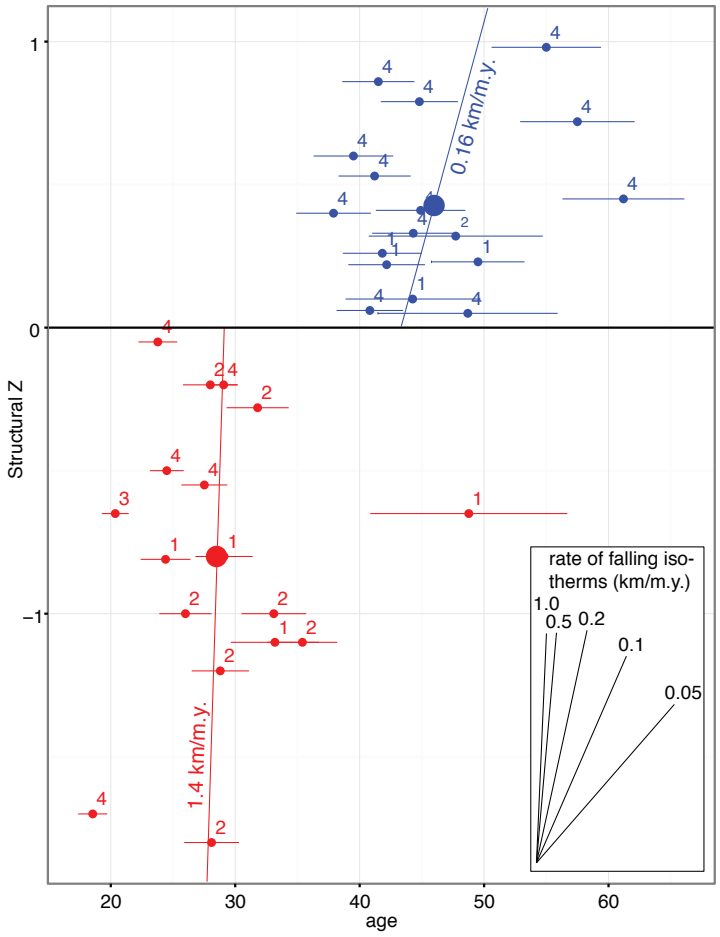

Fig. 1.11. Composite plot of subset of ZHe ages for samples <1 km above the fault for the Austroalpine hanging wall and <2 km below the fault for the Pennine footwall extracted from Profiles 1-4. Large dots show mean age of the datasets plotted at the median structural depth. Slopes through the dots represent nominal vertical age gradients (see discussion in main text) and are not formal regressions through the data.

a subset of ages (0-100 Ma), colored by system, plotted versus structural-Z (Fig. 1.10). In general, for mineral systems with closure temperatures of ZHe (180°C) or higher, all profiles show distinct discontinuities between hanging wall and footwall cooling ages at Z=0, with age differences of a few 10s of m.y. In contrast, for systems with closure temperatures of AFT (110°C) or lower, no age discontinuity is apparent at Z=0 or elsewhere. Two exceptions to this general pattern are the ZFT system on Profile 1 and the ZHe system on Profile 5 where no age discontinuity is apparent at Z=0. However, there is an indication that an additional discontinuity exists at c. +5 km structural-Z associated with the Corvatsch detachment fault (CDF in Profile 5, Fig. 1.10; also termed "Corvatsch normal fault" by Schmid et al., 1996 and "Corvatsch mylonite zone" by Nievergelt et al., 1996 and Liniger, 1992), particularly defined by a pair of disparate $^{40}Ar/^{39}Ar$ white mica ages above and below that fault.

Of the 358 ages used in our study, only nine outliers (2.5%) do not conform to the general cooling pattern and are labeled individually on Figure 10. For the ZHe system, they include one relatively old footwall age from the Lower Tertiary Ruchberg Formation (Rb) in Profile 1, two relatively young footwall ages from Bundnerschiefer at the Pragmartin quarry (Pq) in Profile 1

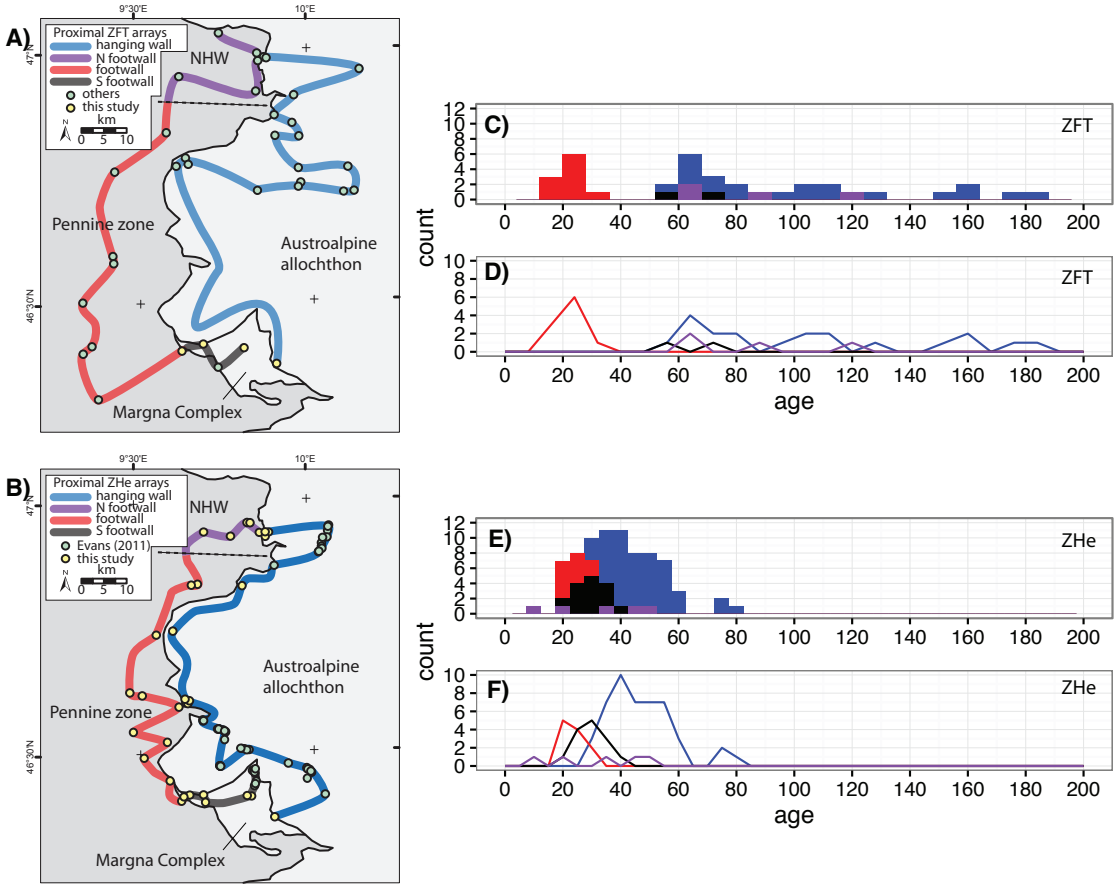

Fig. 1.12. 'Pincher' plots of age constraints on the Austroalpine allochthon from samples closest to the fault contact. A, B) Location maps of ZFT and ZHe, respectively, ages. NHW: Northern Half-Window. C, E) Age stacked-histograms of ZFT and ZHe, respectively, colored as per the legends in A and B. D, F) Age frequency-polygons of ZFT and ZHe, respectively. Same data as in C and D. Purple line has been dotted to make it more legible.

and at Trimmis (Tr) in Profile 2, and three relatively young hanging wall ages in crystalline rocks of the Err nappe (Er) and Julier granite (Ju) on Profile 4. In terms of the total population of ZHe ages represented in Fig. 1.10, labeled outliers represent 3/28 (10.7%) of the footwall subset, whereas labeled outliers represent 3/69 (4.3%) of the hanging wall subset. Other data outliers include one young RbSr-white mica age from the Carungas nappe (Ca) in Profile 4, one young ZFT age from the Forno unit (F) and one young KAr-biotite age from the Margna nappe (Ma), both in Profile 5. Given the very small representation of these outliers in the dataset, we ignore them in our analysis and interpretation of the data.

1.3.5.1. Geographic Pattern of Mid-Tertiary Cooling

Perhaps the most significant pattern, other than the contrast in cooling history of the hanging wall and footwall, is the geographic pattern within the Austroalpine allochthon in ZHe ages,as alluded to above. Rocks within a few km above the base of the Austroalpine allochthon have ZHe ages of 40 to 50 Ma in Profiles 1 to 4, which decrease to 20 to 30 Ma in Profile 5, assuming

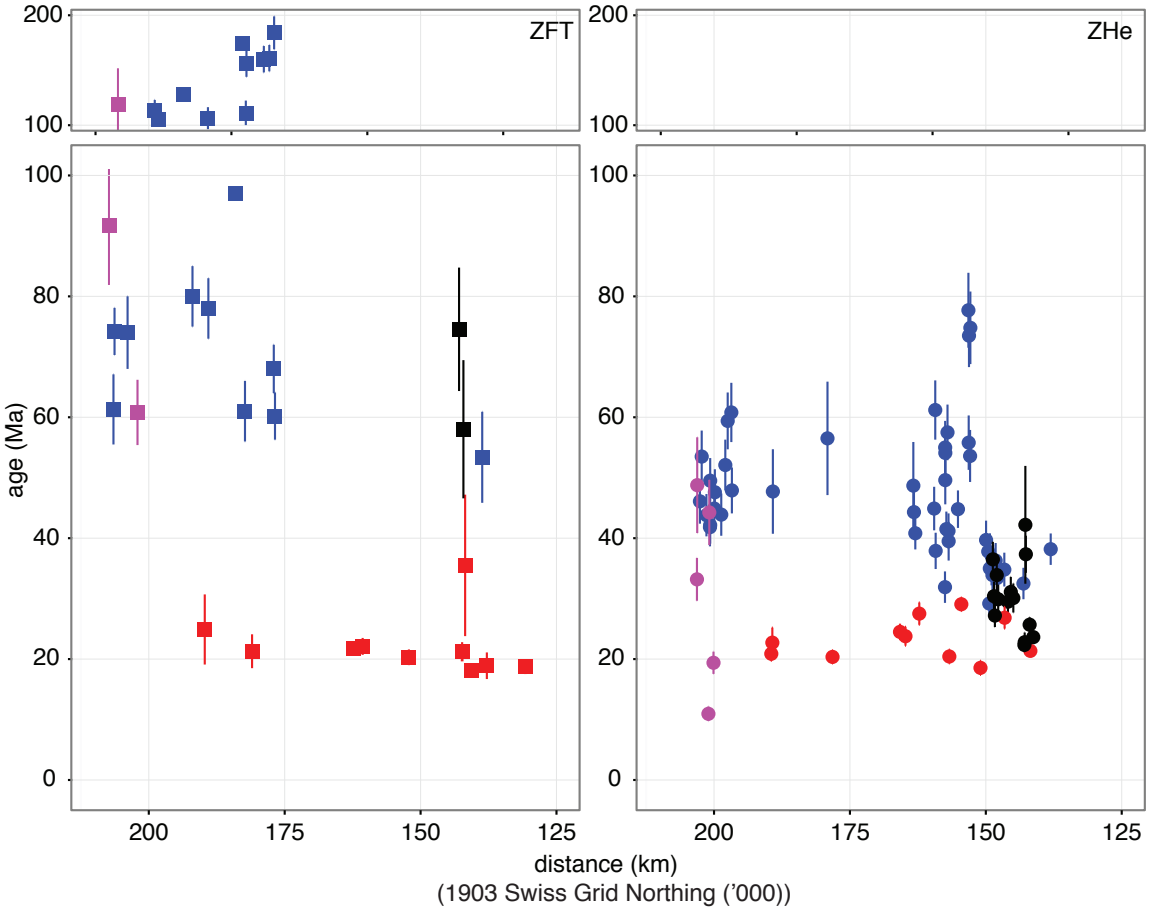

Fig. 1.13. Age vs. latitude subset showing gaps in ages between the hanging wall and footwall, especially evident in the ZFT data but persistent still in the ZHe data between 150 and 190 km N. Blue indicates hanging wall; red indicates footwall; magenta indicates Prättigau half-window (Profile 1); black indicates Margna complex (color scheme same as in Fig. 12).

the base of the allochthon corresponds to the Turba mylonite zone. For Profiles 1 to 4, there appears to be no systematic differences in ages of footwall samples within c. 2 km of the top of the Pennine Zone (Fig. 1.10). From north to south across these transects, there is also no systematic trend in either footwall or hanging wall ZHe ages. Averaging the ages and projecting the mean age to the fault (structural-Z = 0), the footwall age is about 29 Ma and the hanging wall age is about 43 Ma, a gap of some 14 m.y (Fig. 1.11)

A second pattern is apparent in ZFT and ZHe age histograms for samples geographically adjacent to the boundary, which suggests the data are divisible into four geographical arrays (Figs. 1.12 and 1.13): 1) the Austroalpine hanging wall, 2) the central portion of the Pennine footwall, 3) a cluster of ages at the north end of the Prättigau half-window, and 4) ages in the "Margna complex," an amalgamation that includes the Margna nappe and surrounding portions of the Platta and lowermost East Alpine nappes, including the Corvatsch "digitation," but excluding the

Err and Bernina nappes. The Prättigau and Margna complex arrays are defined by distinctive age patterns in the footwall. In the former, footwall ZFT and ZHe ages increase and become similar to hanging wall ages (magenta points in Figs. 1.12 and 1.13). In the latter, hanging wall ZHe ages decrease and become similar to footwall ages, whereas ZFT ages remain similar to the rest of the hanging wall (black points in Figs. 1.12 and 1.13). Even though the Margna complex has late Cretaceous-early Tertiary ZFT ages similar to the Austroalpine allochthon, it has much younger ZHe ages (consistently 22-30 Ma) than most of the Austroalpine (which is generally >35 Ma). This is seen in Profile 5 where the Margna complex age distribution overlaps the Austroalpine population at its upper end and the Pennine population at its lower end. Thus, the Margna complex appears to have a thermal history that requires a tectonic history that is distinct from both the Austroalpine and Pennine zones.

1.4. Discussion

The northern and southern extremes of the dataset (Prättigau half-window and Margna complex) appear to be the "exceptions that prove the rule," that the hanging wall and footwall each yield a characteristic age pattern involving multiple thermochronometers, and that the two patterns differ markedly. We return to the question posed earlier (Section 1.2.4, Previous thermochronology) of whether the contrast in ages between hanging wall and footwall resulted from erosion through an intact crustal section, or upward motion of heat across a crustal-scale fault. The data argue strongly in favor of the latter, both at the level of individual transects (Fig. 1.10) and at the level of composite datasets for samples closest to the boundary (Figs. 1.11, 1.12, and 1.13). Below, we use these age patterns and petrologic depth constraints to estimate Tertiary temperature and depth histories of the hanging wall and footwall, and we speculate on their significance for the timing and mode of juxtaposition.

1.4.1. Model Thermal Histories

In modeling thermal histories, our goal is to estimate the first-order pattern using a traditional blocking temperature approach (e.g., Hurford et al. 1989), where each mineral system defines a closure event which records the downward passage of an isotherm at a particular time and place. This basic approach is justified, first, by the fact that constraints on the thermal history of the Austroalpine-Pennine boundary zone between 300 °C (lowest closure temperatures of Ar/Ar and Rb/Sr mineral systems) and 100 °C (AFT) are, to date, only available in unpublished theses (e.g., Weh (1998), Evans (2011), and Augenstein (2012)). Second, the abundant data that now exist record, with considerable spatial and temporal redundancy, the relatively rapid descent through mineral closure temperatures of at least six key systems, which in descending order of closure at nominal cooling rates include Ar white mica (425 °C), Rb/Sr biotite (300 °C), ZFT

(240 °C), ZHe (180 °C), AFT (110 °C) and AHe (70 °C) (Hunziker et al., 1992; Farley, 2002). Clearly, uncertainties in the thermal histories of the major rock masses can be better estimated by: (1) multi-domain diffusion modeling of K-feldspar, (2) closure temperature studies of individual grains; (3) numerical modeling of cooling curves (e.g., HeFTy), and (4) joint, multidimensional thermal modeling of heat conduction and mineral system diffusivity (e.g. Pecube, QTQt, and similar approaches). Nonetheless, we are confident that the signal of strongly contrasting thermal histories in the hanging wall and footwall are well enough defined by both sample distribution and reproducibility of individual ages that a simple "closure event" approach is sufficient to address the fundamental issue of the timing and kinematics of juxtaposition of the Pennine and Austroalpine zones.

The first-order pattern of the dataset (Figs. 1.10, 1.11, 1.12, and 1.13) indicates that any differences that may exist within either the Austroalpine or Pennine masses adjacent to the boundary, except at the extreme northern and southern limits of its exposure, are negligible in comparison to the difference observed between the masses. The lower age-structural-Z gradients in, and wider spacing of ages between, systems in the hanging wall versus the footwall both indicate earlier, slower cooling of the hanging wall. We therefore assume that below c. 300 °C each plate cooled monotonically, such that each mineral system experienced a single closure event at a certain time in the hanging wall and footwall of each profile area. We also assume that within each plate, temperature varied with structural-Z at a rate of 25 °C/km.

We estimate the closure event to have occurred at the mean age for each mineral system in each plate and each profile of the dataset and estimate the depth (structural-Z) of the event to be the median depth of the sample set for a given system. We then account for vertical variation in the time of closure events using our estimated age gradients converted to depth (Figs. 1.9, 1.10), which yield 0.1 to 0.2 mm/yr in the hanging wall and 1.0-1.5 mm/yr in the footwall. The precise choice of geothermal gradient (say, 20°C/km versus 25 °C/km) introduces proportionate error in our conversion of temperature to depth, but the error is small (c. 20%) in comparison to the range of possible age gradients (which vary by more than a factor of two). We note that, despite this relatively large uncertainty, the scaling between the gradients and total vertical variation in the sample set introduces only a small error in assigning a precise depth for a given closure event. For 0.1-0.2 mm/yr and 1.0-1.5 mm/yr rates of falling isotherms in hanging wall and footwall respectively, error in the timing of closure events are 0.5-1.0 m.y. and 0.067-0.1 m.y., respectively, per 100 m of error in vertical position of the sample. Thus, even if our approach of using the median depth of the samples is in error by several hundred meters, the age error introduced to the closure event is small compared to the standard error in the mean age for the mineral system. We estimate a nominal age error in the model closure event curves to be the standard error in the radiometric age of the main systems, or about ± 10% of the measured age. For the hanging wall

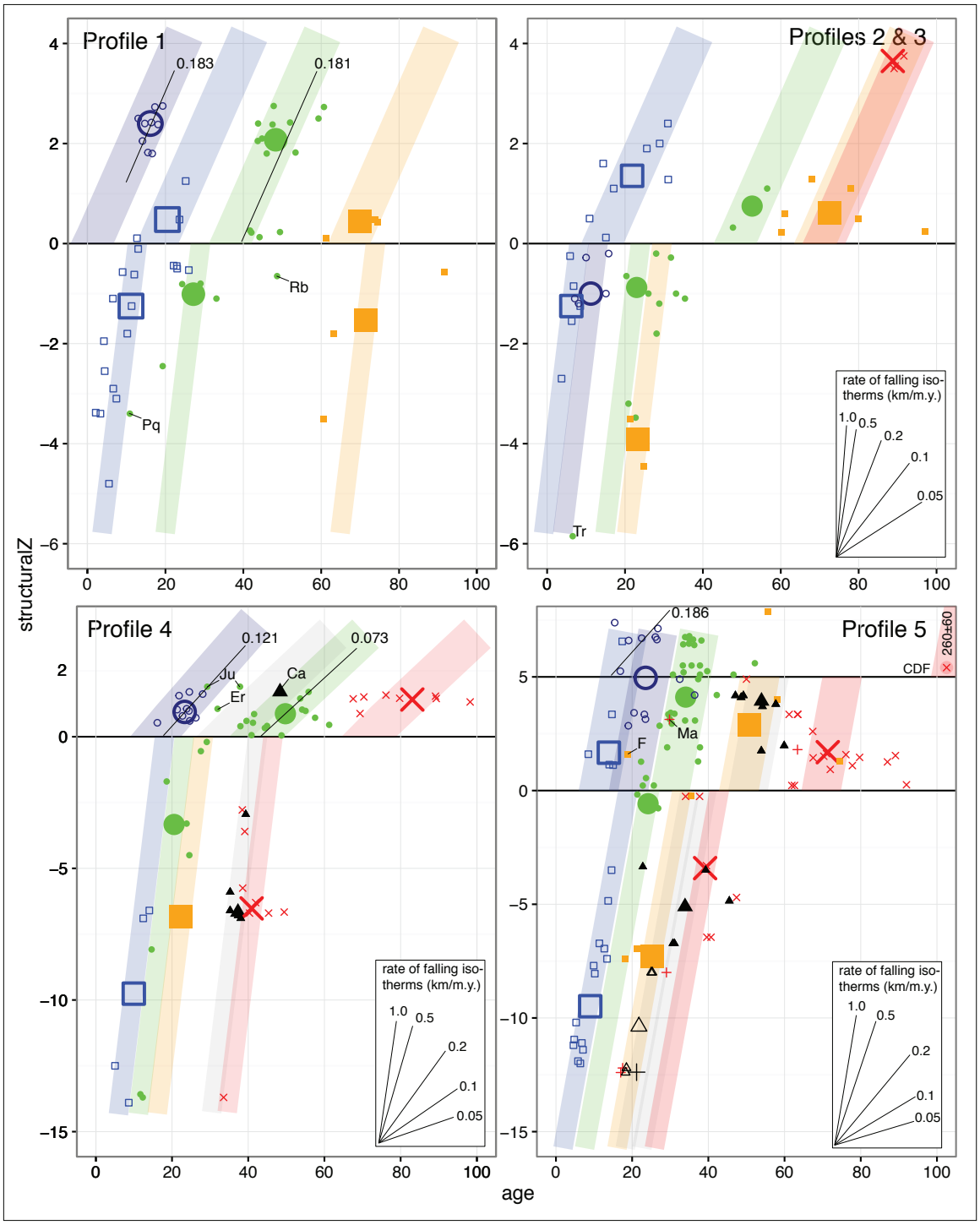

Fig. 1.14 . Structural-Z vs. age models from the five profiles defined in this study, based on the raw data shown in Figs. 4, 7, 8, and 10. Shaded swaths have been given a cooling slope that approximates what is observed by either formal regression of raw points and their errors (as for curves in the hanging wall of Fig. 9) or by a generalized best fit "region," particularly for the footwall points. Large summary points for each system are plotted according to calculated mean age and median structural Z. Outlier abbreviations same as in Fig. 10. Note that scale is the same in the top two plots but varies in the bottom two plots.

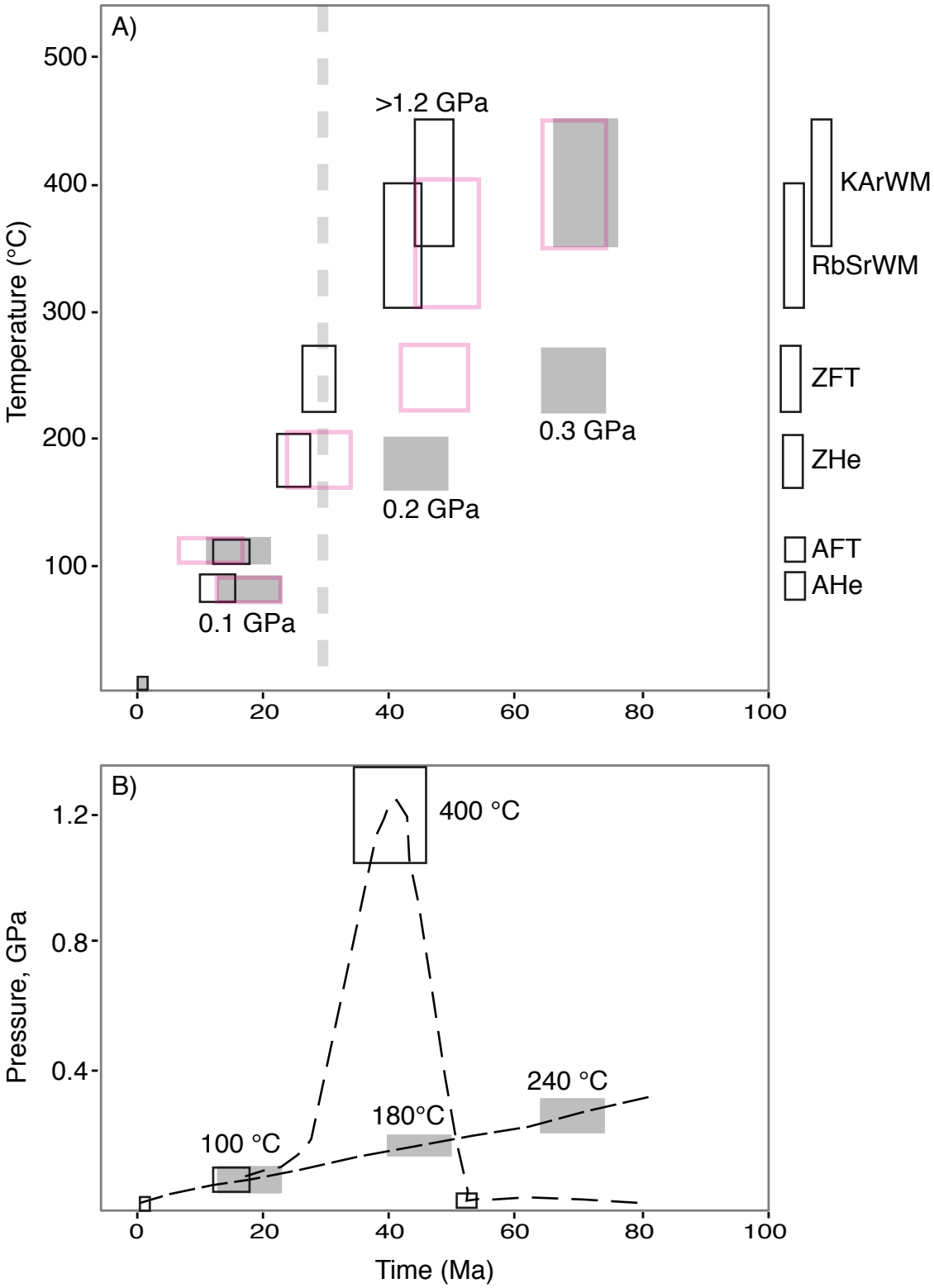

Fig. 1.15. A) Temperature vs. time cooling paths and B) Pressure vs. time decompression paths derived from our thermal model for the Austroalpine hanging wall (closed grey boxes) and Pennine footwall (black rectangles) based on average and projected data shown in Fig. 14 and Table 3. The Margna complex (pink rectangles) departs from the rest of the Austroalpine hanging wall at c. 50 Ma and joins the footwall at c. 25 Ma. Vertical dashed line is approximate age of Bergell intrusion. Rectangles on the side of the plot show the range of likely closure temperatures for each of the indicated systems. This range is what determines the vertical extent of the boxes representing the geologic units.

Hanging wall

Profile	AHe	AFT	ZHe	ZFT	RbSrWM	KArWM
1	3	18	37	68	-	-
2,3	-	14	45	69	-	72
4	18	-	43	-	35	72
5*	18	12	29	47	49	69

Footwall

	AHe	AFT	ZHe	ZFT	RbSrWM	KArWM
1	-	13	29	74	-	-
2,3	13	8	24	30	-	-
4	-	18	23	28	42	47
5	-	19	25	33	43	43

Table. 1.3. Ages used to make the T-t plot in Fig. 15, determined by projecting age gradients in Fig. 14 to the intercept at Z=0. Uncertainty on the ages is 5 m.y. for the hanging wall and 2.5 m.y. for the footwall.

this is (0.1)(50 Ma) = ± 5 m.y., and for the footwall (0.1)(25 Ma) = ± 2.5 m.y.

According to this approach, Figure 1.14 shows our estimates of the time of closure events for each mineral system, as a function of structural-Z in both the hanging wall and footwall. In general, closure events at Z=0 are, within error, the same for AFT, at about 10 to 20 Ma, but differ markedly for all higher temperature systems. The models are very similar for Profiles 1 through 4, with the exception of pre-Alpine (>60 Ma) ZFT ages in the footwall on Profile 1. The abrupt younging of the ZFT ages moving from Profile 1 to Profile 2 appears to "capture" the presence of the ZFT closure isotherm (240 °C) in the footwall at c. 25 Ma, because there is no (known) major structural break in the footwall between these two profiles.

Profile 5 is distinctive in having younger hanging wall ZHe and ZFT ages than Profiles 1 through 4. There are important differences between the Pennine, Margna complex, and Austroalpine structural levels along Profile 5. As originally noted by Bachmann et al. (2009), there are a series of anomalously young mica Rb/Sr ages (c. 50 Ma) located along the top of the Margna complex (black triangles in Fig. 1.4) that appear to record the onset of Tertiary Alpine deformation and metamorphism. We corroborated this result with a Tertiary $^{40}Ar/^{39}Ar$ white mica age (50.0 ± 0.6 Ma) from an S-C mylonite near the top of the Margna complex in the Corvatsch digitation (summit of Piz Corvatsch). These early Tertiary ages contrast with Paleozoic Ar-mica ages that occur a few hundred meters structurally above the mylonite in the lower Bernina nappe, and hence we refer to this contact between the Margna complex with its Corvatsch digitation and the Lower East Alpine Bernina nappe as the Corvatch detachment fault (CDF on Figs. 1.10 and 1.14, Profile 5). The Margna "complex" forms a unique cooling curve (pink boxes, Fig. 1.15) that indicates rapid cooling from middle to lowest greenschist facies by the Early Tertiary followed by a "stewing" and/or slow-cooling period until near the end of the Oligocene at which time it

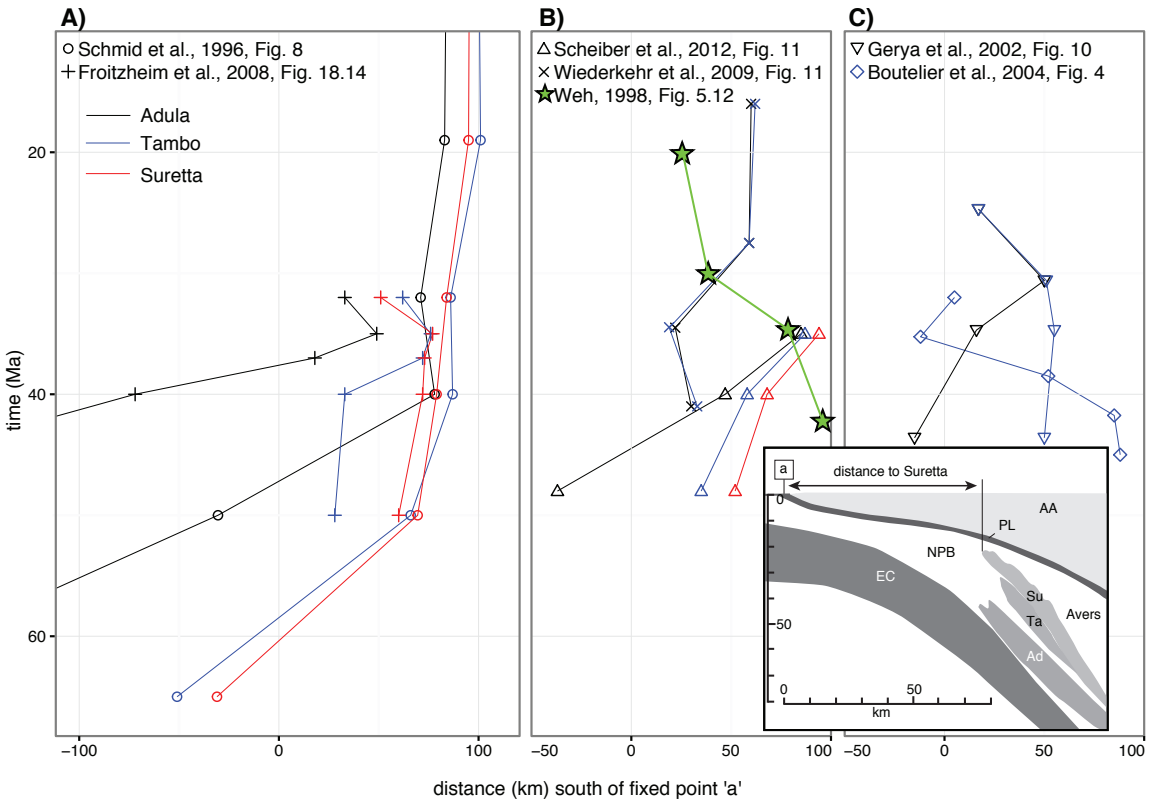

Fig. 1.16. North-south motion of material points in the Alpine accretionary wedge relative to a fixed point in the Austroalpine allochthon (i.e., Austroalpine overlap distance), measured from the front (N-end) of the Austroalpine allochthon to the front (N-end) of the nappe in question (see inset for example). Plot is organized by A) regional reconstructions, B) local nappe-scale reconstructions, and C) Numerical and analogue modeling. Inset profile from Schmid et al., 1996.

reaches ZHe closure temperature. This general pattern of rapid cooling followed by an isothermal "stewing" is very similar to that recorded in the Sesia-Lanzo zone in the Western Alps (cf. Fig. 9 in Hurford et al., 1989).

We use the vertical age gradients (Fig. 1.14) to estimate the mean age of a closure event for each system at Z = 0 to construct a composite cooling history for the central parts of the hanging wall, footwall, and Margna complex (Fig. 1.15**;** Table 1.3). We average the age estimates for cooling events in Profiles 2, 3 and 4, which are very similar, but treat Profiles 1 and 5 as separate entities. The thermal history allows us to make an estimate of the two parameters defined in the Introduction: the time of thermal equilibration of the hanging wall and footwall, t_e, and the difference in temperature between hanging wall and footwall at a given time during Pennine metamorphism, ΔT. If we have interpreted the thermal history correctly, the temperature contrast between hanging wall and footwall at 40 Ma, ΔT_{40} was approximately 170 °C, when the difference in depth between the Pennine and Austroalpine realms may have been c. 1.0 GPa (c. 30 km depth) (Fig. 1.15B). According to our model, t_e occurs somewhere between 29 and 18 Ma. The juxtaposition of Austroalpine and Pennine domains is traditionally regarded as having occurred

prior to the intrusion of the Bergell pluton at 32-30 Ma (Schmid et al., 1996; Nievergelt et al., 1996). However, the footwall did not pass through 240 °C (Tc for ZFT) until c. 29 Ma at the earliest, whereas the hanging wall was already residing below the Tc for ZHe for approximately 15 m.y. prior to this time (Figs. 1.11, 1.14, and 1.15; Table 1.3). Even at 30 Ma, our cooling curves demonstrate that the hanging wall and footwall had not yet thermally equilibrated, and their temperature difference, ΔT_{30}, was still c. 90°C, greater than the difference between ZFT and ZHe closure (c. 60°C). We note that our samples come from outcrops that are too distant from the Bergell intrusion for the closure systematics to have been perturbed by its thermal aureole or any form of contact metamorphism.

AHe and AFT fission-track ages are somewhat complex and locally inverted with AHe ages being slightly older, as has been observed before in these two systems (Flowers and Kelley, 2011). Age intercepts at Z = 0 for the AFT and AHe transects from Profiles 2, 3, and 4 are roughly the same: 18, 13, and 8 Ma in the footwall versus 18 and 14 Ma in the hanging wall (Table 3), which indicates that thermal equilibration occurred by the time the two domains reached AFT and/or AHe closure. Thus, our thermal model allows the lower bound on the timing of footwall and hanging wall thermal equilibration, t_e, to be as young as 18 Ma (ΔT_{18} = 0 °C). However, we favor thermal equilibration to have occurred closer to 29 Ma to perhaps as young as 25 Ma.

1.4.2. Palinspastic Implications

A survey of published cross sectional reconstructions for the Alps, particularly through the easternmost part of the Pennine zone (755,000 easting; e.g., Schmid et al., 1996), indicates very little enthusiasm among most authors for large amounts of top-south motion of the Austroalpine allochthon relative to the Pennine zone. For these models, where possible, we compiled the relative north-south position of key material points in the Pennine zone relative to a fixed point ‘A’ within the Austroalpine allochthon through time (Fig. 1.16). Material points include what are now the lobate northern “noses” of the three highest crystalline nappes (Adula, Tambo, and Suretta, e.g., Fig. 1.16 inset). Two of the models are reconstructions of cross sections spanning the entire orogen (Schmid et al., 1996; Froitzheim et al., 2008; Fig. 1.16A). Three are based on more local, nappe-scale, reconstructions (viz. Suretta, Scheiber et al., 2012; Gotthard-Adula, Wiederkehr et al., 2008; and Grava, Weh, 1998; Fig. 1.16B). Two are based on physical models using numerical (Gerya et al., 2002) and experimental (Boutelier et al., 2004) techniques (Fig. 1.16C). Of the five geologically-based models, two present little to no southward motion of the upper nappes relative to the Austroalpine allochthon, two indicate c. 20 km of top-south motion between 40 and 30 Ma, and one presents approximately 70 km of top-south motion between 40 and 20 Ma. In comparison, the numerical model predicts c. 40 km of top-south motion, and the experimental model features nearly 100 km top-south motion.

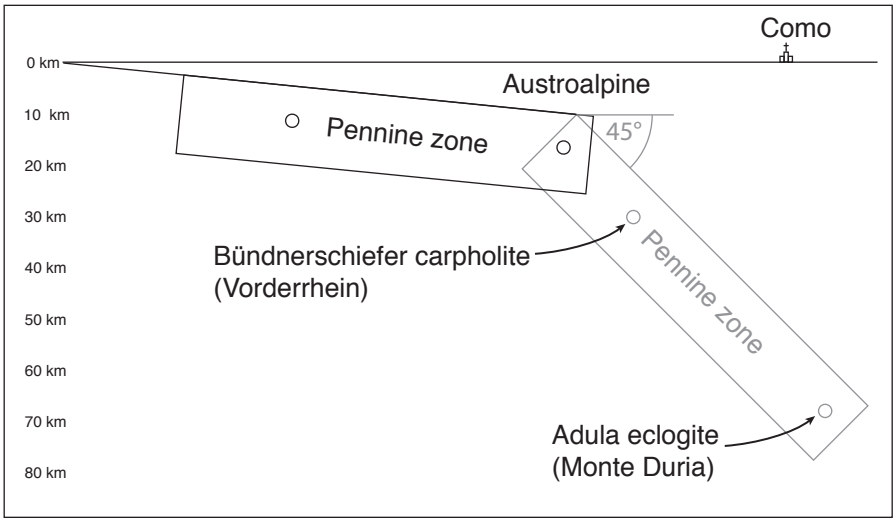

Fig. 1.17. Schematic north-south reconstruction of the Central Alps at c. 35 to 40 Ma which emphasizes that the high-P metamorphic grade of rocks in the Pennine zone can be accounted for by subducting a coherent slab approximately 80 km in length by 15 km thick to 10 to 80 km depth. Sketch also emphasizes the distance the exhumed Pennine zone had to travel to become juxtaposed against the thin overriding Austroalpine plate.

A simple palinspastic reconstruction, based on our models of the low-temperature cooling histories, places the Penninic footwall in a subduction channel just south of the present-day Insubric fault,with an upper end at a paleodepth of 10 km (approximate thickness of the orogenic lid) at 29 Ma, just after intrusion of the Bergell complex (Fig. 1.17). For a nominal inclination of the channel of 45° (modern Mediterranean Benioff zones tend to be steeper than this), the lower end of the Penninic mass (southern part of the Adula-Simano nappe complex) would have lain at a paleodepth of at least 10 + 80/(cos 45) = 74 km, corresponding to a pressure of about 2.2 GPa, which is within the observed range of 2.0-3.0 GPa estimates for (U)HP metamorphism at c. 32-34 Ma in the Monte Duria area (Meyre et al., 1999; Hermann et al., 2006; Herwartz et al., 2011). Assuming this geometric analysis is basically correct, it provides independent confirmation that pressures recorded by (U)HP metamophic assemblages reflect paleodepth, rather than zones of localized “tectonic overpressure” (e.g. Mancktelow, 1993, 1995; Pleuger and Podladchikov, 2014).

Given that the Austroalpine allocthon lay above the Pennine zone during mid-Paleogene exhumation (Fig. 1.17), the steep, closely-spaced age-depth curves in the footwall (Figs. 1.10 and 1.14) cannot be the result of rapid erosion, at least within the study area outlined in Figure 4. Rather, they record rapid cooling in the wake of fault juxtaposition of the subduction channel assemblage against shallow upper crustal rocks in the forearc wedge, which had a thickness of <10 km by that time (Fig. 1.15).

From a methodological perspective, we stress the fact that, without the use of the two zircon thermochronometric systems (Fig. 1.15), the primary contrasts and estimates of the timing of key tectonic events are difficult to recover in upper crustal exposures of accretionary systems, where temperatures of deformation are < 300°C. In this case, to rely solely on AFT, AHe, and

Ar-Ar systematics in micas, the null hypothesis, that the hanging wall and footwall had identical thermal histories between c. 40 Ma and the present, could not be falsified (Fig. 1.15).

1.4.3. On the steady state theory of the Alps

In the past two decades, there have been numerous attempts to use thermochronometric systems to determine uplift and exhumation rates across the Alps (e.g., Hurford, 1986; Hurford et al., 1989; Bernet et al., 2001, 2004, 2009; Fox et al., 2016), the accuracy of which depends upon the initial assumption that the Alps have behaved as a steady-state, erosionally dominated, tectonically inert system since at least middle Miocene, c. 15 Ma (Bernet et al., 2001, 2004) to possibly early Oligocene time, c. 30 Ma (Fox et al., 2016), the latter time period determined approximately by the intrusion age of the Bergell pluton. In order to model steady-state behavior, some representative or "*a priori*" exhumation rate must be applied and modulated across the entire orogen without regard for any bounding structures that may control exhumation rate. To the extent that the models go far enough back in time to overlap with the differential unroofing rates of the Pennine and Austroalpine domains in eastern Switzerland (e.g., Fox et al., 2016), they are not an accurate description of Alpine unroofing.

Despite the flawed initial assumption of steady-state behavior for the Alps in pre-Miocene time, at least two conclusions drawn from these studies support our conclusions: 1) Table 1 in Bernet et al. (2004) presents peak ages for detrital ZFT populations that support the model of Pennine zone exhumation that we present here. In particular, for every major drainage on the southern end of the orogen there is a ZFT population (viz, their P3) that falls in the range 24 to 36 Ma, indicating that Pennine zone cooling through 240°C occurred from late Eocene well into the Oligocene. Given that detrital rocks represent non-specific sampling over a wide catchment area, these detrital ZFT ages agree rather well with the bedrock data compilation presented here. 2) Fox et al. (2016) conclude that there was a "major reorganization" of the Alpine orogen at 20 Ma. This is consistent with our prediction that Pennine zone thermal equilibration could have occurred as late as c. 18 Ma. Thus, we posit that this "major reorganization" occurred at the end of the emplacement of the Penninic wedge. The Alps were not in any kind of steady-state until after this reorganization.

1.5. Conclusions

The mismatch in Tertiary thermal histories between the Austroalpine allochthon and its Penninic substrate across the strike of the central Alps (Fig. 1.14), indicates that no point currently exposed in the footwall had been emplaced against the hanging wall until some time between 29 and 18 Ma. Given that the strata within the Grava nappe in northern half-window experienced peak metamorphic pressures of order 1.0-1.2 GPa, and the Austroalpine allochthon

was already at temperatures of ≤180 °C at the same time (c. 35 Ma), top-south to top-southeast normal fault motion of at least 60 km along the base of the allochthon is required to juxtapose the two rock masses. Our data strongly support the kinematic analysis of Weh (1998) and at least the kinematic consequences of the models of Gerya et al. (2002) and Boutelier et al. (2004). We note that even if the displacement rate on the fault system were 1 to 2 cm/yr, it would still take at least 3 to 6 Myr to accommodate the 60 km of minimum motion. At a rate of 1 cm/yr with 100 km of displacement, the duration of motion may have been in the 10 Myr range, between 29 and 18 Ma. We note also that the timing of motion during this interval agrees well with the timing of thermal equilibration between hanging wall and footwall in the Tauern Window, which occurred between c. 25 and 15 Ma (Luth and Willingshoffer, 2008).

Much or all of the normal motion occurred during two key events in Alpine evolution. The first is at the onset of foredeep sedimentation on both the European and Apulian continental masses at about 32 Ma (Lower Marine Molasse in Europe, Villa Olmo conglomerate in Apulia), with most subsidence occurring between 30 and 15 Ma. The second is major horizontal shortening of the European passive margin that formed the Helvetic nappes (e.g., Trümpy, 1980; Price and Wernicke, in prep.). In regard to the latter, the most rapid period of flysch deposition in the Helvetic foredeep occurred in latest Eocene to early Oligocene time c. 34 to 30 Ma, and estimates of the timing of the various phases of thrust and nappe formation range from early Oligocene to early Miocene time (c. 30 to 15 Ma). The formation of the Helvetic nappes thus may have been coeval with final juxtaposition of the Austroalpine and Penninic domains, rather than post-dating it as is commonly assumed. If so, then the Oligocene to early Miocene collisional history of the Alps would represent an analogy to the Miocene phase of collision in the Himalaya, when the South Tibetan detachment system and the Main Central thrust simultaneously accommodated large-magnitude normal and thrust motion, respectively (Burchfiel et al, 1992).

In regard to the development of the peri-Alpine foredeep basins, the interposition of a c. 15 km-thick mass of subduction complex material between the thin upper crustal ‘flake’ of the Austroalpine allochthon and the southern margin of Europe would have represented a major crustal thickening event. This was likely the first time at which crustal thickness anywhere in the system exceeded 30 to 35 km, driving range-scale redistribution of crustal mass via rapid subaerial erosion of the newly forming mountain belt. If we measure the collision of Adria and Europe by, for example, the position of the Adula nappe (Monte Duria) relative to the Austroalpine allochthon, then collision was well underway by c. 40 Ma, as generally depicted in cross-sectional models of the Alps (e.g. Schmid et al., 2005). If the emplacement of a combined Pennine-Helvetic mass occurred mainly between 30 and 20 Ma, along with development of the foredeep basins, then mountain building in the Alps is not so much a result of continent-continent collision as it is the result of an episode of buoyant return flow and concentrated accumulation of subduction chan-

nel material near the top of the channel (e.g. Chemenda et al., 1995; Butler et al., 2013). The relatively late (post-Bergell intrusive) timing of a culminating phase of unroofing via such return flow is consistent with the proposed timing of a slab-breakoff event in the interval 35-30 Ma (von Blanckenburg and Davies, 1995; Froitzheim et al., 2008).

1.6. Acknowledgements

We thank Becky Flowers and Jim Metcalf at the CU TRaiL facility for providing ZHe analyses; Ray Donelick at A to Z, Inc. for providing ZFT analyses; Mark Garcia, Janet Harvey, Nathan Niemi, Sarah Bala, and Renee Pillers for help with mineral separations; Lindsey Hedges for sharing her considerable experience in the laboratory; Bryan Palmintier, Lukas Flükiger Nibourel, Luca Malatesta, Kari Price, Peter Nievergelt, and Dominik Letsch for help in the field and with navigating Switzerland (white gas = reinbenzin, available at the Apotheke). Funding for this work was supported by the NSF Tectonics program, through award EAR 14-51055 to Brian Wernicke.

1.7. References Cited

Allen, P.A. and Allen, J.R., 2006, Basin Analysis: Principles and Application to Petroleum Play Assessment, 3rd ed., Wiley-Blackwell, Oxford, U.K., 451 p.

Angiboust, S., Agard, P., Raimbourg, H., Yamato, P., and Huet, B., 2011, Subduction interface processes recorded by eclogite facies shear zones (Monviso, W. Alps). Lithos, v. 127, p. 222-238. doi: 10.1016/j.lithos.2011.09.004

Angiboust, S., Glodny, J., Oncken, O., and Chopin, C., 2014, In search of transient subduction interfaces in the Dent Blanche-Sesia tectonic system (W. Alps). Lithos, v. 205, p. 298-321. doi: 10.1016/j.lithos.2014.07.001

Argand, É., 1916, Sur l'arc des Alpes Occidentales, Eclogae Geologicae Helvetiae, v. 14, p. 145-191.

Augenstein, C., 2012, The formation of the Lepontine Dome, unpublished PhD thesis, Australian National University, 357p.

Axen, G.J., Bartley, J.M., and Selverstone, J., 1995, Structural expression of a rolling hinge in the footwall of the Brenner Line normal fault, Eastern Alps. Tectonics, v. 14, p. 1380-1392. doi: 10.1029/95TC02406

Bachmann, R., Glodny, J., Oncken, O., and Seifert, W., 2009, Abandonment of the South Penninic–Austroalpine palaeosubduction zone, Central Alps, and shift from subduction erosion to accretion: constraints from Rb/Sr geochronology. Journal of the Geological Society, v. 166, p. 217-231.

Beaumont, C., Jamieson, R. A., Butler, J. P., and Warren, C. J., 2009, Crustal structure: A key

constraint on the mechanism of ultra-high-pressure rock exhumation. Earth and Planetary Science Letters, v. 287, p. 116-129. doi: 10.1016/j.epsl.2009.08.001

Beltrando, M., Lister, G.S., Rosenbaum, G., Richards, S., & Forster, M.A., 2010, Recognizing episodic lithospheric thinning along a convergent plate margin: The example of the early Oligocene Alps. Earth-Science Reviews, v. 103, p. 81-98. doi: 10.1016/j.earscirev.2010.09.001

Bernet, M., Zattin, M., Garver, J.I., Brandon, M.T. and Vance, J.A., 2001, Steady-state exhumation of the European Alps. Geology, v. 29, p. 35-38.

Bernet, M., Brandon, M.T., Garver, J.I. and Molitor, B.R., 2004, Fundamentals of detrital zircon fission-track analysis for provenance and exhumation studies with examples from the European Alps. Geological Society of America Special Papers, v. 378, p. 25-36.

Bernet, M., Brandon, M., Garver, J., Balestieri, M. L., Ventura, B., and Zattin, M., 2009, Exhuming the Alps through time; clues from detrital zircon fission-track thermochronology. Basin Research, 21(6), 781-798. doi: 10.1111/j.1365-2117.2009.00400.x

Blanckenburg, F. von, and Davies, J.H., 1995, Slab breakoff: a model for syncollisional magmatism and tectonics in the Alps. Tectonics, v. 14, p. 120-131.

Boutelier, D., Chemenda, A. and Jorand, C., 2004. Continental subduction and exhumation of high-pressure rocks: insights from thermo-mechanical laboratory modelling. Earth and Planetary Science Letters, 222(1), pp.209-216.

Burchfiel, B.C., Zhiliang, C., Hodges, K.V., Yuping, L., Royden, L.H., Changrong, D. and Jiene, X., 1992, The South Tibetan detachment system, Himalayan orogen: Extension contemporaneous with and parallel to shortening in a collisional mountain belt. Geological Society of America Special Papers, v. 269, p.1-41.

Burchfiel, B.C. and Royden, L.H., 1985, North-south extension within the convergent Himalayan region. Geology, v. 13, p. 679-682.

Burg, J.P., and Gerya, T. V., 2005, The role of viscous heating in Barrovian metamorphism of collisional orogens: Thermomechanical models and application to the Lepontine Dome in the Central Alps. Journal of Metamorphic Geology, v. 23, p. 75-95.

Butler, J.P., Beaumont, C., and Jamieson, R.A., 2013, The Alps 1: A working geodynamic model for burial and exhumation of (ultra)high-pressure rocks in alpine-type orogens. Earth and Planetary Science Letters, v. 377-378, p. 114-131. doi: 10.1016/j.epsl.2013.06.039

Butler, J.P., Beaumont, C., & Jamieson, R.A., 2014, The Alps 2: Controls on crustal subduction and (ultra)high-pressure rock exhumation in Alpine-type orogens. Journal of Geophysical Research: Solid Earth, v. 119, p. 5987-6022. doi: 10.1002/2013JB010799

Campani, M., Mancktelow, N., Seward, D., Rolland, Y., Muller, W., and Guerra, I., 2010, Geochronological evidence for continuous exhumation through the ductile-brittle transition

along a crustal scale low-angle normal fault: Simplon fault zone, Central Alps. Tectonics, v. 29, TC3002. doi: 10.1029/2009TC002582.

Chemenda, A.I., Mattauer, M., Malavieille, J. and Bokun, A.N., 1995, A mechanism for syn-collisional rock exhumation and associated normal faulting: results from physical modelling. Earth and Planetary Science Letters, v. 132, p. 225-232.

Chopin, C., 2003, Ultrahigh-pressure metamorphism: Tracing continental crust into the mantle. Earth and Planetary Science Letters, v. 212, p. 1-14. doi: 10.1016/S0012-821X(03)00261-9

Ciancaleoni, L., and Marquer, D., 2008, Late Oligocene to early Miocene lateral extrusion at the eastern border of the Lepontine Dome of the Central Alps (Bergell and Insubric areas, eastern Central Alps). Tectonics, v. 27. doi: 10.1029/2007TC002196

Dalrymple, G.B., Alexander, E.C., Lanphere, M.A., and Kraker, G.P., 1981, Irradiation of samples for $^{40}Ar/^{39}Ar$ dating using the geological survey TRIGA reactor. In: USGS Professional Papers. U.S. Geological Survey, Reston, VA, United States. v. 1176, 29 p.

Dewey, J.F., 1988, Extensional collapse of orogens. Tectonics, v. 7, p. 1123-1139.

Donelick, R.A., O'Sullivan, P.B., and Ketcham, R.A., 2005, Apatite fission track analysis. Reviews in Mineralogy and Geochemistry, v. 58, n. 1, p. 49-94.

Engi, M., Bousquet, R., and Berger, A., 2004, Central Alps. Mitteilungen der Oesterreichischen Mineralogischen Gesellschaft, v. 149, p. 157-173.

Ernst, W.G., 1975, Systematics of large-scale tectonics and age progressions in Alpine and Circum-Pacific blueschist belts. Tectonophysics, v. 26, p. 229-246.

Ernst, W.G., 2005, Alpine and Pacific styles of Phanerozoic mountain building: Subduction-zone petrogenesis of continental crust. Terra Nova, v. 17, p. 165-188.

Evans, S., 2011, Timing of exhumation of the eastern Central Alps from zircon and apatite (U-Th)/He thermochronology (Graubünden, Switzerland), Unpublished M.S. thesis, University of Kansas, 226p. https://kuscholarworks.ku.edu/bitstream/handle/1808/9746/Evans_ku_0099M_11901_DATA_1.pdf?sequence=1&isAllowed=y

Farley, K., 2002, (U-Th)/He Dating: Techniques, Calibrations, and Applications: Reviews in Mineralogy and Geochemistry, v. 47, p. 819-844.

Fitzgerald, P.G., Fryxell, J.E., and Wernicke, B.P., 1991, Miocene crustal extension and uplift in southeastern Nevada: Constraints from fission track analysis. Geology, v. 19, p. 1013-1016. doi: 10.1130/0091-7613(1991)019<1013:MCEAUI>2.3.CO;2

Flowers, R.M., and Kelley, S.A., 2011, Interpreting data dispersion and "inverted" dates in apatite (U-Th)/He and fission-track datasets: An example from the U.S. midcontinent. Geochimica et Cosmochimica Acta, v. 75, p. 5169-5186.

Fox, M., Herman, F., Willett, S.D. and Schmid, S.M., 2016, The Exhumation history of the Euro-

pean Alps inferred from linear inversion of thermochronometric data. American Journal of Science, v. 316, p. 505-541.

Froitzheim, N., Schmid, S.M., and Conti, P., 1994, Repeated change from crustal shortening to orogen-parallel extension in the Austroalpine units of Graubunden. Eclogae Geologicae Helvetiae, v. 87, p. 559-612.

Froitzheim, N., Schmid, S.M., and Frey, M., 1996, Mesozoic paleogeography and the timing of eclogite-facies metamorphism in the Alps: A working hypothesis. Eclogae Geologicae Helvetiae, v. 89, p. 81-110.

Froitzheim, N., Pleuger, J. and Nagel, T.J., 2006, Extraction faults. Journal of Structural Geology, v. 28, p. 1388-1395.

Froitzheim N., Plašienka D., Schuster R., 2008, Alpine tectonics of the Alps and Western Carpathians. *In*: McCann, T., ed., *The Geology of Central Europe, Volume 2, Mesozoic and Cenozoic*, Geological Society, London, p. 1141-1232.

Gerya, T.V., Stöckhert, B., and Perchuk, A.L., 2002, Exhumation of high-pressure metamorphic rocks in a subduction channel: A numerical simulation. Tectonics, v. 21., TC1056, doi: 10.1029/2002TC001406

Handy, M.R., Herwegh, M., Kamber, B.S., Tietz, R., and Villa, I.M., 1996, Geochronologic, petrologic and kinematic constraints on the evolution of the Err-Platta boundary, part of a fossil continent-ocean suture in the Alps (eastern Switzerland). Schweizerische Mineralogische und Petrographische Mitteilungen, v. 76, p. 453-474.

Hansmann, W., 1996, Age determination of the Tertiary Masino-Bregaglia (Bergell) intrusives (Italy, Switzerland): A Review, Schweizerische Mineralische und Petrographische Mitteilungen, v. 76, p. 421-451.

Hermann, J., Rubatto, D., and Trommsdorff, V., 2006, Sub-solidus Oligocene zircon formation in garnet peridotite during fast decompression and fluid infiltration (Duria, Central Alps). Mineralogy and Petrology, v. 88, p. 181-206. doi: 10.1007/s00710-006-0155-3

Herwartz, D., Nagel, T.J., Münker, C., Scherer, E.E. and Froitzheim, N., 2011, Tracing two orogenic cycles in one eclogite sample by Lu-Hf garnet chronometry. Nature Geoscience, v. 4, pp.178-183.

Hunziker, J.C., Desmons, J., and Hurford, A.J., 1992, Thirty-two years of geochronological work in the Central and Western Alps: A review of seven maps (Vol. 13). Switzerland: [Universite de Lausanne, Institut de Geologie et Paleontologie] : [Lausanne], Switzerland.

Inger, S., Ramsbotham, W., Cliff, R.A., and Rex, D.C., 1996, Metamorphic evolution of the Sesia-Lanzo zone, Western Alps: Time constraints from multi-system geochronology. Contributions to Mineralogy and Petrology, v. 126, p. 152-168.

Jäger, E., 1962, Rb-Sr age determinations on micas and total rocks from the Alps. Journal of Geo-

physical Research, v. 67, p. 5293-5306.

Janots, E., Engi, M., Rubatto, D., Berger, A., Gregory, C. and Rahn, M., 2009, Metamorphic rates in collisional orogeny from *in situ* allanite and monazite dating. Geology, v. 37, p.11-14.

Ketcham, R.A., Gautheron, C., and Tassan-Got, L, 2011, Accounting for long alpha-particle stopping distances in (U–Th–Sm)/He geochronology: Refinement of the baseline case. Geochimica et Cosmochimica Acta, v. 75, p. 7779-7791.

Koppel, V., and Grünenfelder, M., 1975, Concordant U-Pb ages of monazite and xenotime from the Central Alps and the timing of the high temperature Alpine metamorphism: A preliminary report. Schweizerische Mineralogische und Petrographische Mitteilungen, v. 55, p. 129-132.

Kuiper, K. F., Deino, A., Hilgen, F. J., Krijgsman, W., Renne, P.R., and Wijbrans, J.R., 2008, Synchronizing Rock Clocks of Earth History. Science, v. 320, p. 500-504.

Laubscher, H. P. (1983). Detachment, shear, and compression in the Central Alps, in: Hatcher, R.D., Williams, H., and Zeitz, I., eds., Geological Society of America Memoir, v. 158, p. 191-211. doi: 10.1130/MEM158-p191

Lee, J-Y., Marti, K., Severinghaus, J.P., Kawamura, K., Yoo, H-S., Lee, J.B., and Kim, J.S., 2006, A redetermination of the isotopic abundances of atmospheric Ar. Geochimica et Cosmochimica Acta, v. 70, p. 4507-4512.

Lister, G.S., Banga, G. and Feenstra, A., 1984, Metamorphic core complexes of Cordilleran type in the Cyclades, Aegean Sea, Greece. Geology, v. 12, p. 221-225.

Luth, S.W., and Willingshofer, E., 2008, Mapping of the post-collisional cooling history of the Eastern Alps. Swiss Journal of Geosciences, vol. 101, supplement 1, S207-S223.

Malusà, M.G., Polino, R., Zattin, M., Bigazzi, G., Martin, S., & Piana, F., 2005, Miocene to present differential exhumation in the Western Alps: Insights from fission track thermochronology. Tectonics, v. 24. TC3004. doi: 10.1029/2004TC001782

Malusà, M.G., Faccenna, C., Garzanti, E., & Polino, R., 2011, Divergence in subduction zones and exhumation of high pressure rocks (Eocene Western Alps). Earth and Planetary Science Letters, v. 310, p. 21-32. doi: 10.1016/j.epsl.2011.08.002

Mahéo, G., Gautheron, C., Leloup, P.H., Fox, M., Tassant-Got, L., and Douville, E., 2013, Neogene exhumation history of the Bergell Massif (southeast Central Alps). Terra Nova, v. 25, p. 110-118. doi: 10.1111/ter.12013

Mancktelow, N.S., 1992, Neogene lateral extension during convergence in the Central Alps: Evidence from interrelated faulting and backfolding around the Simplonpass, Switzerland. Tectonophysics, v. 215, p. 295-317.

Mancktelow, N. S., 1993, Tectonic overpressure in competent mafic layers and the development of isolated eclogites. Journal of Metamorphic Geology, v. 11, p. 801-812.

Mancktelow, N. S., 1995, Nonlithostatic pressure during sediment subduction and the development and exhumation of high pressure metamorphic rocks. Journal of Geophysical Research: Solid Earth, v. 100(B1), p. 571-583.

McKenzie, D., 1972. Active tectonics of the Mediterranean region. Geophysical Journal International, v. 30, p. 109-185.

McKenzie, D. and Sclater, J.G., 1971, The evolution of the Indian Ocean since the Late Cretaceous. Geophysical Journal International, v. 24, p. 437-528.

Meyre, C., De Capitani, C., Zack, T., and Frey, M., 1999, Petrology of high-pressure metapelites from the Adula Nappe (Central Alps, Switzerland). Journal of Petrology, v. 40, p. 199-213.

Milnes, A.G., and Pfiffner, O.A., 1980, Tectonic evolution of the Central Alps in cross section St. Gallen-Como. Eclogae Geologicae Helvetiae, v. 73, p. 619-633.

Min, K., Mundil, R., Renne, P.R., and Ludwig, K.R., 2000, A test for systematic errors in $^{40}Ar/^{39}Ar$ geochronology through comparison with U/Pb analysis of a 1.1-Ga rhyolite. Geochimica et Cosmochimica Acta, v. 64, p. 73-98.

Miron, G.D., Wagner, T., Walle, M., and Heinrich, C.A., 2013, Major and trace element composition and pressure-temperature evolution of rock-buffered fluids in low-grade accretionary wedge metasediments, Central Alps. Contributions to Mineralogy and Petrology, v. 165, p. 981-1008. doi: 10.1007/s00410-012-0844-3

Mohn, G., Manatschal, G., Masini, E., and Müntener, O., 2011, Rift-related inheritance in orogens: A case study from the Austroalpine nappes in Central Alps (SE-Switzerland and N-Italy). International Journal of Earth Sciences (Geologische Rundschau), v. 100, p. 937-961. doi: 10.1007/s00531-010-0630-2

Mohn, G., Manatschal, G., Beltrando, M., Masini, E., and Kusznir, N., 2012, Necking of continental crust in magma-poor rifted margins: Evidence from the fossil Alpine Tethys margins. Tectonics, v. 31, TC1012. doi: 10.1029/2011TC002961

Nänny, P., 1948, Zur geologie der Prättigauschiefer zwischen Rhättikon und Plessur, Gebr. Fretz A.G., Zürich, Switzerland, 128 p., 3 plates.

Nievergelt, P., Liniger, M., Froitzheim, N., and Mählmann, R.F., 1996, Early to mid Tertiary crustal extension in the Central Alps: The Turba mylonite zone (eastern Switzerland). Tectonics, v. 15, p. 329-340. doi: 10.1029/93TC02312

Oberli, F., Meier, M., Berger, A., Rosenberg, C.L., and Giere, R., 2004, U-Th-Pb and 230Th/238U disequilibrium isotope systematics: Precise accessory mineral chronology and melt evolution tracing in the Alpine Bergell Intrusion. Geochimica Et Cosmochimica Acta, v. 68, p. 2543-2560. doi: 10.1016/j.gca.2003.10.017

Oldow, J. S., Ferranti, L., Lewis, D.S., Campbell, J.K., D'Argenio, B., Catalano, R., Pappone, G.,

Carmignani, L., Conti, P., and Aiken, C.L.V., 2002, Active fragmentation of Adria, the North African promontory, central Mediterranean Orogen. Geology, v. 30, p. 779-782. doi: 10.1130/0091-7613(2002)030<0779:AFOATN>2.0.CO;2

Oxburgh, V.E.R., Lambert, R.S.J., Baadsgaard, H., and Simons, J, 1966, Potassium-argon age studies across the southeast margin of the Tauern window, the eastern Alps. Verhandlungen der Geologischen Bundesanstalt [Wien], v. 1-2, p. 17-33.

Peacock, S.M.,1989, Thermal modeling of metamorphic pressure-temperature-time paths: A forward approach; in, Spear, F. and Peacock, S.M., eds. Metamorphic Pressure-Temperature-Time Paths: Short Course in Geology, v.7, American Geophysical Union, Washington D.C., p. 57-102.

Platt, J. P., 1986, Dynamics of orogenic wedges and the uplift of high-pressure metamorphic rocks. Geological Society of America Bulletin, v. 97, p. 1037-1053.

Pleuger, J. and Podladchikov, Y.Y., 2014, A purely structural restoration of the NFP20-East cross section and potential tectonic overpressure in the Adula nappe (central Alps). Tectonics, v. 33, pp.656-685.

Ratschbacher, L., Frisch, W., Linzer, H.G., and Merle, O., 1991, Lateral extrusion in the Eastern Alps; Part 2, Structural analysis. Tectonics, v. 10, p. 257-271. doi: 10.1029/90TC02623

Reiners, P.W., Brady, R., Farley, K.A., Fryxell, J.E., Wernicke, B.P., & Lux, D., 2000, Helium and argon thermochronometry of the Gold Butte Block, South Virgin Mountains, Nevada. Earth and Planetary Science Letters, v. 178, p. 315-326.

Scharf, A., Handy, M. R., Favaro, S., Schmid, S. M., and Bertrand, A., 2013, Modes of orogen-parallel stretching and extensional exhumation in response to microplate indentation and roll-back subduction (Tauern Window, Eastern Alps). International Journal of Earth Sciences (Geologische Rundschau), v. 102, p. 1627-1654. doi: 10.1007/s00531-013-0894-4

Scheiber, T., Pfiffner, O.A., and Schreurs, G., 2012, Strain accumulation during basal accretion in continental collision; a case study from the Suretta Nappe (Eastern Swiss Alps). Tectonophysics, v. 579, p. 56-73. doi: 10.1016/j.tecto.2012.03.009

Schlunegger, F., and Willett, S., 1999, Spatial and temporal variations in exhumation of the central Swiss Alps and implications for exhumation mechanisms. In: Ring, U., Brandon, M.T., Lister, G.S., and Willett, S.D., eds., Exhumation Processes: Normal Faulting, Ductile Flow, and Erosion. Geological Society, London, Special Publications 154, p. 157-179.

Schmid, S.M., Pfiffner, O.A., Froitzheim, N., Schönborn, G., & Kissling, E., 1996, Geophysical-geological transect and tectonic evolution of the Swiss-Italian Alps. Tectonics, v. 15, p. 1036-1064. doi: 10.1029/96TC00433

Schmid, S.M., Fügenschuh, B., Kissling, E., and Schuster, R., 2004, Tectonic map and overall architecture of the Alpine orogen. Eclogae Geologicae Helvetiae, v. 97, p. 93-117.

Schreurs, G., 1993, Structural analysis of the Schams nappes and adjacent tectonic units; implications for the orogenic evolution of the Penninic Zone in eastern Switzerland. Bulletin de la Société Géologique de France, v. 164, p. 415-435.

Schuster, R. and Frank, W., 1999, Metamorphic evolution of the Austroalpine units east of the Tauern Window: Indications for Jurassic strike slip tectonics, Mitt Ges Geol Bergbaustud Österreich, v. 42, p. 37-58.

Schuster, R., Scharbert, S., Abart, R., and Frank, W., 2001, Permo-Triassic extension and related HT/LP metamorphism in the Austroalpine–Southalpine realm. Mitt Ges Geol Bergbaustud Österreich, v. 45, p. 111-141.

Selverstone, J., 1988, Evidence for east-west crustal extension in the Eastern Alps: Implications for the unroofing history of the Tauern Window. Tectonics, v. 7, p. 87-105.

Selverstone, J., 2005. Are the Alps collapsing?. Annual Reviews in Earth and Planetary Science, v. 33, p. 113-132.

Steiger, R.H., 1964, Dating of orogenic phases in the central Alps by K-Ar ages of hornblende. Journal of Geophysical Research, v. 69, p. 5407-5421.

Steinmann, 1994, Ein Beckenmodell für das Nordpenninikum der Ostschweiz. Jahrbuch der Geologischen Bundesanstalt, v. 137, p. 675-721.

Stöckli, D.F., 2005, Application of low-temperature thermochronometry to extensional tectonic settings. Reviews in Mineralogy and Geochemistry, v. 58, p. 411-448. doi: 10.2138/rmg.2005.58.16

Trümpy, R., 1980, Geology of Switzerland: An outline of the geology of Switzerland: Interbook.

Vance, D., and O'Nions, R.K., 1992, Prograde and retrograde thermal histories from the Central Swiss Alps. Earth and Planetary Science Letters, v. 114, p. 113-129.

Vernon, A.J., Van der Beek, P.A., Sinclair, H.D., and Rahn, M.K., 2008, Increase in late Neogene denudation of the European Alps confirmed by analysis of a fission-track thermochronology database. Earth and Planetary Science Letters, v. 270, p. 316-329. doi: 10.1016/j.epsl.2008.03.053

Wagner, G.A., Reimer, G.M., and Jäger, E., 1977, Cooling ages derived by apatite fission-track, mica Rb-Sr and K-Ar dating: the uplift and cooling history of the Central Alps, in: Memorie degli Instituti di Geologia e Mineralogia dell'Università di Padova, Vol. 30, Società Cooperativa Tipografica, p. 3-25.

Weh, M., 1998, Tektonische Entwicklung der penninischen Sediment-Decken in Graubünden (Prättigau bis Oberhalbstein). Unpublished PhD thesis, University of Basel, 230 p., 1 Appendix.

Weh, M., and Froitzheim, N., 2001, Penninic cover nappes in the Prättigau half-window (eastern Switzerland): Structure and tectonic evolution. Eclogae Geologicae Helvetiae, v. 94, p.

237-252.

Wheeler, J., Reddy, S. M., and Cliff, R. A., 2001, Kinematic linkage between internal zone extension and shortening in more external units in the NW Alps. Journal of the Geological Society of London, v. 158, Part 3, p. 439-443.

Wust, G. H., and Silverberg, D. S., 1989, Northern Combin zone complex-Dent Blanche nappe contact: Extension within the convergent Alpine Belt. Schweizerische Mineralogische und Petrographische Mitteilungen, v. 69, p. 251-259.

Wyss, R., and Isler, A., 2011, 1214 Ilanz Erläuterungen, Geologischer Atlas der Schweiz, Bundesamt für Landestopografie swisstopo.

Ziegler, W.H., 1956, Geologische studien in den flyschgebieten des Oberhalbsteins (Graubünden), Eclogae Geologicae Helvetiae, v. 49, p. 1-81.

Chapter II

Kinematic analysis of the upper and lower boundaries of the Pennine Zone, Oberhalbstein and Vorderrhein regions, Switzerland

A manuscript submitted to Journal of Structural Geology

2.1 Introduction

Ever since plate tectonics was recognized as a framework for understanding geologic processes, orogens have been viewed in large part as loci of plate convergence, wherein one continental plate collides with, and typically overrides, another, or where continent-ocean convergence deforms the overriding continental plate. The collision of two masses of continental lithosphere should lead to contractile tectonics (i.e., horizontal shortening and vertical thickening of the crust). Because orogens typically exhibit structural 'overlap' of diverse geological elements on the order of 10s to 100s of kilometers via thrust and nappe tectonics, such overlap is typically viewed as a direct expression of plate convergence.

If we were to restrict our discussion to first-order models that challenge this theme over the last 40 years, it is the concept that buoyancy-driven upward or "return" flow is, at least in part, responsible for many of these structural features. From a purely kinematic point of view, such flow need not be accompanied by plate convergence (Fig. 2.1) although it certainly does not preclude it. The upward return to the surface of buoyant elements is to be expected given that they are strongly coupled to sinking lithosphere at the onset of collision, but ultimately lose their coupling through thermal weakening, such that their motions may then be governed by buoyancy forces (e.g. England and Holland, 1979). This mechanism could affect not merely volumetrically minor components of the "metamorphic cores" of orogens, but also act as the main driver of thrust and nappe formation in the brittle crust. Seminal papers by Ernst (1971, 1975) and Cloos (1982) suggested that significant components of crustal assemblages in the subduction wedge are the result of such upward flow. Since then, numerical (e.g., Cloos, 1993; Ernst and Peacock, 1996; Gerya et al., 2002 Beaumont et al., 2009) and experimental (e.g., Chemenda et al., 1995; Boutelier et al., 2004) models demonstrate that large-scale buoyancy-driven return flow is likely or even expected in subduction zone and collisional settings.

The influence of buoyancy-driven return flow is particularly important when continental crust ap-

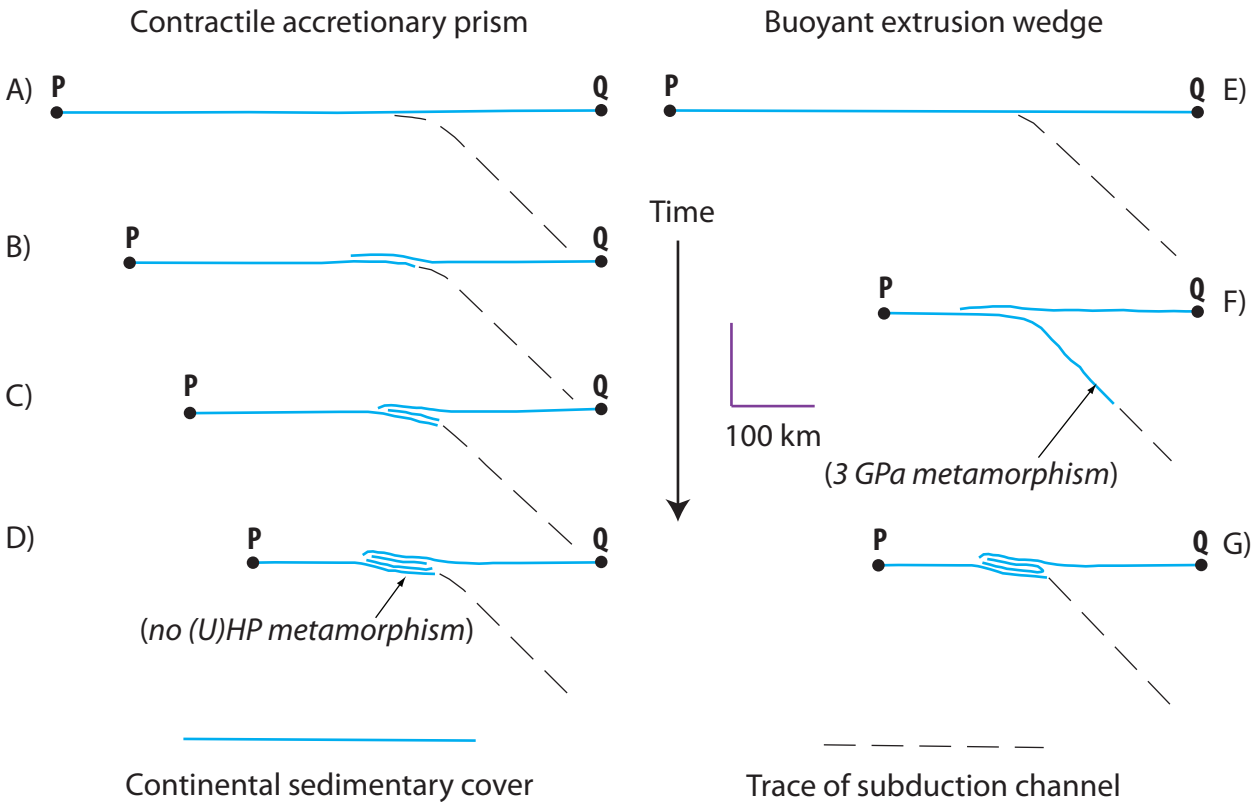

Fig. 2.1. Contrasting tectonic processes that lead to crustal thickening. In a contractile accretionary prism (frames A through D), shortening is accommodated by thin-skinned thrust faulting which forms a stack of duplicated supracrustal rocks and their shallow crystalline substrate. In this tectonic setting preservation of HP metamorphism is rare, and UHP metamorphism is absent. In a buoyant extrusion wedge (frames E through G), a similar amount of shortening occurs via subduction and later extrusion owing to a buoyancy contrast between the subducted shallow crustal rocks and surrounding mantle. In this tectonic setting, preservation of HP metamorphism is common, and relics of UHP metamorphism may also be preserved. Note that line length P-Q is the same in each tectonic scenario, and that point P need not converge on point Q during crustal thickening between (E) and (F).

proaches a subduction zone, because it is far more massive and more buoyant than oceanic crust relative to enveloping lithospheric mantle (Cloos, 1993) that, if able to be subducted at all, it can be ejected from the subduction zone in semi-coherent form, and if sufficiently strong and rigid, it may act as a stress guide to propagate deformation into high crustal levels. Thus buoyancy-driven flow may not only result in the incorporation of blueschist and eclogite blocks within much shallower components in mélanges (Cowan, 1978, Cloos, 1982), but also in the exhumation much larger (100s of km^3) crustal blocks to a supracrustal structural position, as apparent in examples such as the Dora Maira massif in the Western Alps (Chopin, 1984), the Adula nappe in the Central Alps (Herwartz et al., 2011), high-pressure granulitic elements in the Bohemian massif (Carswell and O'Brien, 1993), the Seve and Köli nappe complexes in the Scandanavian Caledonides (Brueckner and van Roermund, 2004), and the Kohistan arc complex in the western Himalaya (Ernst, 2006). In kinematic terms, rock masses exhumed from a subduction zone may exhibit synchronous normal-sense shear relative to the overriding plate, and reverse-sense shear relative to the down-going slab (e.g. Ernst, 1975; Ernst and Peacock, 1996; Brueckner and van Roermond, 2004). The

question then becomes not whether some aspect of upper crustal thrust and nappe structure is the result of buoyancy-driven return of deep, bouyant fragments, but the extent to which most or all structures are driven by return flow, independently of whether relative plate motion is convergent or divergent at the time of emplacement.

A recent analysis of K/Ar, fission track, and U-Th/He cooling ages has demonstrated that, in the Central Alps, a series of South-, Middle-, and North-Penninic nappes were exhumed during the main phase of Alpine nappe development in late Eocene to early Miocene time (~35-18 Ma) by normal-sense movement of the Austroalpine allochthon relative to the Pennine zone (Chapter 1, Price et al., in review). The now-extinct Tethyan subduction zone that formed the Alps is widely accepted to have been south-dipping (Schmid et al., 1996; Froitzheim et al., 2008), although it is still unclear whether the deep lithospheric structure beneath the Alps is the product of slab-breakoff (e.g., Davies and von Blanckenburg, 1995; Schmid et al., 1996; Schmid et al., 2004) or a downward-facing lithospheric welt (cf., Laubscher, 1978; St. Mueller, 1989). Regardless, numerous kinematic studies in the Central Alps at structural levels throughout the Pennine zone (Ring et al., 1989; Ring, 1992; Marquer et al., 1996; Nievergelt et al., 1996; Scheiber et al., 2012; Weh and Froitzheim, 2001) indicate that an important phase of top-E or top-SE "D2" shearing occurred after an initial top-N "D1" nappe stacking event. Some of these studies indicate a small component of true top-S shear, but the dominant vector is more easterly in present-day coordinates, with a strong component parallel to the easterly plunge direction of the nappe stack. Kinematic studies along the base of the Pennine overthrust in the Central Alps are comparatively few (Weh and Froitzheim, 2001; Wiederkehr et al., 2008), but indicate solely top-N kinematics without any top-E or top-S movement.

The purpose of this study is to help constrain the kinematics of the upper and lower boundaries of the Pennine nappe complex in the Central Alps using detailed, field-based, mesoscopic structural measurements. To examine the top of the Pennine zone, a traverse was completed in the Oberhalbstein Valley region from (1) the east flank of Piz Curvér to (2) the town of Savognin to (3) the alp below Piz Mitgel (Nassegl-Colm da Betschs), which includes at its base a structural zone called the Martegnas shear zone ("Martegnas Zug", Fig. 2.2). To examine the base of the Pennine zone, two study locations were chosen: (1) along the basal Pennine thrust near the towns of Luven, Pitasch, and Duvin, known as the Peidener imbricate fault zone ("Peidenerschuppe"), and (2) approximately 100-500 m above the basal Pennine thrust (the trace of which is buried in the Chur Rhein Valley) near the town of Trimmis.

A total of 440 measurements were made using a Brunton compass, iPhone, and iPad, the latter two equipped with the Fieldmove Clino application from *Midland Valley* software, at the three sites over a five-day period in August, 2015. Reproducibility between the compass and iPhone was generally good, of order $\leq 8°$ in strike and $\leq 3°$ in dip. Declination on the compass was set to 2° east according to the National Oceanic and Atmospheric Administration magnetic declination calculator (http://www.ngdc.noaa.gov/geomag-web/) for the time period August, 2015, using the geographic coordinates of Savognin

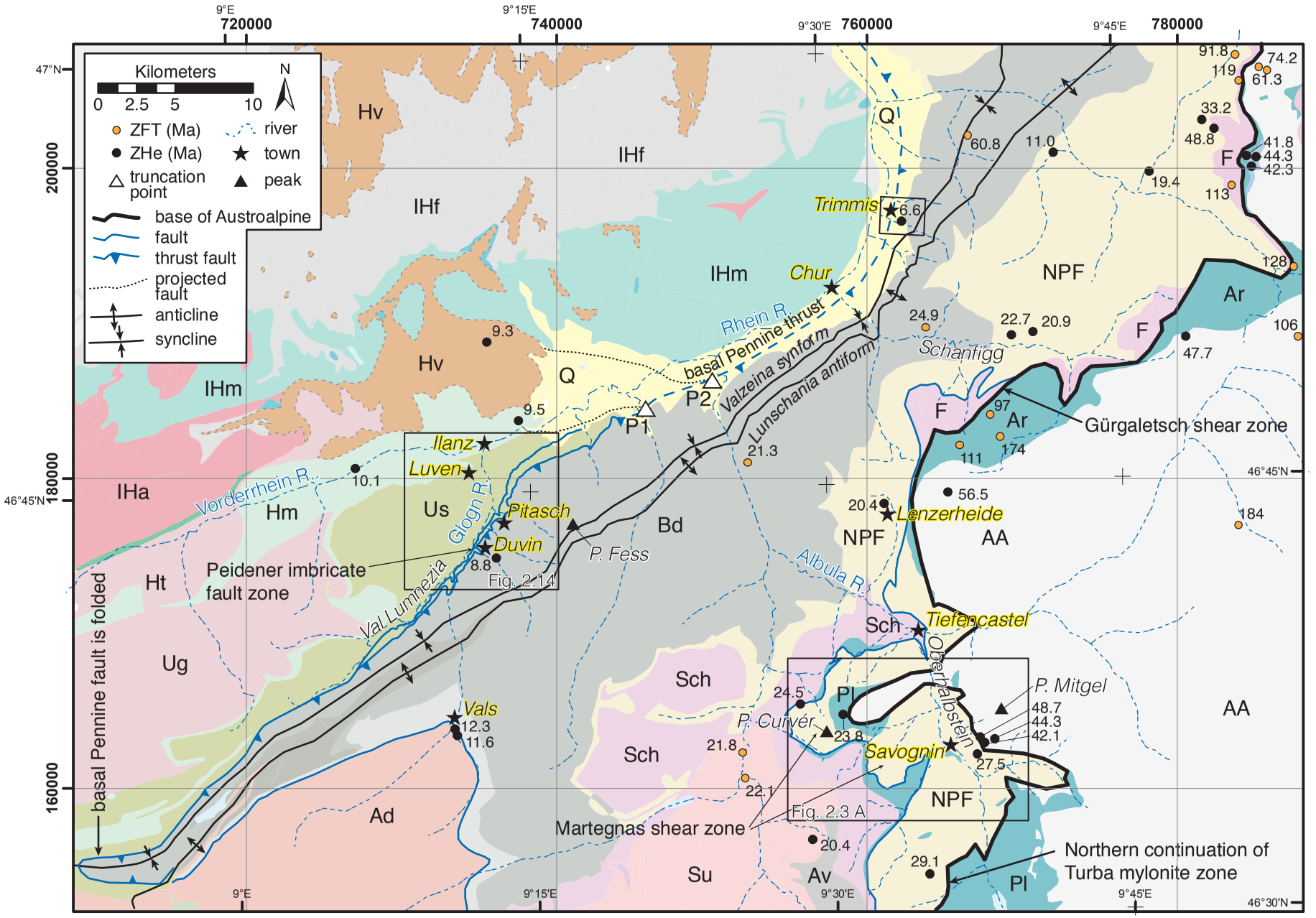
Kilometers
0 2.5 5 10
N
ZFT (Ma)
ZHe (Ma)
truncation point
river
town
peak
base of Austroalpine
fault
thrust fault
projected fault
anticline
syncline
9°E
720000
9°15'E
740000
9°30'E
760000
9°45'E
780000
47°N
200000
180000
160000
46°45'N
46°30'N
Hv
IHf
IHm
Q
NPF
Ar
F
IHa
Hm
Us
Bd
Ht
Ug
Sch
Pl
AA
Ad
Su
Av
Trimmis
Chur
Rhein R.
basal Pennine thrust
Valzeina synform
Lunschania antiform
Schanfigg
Gürgaletsch shear zone
Ilanz
Luven
Pitasch
Duvin
Glogn R.
Vorderrhein R.
Peidener imbricate fault zone
Fig. 2.14
P. Fess
P1
P2
Albula R.
Lenzerheide
Tiefencastel
Oberhalbstein
P. Mitgel
P. Curvér
Savognin
Fig. 2.3 A
Martegnas shear zone
Northern continuation of Turba mylonite zone
Vals
Val Lumnezia
basal Pennine fault is folded
91.8
74.2
119
61.3
33.2
48.8
41.8
44.3
42.3
113
19.4
60.8
11.0
6.6
128
106
24.9
22.7
20.9
47.7
9.3
9.5
21.3
97
111
174
10.1
56.5
20.4
184
8.8
12.3
11.6
24.5
48.7
44.3
42.1
23.8
27.5
21.8
22.1
20.4
29.1

(46.5974° N , 9.5970° E, magnetic declination 2.3° E, changing 0.12° E/year) for the top of the Pennine zone and Duvin (46.7150° N, 9.2117° E, magnetic declination 2.2° E, changing 0.12° E/year) for the bottom of the Pennine zone. The coordinate system used on the maps and for sample locations is the 1903 Swiss Grid (CH1903).

2.2. Top of the Pennine Zone

Near the latitude of the Schanfigg Valley (46°50'N, ~190,000N, CH1903), the top of the Pennine zone is generally located where Cretaceous-Tertiary marine metasedimentary rocks (Bündnerschiefer or North Penninic flysch) come into contact with overlying Jura-Cretaceous marine rocks and associated granitic and ophiolitic slices by a series of named faults (Fig. 2.2). From north to south, these are (1) the Gürgaletsch shear zone, whose eponymous mountain peak (2441 m, 763663,185121) lies on the south side of the Schanfigg Valley, which terminates near and may connect with, (2) the Martegnas shear zone, whose eponymous mountain peak (2680 m, 760133,160545) lies on the southwest side of the Oberhalbstein Valley, which terminates near and may connect with (3) the Turba mylonite zone, whose eponymous mountain peak (3018 m, 766608,142181) lies at the head of the Juferrhein River west of Val Bregaglia. South of the region shown in Fig. 2.2, the Turba mylonite zone is truncated by the c. 31 Ma Bergell pluton (Nievergelt et al., 1996), but along the east margin of the pluton, a shear zone juxtaposes it with the Malenco ophiolites, termed the Muretto Line (Berger and Gieré, 1995), which continues southward and may connect with the Preda Rossa shear zone on the southeast side of the Bergell intrusion (Schmid et al., 1996B). Another fault, termed Corvatsch detachment fault, splays off the Turba mylonite zone and separates the intervening Margna and Corvatsch nappes from higher tectonic elements of the Lower East Alpine nappe complex (see Chapter 1, 'CDF' in Figs. 1.12 and 1.14). This is the same structure as the 'D4' normal fault previously described by Handy et al. (1996, their Fig. 2). The precise age(s) of movement on these various fault strands are poorly constrained as post-early Eocene (c. 50 Ma, the age of the youngest North Penninic flysch) and in the case of the Turba mylonite, pre-31 Ma,, but they are believed to be kinematically linked (e.g., Weh and Froitzheim, 2001), because they all exhibit a significant stage of movement that is top-east or top-southeast. North of the Gürgaletsch shear zone, the upper Pennine zone does not correspond with a particular named shear zone other than the general "Austroalpine overthrust" as historically recognized by Alpine geologists, marked by thin, discontinuous slivers of the ophiolitic Arosa Zone of south Penninic origin (Fig. 2.2).

A transect to collect mesoscopic structural data was completed across the gently east-dipping, c.

Fig. 2.2. Overview geologic map of the areas of interest for this study. Tectonic units are labeled as follows: Infrahelvetic units: IHa, Aar massif, IHm, autochthonous Mesozoic cover of Aar massif, IHf, allochthonous flysch nappes, undivided. Helvetic units: Ht, Tavetsch massif, Hm, Mesozoic, undivided, Hv, Verrucano. Ultrahelvetic units: Ug, Gotthard crystalline basement, Us, Scopi zone, allochthonous Gotthard cover. Penninic units: Ad, Adula, Ar, Arosa zone, Av, Avers Bündnerschiefer, Bd, Bündnerschiefer, NPF, North Penninic flysch, Pl, Platta, Sch, Schams, Su, Suretta. Austroalpine units: AA, Austroalpine undifferentiated. Q: Quaternary, undivided. P1 and P2 are projected truncation points of the Infrahelvetic-Ultrahelvetic and Helvetic-Infrahelvetic structural boundaries, respectively, by the basal Pennine fault.

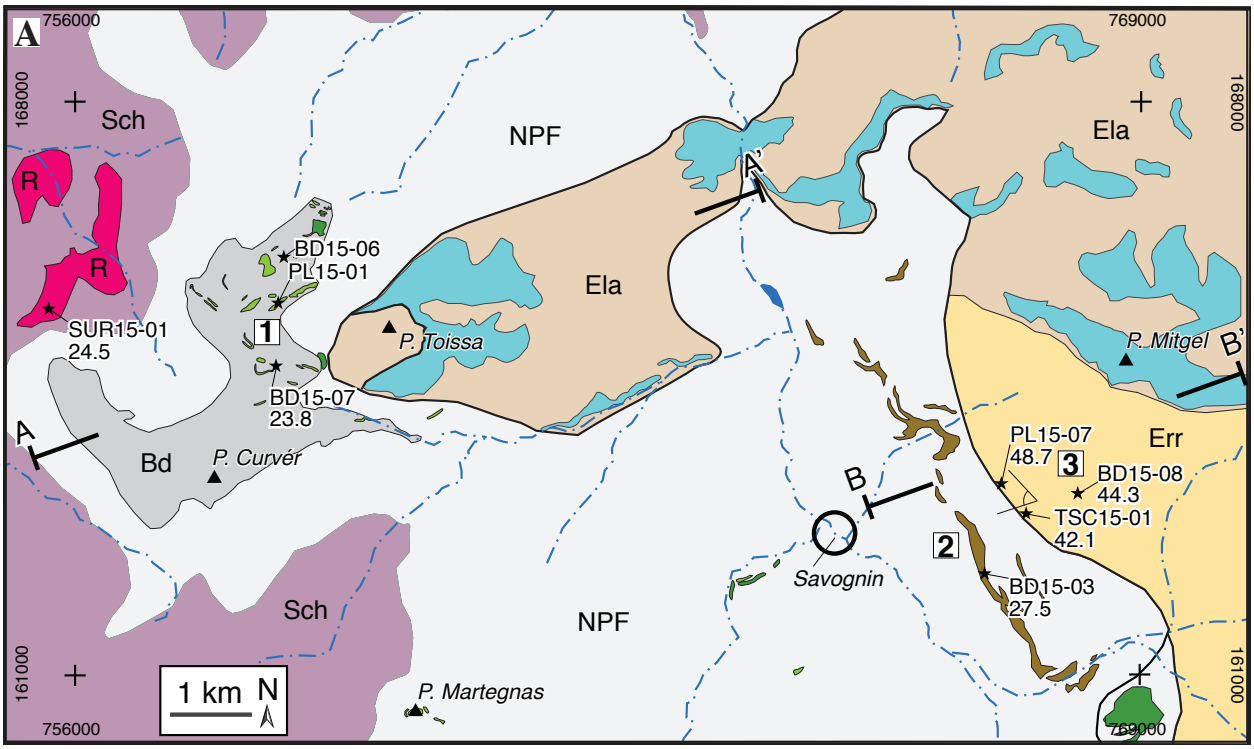

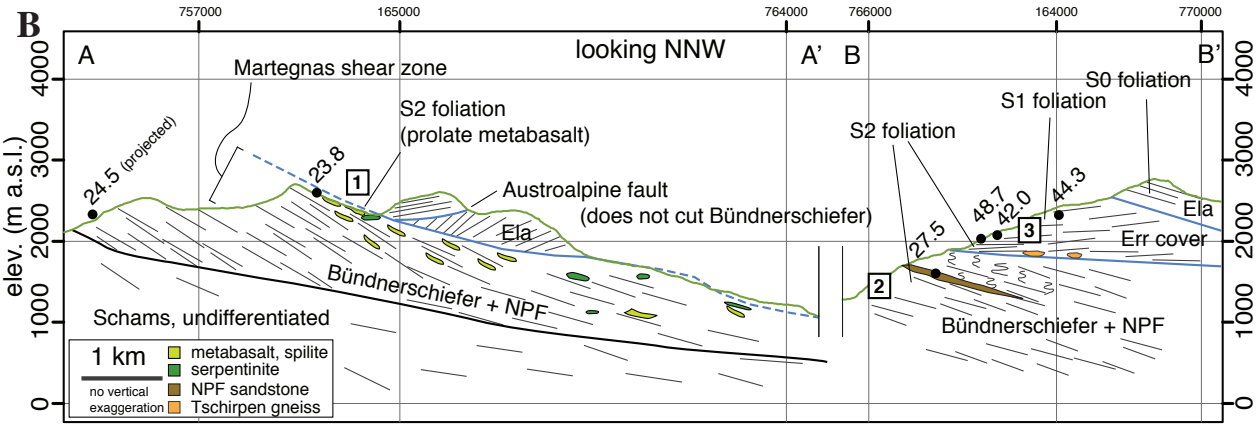

LEGEND

- NPF — North Penninic flysch
- NPF sandstone
- Bd — Bündnerschiefer
- Sch — Schams nappe
- R — Rofna porphyry, Suretta
- Platta serpentinite
- Platta basalt
- Ela nappe undivided
- Hauptdolomite
- Err nappe, undivided
- ★ sample with ZHe age, if measured
- ▲ mountain summit
- 1 site of investigation
- look direction (Fig. 2.3 C)
- town

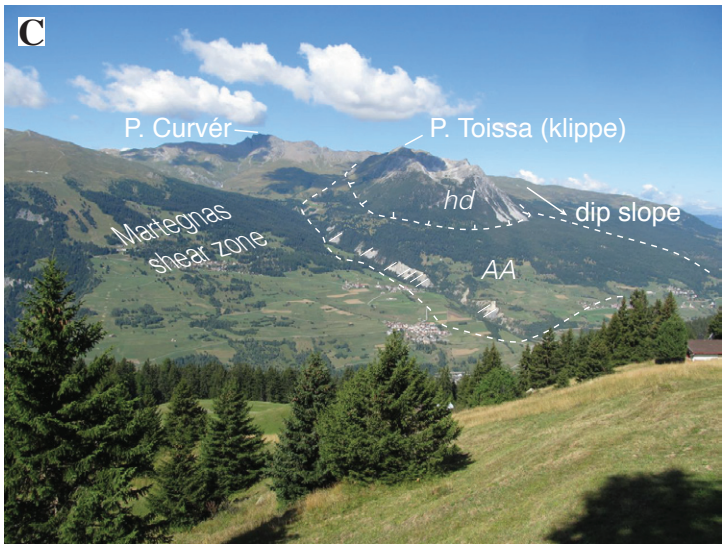

500 m-thick Martegnas shear zone in the Oberhalbstein region near the town of Savognin (Figs. 2.2, 2.3). The structurally lowest measurements were made on the east flank of Piz Curvér near the Ziteil chapel and adjacent to Piz Toissa (Site 1) in ophiolitic Platta nappe *sensu lato* (*s.l.*, a southward continuation of the Arosa zone which includes non-ophiolitic rock types of possible Penninic or East Alpine affinity; Schmid et al. 1996A). Moving up tectonostratigraphic section, measurements were made in roadcuts on the outskirts of Savognin at the foot of the large Sursés alp (Site 2). This traverse continued up to a few tens of meters below the overriding Austroalpine plate in rocks that are mapped as North Penninic flysch. Continuing up tectonostratigraphic section, the highest structural measurements were made in the Sursés alp above the village of Tussagn-Nassegl and beneath Piz Mitgel (Site 3) in sedimentary rocks considered to be cover rocks of the Err nappe (Lower East Alpine).

2.2.1. Local geological observations at the top of the Pennine zone

Piz Curvér and the Oberhalbstein Valley are part of the Martegnas shear zone, named after Piz Martegnas, which lies ~5 km southeast of Piz Curvér (Figs. 2.3, 2.4A). The Curvér Series lithostratigraphy is described by Staub (1958) and Ziegler (1954), who determined an age range of uppermost Paleocene to middle Eocene for the flysch based on the Tertiary index-fossil *Nummulites*, and as result, Curvér Series is considered to be part of the North Penninic flysch. Eiermann (1988) described the lithologic elements, particularly the many types of Platta-affinity ophiolitic blocks at Piz Martegnas, and also confirmed an uppermost Paleocene to middle Eocene age for the 'Parsonzer' flysch found there, also based on the rare occurrence of *Nummulites*. At the base of the shear zone, Eiermann (1988) described a carbonate breccia that accompanies the Parsonzer flysch that has elongated pebbles and is in tectonic contact with elements of the ophiolite. Although Weh (1998) places the Martegnas shear zone into an overall tectonic context of top-South movement that juxtaposes North Penninic flysch against Middle (Schams and Suretta) and South Penninic (Platta *s.l.*) tectonic elements, this study is the first (that we know of) to present mesoscopic, outcrop-scale structural data for the Martegnas shear zone.

2.2.1.1. Site 1, Ziteil, local geology and thermochronology

Site 1 is located on the east flank of the Piz Curvér ridge, on an extensive structural dip-slope that strikes generally north-northeast-south-southwest from south of Piz Martegnas to north of Tiefencastel and the Albula River Valley (Figs. 2.2, 2.3). The rocks from Piz Martegnas, the location of the Martegnas shear zone, to the valley at Tiefencastel, including Piz Curvér, contain elements of the Martegnas

Fig. 2.3. A) Bedrock geologic map of the Savognin area. Major nappes are labeled. Largest resistant 'knockers' in the Pennine nappes are mapped separately. Acute-angle symbol between sites 2 and 3 is the "look" direction and approximate field-of-view for photograph shown in Fig. 2.2C. B) Composite ENE-WSW cross section through the major Pennine-Austroalpine contact near Savognin. Because of the significant N-ward dip of the Austroalpine sheet on the east side of the cross section, it would be erroneous to connect contacts across the cross section. Boxed numbers correspond to the structural data plotted in Fig. 3. Black dots are ZHe ages as reported in Chapter 1 and Appendix 1. C) Overview photo looking west towards Piz Curvér from the east side of Oberhalbstein valley. Major tectonic and geographic features are labeled. AA: Austroalpine undivided (probably Err cover), hd: hauptdolomite.

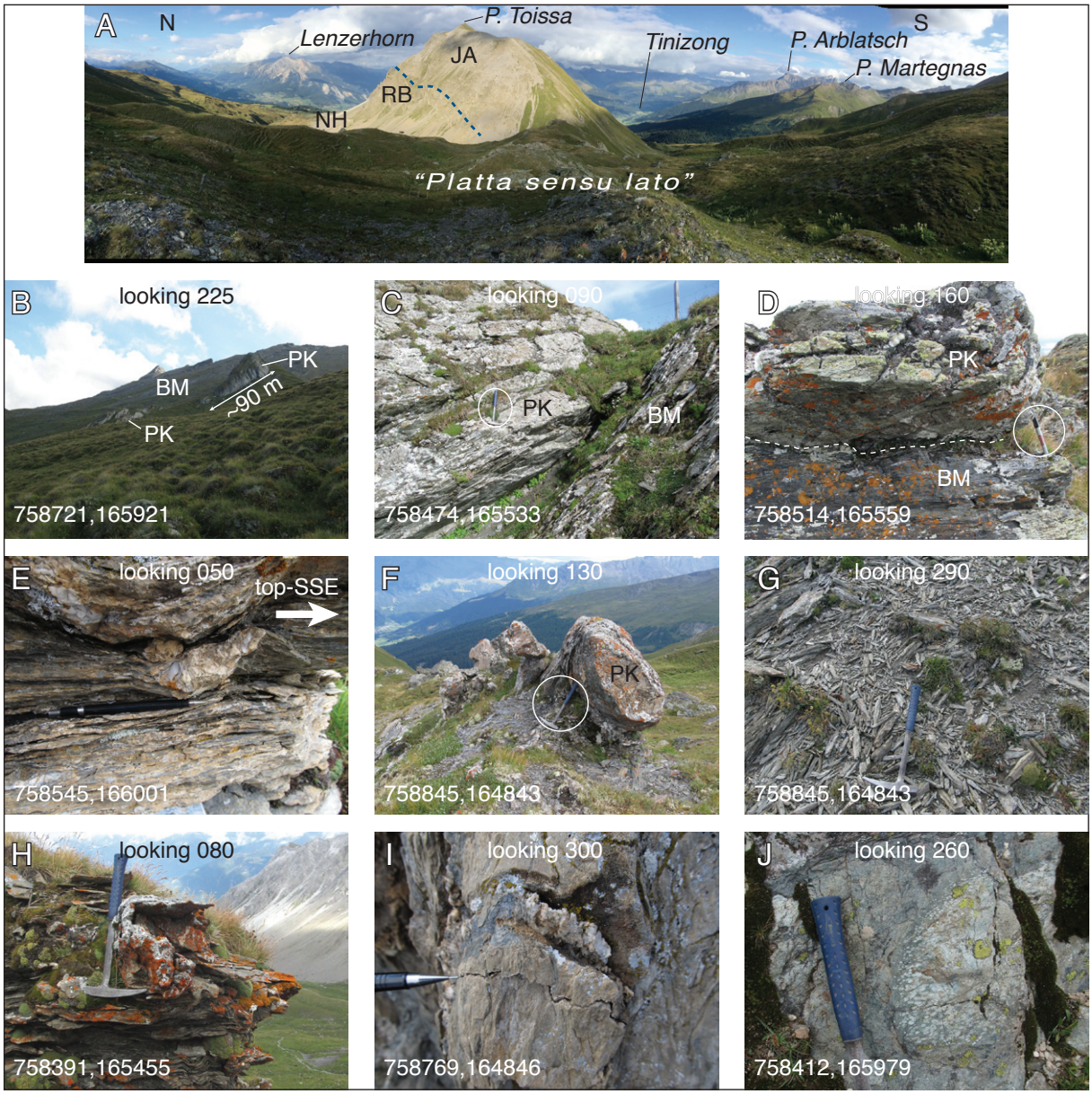

Fig. 2.4. Photographs of the Martegnas shear zone, Site 1, Ziteil. All coordinates in Swiss grid CH 1903. Hammer is 42 cm long. A) Panorama looking east from east flank of Piz Curvér to Oberhalbstein valley. Piz Toissa is an Austroalpine klippe of Jurassic Allgäu (JA) in fault contact (blue dashed line) with Rhätian Blue-kalk (RB) and Norian Hauptdolomite (NH) that overlies Platta *sensu lato*. Note hummocky topography on dip slope of Piz Curvér. Lenzerhorn to Piz Arblatsch is ~19 km. B) Looking SW toward summit of Piz Curvér, 'Shark fin' ridges are Platta knockers (PK) plunging easterly ± 30° (c.f. green polygons in Fig. 2.2) encased in Bündnerschiefer matrix (BM). C) Ductile fault contact between Platta knocker (PK) and Bündnerschiefer matrix (BM); hammer (circled) for scale. Location of sample PL15-01 (cf. Fig. 2.4 A,B). D) Brittley-deformed Platta knocker (PK) cut by quartz veins encased in ductiley-deformed, protomylonitic Bündnerschiefer matrix (BM), typical of the Martegnas shear zone; 13.6-cm-long marker (circled) for scale. E) Coarse-grained calcite porphyroclast in Platta ophicalcite block indicating top-S30E shear; black 14-cm-long pencil for scale. Locatin of sample BD15-06 (cf. Fig. 2.4 C through E). F) Elliptical cross section of Platta spilite knocker (PK) near Ziteil chapel. Prolate form plunges S50E. Hammer (circled) for scale. View towards Tinizong. G) Isoclinally-folded (S2-foliation) calcareous schists that have been overprinted by a strong stretching fabric to form modified "pencils" that surround the prolate spilite shown in F. H) Minor S-fold in crenulated Bündnerschiefer indicates top-N shortening and occurs down structural section from the Platta knockers. Crenulated fabric appears to be less strained compared to the overlying zone of Platta knockers. I) Early tectonic stylolite filled by later quartz vein with c-axis growth parallel to stylolite teeth (that plunge S60E) indicates incompatible strain fields, requiring a period of compression to the NW followed by a period of extension to the SE. J) Flattened pocket of vesiculated basalt is interpreted to be a pillow. Hammer handle for scale.

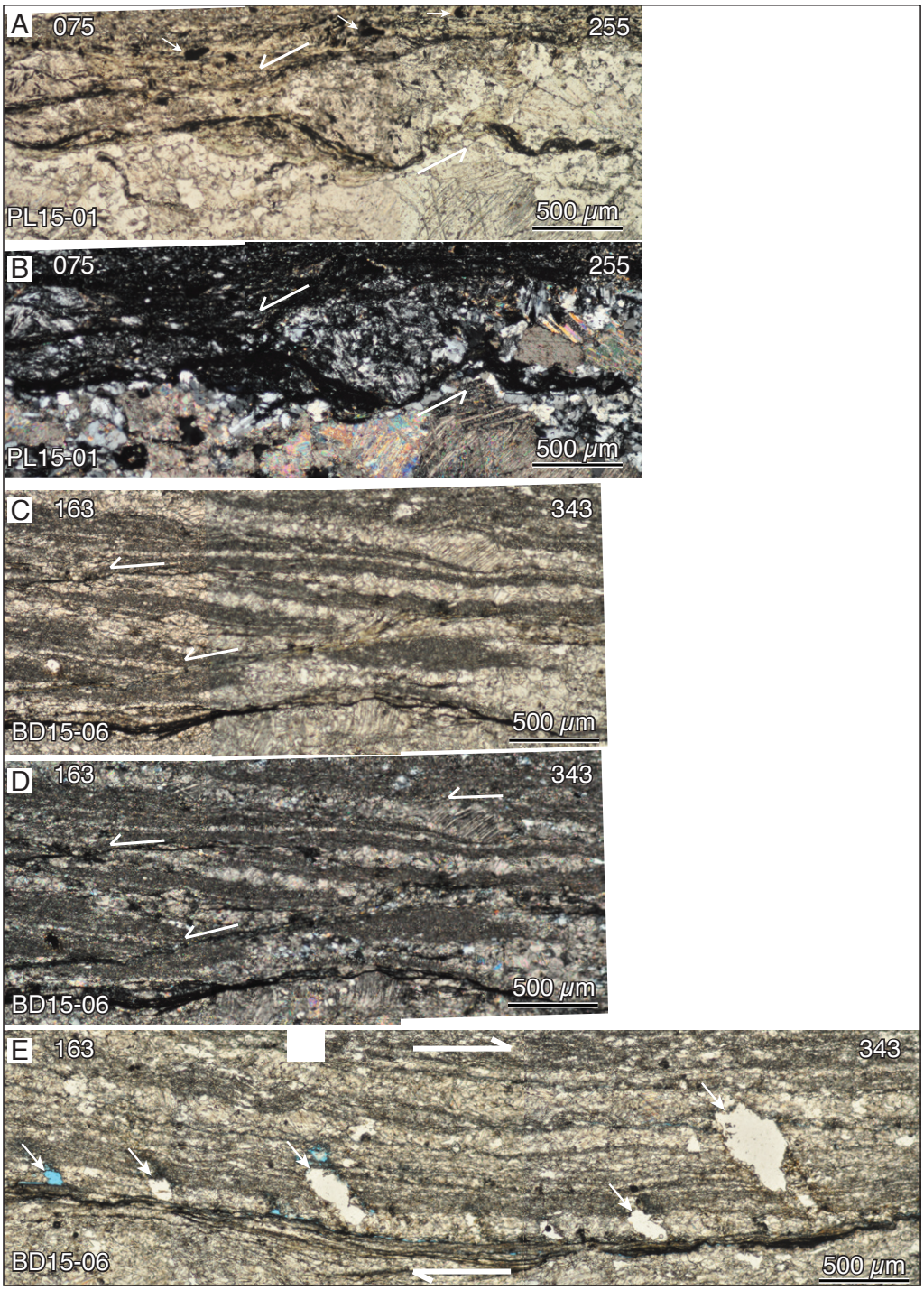

Fig. 2.5. Photomicrographs of two samples from Site 1, Ziteil. A and B are from sample PL15-01; C, D, and E are from sample BD15-06. A) Plane-polarized light (PPL) image of chloritized Platta metabasalt (sample PL15-01). Fine-grained plagioclase is largely replaced by fine-grained chlorite (clinochlore, 72% match to Raman spectroscopic library) and in-filled with coarse-grained calcite. Dark grains (small double-barbed arrows) are anatase (85% match to Raman spectroscopic library). Note the dark seams of very fine-grained chlorite and/or organic material that form stylolitic margins along coarse-grained calcite. Top-left towards 075 (plunging 30°). B) Cross-polarized light (XPL) image of A. Nearly all of the extinct grains in the upper half of the image are chlorite. C) PPL image of Platta *s.l.* ophicalcite (sample BD15-06) exhibiting coarse-grained recrystallized calcite bands that are inclined and cut-off along their bases which indicates top-left motion towards 163 (plunging -5°). D) XPL image of C. E) PPL image of BD15-06 shows that early recrystallized calcite fabric is cut by later unfilled en-echelon shear fractures (arrows) that indicate top-right brittle motion towards 343 (plunging 5°). Blue cavity at left side of image is blue-stained epoxy filling the void.

Fig. 2.6. Photographs of field relationships above the Martegnas shear zone at Site 2, Savognin, displayed from structurally lowest to highest, up to ca. 100 m below the Austroalpine contact. A) Recumbent folds of sandstone layers form dramatic, knobby relief in a cliff face of North Penninic flysch. Yellow lines emphasize resistant sandstone layers, which form macroscopic Z-folds indicating top-southeast motion. Dashed white line traces a later normal fault (also shown at left edge of C). B and C are inset photos from A. B) Prominent stretching lineation observed on the sides of sandstone folds parallels the orientation of the axial hinges and plunges gently east. C) Centimeter-thick sandstone beds recumbently Z-folded and cut by a small normal fault. D) Thick, resistant North Penninic sandstone bed ca. 8 m thick outcropping in the Sursés alp above Savognin. These sandstone beds are depicted as discontinuous NW-striking brown polygons on the geologic map (**Fig. 2.3 A**). Geologist for scale. E is an inset photo of D. E) Weakly deformed sandstone exhibiting crenulations and subtle mullions at the base of the small cliff shown in D. Mullions plunge gently east, approximately parallel to the lineations shown in B. Note that the view direction in D and E are not the same. Hammer for scale. F) Quartz+calcite acicular fibers (pseudomorphs after carpholite?) growing eastwards is an example of the penetrative lineation seen in the stereonet data (**Fig. 2.9 C**). Photo is looking up underneath an overhang. Pencil for scale. G, H) Uncommon sheared porphyroclast of sandstone in grey phyllitic matrix. Subtle drag-folding (enlarged in H) along margins of porphyroclast indicates top-ESE motion. Swiss coin for scale. I) Incipient S-C fabric in phyllitic siliciclastics show top-SSE motion. Dashed line on S-plane for emphasis. Pencil for scale. J) Recumbent folds of discontinuous sandstone beds and dark grey phyllite is a typical texture of North Penninic flysch at this locality. Yellow line traces the edge of a ca. 10-cm-thick sandstone bed that has been necked and recumbently folded. Dissertation writer for scale. K) Antithetic low-angle normal fault cuts ductile fabric with top-N motion. Hammer (circled) for scale. L) Mesoscopic *en echelon* high-angle faults cut the ductile deformation fabric and indicate sinistral shear (south block-up). Hammer (circled) for scale.

shear zone as described by Dietrich (1969), Eiermann (1988), and Weh (1998), and here we treat it as the northern continuation of the zone. Because of the dip-slope, structural relief is limited to c. 100 m when traversing from the top of Piz Curvér to the saddle formed by Piz Toissa near the Ziteil chapel (Figs. 2.3, 2.4 A, B). The rocks of Piz Curvér are mapped by the Swiss Federal Office for Water and Geology (Streiff et al., 1976) as Platta *s.l.*, defined by discontinuous outcrops of resistant 1 m- to 100-m-scale exotic blocks, i.e., knockers, of Platta *sensu stricto* (*s.s.*)-type lithologies, such as greenish grey spilitized basalt and pillow lava (Figs. 2.4 C, D, F, J, 2.5 A, B), grey ophicalcite (Figs. 2.4 E, 2.5 C, D, E), thin bands of red radiolarian chert, and amorphous masses (boudins?) of dark green, vegetation-free, serpentinite. Ophiolitic elements are encased in a non-resistant matrix comprising dark grey to brown, thinly-foliated phyllites and calcareous metapelites (Figs. 2.3 A, 2.4 B, C, D; Eiermann, 1988). Platta *s.s.* knockers were observed to vary in size from roughly 10,000 m^3 (50 x 20 x 10 m) for an amorphous block of serpentinite near Piz Toissa to <1 m^3 for certain blocks of spilitized and pillow basalt (Fig. 2.4 D, F, J) and radiolarite. Platta knockers occur in a preferential horizon from 0-200 m below the contact with the Austroalpine allochthon, and thus, in map view, more Platta knockers occur on the east flank of Piz Curvér than on either Piz Martegnas or the west flank of Piz Curvér, the latter being deeper in the structural section (Fig. 2.3 A). As a result of the interposed Platta *s.l.* lithologies, resistant knockers protrude from the alp, but less resistant Bündnerschiefer-like phyllites are largely covered by vegetation, which results in a mounded, hillocky topography with local relief of order 1-10 meters and no large cliffs (Fig. 2.4 A, B, F). In that resistant knockers are encased in a weaker, tectonized matrix, Platta *s.l.* resembles the Franciscan mélange of California, USA, as described by, e.g., McLaughlin and Olin (1984) and Aalto and Murphy (1984).

In contrast, Piz Toissa (Figs. 2.3, 2.4A) comprises an unmetamorphosed, weakly-strained klippe of Austroalpine carbonate rocks of the Ela nappe of lower East Alpine affinity. In the klippe, dark grey Jurassic Allgäu formation is discordantly faulted against underlying Triassic carbonate rocks, including concordant, upright Rhaetian “Blue kalk” and subjacent Norian Hauptdolomite. Younger-on-older faulting indicates the discordance is most likely a normal fault, and the age of the fault must predate Alpine deformation, as the fault does not cut Pennine rocks beneath the klippe. The striking contrast between weak penetrative deformation in the Austroalpine klippe versus strong penetrative deformation in the subjacent Pennine zone is remarkable and has been recognized in the literature at least as far back as Ott (1925). Across the Oberhalbstein Valley below Piz Mitgel, Ela carbonate rocks sit structurally above Err nappe cover rocks, but Err nappe cover rocks are completely absent from the klippe at Piz Toissa, having been faulted out. Lastly, Streif et al. (1976) point out that Piz Toissa has been preserved because it sits in the trough of a synformal depression which plunges moderately to the ENE, parallel to the Martegnas shear zone (indicated by the map pattern in Fig. 2.3 A).

One vitrinite reflectance measurement has been made in the Martegnas shear zone near Savognin and has a high epizonal to lowest greenschist facies, nearly graphitic, value of 8.8 (Rmax%; c. 350°C; Ferreiro-Mählmann, 1995). One zircon (U-Th)/He (ZHe) cooling age of 23.8 ± 1.6 Ma (sample BD15-

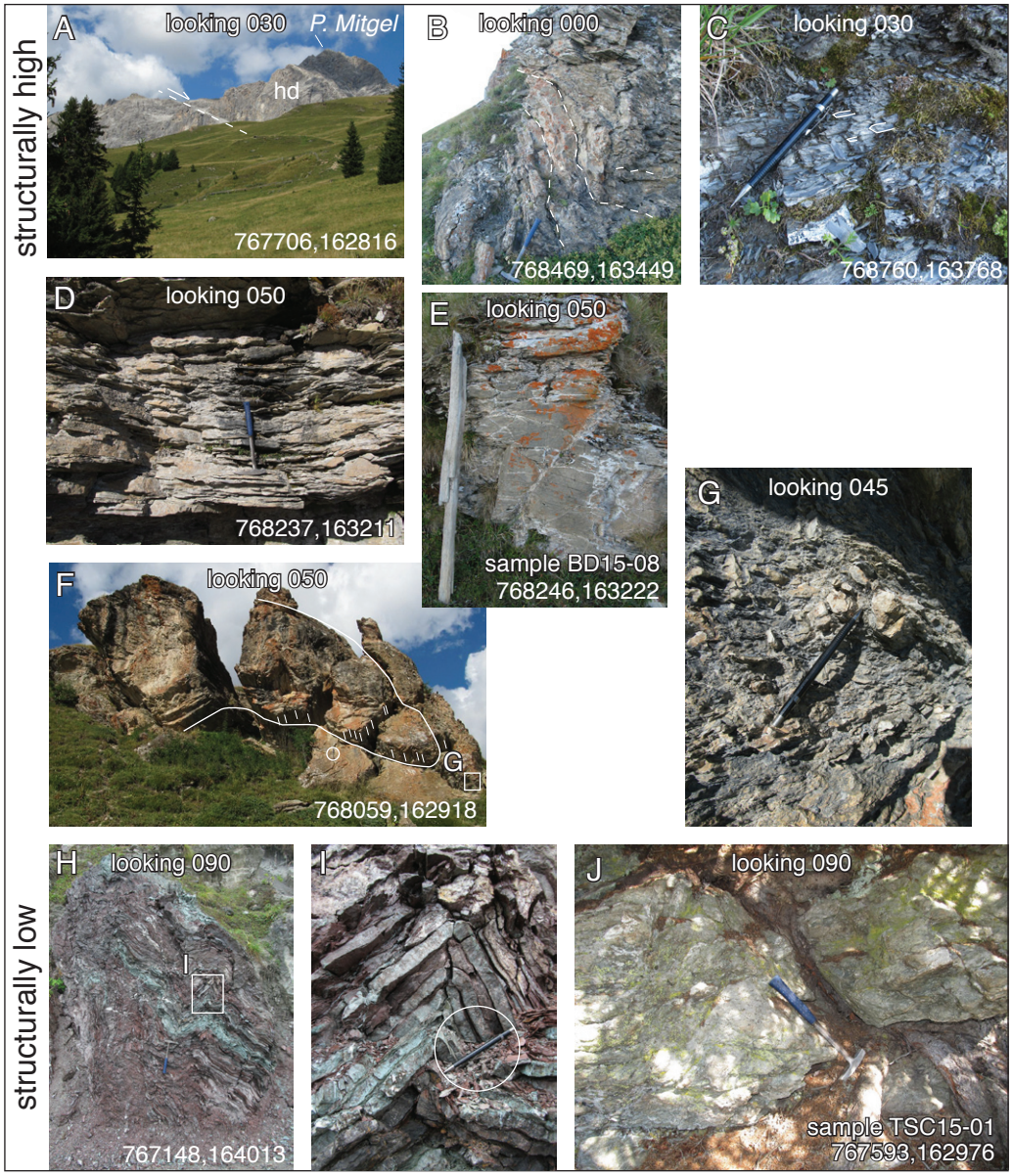

Fig. 2.7. Photographs of field relationships in Austroalpine Err cover rocks, Site 3 below Piz Mitgel. Structurally lowest outcrops occur <50 m above the Austroalpine-Pennine contact; structurally highest outcrops occur about 500 m above the Austroalpine-Pennine contact and ~50 m below the thrust fault contact with the overlying Ela nappe. A) Overview photo taken near Nassegl farmhouse looking up the Sursés alp towards Piz Mitgel. Normal fault with ~100 m of throw cuts Norian Hauptdolomite (hd) in the Ela nappe but apparently does not cut down into the underlying Err nappe. Pine trees for scale. B) Mesoscopic open Z-fold in irregularly crenulated limestone of the Liassic Agnelli Formation. Hammer for scale. C) Intersection cleavage pencils oriented 06/070 in slatey layer in Agnelli Formation about 50 m below the Hauptdolomite thrust fault. Pencil for scale. D) Weakly to undeformed thin-bedded Agnelli limestone. Hammer for scale. E) Weakly to undeformed Err sandstone (Agnelli Formation?). ZHe age of this outcrop is ~44 Ma (Fig. 2.3). 1.3 m-long-pencil--a "Jacobs lithostaff"--for scale. F) Recumbently-folded Cretaceous *Aptychus* limestone breccia about 100 m structurally-above the Austroalpine-Pennine boundary. Well developed linear fabric (indicated by short white lines) is axial planar intersection cleavage. Hammer (circled) for scale. G) Inset of 'F' showing detail of the limestone breccia including clasts that trend NE. H) Red and green radiolarian chert beds with upright chevron folds mark the base of the Austroalpine allochthon. These are the only upright or harmonic folds observed in the Savognin region which suggests an earlier period (Cretaceous?) of deformation that was not overprinted by Alpine deformation. I) Inset of 'H'. Pencil (circled) for scale. J) Tschirpen gneiss at the same structural horizon (base of the Austroalpine) as 'H' and 'I' has abundant chlorite and white mica overgrowths but does not exhibit a strong asymmetric fabric. ZHe age of this outcrop is ~42 Ma (Fig. 2.3)

07, 758449, 164781, 2589 m above sea level, a.s.l.) has been measured from the east flank of Piz Curvér, near the bottom of the Martegnas shear zone. A second, nearby, ZHe age of 24.5 ± 2.7 Ma (sample SUR15-01, 755690, 165478, 2355 m a.s.l.) was measured from the Rofna porphyry at the top of the Suretta nappe, a few hundred meters structurally below the Martegnas shear zone and approximately 2.8 km to the west-northwest (Figs. 2.2, 2.3; see also Chapter 1).

2.2.1.2. Site 2, Savognin, local geology and thermochronology

Site 2 is located along the roadcuts and outcrops in the lower third of the large alp directly east of the towns of Savognin and Tinizong and below (southwest of) Piz Mitgel. This site is positioned structurally above Site 1, Ziteil by, at most, a few hundred meters. The rocks here are mapped as Tertiary North Penninic flysch, correlative to both the 'Parsonzer' flysch which crops out on the southwest side of the valley at Piz Martegnas (Eiermann, 1988) and the Arblatsch flysch found at Piz Arblatsch located about seven kilometers to the south-southwest. Owing to the stratigraphic continuity of Lower Tertiary flysch across the Oberhalbstein Valley, we regard Sites 1 and 2 to be a coherent, kinematically-linked tectonic zone that exhibits a persistent top-east to -southeast sense of shear. Even so, it should be noted that the North Penninic flysch at Site 2 does not closely resemble the more coarse-grained and penetratively-deformed North Penninic flysch (Arblatsch flysch *s.s.)* as found on Piz Arblatsch.

At the structural bottom of Site 2, the flysch is a remarkably homogeneous body of tectonized and recumbently-folded grey phyllite with intercalated brown sandstone beds up to 25 cm thick. Sandstone beds form discontinuous lenses and ribbons that are cut by ubiquitous quartz-calcite veins. Thin sandstone beds may be sheared and rotated as rigid porphyroclasts in the ductile phyllitic matrix which exhibits a mm-scale penetrative S1 cleavage (Fig 2.6 G, H, I, J). Penetrative foliation defined by recumbently-folded S1 foliation and layer-parallel quartz veins indicates that the dominant cleavage in the lower roadcuts is S2 and parallels the axial planes of recumbent folds (Fig. 2.6 J). Acicular quartz vein fabric elongate to the east (Fig. 2.6 F) may indicate pseudomorphic growth after carpholite, heretofore not described from the Oberhalbstein Valley. Moving up structural section, one encounters elongate, weakly deformed lenses of medium-grained sandstone (shown as brown polygons on the map in Fig. 2.3 A; photographs in Fig. 2.6 D, E). Deformation is focused on the peripheries of the sand bodies where mullions and/or a weakly developed crenulation cleavage is observed (Fig. 2.6 E). In map pattern (Fig. 2.3 A), the sand bodies form a series of discontinuous stratiform zones, which are likely large tectonic boudins, although outcrop is obscured by thick vegetation on the hillslope (Fig. 2.6 D), so a direct observation of boudinage at this map scale could not be made.

One vitrinite reflectance measurement was made in the North Penninic flysch near Savognin and has a high epizonal value of 6.0 (Rmax%; c. 300°C; Ferreiro-Mählmann, 1995). A single zircon U-Th/He age of 27.5 ± 3.6 Ma from a sample of medium-grained sandstone (sample BD15-03, 767098, 162243, 1631 m a.s.l.) has been measured in this zone. This North Penninic flysch sample cooled approximately

three million years earlier and experienced a lower overall metamorphic peak temperature (approximately 50°C less) compared to the Platta *s.l.* phyllite sample measured on Piz Curvér.

2.2.1.3. Site 3, Mitgel, local geology and thermochronology

Site 3 is located entirely within Austroalpine Err nappe cover rocks at and above the tectonic contact with the Pennine zone. The contact is exposed in discontinuous, small roadcuts and outcrops along the road to the farmhouses at Nassegl village. The contact is marked by a subtle change in deformation fabrics and an appearance of discontinuous lenses of lithologies associated with the Austroalpine domain, including meter-scale outcrops of upright, harmonically folded radiolarian chert associated with the Platta nappe *s.s.* (Fig. 2.7 H, I) and boudinaged blocks of chlorite-rich, poly-deformed, gneissose plagiogranites associated with the Tschirpen slice *s.l.* (Fig. 2.7 J). This basal mélange-like zone of disparate lithologies is approximately 50 meters thick. Moving up tectonostratigraphic section, occasional outcrops reveal *Aptychus* (Lower Cretaceous) limestone overlain by and/or interleaved with Malm (Upper Jurassic) and Liassic (Lower Jurassic) micritic and sandy limestones. Marmot holes burrowed into the alp between these discontinuous outcrops indicate that the covered units on the hillside are siltstones with a weakly-developed micaceous cleavage. In that there is Lower Cretaceous at the base of the alp and Lower Jurassic (Liassic) units at the top of the alp and that the section appears to be concordant, this c. 450-m-thick section of Austroalpine (Err nappe cover rocks) is overturned. The alp is capped by an impressive c. 350-m-high cliff culminating in Piz Mitgel (3159 m, 769110,164934; Fig. 2.7 A) that comprises upright Norian hauptdolomite, Rhaetian Bluekalk, and Jurassic Allgäu Formation (similar to that found at Piz Toissa, Site 1), which has been thrust over the overturned Jura-Cretaceous stratigraphy. A large, late normal fault with about one hundred meters of throw cuts this entire cliff dropping the south block down (Fig. 2.7 A), and a climbing route, "*klettersteig*", has been pioneered directly up this fault surface.

Estimates of peak metamorphic temperature and pressure for the Err nappe are approximately 300°C and 7 kbar (Handy et al., 1996), achieved during the Cretaceous. Four vitrinite reflectance measurements have also been made with values of 5.2, 4.8, 4.8, and 3.9, indicating low epizonal peak metamorphism (Rmax%; c. 280°C; Ferreiro-Mählmann, 1995), which is in approximate agreement with Handy et al. (1996). None of the carbonate units are marbleized in the study area. Three zircon U-Th/He ages have been measured in the Err cover rocks of Site 3 (Chapter 1): 48.7 ± 7.2 Ma (sample PL15-07, Platta *s.s.* diorite, 767297, 163336, 1972 m a.s.l.), 44.3 ± 6.5 Ma (sample BD15-08, Err sandstone, probably Agnelli Formation, 768247, 163222, 2288 m), and 42.1 ± 5.7 Ma (sample TSC15-01, Tschirpen *s.l.* chloritized gneissose granitoid, 767593, 162976, 2010 m). These cooling ages indicate that this part of the Austroalpine was buried by approximately 6 to 8 km during the lower half of the Eocene and had cooled through zircon-helium-closure some 15 to 20 million years before either of the samples in the Martegnas shear zone c. 500 m structurally below the Eocene cooling ages.

2.2.2. Mesoscopic structural data at the top of the Pennine zone

In outcrop and road cut, a variety of elements of structural fabric were measured, including : 1) foliations, where S0 is defined as bedding; S1 is the first metamorphic cleavage to overprint S0; S2 overprints S1; etc. At times, particularly in discontinuous outcrops, it was ambiguous whether foliation was S2 or S1. 2) fold axes and fold axial planes, 3) penetrative mineral lineations and "pencil" intersection cleavages, 4) veins, exclusively quartz or calcite in composition everywhere we took measurements, and 5) Brittle faults with slickenfiber slip lineations. Brittle faults were not observed at every site. For the purposes of mesoscopic structural measurements, road cuts are preferred to outcrop because they provide a clean, continuous, unambiguous exposure of rock units that does not preferentially favor harder, more competent units to the exclusion of softer, less competent units, as does outcrop. Owing to past glaciation and the presently thick vegetative cover in the Central Alps, outcrops of poorly indurated units are virtually non-existent below ~2400 m elevation. This is mainly a concern for measurements of finer-grained flysch units.

All structural measurements are plotted on lower-hemisphere, equal-area (Schmidt) stereographic projections (Figs. 2.8, 2.9, 2.10, 2.18, 2.20, 2.21, 2.22), and a distillation of summary data is presented in the final stereogram in each plot. Contouring of linear elements, including poles to planes, are done at 1% area of the stereonet and contoured with integers (1%, 2%, 3%, etc.). All plots were made using Stereonet 9.5 and FaultKin 7.4.1 software (Marrett and Allmendinger, 1990; Allmendinger et al., 2012; Cardozo and Allmendinger, 2013). Attitudes of planar elements are reported as azimuth strike/dip using the right-hand rule convention; orientations of linear elements are reported as plunge/trend in order to minimize confusion with planar attitudes. The following data presentation will largely refer to the summary stereograms (panel 'F' in each stereogram figure).

2.2.2.1. Site 1, Ziteil, mesoscopic and microscopic structural data

At Site 1, Ziteil (Figs. 2.3, 2.4, 2.8), two principal orientations of S2 foliation exist, one striking northwesterly, dipping 41° northeast, the second striking northerly, dipping 31° east. The attitude of the mean axial plane of folds, particularly folded quartz veins, is 330/33 and bisects the two S2 foliation directions. About half (n=6) of the fold axial planes are concordant with S2-foliation, but the other half of the axial planes (n=5) are 'transverse folds' that strike northeast and dip either northwest or southeast. Fold hinges plunge shallowly, 24° to the ESE. Penetrative lineations generally plunge from 25° to 50° and have trends that vary between 060 and 290 but are not observed in the northerly approximately one-third of the stereogram between 290 and 060. Two local maxima exist for penetrative lineations, one plunging 28° northeast and the other plunging 34° southeast. The more southerly penetrative lineation parallels the maximum orientation of fold hinges. Veins are primarily late, post-date the ductile fabric, and strike both northerly and northeasterly. The stereogram pattern for veins suggests there is a conjugate set for both the northerly and northeasterly strike directions. At least one vein was observed to have

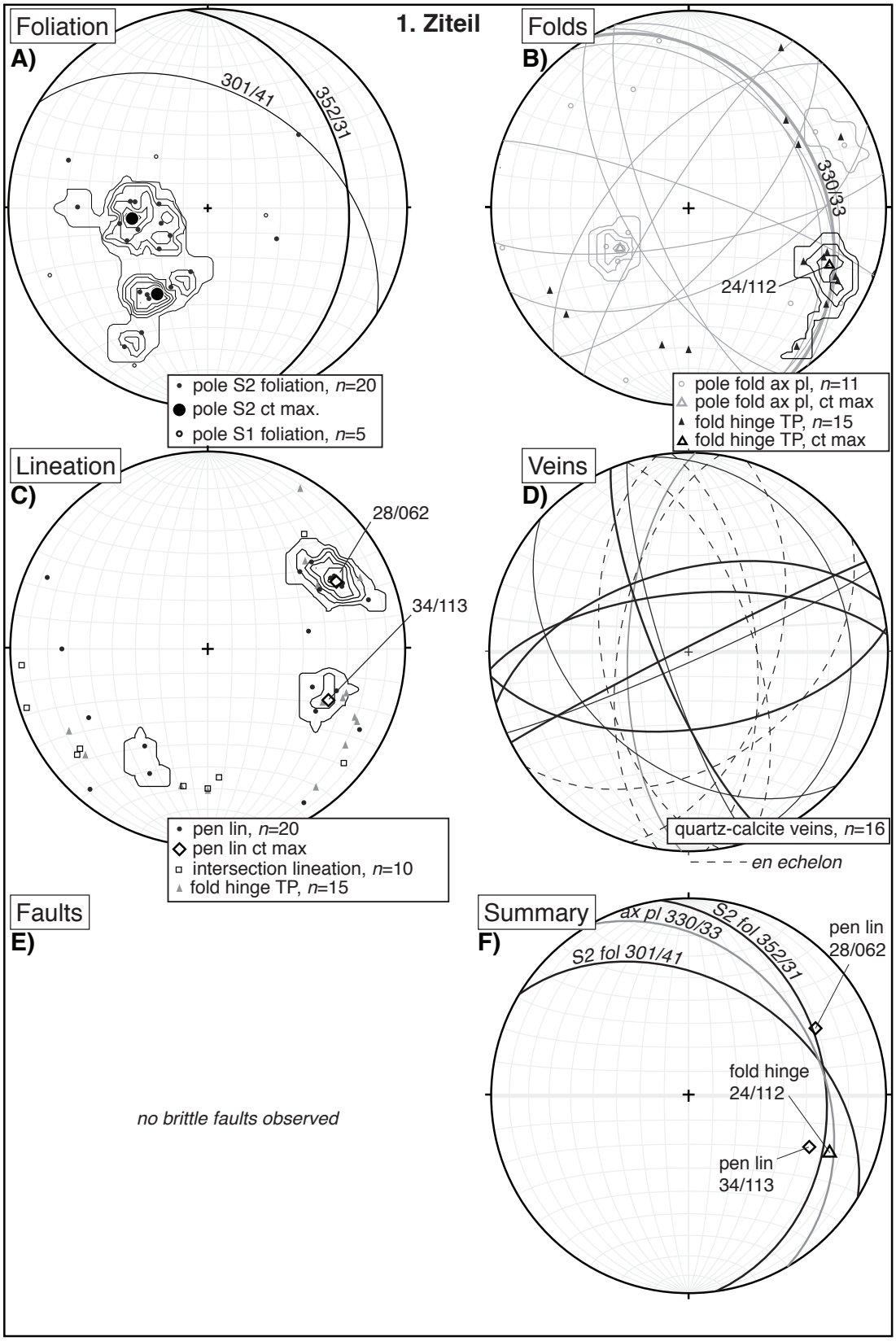

Fig. 2.8. Stereographic projections of field measurements at Site 1, Ziteil. Label at top-left corner of stereogram indicates general category of data plotted; number of data shown in legend at bottom of each stereonet. Abbreviations used in this and all subsequent stereogram plots: ax pl: axial plane; ct max, contour maxim(um/a); fol: foliation; pen lin: penetrative lineation; TP: trend/plunge.

fibers that grew oblique to vein walls showing evidence of dilatation toward the southeast. In a marl unit, some calcite veins occupy former tectonic stylolites (Fig. 2.4 I), which clearly indicates multiple periods and styles of deformation, i.e., compression in one (northwesterly) direction followed by extension in a parallel, but opposite (southeasterly), direction. There were no brittle faults observed in outcrop at Ziteil. Nearly all of the deformation is accommodated in an overall ductile regime with only minor centimeter- to meter-scale brittle structures, namely joints and veins, that primarily affect the spilitized basalt blocks (Fig. 2.4 D).

Photomicrographs of two samples (Fig. 2.5), one ophicalcite (BD15-06) and one spilitized basalt (PL15-01), indicate variable top directions. The ophicalcite contains an earlier ductile fabric that shows minor C-plane development that indicates top-south-southeast (163) movement which is cut by brittle, dry (unfilled) *en echelon* shear fractures that indicate top-approximately-north movement [N.B. The sample was cut parallel to the lineation in the YZ plane so as to measure the ductile shearing direction. The apparent motion indicated by the *en echelon* fractures was not taken into consideration during sample preparation and therefore, the top-right sense-of-shear indicated by the fractures is likely not exactly in the direction of 343. Furthermore, the difference in size of the *en echelon* fractures suggests that the brittle plane of shearing is oblique to the YZ plane]. The spilite has been extensively chlorite-calcite altered and shows both stylolite formation and minor C-plane development that indicates top-east-northeast (075) movement. These outcrops are located only a few hundred meters apart and the inconsistency in their shear direction indicators may be the result of late broad folding, local block rotation in the mélange zone, or the individual lithologies recording separate, localized strain events.

2.2.2.2. Site 2, Savognin, mesoscopic structural data

At Site 2, Savognin (Figs. 2.6, 2.9), S2 foliation forms two maxima, one striking WNW, dipping 28° NE, the other striking N, dipping 17°E. The mean fold axial plane strikes NNW and dips 17°E and essentially bisects S2 foliation. The orientation of fold hinges plunges shallowly over a range of easterly trends from 030 to 130 with a contoured maximum that plunges 15° northeast (051). The penetrative lineations commonly observed on S2 foliation planes dominantly plunge shallowly between 078 and 124 and have a contoured maximum that plunges 12° east (086), indicating elongation in that direction. High-angle veins strike northerly, northeasterly, and, for a few, easterly. There is also clearly a low-angle population of veins that are conformable to S2 foliation and help to define that foliation. Late meter- to decameter-scale brittle faults (n=37) cut the earlier ductile deformation and form two contour-maxima sets, one striking WSW dipping 34°, the other striking NE dipping 47°. On eight of these faults, slickenfiber orientation and fault slip-sense were recorded and, when modeled, yield principal shortening (P) and principal extension (T) axes of high-angle to the southwest (65/246) and low-angle to the southeast (12/129), respectively. At least one meter-scale brittle fault was observed to jog in an *en echelon* fashion indicating south-block-up motion (Fig. 2.6 H).

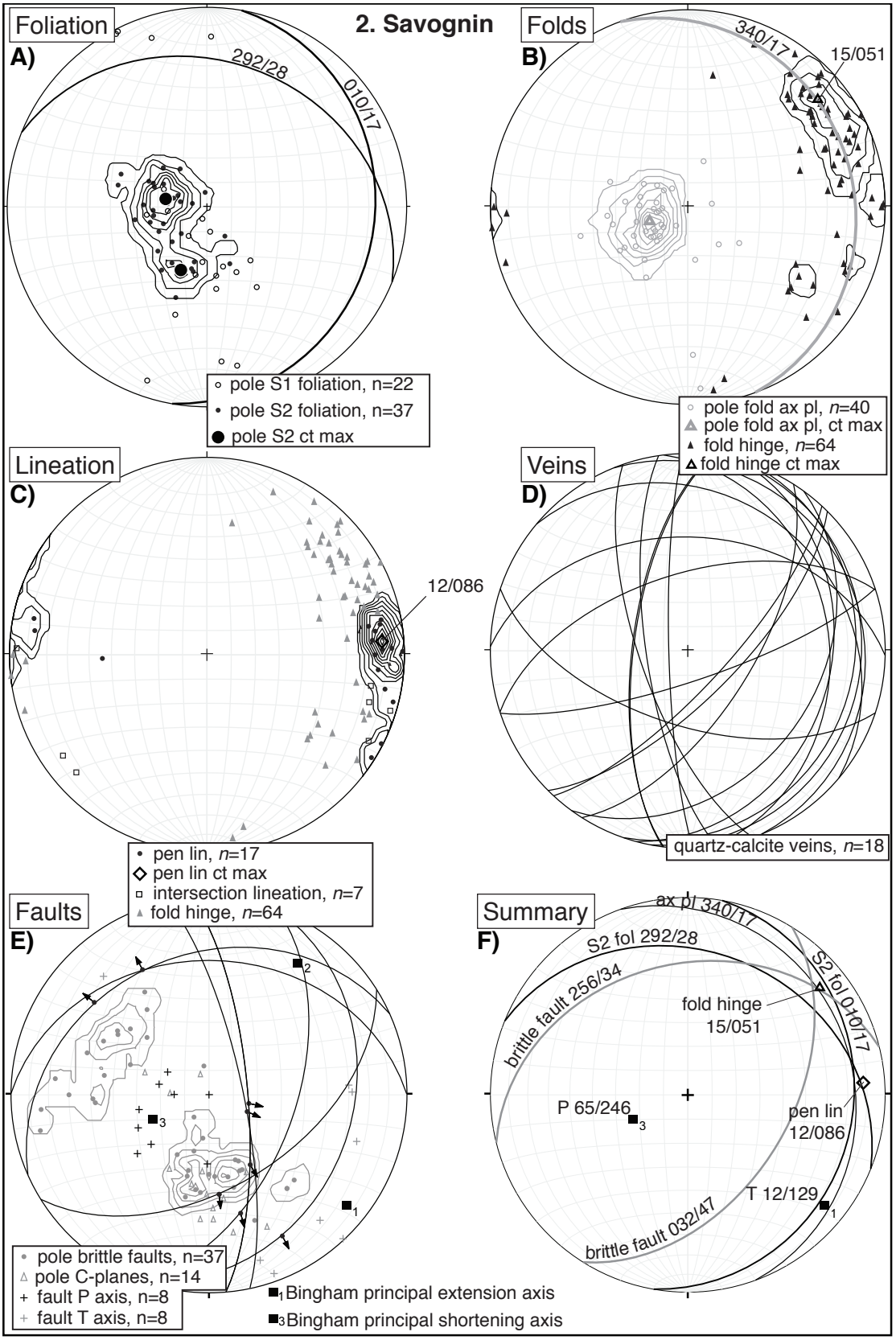

Fig. 2.9. Stereographic projections of field measurements at Site 2, Savognin. Label at top-left corner of stereogram indicates general category of data plotted; number of data shown in legend at bottom of each stereonet.

2.2.2.3. Site 3, Mitgel, mesoscopic structural data

At Site 3 (Figs. 2.7, 2.10), the intensity of the deformation decreases, and generally there is no unequivocal penetrative S2 foliation. Most measured foliation was S1, and in some places original bedding S0 is still apparent. S1 foliation displays two maxima, a global maximum striking east and dipping 36° south and a local maximum striking west and dipping 46° north. A tentative π-girdle through all S1 poles may indicate a large, km-scale, fold plunging shallowly east (09/099); however such a fold was not directly observed in outcrop. Mesoscopic folds observed in outcrop have a mean axial plane striking northeast and dipping sub-vertically and a mean fold hinge plunging very shallowly to the west (09/271). Penetrative lineations were scarce but plunge shallowly towards northeast, west-northwest, and west (black circles in Fig. 2.10 C). Scarce late veins are exclusively high-angle and strike east or northwest. Brittle faults were likewise scarce and strike generally east-northeast and dip moderately to steeply southeast.

2.2.3. Summary of field observations and structural measurements, top of the Pennine zone

Dominant rock fabric at the three sites is almost entirely shallowly-dipping and/or -plunging (Figs. 2.3 B, 2.11), including the S2 foliation found throughout the Upper Pennine zone (Site 1, Ziteil and Site 2, Savognin), the S1 foliation in the overturned Err nappe (Site 3, Mitgel), and even the S0 bedding in the Ela nappe on Piz Toissa (Site 1, Ziteil). The one tectonostratigraphic horizon where there is no coherent penetrative foliation development is in the basal ca. 50 meters of the Austroalpine allochthon where there exists a kind of mélange of Platta *s.s.*, Tschirpen *s.l.*, and Err cover rocks exhibiting various foliation directions that are not consistent from outcrop to outcrop.

S2 foliation in the Upper Pennine zone has bi-modal maxima, in which one set strikes northwest and dips moderately northeast (301/41 and 292/28, Sites 1 and 2, respectively), and a second set strikes north and dips moderately or shallowly east (352/31 and 010/17, Sites 1 and 2, respectively). For both sets, the steeper dips occur in the Martegnas shear zone of Site 1, and, remarkably, the dips of both sets shallow almost identically, 13° for the northwest-striking set, 14° for the north-striking set, moving up tectonostratigraphic section to Site 2. The set with northwest-strike, northeast-dip is consistent with the regional structural grain evident in the geologic map of the Oberhalbstein Valley (Figs. 2.2, 2.3), and the set with north-strike, east-dip suggests that broad, open folding may overprint the dominant foliation in the Upper Pennine zone. In contrast, S1 foliation in the Austroalpine Err nappe strikes almost exclusively east-west and dips at a variety of angles, from shallow to steep, but has maxima at 080/36 and 276/46, consistent with east-west trending fold hinges that most likely pre-date Alpine deformation (per the descriptions and age dates in Handy et al., 1996). In contrast to Err nappe at Piz Mitgel, Ela nappe units at Piz Toissa strike northwest and dip southwest into the fault that separates Ela from the underlying Platta *s.l.* on the flank of Piz Curvér.

Penetrative, stretching lineations are readily evident at Site 1, where basaltic knockers and their phyllitic matrix have been stretched in the direction of east-northeast, east, and east-southeast and yield

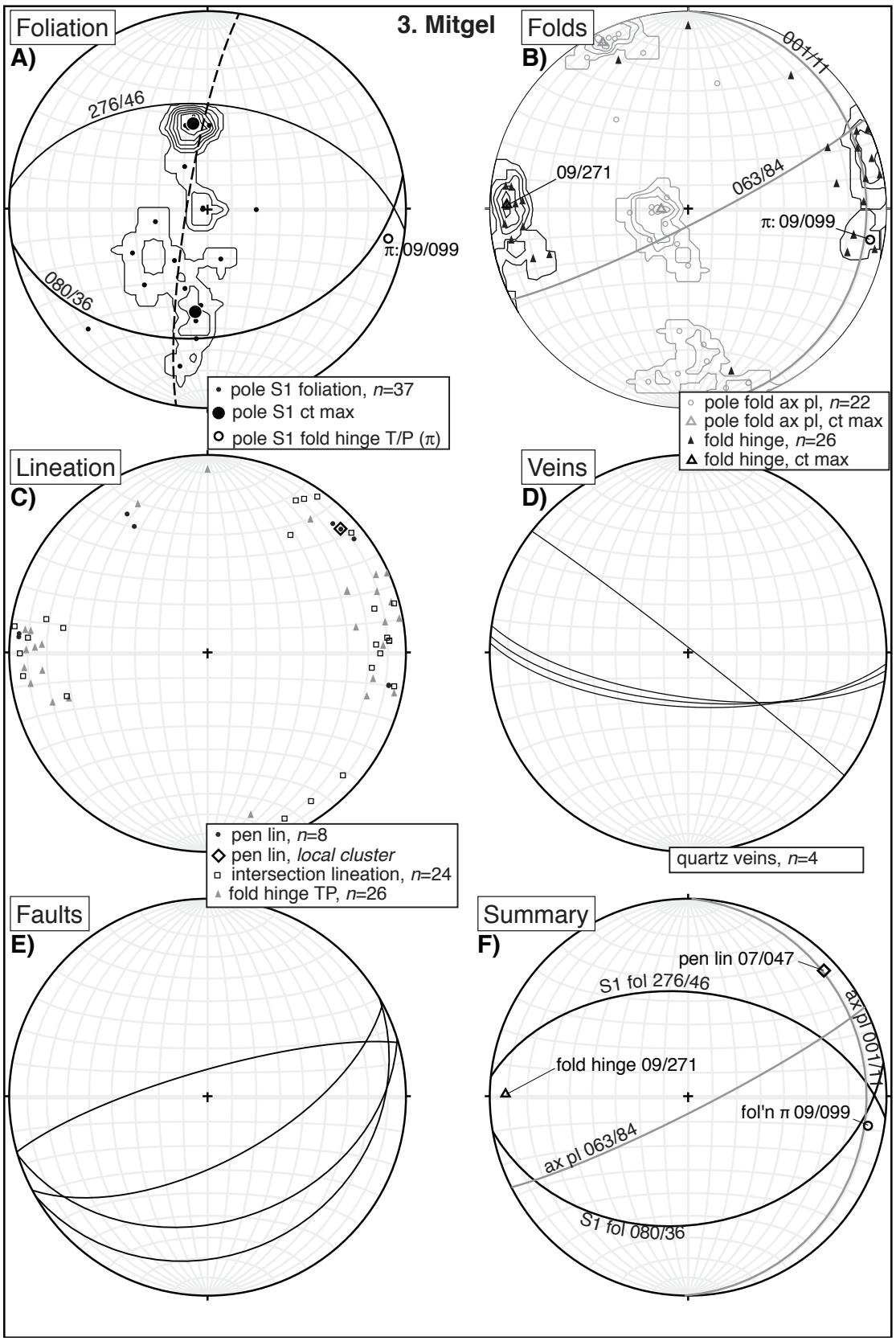

Fig. 2.10. Stereographic projections of field measurements at Site 3, Mitgel. Label at top-left corner of stereogram indicates general category of data plotted; number of data shown in legend at bottom of each stereonet.

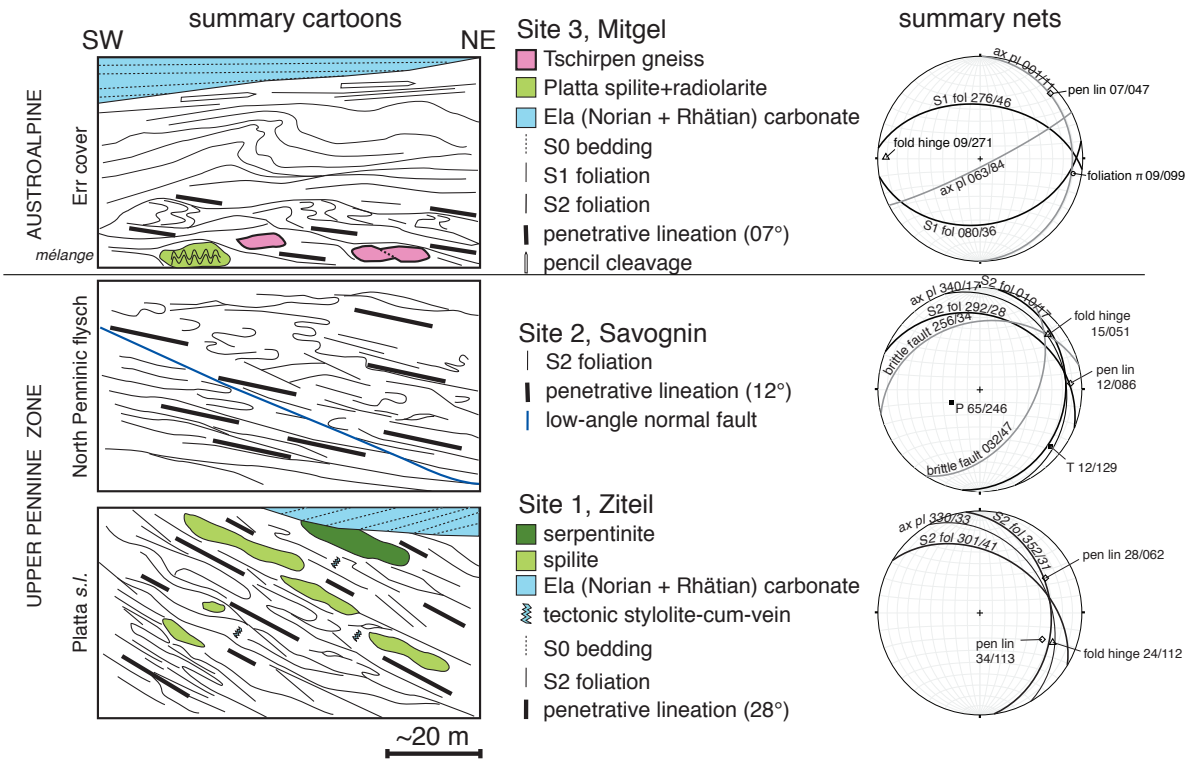

Fig. 2.11. Decameter-scale sketches and summary stereonets of geologic features observed in outcrop or roadcut along the Upper Pennine traverse. Panels are arranged according to structural position. On the Piz Curvér side of the Oberhalbstein valley, all of the middle and most of the upper panel have been cut out by Alpine-stage faulting, totaling approximately 600 m of tectonostratigraphic section missing at Site 1 where Ela cover rocks are faulted down on Platta *s.l.* (black arrow).

two statistical maxima, one plunging moderately northeast (28/062) and the other plunging moderately east-southeast (34/113). One oriented thin section corroborates the east-northeast movement (top-to-075 for the spilite), but the other shows even more southerly movement (top-to-162 for the ophicalcite), an orientation not readily supported by the mesoscopic field data. Fold hinges (24/113) have an almost identical orientation to the east-southeast stretching lineation, and the attitude of fold axial planes is concordant with, and helps define, overall S2 foliation fabric. Site 2 shows much less variation in the orientation of penetrative lineations and has a single maximum that plunges shallowly east (12/086), despite the fact that much of the shearing motion is indicated to be in direction other than top-east. Site 2 fold hinges plunge shallowly northeast (15/051), and, in contrast to Site 1, do not correspond to the persistent stretching lineation. Kinematic indicators at Site 2, including asymmetric porphyroclasts, Z-fold geometries, and incipient S-C fabric indicate top-east-southeast to top-southeast motion accompanied by antithetic top-north motion and also strong flattening, particularly evidenced by the ubiquitous recumbent folds found in the phyllitic portions of this tectonostratigraphic section. Given the persistence of the stretching lineation in strongly folded rocks, it is likely that the easterly penetrative lineation overprints the folds. In contrast to Sites 1 and 2, the lower portion of Site 3, particularly its basal c. 50 meters, contains only scarce shallowly-plunging penetrative lineations with no reproducible trend. Moreover, the upright,

harmonic folds in the Platta *s.s.* chert beds, a form of deformation not observed anywhere else on this transect, coupled with the near-by polydeformed Tschirpen gneissose granitoid demonstrate that deformation in the basal 'Austroalpine mélange' is not penetrative. In the upper part of Site 3, viz. just beneath the level of the Hauptdolomite thrust fault, penetrative lineations are entirely absent, whereas intersection 'pencil' cleavage is prevalent.

Stereographic data from Site 1, Ziteil (Platta *s.l.*) and Site 2, Savognin (North Penninic flysch) are very similar, and we conclude, independent of thermochronometric constraints, that they share a similar kinematic history. In contrast, above the Austroalpine fault, the intensity of penetrative deformation diminishes over a very short tectonostratigraphic distance, and the orientation of the structural fabric changes wholesale. This indicates that the Austroalpine allochthon, except along its basal c. 50 meters, was completely decoupled from the underlying North Penninic flysch and Platta *s.l.* during the most intense phase(s) of deformation responsible for its bulk penetrative fabric.

2.3. Bottom of the Pennine Zone

The bottom of the Pennine zone is defined by the basal Penninic thrust fault which places Lower Penninic (Valaisan) Bündnerschiefer of the Grava nappe onto the Infrahelvetic complex in the northeast near Chur or, along strike to the southwest, onto Gotthard cover rocks (Scopi zone) in the Glogn River Valley (Val Lumnezia) near Ilanz. At its southwestern terminus, the basal Pennine thrust is folded into an antiform. In the northeast, in the Prättigau half-window, Bündnerschiefer is shown to be stratigraphically continuous beginning with its Cretaceous "pre flysch" base up into the Prättigau flysch, which is capped by Lower Tertiary (Paleocene-Lower Eocene) Ruchberg formation (Nänny, 1948; Thum and Nabholz, 1972; Steinmann, 1994). In the Swiss 1:25,000-scale geologic atlas, the formations of the Prättigau half-window at deep structural levels are named as far southwest as Chur, but farther southwest, owing to a slight increase in metamorphic grade and deformation, the formations are no longer easily discernible and the lithostratigraphy becomes synonymous with the tectonic unit, i.e., Bündnerschiefer, undivided.

The structural fabric in the Bündnerschiefer has not been well-documented historically. In the northern half-window Marcus Weh's (1998) PhD thesis is the most important contribution to date that addresses deformation within the Grava nappe. Wiederkehr et al. (2008, 2009) worked at the southwestern-most extent of the Grava nappe where it interleaves with the Adula and Simano nappes on the edge of the Lepontine dome. Wiederkehr et al. (2009) provided key $^{40}Ar/^{39}Ar$ age constraints on synmetamorphic minerals and documented, unequivocally for the first time, that peak HP-metamorphism indicated by fibrous pseudomorphs of quartz-after-carpholite predated peak T-(Barrovian) metamorphism by at least 20 m.y. Specifically, HP-metamorphism occurred at c. 42-40 Ma based on in-situ laser probe $^{40}Ar/^{39}Ar$ measurements of white mica, whereas peak-T Barrovian metamorphism did not finally wane until c. 19-16 Ma, based on in-situ laser probe $^{40}Ar/^{39}Ar$ of biotite. The peak-T Barrovian age has been confirmed by Janots et al. (2009),who dated synmetamorphic monazites in the nearby Lepontine dome at 19-18 Ma.

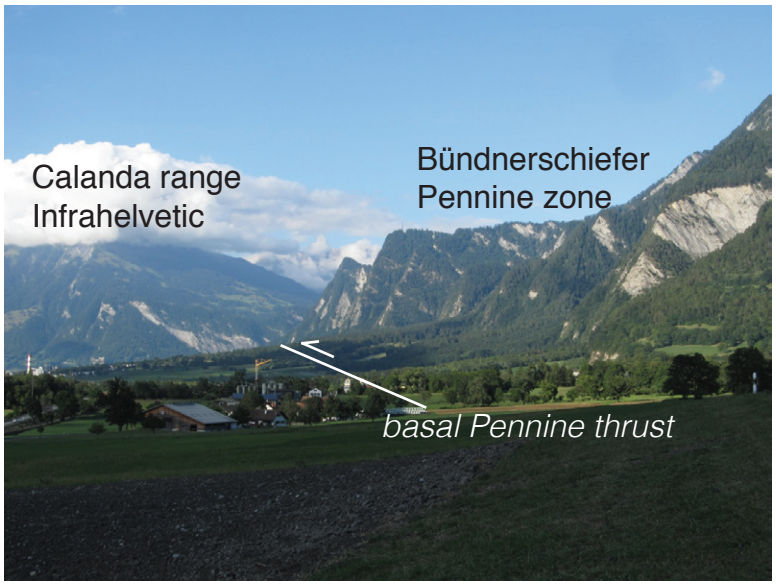

Fig. 2.12. Photograph looking north of the Chur Rhein Valley near the town of Trimmis (in the foreground) which shows the juxtaposition of the base of the Bündnerschiefer and Pennine zone to the Calanda range Infrahelvetic units, which marks the southernmost part of the Helvetic domain at this longitude.

Historically, the basal Pennine fault zone has been regarded as a single fault plane over ca. 100 km of strike length, and Wiederkeher et al. (2009) describe it as such. However, Weh (1998) and Weh and Froitzheim (2001) state that the penetrative fabrics and deformation history northeast of Chur are dissimilar enough from those southwest of Ilanz that the two ends of the same fault zone should not be regarded as a single contiguous fault plane. Moreover, Weh and Froitzheim (2001) conclude that the northeastern portion of basal Pennine thrust (in the northern half-window) projects directly into the Glarus overthrust, and therefore a northward "shove" from the Bünderschiefer was ultimately responsible for forming the Glarus overthrust.

To confirm the field observations of Weh (1998), to supplement with kinematic analyses the general observations and excellent isotopic measurements made by Wiederkehr et al. (2008; 2009), and to place the basal Pennine zone into its overall tectonic context in light of our cooling ages (Chapter 1) and our observations from the top of the Pennine zone (section 2.2), we measured mesoscopic structures in two transects along the basal Pennine thrust. The first transect crosses the Peidenerschuppenzone ('schuppenzone' translates as 'imbricate fault zone') in Val Lumnezia near the towns of Luven, Pitasch, and Duvin, a few kilometers south of Ilanz (western box in Fig. 2.2). The second location is along the Trimmis-Says road, a few kilometers northeast of Chur (northeastern box in Fig. 2.2), a site which lies directly across the Chur Rhein Valley from the Infrahelvetic Calanda range, a mere two kilometers separating exposures of the Penninic and Helvetic zones (Fig. 2.12)

2.3.1. Local geology at the bottom of the Pennine zone

The Val Lumnezia transect crosses three tectonostratigraphic units that are sedimentary cover rocks

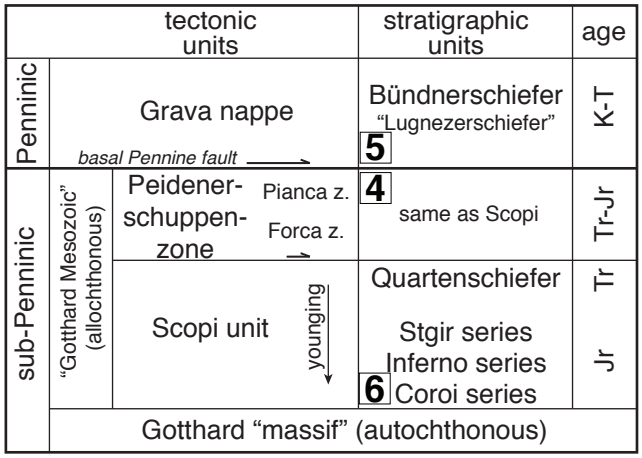

Fig. 2.13. Simplified tectonostratigraphic table for the geologic units at the bottom of the Pennine zone, Val Lumnezia. Bold numbers indicate structural position of sites where measurements were made. Modified after Wiederkehr et al., 2008.

of Mesozoic age. Summarizing from the useful description in Wiederkehr et al. (2008; Fig. 2.13), going up-structural-section the rocks are: (1) Scopi allochthonous unit of Ultrahelvetic affinity, (2) Peidener imbricate fault zone of apparent Ultrahelvetic affinity, and (3) Bündnerschiefer of the Grava nappe. The structural contact of Bündnerschiefer against the Peidener imbricate fault zone is the basal Pennine fault. The Scopi unit and Peidener imbricate fault zone are called "sub-Penninic" and comprise allochthonous Gotthard cover and, thus, are of distal European origin (Milnes, 1974). The Scopi unit is upside down and progresses structurally upward (and stratigraphically downward) from Coroi to Inferno to Stgir Series (all Jurassic) to Triassic Quartenschiefer (Baumer et al., 1961), all of which comprise low-grade metasedimentary rocks in the Val Lumnezia study area but achieve higher metamorphic grade to the southwest adjacent to the Lepontine dome (Wiederkehr et al., 2008). The allochthonous Scopi unit is overlain by the Peidener imbricate fault zone, which is subdivided into the Pianca (upper) and Forca (lower) fault zones. These designations are purely tectonic in that the lithologies are structurally imbricated Scopi units, and therefore from a lithologic standpoint, the Peidener zone is simply the most strongly deformed "top" of the underlying Scopi zone manifested by units that are imbricated and/or pinched-out repeatedly (Baumer et al., 1961). Above this, in presumed thrust-fault contact, is the basal Bündnerschiefer ("Lugnezerschiefer" in this area) of the Penninic Grava nappe. The basal Pennine thrust, when traced to its end in southwestern Val Lumnezia near the town of Vals, is folded in a north-closing antiform. This late fold, termed the Lunschania antiform (type locality is the village of Lunschania, near Vals) persists all the way along the front (i.e., base) of the Pennine zone (Fig. 2.2). An accompanying fold, the Valzeina synform [NB. The two names are easily distinguished and recalled by the fact that the "V" in "Valzeina" looks like a synform], develops parallel to the antiform and then, in the northern half-window, splays off to the North and dies out. Weh (1998) reports that the Lunschania antiform persists all the way to the Austroalpine hanging wall and is responsible for the sudden change in strike of the hanging wall from northerly to northwesterly in the northeast corner of the northern half-window (just out of view in Fig. 2.2 but evident at the far north end of the map in Fig. 1.4 in Chapter 1). Wiederkehr et al. (2008, their Figs. 2 and 3) show the traces of both folds persisting to the southwest all the way to the Lepontine dome region, where they bifurcate: the Lunschania antiform into the Soja zone on eastern side of the Simano nappe (between Simano and Adula), and the Valzeina

synform into the Molare zone on the west side of the Simano nappe (between Simano and Leventina-Lucomagno gneiss). However, it should be noted that careful study of the Ilanz 1:25,000-scale geologic map (Wyss and Isler, 2011) reveals that Grava nappe Bündnerschiefer dips moderately southeast very regularly from the Glogn River Valley up over the Cadeina dil Signina to the Rabiusa River Valley (Safiental), right across the purported traces of both the Lunschania and Valzeina folds (Fig. 2.14).

Zircon U-Th/He (ZHe) ages in the region between the Adula nappe and the Vorderrhein Valley (including Val Lumnezia) are in the range c. 12-8 Ma, which is the age attributed to uplift of the Aar massif (e.g., Aramowicz, 2008). The ages appear to be unaffected by the basal Pennine thrust or any other mapped tectonic contact. The Peidener imbricate fault zone is relatively distal to the 18-16 Ma Barrovian metamorphism of the Lepontine dome (Weiderkehr et al., 2009), and, according to contours of isotherms in Weiderkehr et al. (2008), the lower Val Lumnezia area where this study took place barely reached greenschist facies (peak temperatures of ≤ 350°C), in contrast to temperatures in excess of 500°C during the Miocene thermal overprint of the Lepontine dome.

2.3.1.1 Sites 4, 5, and 6, Pitasch-Duvin-Luven (Peidener and Scopi zones), local geology

The first transect at the bottom of the Pennine zone comprised three locales in Val Lumnezia. The first locale is "Site 4, Pitasch-Duvin" (Figs. 2.14, 2.15) at the level of the Glogn River to about 100 m above the river, and just below the towns of Pitasch and Duvin. The rocks in this zone are mapped on the 1:25,000 Ilanz sheet (Wyss and Isler, 2011) as a thin slice of Upper Stgir Series at the structural top (stratigraphic bottom) of the Scopi unit in the Pianca zone. Upper Stgir Series is a ca. 50 m-thick siliciclastic package of medium- and fine-grained sandstones and siltstones with interbeds of very-coarse-grained sandstone to pebble conglomerate. Beds may be as thick as ca. 10 m, but commonly, faulting has thinned or otherwise obscured these thickest beds (Baumer et al., 1961). This is a carpholite locality according to Wyss and Isler (2011). Although no fresh carpholite was observed during the field work for this study, quartz pseudomorphs after carpholite were possibly found (Fig. 2.15 I).

The second locale, above the town of Duvin, is "Site 5, Duvin Upper" (Figs. 2.14, 2.16) in basal Bündnerschiefer metapsammites on the northwestern limb of the Lunschania antiform. This section of Bündnerschiefer is extremely thick, ≥ 1000 m (assuming a 30° dip on the homoclinal section and using the elevation from Duvin (1175 m a.s.l.) to Piz Fess (2881 m a.s.l.)), and somewhat monotonous, in both its lithostratigraphy and mesoscopic structure. All foliation on the west flank of the Cadeina dil Signina (the mountain crest east of the towns of Pitasch and Duvin), where Piz Fess is located (Fig. 2.2), dips uniformly moderately to the southeast. One ZHe age of 8.8 ± 0.8 Ma (sample BD15-16, 736117, 174853, 1257 m elev.) was measured at Site 5 from a medium-grained sandstone in the Bündnerschiefer about 500 m southeast of Duvin. This is one of the youngest ZHe ages reported in this current study (refer to Appendix 2.3 for range of ZHe ages).

The third locale, "Site 6, Luven," (Fig. 2.14, 2.17) is near the town of Luven, approximately four

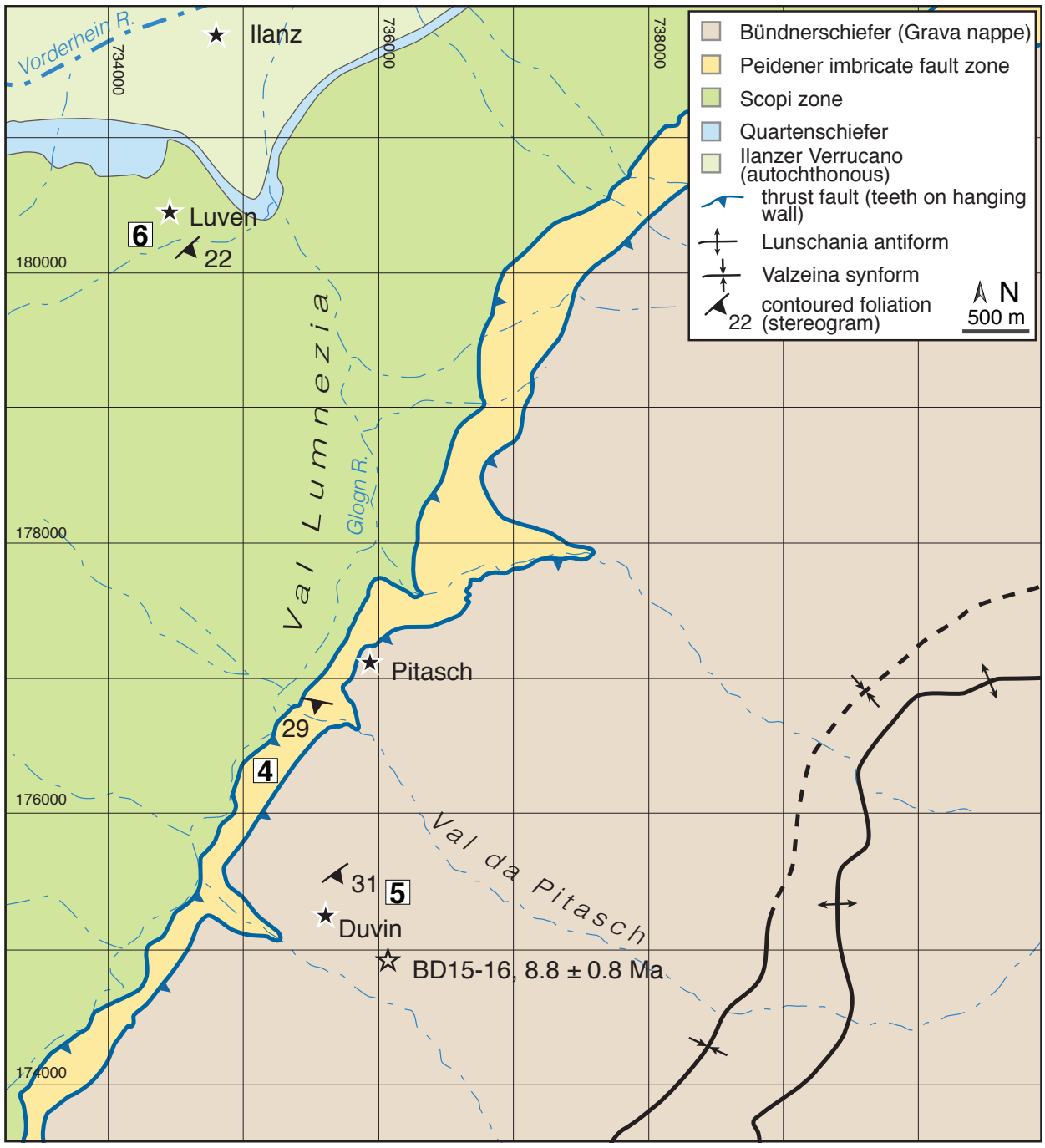

Fig. 2.14 Simplified tectonic map of Val Lumnezia and the Peidener imbricate fault zone. Foliations are taken from the stereograms shown in Figs. 2.19, 2.21, and 2.22. Geology modified after Wyss and Isler, 2011, which maps out the trace of the Lunschania antiform but not the full trace of the Valzeina synform, which is estimated here with a dashed line.

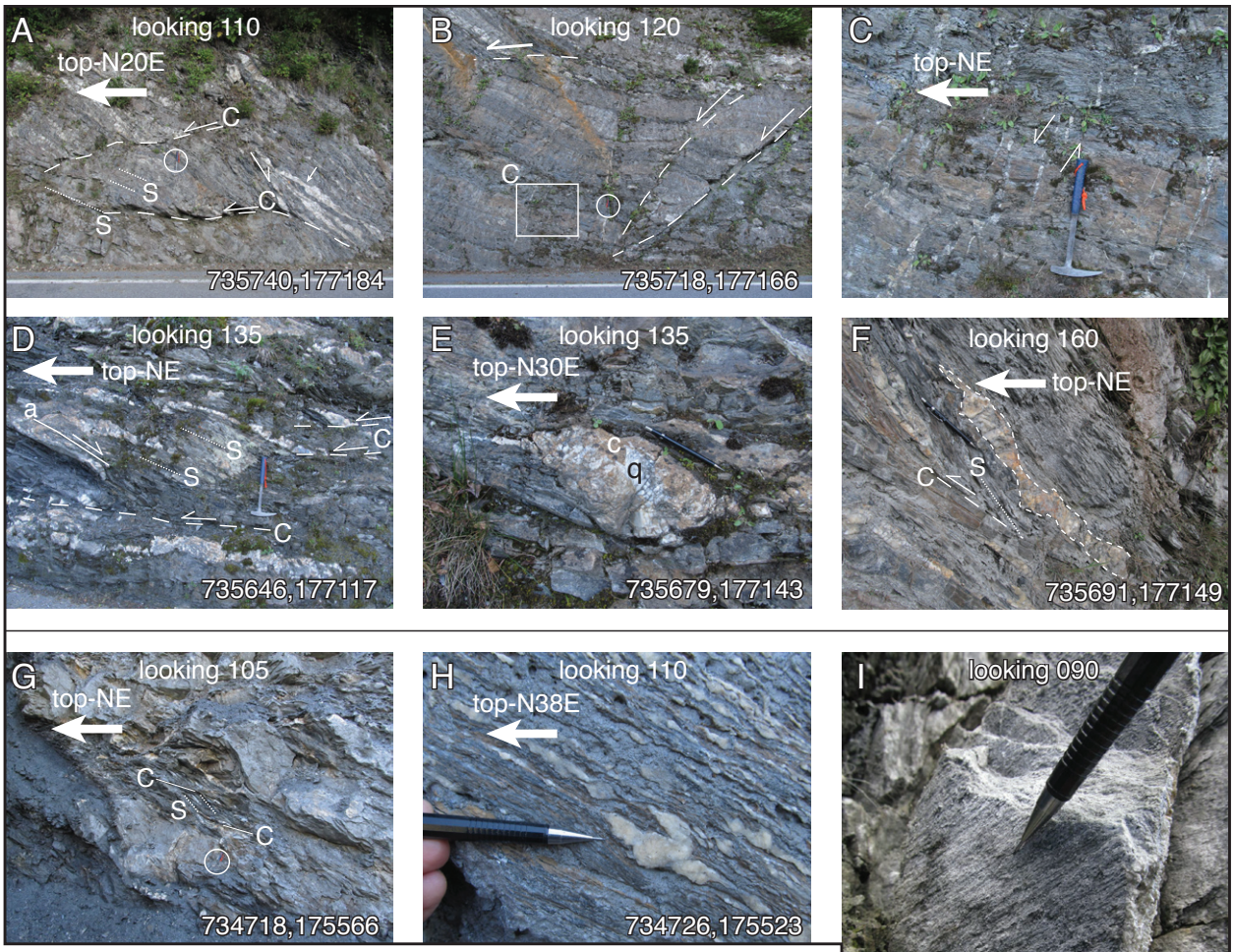

Fig. 2.15. Photographs of field relationships at Site 4, Pitasch-Duvin, in the Peidener imbricate fault zone in Val Lumnezia arranged according to structural position. Black horizontal line represents an internal contact (fault?) that separates different facies of the Upper Stgir series (Pianca zone): G to I is more coarse-grained and structurally lower (stratigraphically higher) and A to F is more fine-grained and structurally higher (stratigraphically lower). A to F are from a road cut below Pitasch about 110 to 130 m above the Glogn River near the top of the Peidener shear zone. G to I are from 10 to 15 m above the Glogn River. A) Brown sandy phyllites cut by boudinaged quartz veins that are now parallel to foliation. Discontinuous C-planes cut at shallow angles across the roadcut (dashed white lines labeled 'C'). Foliation 'S' marked with dotted line. Arrow indicates incipient boudinage. Hammer for scale (circled). B) Down to the north normal faults cut earlier ductile fabric. Note in upper left corner the very low-angle C-plane-like normal fault. Hammer (circled) for scale. Box indicates inset photo C. C) Inset photo from B showing *en echelon* tension gash quartz veins that indicate top-down-to-northeast sense of shear. Hammer for scale. D) Example of pseudo-S-C fabric found in the Peidener shear zone. C-planes are discontinuous low-angle normal faults (white lines labeled 'C') which bend into foliation S-planes (dotted lines labeled 'S') and become hard to trace. S-planes are highlighted by several prominent foliation-parallel quartz veins. Hammer for scale. E) Quartz (white mineral labeled 'q')-calcite (brown mineral labeled 'c') porphyroclast indicates top-NE sense of shear. Pencil for scale. F) Boudinaged quartz vein resembles a porphyroclast and indicates top-northeast sense of shear. Pencil for scale. G) Marly sandstones and slates exhibit a weak pseudo-S-C fabric that indicates top-northeast sense of shear. Hammer (circled) for scale. H) Flayed porphyroclast in which the stretched tail has been bent back around on itself, à la 'fingers of Suretta', indicating top-northeast sense of shear. I) Distinct mineral fibers growing on foliation may be relict pseudomorphs after carpholite, consistent with the textures shown in Wiederkehr et al. (2008) for this structural zone. Plunge/trend of fibers indicated, and a slight distortion has been introduced by tilting the camera upward which makes the illusion that the lineations are plunging to the northeast.

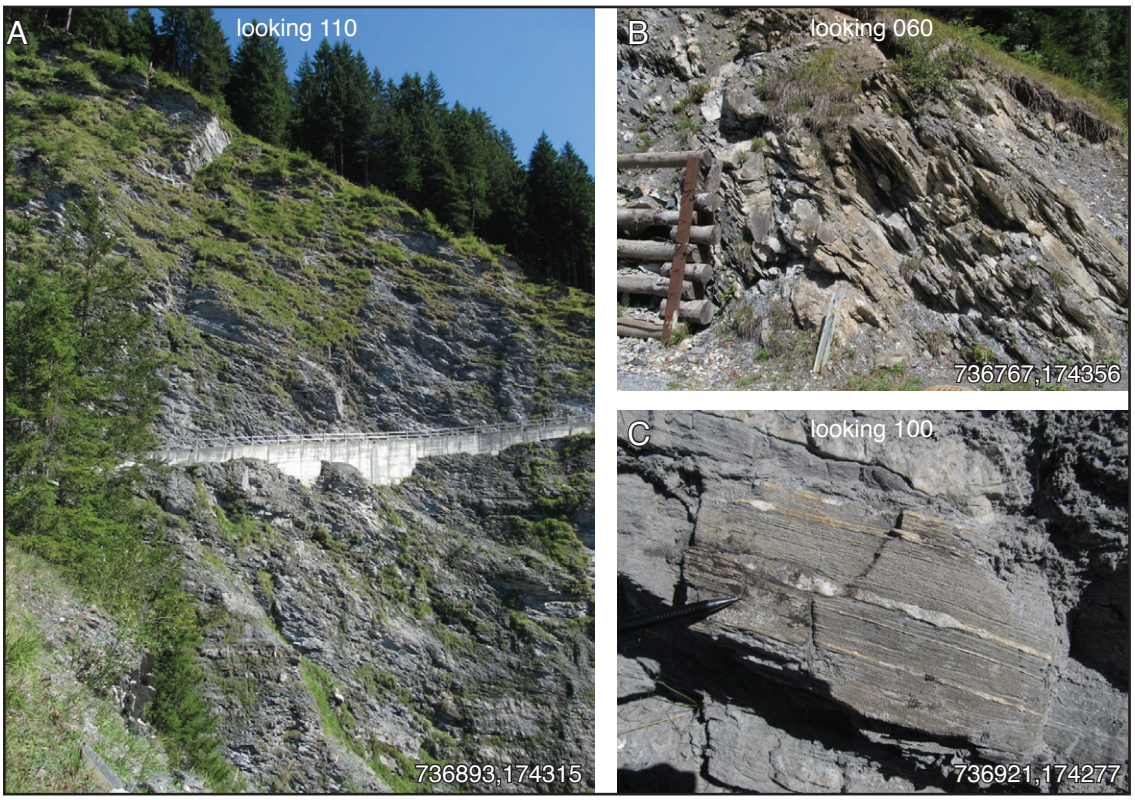

Fig. 2.16. Photographs of field relationships at Site 5, Upper Duvin, in the Bündnerschiefer above Duvin. A) Approximately 100-m-tall cliff exposure of phyllitic Bündnerschiefer exhibiting regular S1 foliation that dips southeast (away from the camera) but few obvious mesoscopic discontinuities. Guardrail is approximately 1 m high for scale. B) Sandstone and shaley beds with S1 foliation dipping 50°SE in typical Bündnerschiefer for this area. Sawn logs 20-25 cm in diameter for scale. C) Rare layer of higher strain in which quartz veins are foliation-parallel and slightly boudinaged but otherwise exhibit no preferred top-direction or kinematic asymmetry. Pencil for scale.

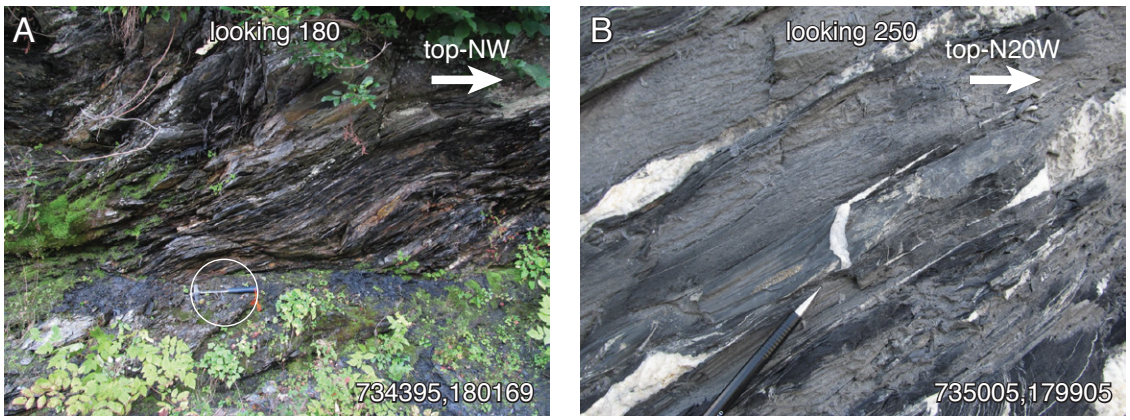

Fig. 2.17. Field photos of Site 6, Luven, <1 km southeast of the town of Luven. A) Pseudo-S-C fabric in dark metapelitic rocks of the Coroi Series of the Scopi Zone. Pseudo-S-C fabric indicates top-NW motion. Hammer (circled) for scale. B) Distinctively dark grey to black metapelites of the Coroi Series. Intense shearing of quartz veins in discrete mylonitic layers shows top-right motion to ~N20W. Pencil for scale.

kilometers north-northwest of Pitasch. The rocks here are uniformly dark grey to black, thin-bedded, fine-grained sandstone and siltstone with incipient slaty cleavage and belong to the Coroi Series, part of the Scopi zone in the footwall of the Peidener imbricate fault zone. The stretching and thinning of quartz veins along proto-mylonitic horizons (Fig. 2.17 B) is very well developed, probably the best observed at any of the sites in this study.

2.3.1.2. Site 7, Trimmis, local geology

A second transect at the bottom of the Pennine zone was completed at "Site 7, Trimmis," (Figs. 2.2, 2.18) adjacent to the town of Trimmis in the Chur Rhein Valley, approximately five kilometers north-northeast of Chur, on the paved road that leads eastward from Trimmis up the mountain to Says. The roadcuts along the Trimmis-Says road are outstanding for detailed study of the mesoscopic rock fabrics. In contrast to the higher (epizonal) metamorphic grade of the Bündnerschiefer in Val Lumnezia, Bündnerschiefer at Trimmis is very low grade (anchizonal) and can still be subdivided at the formation level (Nänny, 1948; Thum and Nabholz, 1972). According to the 1:25,000-scale geologic map (Schiers, no. 1176; Nänny, 1948) and Pantic and Isler (1978), on the outskirts of Trimmis and north from there, but not exposed along our traverse on the Trimmis-Says road, the lowest Klus Formation crop out, which is Lower Cretaceous (Hauterivian) in age. Overlying this, and representing the principal unit of our structural study for this transect, is the Valzeina formation, which is also Lower Cretaceous (Aptian-Albian) in age. Although no structural measurements were taken in formations above the Valzeina, the formations succeeding upward that comprise the main body of Bündnerschiefer in the Grava nappe include: Sassauna (Albian-Cenomanian), Pfäffigrat (Turonian), Fadura (Coniacian), Gyrenspitze (Campanian-Maastrichtian), Eggberg (Maastrichtian), Oberälpli (Paleocene), and finally Ruchberg (Lower Eocene, Yprésian) formations, for a total preserved structural thickness approaching 3800 meters (Nänny, 1948, his Fig. 1). According to the nomenclature of R. Trümpy (e.g., Trümpy, 1960), the seven Cretaceous formations may be considered "pre-flysch", while the two Paleogene formations should be called "flysch" *s.s.* The Valzeina Formation, where the structural measurements were made, comprises grey and brown medium- to fine-grained sandstones, siltstones, and marls cut by common foliation-parallel quartz-calcite veins up to about 20 cm thick. Deformation is pervasive enough that original S0 bedding is Deformation is pervasive enough that original S0 bedding is generally transposed into a strong S1 foliation.

The compilation of cooling ages presented in Chapter 1 shows that zircon fission track ages in the core of the Grava nappe change from Upper Oligocene (c. 24 Ma) toward the south to Paleocene and Upper Cretaceous (>60 Ma) to the north, at the latitude of the middle of the Prättigau (northern) half-window, which is essentially at the location of the Trimmis transect. Our ZHe age at the bottom of the nappe at Trimmis is 6.6 Ma, the youngest ZHe age recorded in our database, and is similar to ZHe ages at deepest structural levels in the Helvetic zone of the Calanda Range a few kilometers to the west of Trimmis. These ages presumably reflect the northernmost effects of the rise of the external massifs, here

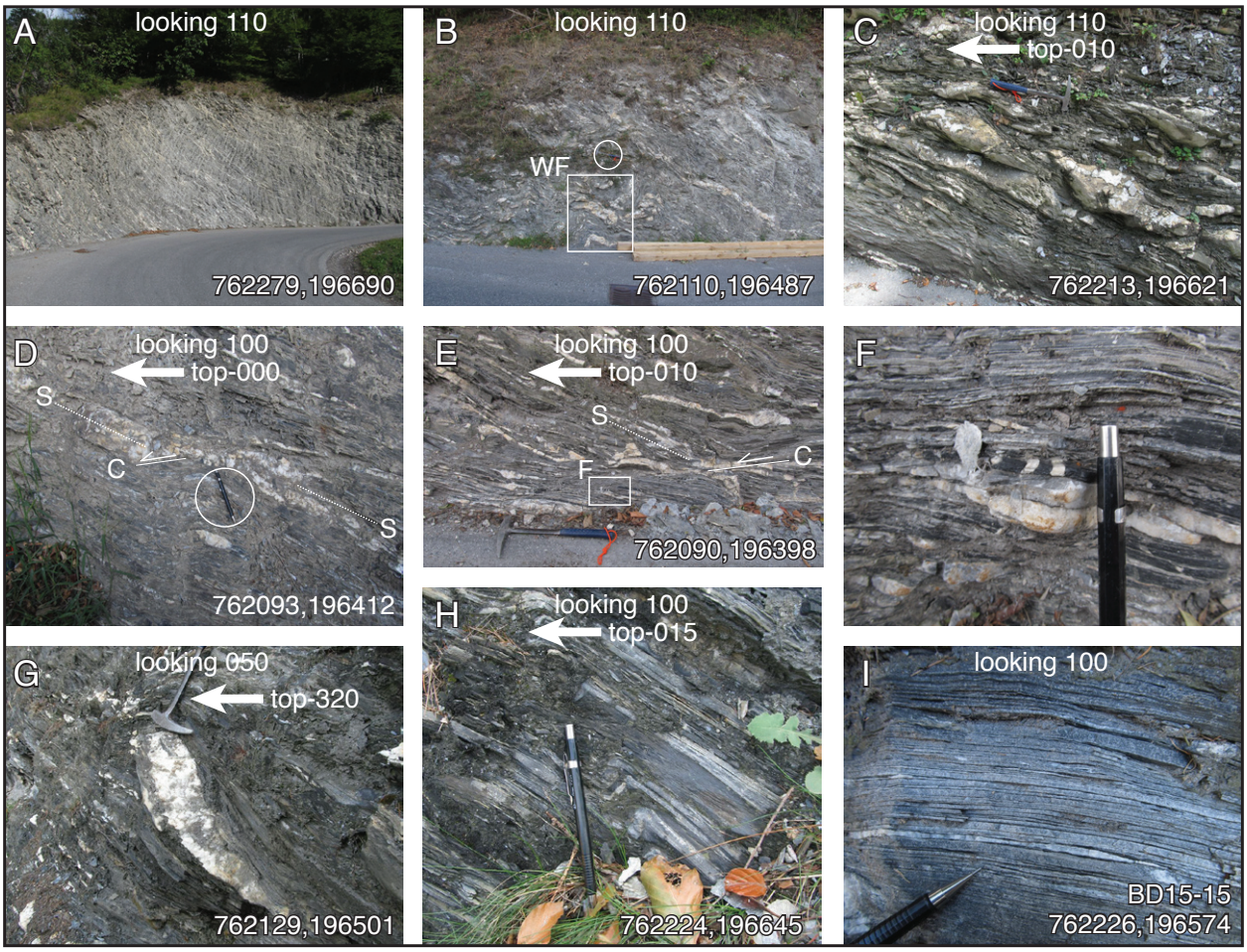

Fig. 2.18. Field photos of Site 7, Trimmis, along the lower half of the Trimmis-Says road. A) Typical-looking outcrop of Valzeina Series Bündnerschiefer. Height of cut ~4 m. B) Location of Weh and Froitzheim (2001) D4 fabric (box labeled 'WF' shows the location of their Fig. 8b). The supposed D4 fabric is merely a parasitic fold in the overall D3 mylonite regime and is not an important later phase of deformation. Hammer (circled) for scale. C) Quartz (white)-calcite (brownish) vein porphyroclasts indicate top-north sense of shear. Hammer for scale. D) Pseudo-S-C fabric in which the plane of flattening (S) is the main body of the thick quartz vein, and the plane of shear (C) is the basal truncation at the bottom of the vein. Asymmetry indicates top-north sense of shear. Pencil (circled) for scale. E) A second example of S-C fabric in the same roadcut a few tens of meters from D indicates top-north displacement. Box labeled 'F' shows location of photo F. Hammer for scale. F) Stretching brittle failure in thin slatey bed is filled with quartz-calcite veinlets that have, themselves, been decapitated. G) S-C porphyroclast indicates top-northwest sense of shear. Hammer for scale. H) Small fault-bend fold exhibiting north vergence. Pencil for scale. I) Medium-grained sandstone layer with strong planar fabric may be a protomylonite. ZHe age for this sample was the youngest measured anywhere in this study at 6.6 Ma (see data table in Appendix 2.3; Fig. 2.2; Chapter 1).

superimposed on rocks on either side of the Pennine-Helvetic boundary. In sum, however, at higher structural levels in the Grava nappe, thermochronologic data suggest that the northern Bündnerschiefer at, and north of, Trimmis never became hot enough to reset ZFT ages, but was hot enough to keep open the ZHe system, and therefore these rocks did not exceed anchimetamorphic grade (c. 200-250°C) at any point during the Alpine orogeny.

2.3.2 Mesoscopic structural data at the bottom of the Pennine zone

2.3.2.1. Sites 4, 5, and 6 Pitasch-Duvin-Luven (Peidener imbricate fault zone), mesoscopic structural data

At Site 4, Pitasch-Duvin, structural fabric in the Stgir series in the Peidener imbricate fault zone, which is in the footwall of the Penninic basal thrust fault (Figs. 2.14, 2.15, 2.19), is characterized by a very regular S2 foliation that has a contour-maximum attitude striking east, dipping 29° south. Two generations of folds were measured, an early generation with axial planes that were approximately concordant to S2 foliation (striking ENE, dipping 21° SE), and a later generation of upright folds that have fold axis attitudes that strike east-west and dip steeply south. A very regular penetrative lineation was observed, the mean vector of which plunges 27° to the south-southwest indicating elongation in that direction. Quartz-calcite veins cut the low-angle foliation with a mean strike of ESE and dip of 81°SW. Several late, high-angle faults strike northwest and dip variably northeast between about 35 and 70°. Kinematic analysis of slickenfibers growing on these faults indicate a high-angle shortening (P) axis and a low-angle NNE-directed extension (T) axis, the latter of which is generally parallel to the elongation axis indicated by the mean penetrative lineation.

Unlike the rock fabric described at the top of the Pennine zone near Savognin, here at the bottom of the Pennine zone, the rock fabric has a regular mesoscopic pseudo-S-C geometry that is plotted separately from other mesoscopic structural features. "S-C" is a term used for the strongly asymmetric fabric commonly observed in mylonites in, e.g., metamorphic core complexes of the U.S. Cordillera (Lister and Davis, 1989) and Cyclades, Greece (Lecomte et al., 2010). The rock fabric observed in the Peidener imbricate fault zone metasedimentary rocks is not a true mylonite, yet it shares the characteristic with true mylonites of having a regular plane of flattening (S, for *schistocité*) which is cut at somewhat regular intervals by parallel planes of shear (C, for *cisaillement*) which originate from and then bend back into foliation. Whereas in a true mylonite the C-planes come and go on a millimeter- to centimeter-scale, in the Peidener imbricate fault zone, C-planes come and go on the meter to decameter scale (Fig. 2.20). Platt and Vissers (1980) describe this fabric as "extensional crenulation cleavage" which tends to develop in sheared pelitic rocks, such as those observed here in the Peidener imbricate fault zone. Thus, in the field, foliation planes that were adjacent to or associated with mesoscopic faults that behaved like C or C' planes were assigned a different designation than typical S2 foliation. Even so, once plotted on the stereonet, it is clear that the average S-plane, which is oriented 107/33, is almost identical to the 'typical'

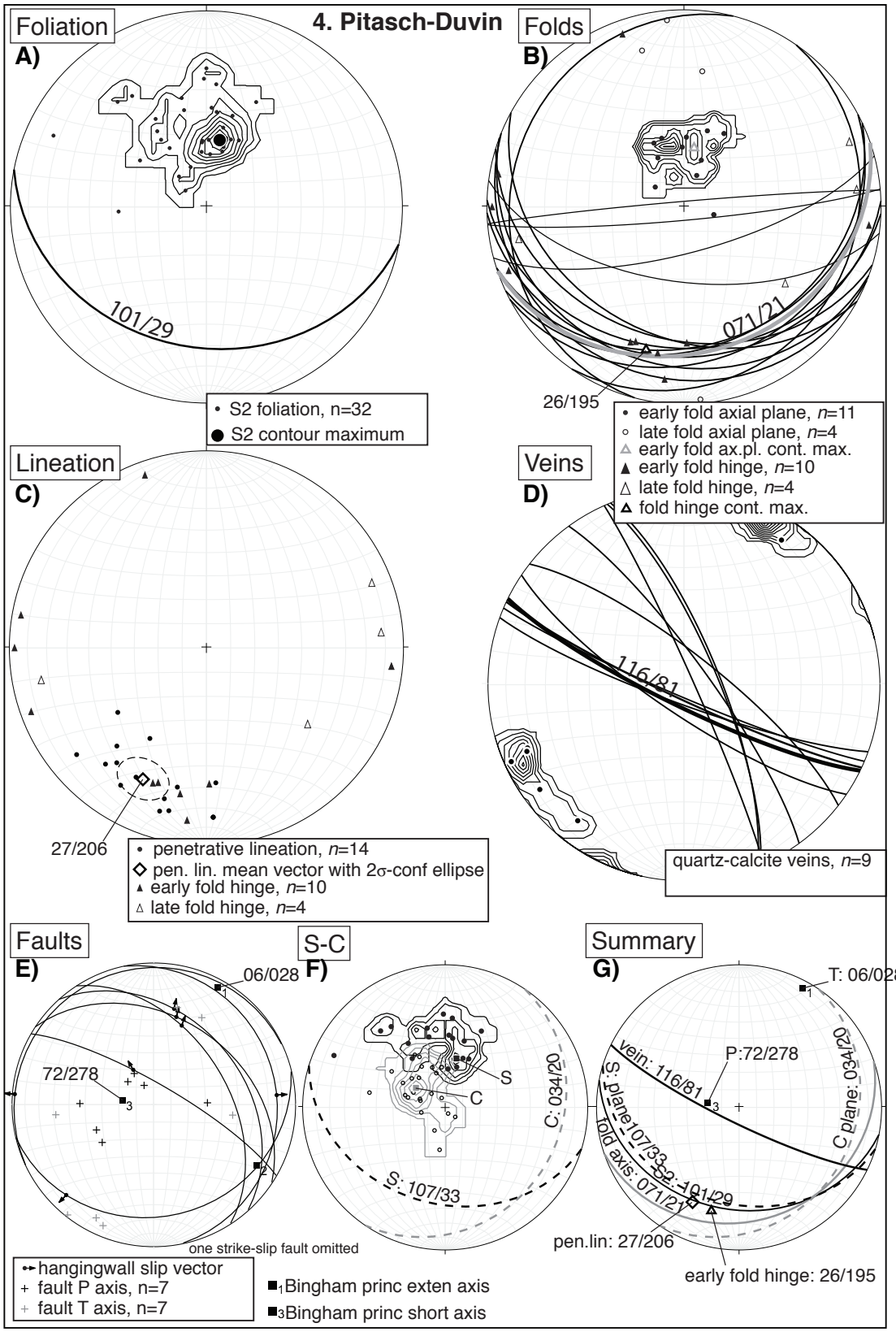

Fig. 2.19. Stereographic projection of mesoscopic field measurements at Site 4, Pitasch-Duvin, in the Peidener imbricate fault zone in Val Lumnezia. Label at top-left corner of stereogram indicates general category of data plotted; number of data shown in legend at bottom of each stereogram.

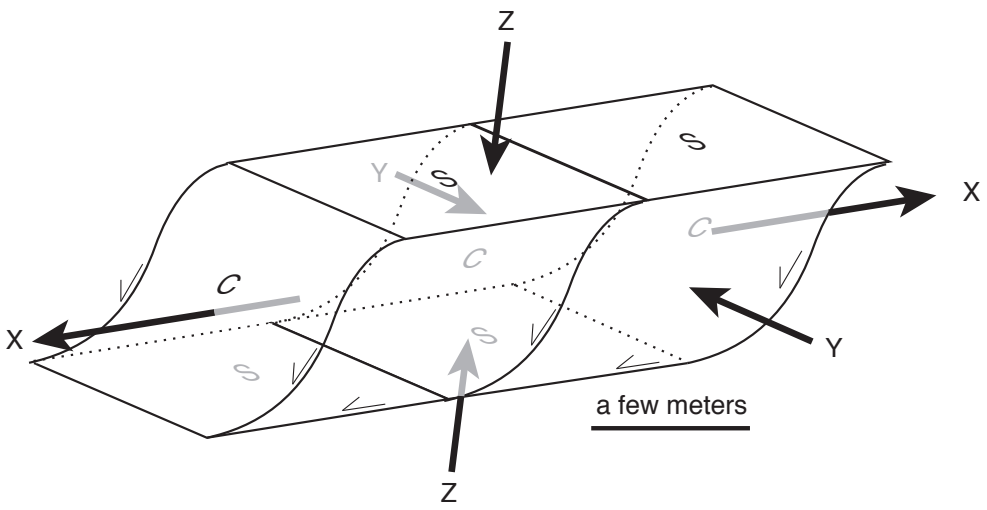

Fig. 2.20. Schematic diagram of mesoscopic S-C fabric observed at Peidener imbricate fault zone (Site 4). Scale bar is for illustrative purposes and indicates that the dimensions of mesoscopic C-planes can be fully resolved in larger roadcuts and outcrops. Bold arrows indicate shortening and extensional strain directions responsible for this configuration of structures.

S2 foliation (101/29) which may have no association with an obvious C-plane. C-planes have a contour-maximum attitude of 034/20. If we assume that S-planes represent planes of flattening (e.g., XY plane of the finite strain ellipsoid) as they do in S-C mylonites, and the pole-to-S represents the principal shortening direction, then shear accommodated by C-planes has an oblique sinistral-normal, top-northeast sense of slip, which is consistent with the penetrative stretching lineation and T-axis extension direction modeled for brittle faults.

At Site 5, Upper Duvin, in the Bündnerschiefer approximately 400 m structurally above the basal Pennine thrust fault, only a very regular, southeast-dipping S1 foliation was observed (Fig. 2.16) in which original bedding (or nearly so) could be distinguished, particularly for sandstone beds. Contour-maximum foliation strikes northeast and dips 31°SE (n = 11, Fig. 2.21 A). On the Ilanz 1:25,000-scale map, an additional 12-15 foliation measurements are recorded, and they all have this same general attitude: northeast-striking, dipping 30-50° southeast in a uniform, almost homoclinal, fashion. Mesoscopic folds are generally isoclinal and have very regular axial planes, the contour-maximum of which strikes northeast, almost identical to S1 foliation, and dips 51° southeast, about 20° steeper than S1 foliation. However, the trends of fold hinges are highly variable and subtend almost the entire great circle defined by the contour-maximum fold axial plane. Nevertheless, a local contour-maximum axial hinge plunges 20° to the south-southwest (Fig. 2.20 B). Given the moderate dip of the mean axial plane, and the fact that it does not conform to S1 foliation suggests that this set of mesoscopic folds predates the formation of the Lunschania and Valzeina folds (the D3 period of Wiederkehr et al., 2008) that are presumably responsible for the attitude of S1 foliation. A very consistent south-southwest-trending penetrative lineation (Fig. 2.21 C) was observed that has a contour-maximum of 13/215, essentially parallel to the contour-maximum fold hinge (20/210). Most of the quartz-calcite veins (Fig. 2.21 D) are foliation parallel, but two high-angle

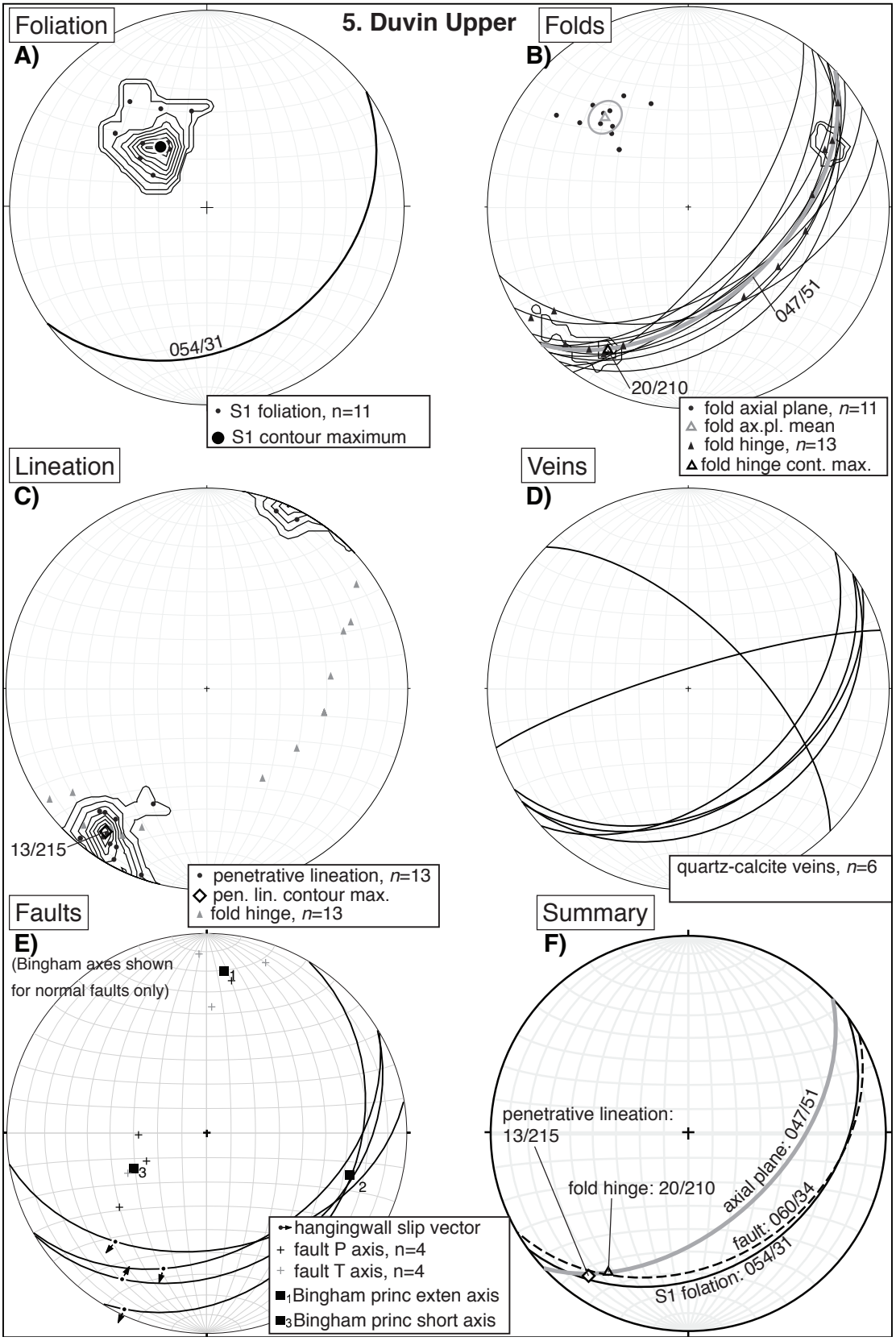

Fig. 2.21. Stereonet projection of field measurements at Site 5, Bündnerschiefer above the town of Duvin. Label at top-left corner of stereogram indicates general category of data plotted; number of data shown in legend at bottom of each stereogram.

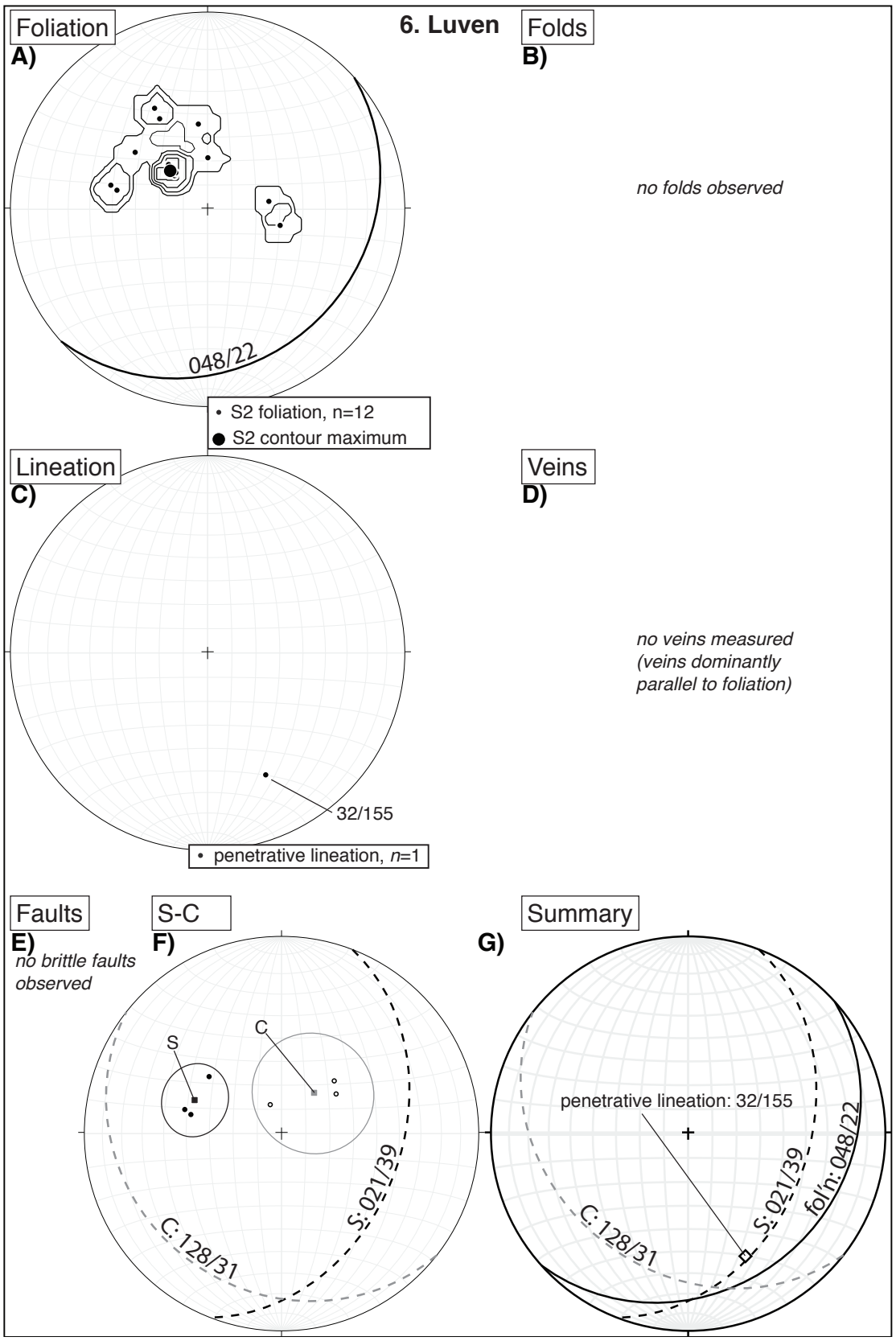

Fig. 2.22. Stereonet projection of field measurements at Site 6, Luven in the Coroi Series of the Scopi Zone. Label at top-left corner of stereogram indicates general category of data plotted; number of data shown in legend at bottom of each stereogram.

veins, which potentially form a conjugate set, suggest a shallowly-plunging west-northwest-trending sigma-1 responsible for their formation. Mesoscopic brittle faults strike northeast to east-northeast and dip moderately southeast (Fig. 2.21 E). Three are normal faults; one is a reverse fault; all have oblique motion. Modeled kinematic axes indicate a high-angle principal shortening (P-) axis and a low-angle, north-trending principal extension (T-) axis for the normal faults, and essentially the opposite for the reverse fault. The reverse fault was observed to be caused by a "room problem" in a meter-scale block with an opposing normal fault on the other side of the block, which means that the normal and reverse faults plotted here probably formed contemporaneously under the same dominant stress regime. In distinct contrast to the fabric observed in the Peidener imbricate fault zone, no pseudo-S-C fabric was observed anywhere in the Bündnerschiefer above Duvin. In addition, asymmetric sense of shear indicators were the most sparse of any of the seven sites that were examined in this study and indicates that flattening was the dominant form of deformation in the Bündnerschiefer in Val Lumnezia.

Site 6, Luven, the final segment of the Val Lumnezia transect, is located in the structurally deepest rocks that we studied, which are Coroi series metapelites that lie at the structural bottom (stratigraphic top) of the Scopi zone (Figs. 2.14, 2.17, 2.22). A contour-maximum foliation is estimated to strike northeast and dip shallowly (22°) southeast, similar to that observed in the Bündnerschiefer at Site 5, Duvin Upper. No folds were observed. A single penetration lineation was measured plunging 32° to the southeast, a direction that differs significantly from the contour-maximum penetrative lineations observed in the Peidener zone and in the basal Pennine zone. No veins were measured, and no brittle faults were observed. Pseudo-S-C fabric was observed in one location (Fig. 2.17 A), and if we assume that the mean-S-plane is the plane of flattening, then the C-planes have an oblique dextral-normal sense of slip, top-northwest (Fig. 2.22 F). Impressive thinning of sheared quartz veins (Fig. 2.17 B) indicate the formation of proto-mylonitic horizons at certain structural levels of the Scopi zone. However, this fabric was only locally observed at Site 7, Luven.

2.3.2.2. Site 7, Trimmis, mesocopic structural data

The second transect at the base of the Pennine zone in the Grava nappe exposed at Trimmis, a few kilometers northeast of Chur (Fig. 2.2). This location was studied by Weh (1998) and Weh and Froitzheim (2001), who report (i.e., their Figs. 8a and 8b) that the fabric in the Bündnerschiefer here consistently indicates top-north sense of shear. We examined the Valzeina series in the lower ca. 500 m of the Grava nappe. At this location the structural thickness of the Valzeina Series is not known precisely because the base of the unit is covered by gravels of the Rhein river, but a minimum structural thickness is approximately 600 m at this location. The majority of measurements were made in the lowest ~100 m of the exposed Valzeina formation, but a few measurements ($n<10$) were also made higher on the Trimmis-Says road (near village of Valtanna) about 300 m above the base of the exposed unit, and they are plotted on stereonets as "lower" and "upper", respectively.

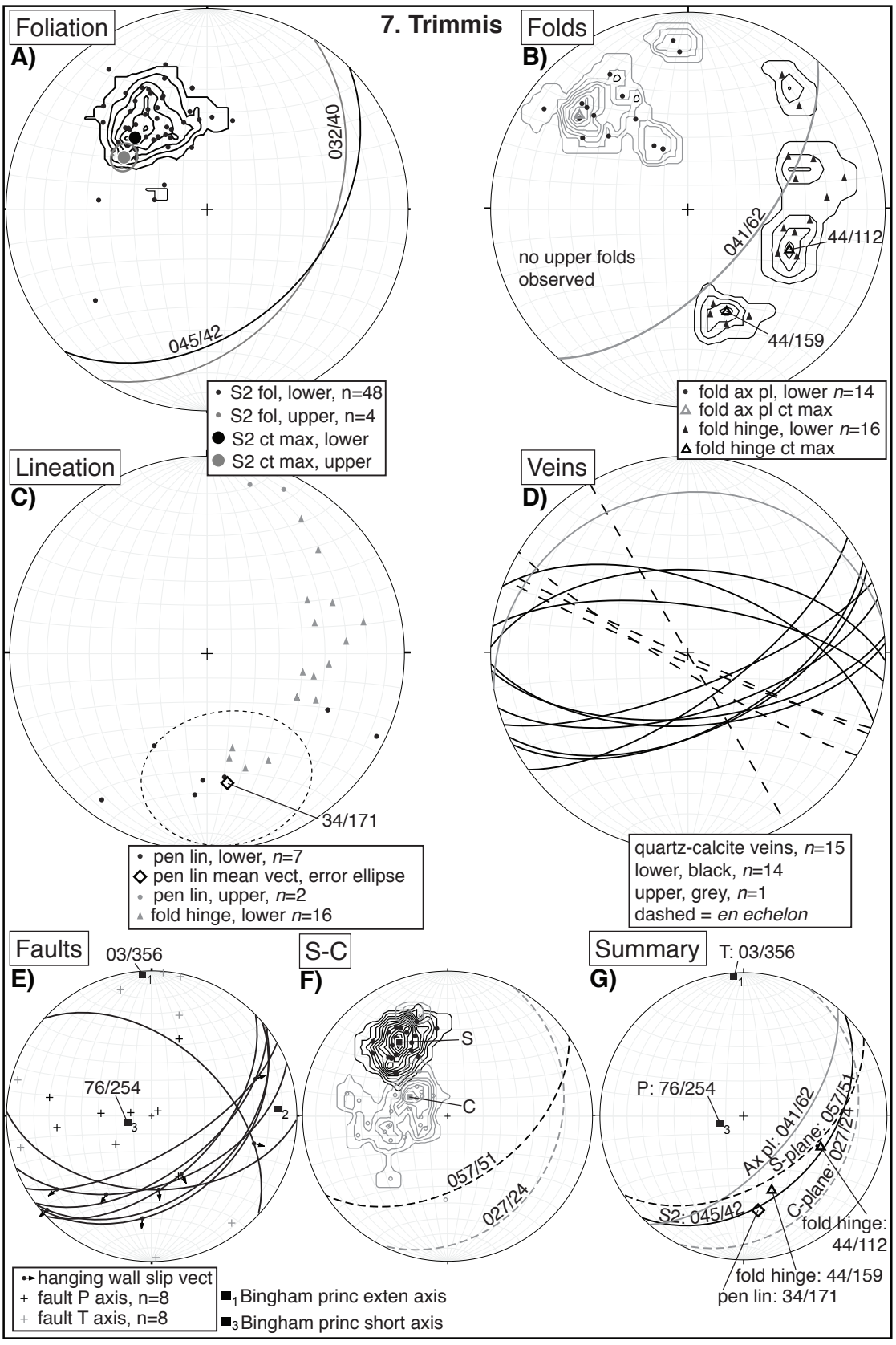

Fig. 2.23. Stereonet projection of field measurements at Site 7, Bündnerschiefer (Valzeina series) near Trimmis. Label at top-left corner of stereogram indicates general category of data plotted; number of data shown in legend at bottom of each stereogram.

Much of the structural fabric that we observed is a protomylonite in which asymmetrical "top-direction" indicators are generally able to be identified. A regular S2-protomylonitic foliation strikes northeast and dips moderately to the southeast (045/42). Higher in the Valzeina formaiton (at the small town of Valtanna) the attitude is 032/40, which may indicate a slight counterclockwise rotation of the foliation moving up structural section (Fig. 2.23 A). The attitude of foliation at Trimmis is similar to that observed Bündnerschiefer at Site 5, Upper Duvin, in Val Lumnezia (cf. Fig. 2.21 A). The attitude of the mean fold axial plane is 041/62, which dips a little more steeply than S2 foliation. Penetrative lineations were not widely observed, and the ones we measured scatter considerably on the stereonet between 110° and 220°plunging shallowly to moderately. Veins observed at Trimmis are exclusively quartz-calcite in composition, many of which are concordant with S2 foliation and therefore are not plotted on the "Veins" stereonet (Fig. 2.23 D). Two dominant sets of late extensional veins, which cross cut foliation, are identified. One principal set strikes approximately east-west and dips moderately north and south and implies a high-angle sigma-1. The second (dashed on Fig. 2.23 D) set strikes northwest and west-northwest and indicates a shallowly-plunging, NW-directed sigma-1. Through-going mesoscopic brittle faults strike almost exclusively northeast and dip moderately southeast. Kinematic models of slip fibers indicate a high-angle principal shortening (P-) axis and a low-angle north-directed principal extension (T-) axis (Fig. 2.23 E). Similar to the fabric observed at Site 4, Pitasch-Duvin, in Val Lumnezia, a pseudo-S-C fabric was observed at Trimmis (Fig. 2.23 F). S-planes are oriented 057/51, which is both a little steeper than and slightly rotated in a clockwise fashion (about a vertical axis) compared to the general S2-foliation at Trimmis (cf. Fig. 2.23 A). C-planes are oriented 027/24, dipping a little more shallowly and rotated counterclockwise (about a vertical axis) compared to the brittle normal fault set at Trimmis (cf. Fig. 2.23 E). If we assume that the S-plane represents a plane of pure flattening, then the C-plane indicates sinistral-oblique motion to almost due-north. Note that the dihedral angle between S- and C-planes at Site 7, Trimmis, is much smaller than the same angle measured in at Site 4, Pitasch-Duvin, in Val Lumnezia (compare Figs. 2.19 F, 2.23 F).

2.3.3. Summary of field observations and structural measurements, bottom of the Pennine zone

A summary of the key kinematic indicators as described in sections 2.2.3. and 2.3.3. for both the top and bottom of the Pennine zone, respectively, is shown in Fig. 2.24.

At the top of the Pennine zone, sites 1 and 2 (Ziteil and Savognin, respectively) share several commonalities in their mesostructural character, but there is a strong change in mesostructure crossing from site 2 (Savognin) up into the Austroalpine domain at site 3 (Mitgel). Likewise, at the bottom of the Pennine zone, there is a well defined contrast in the orientations of structural fabric in the Peidener imbricate fault zone (site 4) compared to higher Pennine (Bündnerschiefer, site 5) and lower Helvetic *s.l.* (Coroi series, site 6) structural levels. Foliation in the Val Lumnezia Bündnerschiefer at the base of the Grava

nappe (site 5) is quite uniform, and generally of a single generation (S1), whose attitude (054/31) matches the general attitude (048/22) of S2 foliation in the Coroi series in the Scopi zone (site 6), which in turn is also similar to the attitude (045/42) of Valzeina Formation Bündnerschiefer at Trimmis (site 7). In contrast, the strike of foliation (101/29) in the Stgir series of the Peidener imbricate fault zone, is oriented approximately 50° clockwise relative to the Bündnerschiefer above and the Coroi series below, which indicates that the strain manifest in foliation development is not homogeneous moving from the Pennine zone down into the Sub-Penninic nappes.

Pseudo-S-C fabric or 'extensional crenulation cleavage' is variably developed at the base of the Pennine zone. In Val Lumenzia, it is found at the Sub-Penninic structural level, i.e., Peidener imbricate fault zone or Scopi zone, but not at all in the Lumnezia Bündnerschiefer. In contrast, at Trimmis, pseudo-S-C fabric is observed in the lower Bündnerschiefer to the top of the structural section that we measured, which is several hundred meters above the basal Penninic thrust fault.

Top-direction for pseudo-S-C fabric also varies according to location (Fig. 2.24, black arrows). In Val Lumnezia, the Peidener zone exhibits oblique sinistral-reverse, top-northeast sense of slip on C-planes, whereas the Scopi zone (Coroi series) exhibits oblique dextral-reverse, top-northwest sense of slip on C-planes. In this case, top-directions differ by approximately 60°, which indicates a divergence in slip direction between the Peidener and Scopi zones. This divergence may be the result of the Grava nappe being faulted in a left-lateral sense past (to the north of) the Gotthard massif. At Trimmis, the Bündnerschiefer exhibits oblique sinistral-reverse, top-due-north sense of slip on C-planes.

Pseudo-S-C fabrics tend to align with other kinematic indicators in the same zone, such as stretching direction (elongation; Fig. 2.24 red arrows), brittle fault slip-sense, and the brittle fault principal extension (T-axis) direction. In every case but the Lumnezia Bündnerschiefer (which has a weakly-developed, non-uniform penetrative lineation but no extensional crenulation cleavage development), penetrative stretching lineations parallel the top-direction indicated by the pseudo-S-C fabric but plunge in the direction opposite transport, indicative of thrust faulting.

Structural fabric at Trimmis is very regular and predictable, and almost every kinematic indicator we observed, including all of the pseudo-S-C fabric, indicates a top-north sense of shear. Folds were almost exclusively recumbent and generally parallel to either the general S2 foliation or, where a pseudo-S-C fabric developed, local S-planes. Except for what appears to be a singular, parasitic fold that does not appear to represent a pervasive fabric, our results agree with the structural analysis of the Trimmis area presented in Weh (1998) and Weh and Froitzheim (2001).

2.4. Discussion

2.4.1. Martegnas Shear Zone

The Martegnas shear zone has been likened to a mélange because its lithostratigraphic and struc-

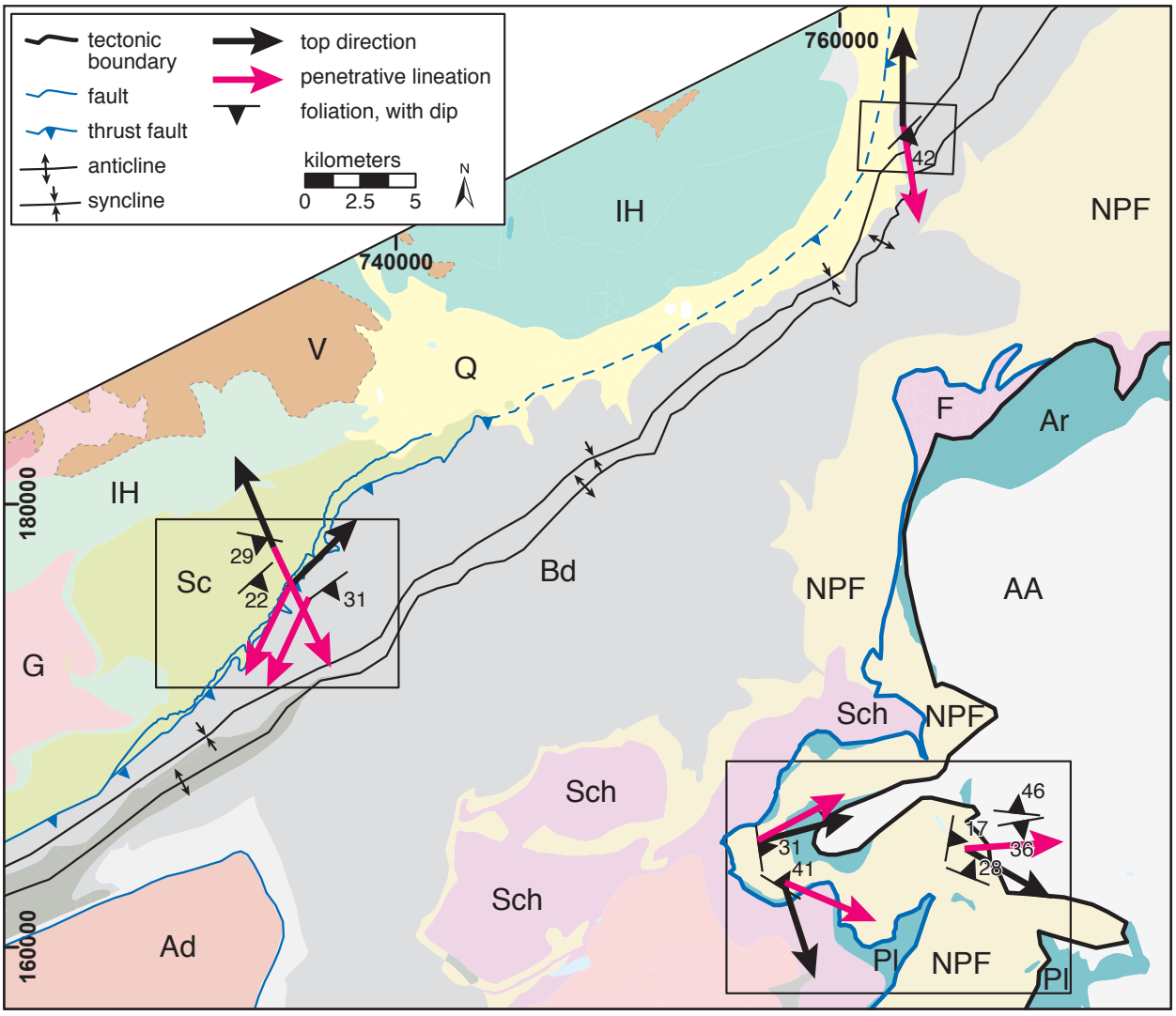

Fig. 2.24. Tectonic map of the Pennine zones showing the data summarized from each field site, one through seven. Top directions have been determined from pseudo-S-C fabric at the bottom of the Pennine zone and petrographic and outcrop kinematic indicators at the top of the Pennine zone. Penetrative lineations and foliations are contour-maxima of field data as shown on the summary stereonets of each respective field location. If a symbol is missing from a certain location (e.g., no top direction for Val Lumnezia Bündnerschiefer), it is because the data are either equivocal or non-existant for that particular parameter. Kinematic indicators shows that the top of the Pennine zone moved top-east and top-southeast whereas the bottom of the Pennine zone moved dominantly top-north with the exception of the thin Peidener imbricate fault zone which moved top-northeast.

tural relationships are not readily evident, even though from the perspective of mesostructural analysis the zone is internally rather coherent. Previous workers (Streiff, 1962; Streiff et al., 1976; Ziegler, 1956; Staub, 1958, Dietrich, 1969, Eiermann, 1988) all suggest that the Martegnas shear zone consists variously of (1) fragments of Platta nappe *s.s.*, (2) Mesozoic carbonate and siliciclastic rocks (essentially Bündnerschiefer), and (3) North Penninic "Parsonzer" flysch. Eiermann (1988) describes a total of 24 different, discontinuous lithologies in the zone and puts question marks next to several of them in terms of assigning them an age and/or greater tectonic significance because they are structurally isolated from their source, and even finding fossil evidence to confirm the presence of North Penninic flysch was a challenge.

We find that previous mapping efforts and the current Swisstopo geological compilation (https://map.geo.admin.ch) have not been sufficiently detailed to capture the complexity of the Martegnas shear zone, in part because the orientations of linear elements and asymmetric fabrics have not been taken into account. For example, on the current 1:25,000-scale Swiss map (Andeer sheet, Streiff et al., 1971) several foliation attitudes plotted on the map show a series of eastward-plunging antiforms and synforms, and Streiff et al. (1971) make the explicit point that Piz Toissa has been preserved because it occurs in the trough of one of these synforms, a hypothesis that cannot be fully tested since there are no other Toissa-like klippe in the area. One of the locations where Streiff et al. (1971) indicate a foliation measurement is the "shark fin" shown in Fig. 2.4 B. This element is a plunging facoidal mass of greenstone, and thus is a linear rather than planar tectonic element that cannot be used to define a fold system. Our observations suggest that foliation is penetratively bi-modal (and therefore does not define dip domains or eastward-plunging cylindrical folds), and is, in part, overprinted by a strong stretching lineation (Fig. 2.4 F, G). Assigning most of the Martegnas shear zone to a "Platta *s.l.*" lithotectonic unit is somewhat misleading because the rocks are predominantly either Bündnerschiefer or North Penninic flysch with volumetrically minor fragments of Platta *s.s.* whose current structural forms result from Alpine strain.

We interpret the SE-trending lineation defined by prolate objects (such as the spilite masses on Piz Curvér) to have formed during a period of top-east to top-southeast extension, parallel to and possibly contemporaneous with the D2 deformation phase of Weh and Froitzheim (2001). Owing to tectonic thinning across the Martegnas shear zone, Norian Hauptdolomite of Piz Toissa lies directly on fragments of Platta and North Penninic flysch. Thus the entirety of the Err nappe and most of the main Platta nappe (at least 2 km of structural section), which are present above the shear zone immediately to the south, has been structurally omitted by faulting. We interpret the faulting to have occurred after the North Penninic flysch was transported into its present (southerly) position, because it is preserved beneath the thicker structural section to the south.

We suggest that the structural omission of the Err-Platta structural section at Piz Curvér is recorded by the c. 27 Ma ZHe cooling age in North Penninic flysch near Savognin and two c. 24 Ma ZHe cooling ages in underlying Bündnerschiefer on Piz Curvér and in Rofna porphyry at Alp Taspegn (Fig. 2.3).. The fact that the Piz Curvér and Alp Taspegn ZHe ages are essentially the same suggests that most

of the displacement on the basal fault of the Martegnas shear zone, which separates the Suretta nappe from the Curvér Series NPF and Platta s.l., occurred prior to c. 24 Ma. The Martegnas shear zone is thus interpreted to be an important Alpine-stage shear zone with mélange-like lithostratigraphic character that was active before and during mid-Oligocene time.

2.4.2. Implications for the nature of the Austroalpine-Pennine contact

Argon and helium thermochronometry (see Chapter 1, Price et al., in review) indicate that a gap in time exists for the same mineral systems (with closure temperatures of 180°C or greater) on either side of the Austroalpine fault, which requires a period of normal-fault exhumation along the contact to have occurred in order to juxtapose relatively hot Pennine rocks against the base of the relatively cold Austroalpine allochthon. Eiermann (1988) and Weh (1998) have suggested that there may be as much as 68 km of top-S-directed shear ("back thrusting") along the base of the Austroalpine allochthon in order to move a large fragment of North Penninic flysch from its original northerly location in the Prättigau half-window to its current southerly location (Piz Arblatsch and environs) over the top of middle Penninic Schams nappe. The Martegnas shear zone would ostensibly function as the structural zone accommodating top-south shear. To support Eiermann's (1988) and Weh's (1998) hypothesis, we should expect to find southerly vergence in both the Martegnas shear zone and within the overlying coherent NPF unit. Although we found only scant evidence for purely top-south motion, we found ample evidence for top-east-northeast to top-south-southeast in both the Martegnas shear zone and in the overlying NPF unit at Savognin. Together, these structures could have accommodated some, although perhaps not all, of the displacement required to place the NPF into its current southerly position. Such displacement may have continued in the purely brittle regime along the base of the Austroalpine allochthon and therefore not be reflected in the mesostructure of the Martegnas shear zone. Alternatively, the structural overlap of the NPF backthrust to the south over the Schams nappe may reflect only the southerly component of a net-southeast displacement. Assuming a total north-south structural overlap of 68 km and top-SE (135) motion, the minimum displacement of Penninic units relative to the Austroalpine allochthon would be 96 km. In any case, our study clearly reinforces the hypothesis that the present juxtaposition of the Austroalpine allochthon and Pennine zone occurred via top-east to -southeast normal motion (in modern day coordinates), and not in via top-north thrust motion as implied by traditional thrust fault models for the Alps (Schmid et al., 1996A).

2.4.3. Implications for the basal Pennine thrust and its relationship to the Gotthard "massif"

In contrast to the top of the Pennine zone, the base exhibits much more evidence for shearing in a top-north sense, which is particularly evident in the lower Bündnerschiefer at Trimmis and, to a lesser extent, in the Scopi allochthonous cover of the Gotthard "massif", which is oriented northwesterly. The unexpected finding at the bottom of the zone is the movement indicated by the Peidener imbricate fault

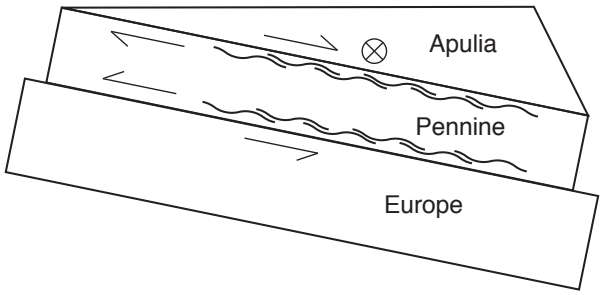

Fig. 2.25. Schematic N-S cross section through the Central Alps illustrating the general behavior of the Pennine zone according to the structural fabrics observed in this study. Circle-X indicates vector moving away from the plane of view.

zone, which is strongly suggested to be top-northeast from the ubiquitous pseudo-S-C fabric present in the zone. The fact that Peidener lithologic units originate from the Scopi zone and that they moved in a northeasterly transport direction both indicate that Gotthard cover rocks deformed in the relatively thin (<100 meters thick) Peidener imbricate fault zone acted as a major tectonic cushion akin to a "jelly sandwich" between the Penninic Grava nappe and the Gotthard crystalline basement and facilitated the uplift of the Gotthard by stripping Sub-Penninic Gotthard cover rocks off the top of the Gotthard "massif" in a top-northeast oblique-sinistral sense of shear. This fault movement likely occurred after the top of the Pennine zone became "locked" against the Austroalpine 'lid' at ca. 29-18 Ma. The very young, ca. 12-8 Ma, ZHe ages in the bottom of the Pennine zone are consistent with late cooling from the Lepontine dome thermal overprint (Weiderkehr et al., 2008; Janots et al., 2009) and is penecontemporaneous with the late uplift of the Aar massif (Aramowicz, 2008). The "jelly sandwich" deformation occurred at a relatively shallow mid-crustal level given that the Peidener imbricate fault zone exhibits some brittle and some ductile deformation.

The presence of well-developed pseudo-S-C fabric at the Bündnerschiefer at Trimmis and the absence of that fabric in Lumnezia Bündnerschiefer at approximately the same structural level suggests that deformation is not homogeneous along the bottom of the Pennine zone. This could potentially be the product of a thermal overprint from proximity to the Lepontine dome erasing the evidence for pseudo-S-C in Lumnezia Bündnerschiefer, but it is likely not the product of overprinting by a later axial-plane foliation associated with the formation of the Valzeina synform and Lunschania antiform. Moreover, the change in this type of fabric in the Bündnerschiefer supports that claim of Weh and Froitzheim (2001) that the basal Penninic thrust may, in fact, not be the same structure all along its length as has historically been regarded to be the case.

To first-order, the Pennine zone acted as a buoyancy-driven "piston," "extrusion wedge," or "mega-pip" (i.e., Fig. 4 B in Wheeler et al., 2001; cf. Fig. 8 C in Schmid et al., 1996 A and Fig. 1 B in Herwartz et al., 2011; Fig. 2.25), active during the middle Eocene to early Miocene (Price et al., in review; Chapter 1) that overrode the European plate at its base via top-north thrust faulting as evidenced by Bündnerschiefer at Trimmis but, at its top, was dragged out from underneath the Austroalpine allochthon via top-east to -southeast normal or oblique-normal faulting as evidenced by the fabrics on the Martegnas shear zone. Local second-order structures, as evidenced by the Peidener and Scopi zones, reveal additional details about the movement along the base of the Pennine zone. The first-order 'mega-pip' morphology

formed during exhumation can explain many of the enigmatic features found at the top of the Pennine zone, including the southerly position of the North Penninic flysch, the south vergence of the Schams nappe (viz. the Schams "dilemma") and the famously "backfolded" fingers of Suretta. Although it is clear that the Penninic units were subducted southward beneath that Austroalpine to great depth in a top-north sense of shear, the final juxtaposition of (ultra)high-pressure, young-cooling-age Penninic rocks against low-pressure, old-cooling-age Austroalpine rocks, as presently exposed, did not occur solely via top-north thrust faulting (Schmid et al, 1996A).

2.4.4. Implications for mechanistic hypotheses as applied to the Alps: orogenic collapse, tectonic mode switching, buoyancy, and critical taper theory

We suggest that the main phase of mountain building in the Alps, viz. the development of thick crust, high topography, most thrust and nappe structure, and the flexurally depressed cratonic basins, was driven by buoyancy forces, originating at depths of 30 to 90 km in the upper mantle, that inserted the ca. 20-km-thick Pennine zone, en masse, between the Austroalpine allochthon and the European margin in latest Eocene through early Miocene time, or about 33 to 18 Ma (Chapter 1). This hypothesis, if correct, has significant implications for basic concepts of mountain building (e.g. Chemenda et al., 1995). As noted in the Introduction, a persistent theme in the tectonics literature is that contractile tectonics in orogens is a direct expression of plate convergence, and is generally aligned with the overall relative motion vector of the colliding plates. Many authors have suggested that once substantial shortening and crustal thickening has occurred, crustal extension, possibly unaligned with the overall plate motion vector, may overprint the shortened crust (e.g, Dewey, 1988 and references therein). It has also long been recognized that extension is required as part of the process to exhume high-pressure metamorphic rocks, which originate at depths well beyond the reach of erosion, requiring crustal-scale normal faulting of the overriding plate, perhaps as a response to tectonic underplating and thickening of the deep crust (e.g., Fig. 8 in Platt, 1986). In contrast, the conclusion drawn here, and from the thermochronologic data presented in Price et al. (in review, Chapter 1), is that large-scale normal faulting accommodated crustal thickening, rather than mitigating it, and occurred coevally with thickening. The relatively rapid onset of emplacement of the Pennine zone between the Austroalpine domain and the European margin was thus the proximate cause of Alpine topography, and hence sedimentation into both the foreland (Molasse) and hinterland (Lombardi) basins began at ca. 32 Ma. Prior to this time, there existed neither the accommodation space nor the topographic highlands to construct the foreland and hinterland basins, even though Europe and Apulia were essentially in their present-day relative positions. Since that time, we suggest that northward or westward motion between Apulia and Europe may have been relatively small, or perhaps southward and eastward, raising the question of what fraction, if any, of Oligocene and younger thrust and nappe structure in the external and foreland fold-thrust belts (Helvetic nappes, external massifs, and Jura Mountains) is an expression of convergence between Apulia and Europe (Fig. 2.1 F and G). Could, instead, the exhumation

of the Pennine zone be responsible for these external features?

Lister and Forster (2009) recognized that many orogenic belts exhibit a "push-pull" or "pull-push" series of deformation phases, termed "tectonic mode switching," that explain many of the overprinting deformation textures found in orogenic belts worldwide. However, Lister and Forster (2009, p. 284) did not favor Chemenda-type buoyancy models as an exhumation mechanism over slab rollback to provide the "pull," whereby the overriding plate is in a state of pure extension. We recognize that elements of this model may well apply to the mid-Tertiary history of the Alps, particularly during the early exhumation history of Penninic rocks (Beltrando et al., 2010). A difficulty with this hypothesis as a general mechanism for exhumation as applied to the Alps is that the overriding Austroalpine plate, which provided the "lid" against which top-southeast motion of Penninic rocks occurred, nearly abuts the Molasse basin along the north flank of the range, which serves as a 'pin' that anchors the allochthon to Europe during emplacement of the Pennine mass. The important high pressure mineral carpholite in the Bündnerschiefer is absent north of Chur, and at this same approximate north-latitude, kinematic indicators along the base of the Austroalpine allochthon change from top-east or -southeast to top-north, which indicates that North Penninic Bündnerschiefer north of Chur never traveled very far down the failed subduction zone.

We recognize that the Austroalpine allochthon and South Alpine belt are cut by significant Miocene and younger strike-slip and normal faults (e.g. Campani et al., 2011; Müller et al., 2001; Mancktelow et al., 2001). But in the Central Alps such faults tend to be limited in trace-length and overall throw to 100s of meters, not kilometers (e.g., the normal fault shown in Fig. 2.7 A on Piz Mitgel), and cannot be responsible for signficant exhumation of (U)HP rocks (e.g., Fig. 8 in Platt, 1986). Thus, there is little kinematic evidence that the Austroalpine allochthon was displaced southward relative to Europe, akin to the distended hanging wall of a Cordilleran-type metamorphic core complex, or well-documented orogen-parallel normal faults in the eastern and western Alps such as the Brenner and Simplon faults, which were active after emplacement of the Pennine zone.

The influential critical taper theory (Dahlen et al., 1990, and references therein), as applied to the Alps, is predicated on the hypothesis that the crust was thickened into an 'orogenic wedge,' where Apulia functioned as a great bulldozer that off-scraped the Pennine zone from the downgoing slab along a major décollement , forming a crustal-scale duplex structure akin to those observed at much smaller scale in foreland fold-thrust belts (e.g., Schmid et al., 2004). During buildup of the wedge, accretion of successive thrust slices propagated from south to north, from the internal Penninic hinterland into the external Helvetic zone and, eventually, into the cratonic Aar massif and Subalpine Molasse. In this model, the entire nappe stack forms by imbricate thrust faulting as a direct expression of plate convergence (Fig. 2.1 A to D). The simple existence of (U)HP rocks in the Adula nappe and Bündenscheifer are not compatible with critical taper theory. The Apulian "backstop" could not have accreted this material because Apulia, even during the Eocene and Oligocene, was a relatively thin plate, possibly <10 km and almost certainly < 30 km thick during nappe stacking (Schmid et al., 2004; Mohn et al., 2012; Chapter 1), far too thin to

have bulldozed up 2 to 3 GPa rocks. In addition, much of the kinematic movement in the Pennine zone and lower Austroalpine allochthon is directed E-W to SE-NW, and of normal sense displacement (Ring et al., 1988; Ring et al., 1989; Nievergelt et al., 1996; Weh and Froizheim, 2001; Beltrando et al., 2008; Beltrando et al., 2010; this study), and therefore it is difficult to reconcile the Alpine system with the basic premises of critical taper theory.

Notwithstanding these difficulties, the contrast in orogenic dynamics between Chemenda-type buoyancy models and critical taper theory is stark. In critical taper theory, the source of energy that drives thrusting of the wedge comes from a combination of the bulldozer's 'motor' (the negative buoyancy of the downgoing slab that drives convergence, perhaps aided by the positive buoyancy of the mid-ocean ridge on the trailing edge of the plate), and the gravitational potential generated by topography at the top of the wedge, which progressively 'collapses' downward according to some critical topographic slope and basal friction. In buoyancy models, the energy for mountain building is derived from the positive buoyancy of the subducted crust, which provides the "push" for nappe emplacement and crustal thickening. In this case, plate motion and topography matter very little, except as a precondition and end result, respectively.

2.5. Acknowledgements

We would like to thank our trusty Swiss field assistant, Lukas Flükiger Nibourel, for his help collecting data in the Oberhalbstein valley and for introducing me to Clino-Move, the highly useful digital compass/clinometer application from *Midland Valley* software for use on the iPhone, and the quirky-cool Savognin Cube, a fantastically affordable (for Switzerland) *pension-complète* right in the middle of the Martegnas shear zone.

2.6. References Cited

Aalto, K.R., and Murphy, J.M, 1984, Franciscan complex geology of the Crescent City Area, Northern California, in: Blake, M.C., Jr., ed., Franciscan Geology of Northern California, Society of Economic Paleontologists and Mineralogists, Los Angeles, California, p. 185-201.

Allmendinger, R. W., Cardozo, N., and Fisher, D., 2012, Structural geology algorithms: Vectors and tensors in structural geology: Cambridge University Press, New York, 289 p.

Aramowicz, A., 2008, Application of low-temperature thermochronology to understanding cooling and exhumation in the Central Swiss Alps. Unpublished Ph.D. thesis, Univ. of Lausanne, 130 p.

Baumer, A., Frey, J.D., Jung, W. and Uhr, A., 1961, Die Sedimentbedeckung des Gotthard-Massivs zwischen oberem Bleniotal und Lugnez (Vorläufige Mitteilung). Eclogae Geologicae Helvetiae v. 54, p. 478–491.

Beaumont, C., Jamieson, R. A., Butler, J. P., and Warren, C. J., 2009, Crustal structure: A key constraint on the mechanism of ultra-high-pressure rock exhumation. Earth and Planetary Science Letters, v.

287, p. 116-129. doi: 10.1016/j.epsl.2009.08.001

Beltrando, M., Lister, G., Hermann, J., Forster, M. and Compagnoni, R., 2008, Deformation mode switches in the Penninic units of the Urtier Valley (Western Alps): Evidence for a dynamic orogen. Journal of Structural Geology, v. 30, p. 194-219.

Beltrando, M., Lister, G.S., Rosenbaum, G., Richards, S. and Forster, M.A., 2010, Recognizing episodic lithospheric thinning along a convergent plate margin: The example of the Early Oligocene Alps. Earth-Science Reviews, v. 103, p. 81-98.

Boutelier, D., Chemenda, A.I, and Jorand, C., 2004. Continental subduction and exhumation of high-pressure rocks: insights from thermo-mechanical laboratory modelling. Earth and Planetary Science Letters, v. 222, p. 209-216.

Brueckner, H.K. and van Roermund, H.L., 2004, Dunk tectonics: A multiple subduction/eduction model for the evolution of the Scandinavian Caledonides. Tectonics, v. 23, 10.1029/2003TC001502.

Campani, M., Mancktelow, N., Seward, D., Rolland, Y., Muller, W., and Guerra, I., 2010, Geochronological evidence for continuous exhumation through the ductile-brittle transition along a crustal scale low-angle normal fault: Simplon fault zone, Central Alps. Tectonics, v. 29, TC3002. doi: 10.1029/2009TC002582.

Cardozo, N., and Allmendinger, R.W., 2013, Spherical projections with OSXStereonet: Computers and Geosciences, v. 51, p. 193 – 205, doi:10.1016/j.cageo.2012.07.021.

Carswell, D.A. and O'Brien, P.J., 1993, Thermobarometry and geotectonic significance of high-pressure granulites: Examples from the Moldanubian Zone of the Bohemian Massif in Lower Austria. Journal of Petrology, v. 34, p. 427-459.

Chemenda, A.I., Mattauer, M., Malavieille, J. and Bokun, A.N., 1995, A mechanism for syn-collisional rock exhumation and associated normal faulting: results from physical modelling. Earth and Planetary Science Letters, v. 132, p. 225-232.

Chopin, C., 1984, Coesite and pure pyrope in high-grade blueschists of the Western Alps: A first record and some consequences. Contributions to Mineralogy and Petrology, v. 86, p. 107-118.

Cloos, M., 1982, Flow melanges: Numerical modeling and geologic constraints on their origin in the Franciscan subduction complex, California. Geological Society of America Bulletin, v. 93, p. 330-345.

Cloos, M., 1993. Lithospheric buoyancy and collisional orogenesis: Subduction of oceanic plateaus, continental margins, island arcs, spreading ridges, and seamounts. Geological Society of America Bulletin, v. 105, p. 715-737.

Cowan, D.S., 1978, Origin of blueschist-bearing chaotic rocks in the Franciscan Complex, San Simeon, California. Geological Society of America Bulletin, v. 89, p. 1415-1423.

Dahlen, F.A., 1990, Critical taper model of fold-and-thrust belts and accretionary wedges. Annual Review of Earth and Planetary Sciences, v. 18, p. 55-99.

Dewey, J.F., 1988, Extensional collapse of orogens. Tectonics, v. 7, p. 1123-1139.

Dietrich, V., 1969, Die Ophiolithe des Oberhalbsteins (Graubünden) und das Ophiolithmaterial der ostschweizerischen Molasseablagerungen, ein petrographischer Vergleich. Verlag Herbert Lang & Cie.. Bern, Switzerland, 179 p.

Eiermann, D., 1988, Zur Stellung des Martegnas-Zuges. Eclogae Geologicae Helvetiae, v. 81, p. 259-272.

England, P.C. and Holland, T.J.B., 1979, Archimedes and the Tauern eclogites: The role of buoyancy in the preservation of exotic eclogite blocks. Earth and Planetary Science Letters, v. 44, p. 287-294.

Ernst, W.G., 1971, Metamorphic zonations on presumably subducted lithospheric plates from Japan, California, and the Alps. Contributions to Mineralogy and Petrology, v. 34, p. 43-59.

Ernst, W.G., 1975, Systematics of large-scale tectonics and age progressions in Alpine and Circum-Pacific blueschist belts. Tectonophysics, v. 26, p. 229-246.

Ernst, W.G. and Peacock, S.M., 1996. A thermotectonic model for preservation of ultrahigh-pressure phases in metamorphosed continental crust. Subduction top to bottom, pp.171-178.

Ernst, W.G., 2006, Preservation/exhumation of ultrahigh-pressure subduction complexes. Lithos, v. 92, p. 321-335.

Ferreiro-Mählmann, R., 2001, Correlation of very low grade data to calibrate a thermal maturity model in a nappe tectonic setting, a case study from the Alps. Tectonophysics, v. 334, p. 1-33.

Ferreiro-Mählmann, R. and Giger, M., 2012, The Arosa zone in Eastern Switzerland: oceanic, sedimentary burial, accretional and orogenic very low-to low grade patterns in a tectono-metamorphic mélange. Swiss Journal of Geosciences, v. 105, p. 203-233.

Gerya, T.V., Stöckhert, B., and Perchuk, A.L., 2002, Exhumation of high-pressure metamorphic rocks in a subduction channel: A numerical simulation. Tectonics, v. 21., TC1056, doi: 10.1029/2002TC001406.

Herwartz, D., Nagel, T.J., Münker, C., Scherer, E.E. and Froitzheim, N., 2011, Tracing two orogenic cycles in one eclogite sample by Lu-Hf garnet chronometry. Nature Geoscience, v. 4, pp.178-183.

Janots, E., Engi, M., Rubatto, D., Berger, A., Gregory, C. and Rahn, M., 2009, Metamorphic rates in collisional orogeny from *in situ* allanite and monazite dating. Geology, v. 37, p. 11-14.

Laubscher, H.P., 1978, Foreland folding. Tectonophysics, v. 47, p. 325-337.

Lecomte, E., Jolivet, L., Lacombe, O., Denèle, Y., Labrousse, L., and Le Pourhiet, L., 2010, Geometry and kinematics of Mykonos detachment, Cyclades, Greece: Evidence for slip at shallow dip. Tectonics v. 29. DOI: 10.1029/2009TC002564.

Lister, G. S., and Davis, G. A., 1989, The origin of metamorphic core complexes and detachment faults formed during Tertiary continental extension in the northern Colorado River region, USA. Journal of Structural Geology, v. 11, p. 65-94.

Lister, G. and Forster, M., 2009, Tectonic mode switches and the nature of orogenesis. Lithos, v. 113, p.

274-291.

Mancktelow, N.S., Stöckli, D.F., Grollimund, B., Müller, W., Fügenschuh, B., Viola, G., Seward, D. and Villa, I.M., 2001, The DAV and Periadriatic fault systems in the Eastern Alps south of the Tauern window. International Journal of Earth Sciences, v. 90, p. 593-622.

Marrett, R. A., and Allmendinger, R. W., 1990, Kinematic analysis of fault-slip data: Journal of Structural Geology, v. 12, p. 973-986.

Maruyama, S., and Liou, J.G., 1998, Initiation of ultrahigh-pressure metamorphism and its signi¢cance on the Proterozoic- Phanerozoic boundary, Island Arc v. 7 p. 6-35.

McLaughlin, R.J., and Olin, H.N., 1984, Tectonostratigraphic framework of the Geysers-Clear Lake Region, California, in: Blake, M.C., Jr., ed., Franciscan Geology of Northern California, Society of Economic Paleontologists and Mineralogists, Los Angeles, California, p. 221-254.

Milnes, A.G. 1974, Structure of the Pennine zone (Central Alps) – new working hypothesis. Geological Society of America Bulletin v. 85, p. 1727–1732.

Mohn, G., Manatschal, G., Beltrando, M., Masini, E., and Kusznir, N., 2012, Necking of continental crust in magma-poor rifted margins: Evidence from the fossil Alpine Tethys margins. Tectonics, v. 31, TC1012. doi: 10.1029/2011TC002961

Müller, W., Prosser, G., Mancktelow, N.S., Villa, I.M., Kelley, S.P., Viola, G. and Oberli, F., 2001, Geochronological constraints on the evolution of the Periadriatic Fault System (Alps). International Journal of Earth Sciences, v. 90, p. 623-653.

Nänny, P., 1948, Zur geologie der Prättigauschiefer zwischen Rhättikon und Plessur, Gebr. Fretz A.G., Zürich, Switzerland, 128 p., 3 plates.

Nievergelt, P., Liniger, M., Froitzheim, N. and Mählmann, R.F., 1996, Early to mid Tertiary crustal extension in the Central Alps: The Turba mylonite zone (eastern Switzerland). Tectonics, v. 15, p. 329-340.

Ott, E., 1925, Geologie der westlichen Bergünerstöcke (Piz Michèl und Piz Toissa, Graubünden). Beiträge zur Geologischen Karte der Schweiz [N.F.] 49/5.

Pantic, N. and Isler, A., 1978, Palynologische Untersuchungen in Bündnerschiefern (II). Eclogae Geologicae Helvetiae v. 71, p. 447-465.

Platt, J. P., 1986, Dynamics of orogenic wedges and the uplift of high-pressure metamorphic rocks. Geological Society of America Bulletin, v. 97, p. 1037-1053.

Platt, J.P., and Vissers, R.L.M., 1980, Extensional structures in anisotropic rocks. Journal of Structural Geology, v. 2, p. 397-410.

Ring, U., Ratschbacher, L. and Frisch, W., 1988, Plate-boundary kinematics in the Alps: Motion in the Arosa suture zone. Geology, v. 16, p. 696-698.

Ring, U., Ratschbacher, L., Frisch, W., Biehler, D. and Kralik, M., 1989. Kinematics of the Alpine plate-margin: structural styles, strain and motion along the Penninic–Austroalpine boundary in the

Swiss–Austrian Alps. Journal of the Geological Society, v. 146, p. 835-849.

Schmid, S.M., Pfiffner, O.A., Froitzheim, N., Schönborn, G. and Kissling, E., 1996A, Geophysical-geological transect and tectonic evolution of the Swiss-Italian Alps. Tectonics, v. 15, p. 1036-1064.

Schmid, S.M., Berger, A., and Davidson, C., 1996B, The Bergell pluton (Southern Switzerland, Northern Italy): Overview accompanying a geological-tectonic map of the intrusion and surrounding country rocks, Schweizerische Mineralogische und Petrographische Mitteilungen, v. 26, p. 329-355.

Schmid, S.M., Fügenschuh, B., Kissling, E., and Schuster, R., 2004, Tectonic map and overall architecture of the Alpine orogen. Eclogae Geologicae Helvetiae, v. 97, p. 93-117.

St. Mueller, 1989, Deep-reaching geodynamic processes in the Alps, in: Coward, M.P., Dietrich, D., and Park, R.G. (eds.), *Alpine Tectonics*, Geological Society Special Publication 45, p. 303-328.

Staub, R., 1958, 958, Klippendecke und Zentralalpenbau; Beziehungen und Probleme: Beiträge zur Geologischen Karte der Schweiz, no. 103, 184 p.

Steinmann, 1994, Ein Beckenmodell für das Nordpenninikum der Ostschweiz. Jahrbuch der Geologischen Bundesanstalt, v. 137, p. 675-721.

Streiff, V., 1962, Zur Beheimatung der östlichen Klippendecken. Eclogae Geologicae Helvetiae v. 55 p. 77-134.

Streiff, V., Jäckli, H., and Neher, J., 1976, Erläuterungen Blatt 1235 Andeer, Geologische Atlas der Schweiz, 1:25,000.

Thum, I., and Nabholz, W., 1972, Zur sedimentologie und metamorphose der Penninschen flysch- und schieferabfolgen im gebiet Prättigau-Lenzerheide-Oberhalbstein. Beiträge zur geologischen karte der Schweiz, 144.

Weh, M., 1998, Tektonische Entwicklung der penninischen Sediment-Decken in Graubünden (Prättigau bis Oberhalbstein). Unpublished PhD thesis, University of Basel, 230 p., 1 Appendix.

Weh, M., and Froitzheim, N., 2001, Penninic cover nappes in the Prättigau half-window (eastern Switzerland): Structure and tectonic evolution. Eclogae Geologicae Helvetiae, v. 94, p. 237-252.

Wiederkehr, M., Bousquet, R., Schmid, S.M. and Berger, A., 2008, From subduction to collision: thermal overprint of HP/LT meta-sediments in the north-eastern Lepontine Dome (Swiss Alps) and consequences regarding the tectono-metamorphic evolution of the Alpine orogenic wedge. Swiss Journal of Geosciences, v. 101, p. 127-155.

Wiederkehr, M., Sudo, M., Bousquet, R., Berger, A. and Schmid, S.M., 2009, Alpine orogenic evolution from subduction to collisional thermal overprint: The $^{40}Ar/^{39}Ar$ age constraints from the Valaisan Ocean, central Alps. Tectonics, v. 28. TC6009, doi:10.1029/2009TC002496.

Wyss, R., and Isler, A., 2011, 1214 Ilanz Erläuterungen, Geologischer Atlas der Schweiz, Bundesamt für Landestopografie swisstopo.

Ziegler, W.H., 1956, Geologische Studien in den Flyschgebieten des Oberhalbsteins (Graubünden). Eclogae Geologicae Helvetiae v. 49, p. 1-78.

Chapter III

Determining crystallization temperatures and paleowater isotopic compositions for the carbonate phases at Kennecott, Alaska: A first application of clumped isotopes to an ore deposit

A manuscript to be submitted to Earth and Planetary Science Letters or Geochimica et Cosmochimica Acta

3.1. Abstract

Nine distinct carbonate phases from the Bonanza Cu-(Ag) mine, Kennecott, Alaska, comprising pre-, syn-, and postmineral calcite (n= 65) and premineral dolomite (n=23) were measured using the clumped isotope thermometer. The motivation for the study was: (1) to put carbonate phases of uncertain paragenetic position into their thermal context, (2) to compare the temperatures of the carbonate phases in known paragenetic positions to theoretical sulfide stabilities, (3) to document time-temperature changes during the evolution of the mineralizing system, and (4) to test previously proposed genetic models for the deposits.

The total range for carbonate temperatures spans 35-180°C, although temperatures above ~140°C are considered suspect. Premineral calcite phases are relatively cool (43-57°C), whereas premineral dolomite phases are hot (91-180°C); synmineral calcite phases are relatively warm (58-139°C); late postmineral phases are the most cool (35-67°C) but overlap premineral and the coldest of the synmineral calcite phases. Zebra dolomite precipitated in the range 92-180°C with a median value of 119°C. Dedolomite, a hallmark alteration feature of the mineralizing fluids, falls into a narrow range of 93-105°C, consistent with the stability field for the low-temperature chalcocite polymorph and on the edge of stability for djurleite.

Calculated compositions for $\delta^{18}O_{water}$ vary from -17.8 to +6.1‰, and the median for the entire dataset is -0.8‰. The most depleted, similar to meteoric, water precipitated late calcite, whereas the most enriched water was associated with both synmineral calcite veins and recrystallized limestone wallrock adjacent to the orebody. Synmineral calcite fluids vary from -2.0 to 6.1‰ $\delta^{18}O_{water}$.

Intriguingly, rhymthic layering in zebra dolomite can be resolved in Δ_{47} space, and pre-

liminary data indicate that some of the coarser-grained baroque dolomite 'stripes' precipitated at temperatures up to c. 10°C cooler than the surrounding, finer-grained dolomite wallrock but other 'stripes' may have precipitated at temperatures greater than the wallrock.

The calculated values of $\delta^{18}O_{water}$ support a genetic model that invokes redox changes associated with fluid mixing as the likely mechanism responsible for copper deposition. In this model a sulfidic, basinal fluid having $\delta^{18}O$ similar to seawater mixes with a cuprous fluid having heavier $\delta^{18}O$ (5-8‰) which was derived from the Nikolai Greenstone during prehnite-pumpellyite-facies metamorphism.

3.2. Geologic Introduction

The Kennecott Cu-(Ag) deposits in eastern Alaska (Fig. 1) are heralded for their extremely high grade and unusual upward-tapering vein morphology (Bateman and McLaughlin, 1920; MacKevett et al., 1997; Price et al., 2014). The deposits occur in the Wrangellia terrane, hosted by the 700-m-thick Triassic (Carnian) Chitistone Limestone within 20-40 m of its contact with the subjacent 3000+-m-thick Triassic (Ladinian) Nikolai Greenstone, a prehnite-pumpellyite facies metabasalt (MacKevett, 1970b, MacKevett, 1971, Schmidt and Rogers, 2007; Greene et al., 2008). The Chitistone Limestone is the lowest formation in a Triassic-Jurassic marine sedimentary basin up to ~3600 m thick at its depocenter near Kennecott (MacKevett et al., 1997). During the late Jurassic to middle Cretaceous (~150-110 Ma) the area underwent a significant orogeny resulting in numerous thrust faults and upright to overturned folds that are interpreted to represent the docking of Wrangellia against North America (MacKevett 1970b, MacKevett 1971, Trop et al., 2002).

Four principal veins—Bonanza, Mother Lode, Jumbo, Erie—and numerous subsidiary veins were mined underground by the Kennecott Copper Corporation during the period 1911-1938, in which nearly 1.8 billion pounds of copper and 9 million ounces of silver were produced (original Kennecott mine records) for an in-ground value of ~US$5B at current metal prices. It is helpful to visualize the largest deposits (particularly Jumbo, Bonanza, and Mother Lode) as being shaped like overturned canoes with exaggerated keels. The veins (keels) strike northeast, and their enlarged fault-bound bases (overturned canoes) plunge approximately 30° northeast down-dip in the limb of an anticline, essentially parallel to the Nikolai Greenstone-Chitistone Limestone contact. The width of the basal enlargements varied from a maximum of 8 meters (Mother Lode) to 18 meters (Jumbo). The down-plunge length of the keels varied from 450 meters (Jumbo) to 1000 meters (Mother Lode) (MacKevett et al., 1997). The orebodies were dominated by the assemblage chalcocite-djurleite with djurleite ($Cu_{1.94}S$) comprising some 40% of the ore (MacKevett et al., 1997). In addition, volumetrically-minor assemblages of chalcopyrite-bornite-covellite-luzonite, digenite-spionkopite-yarrowite, malachite-azurite and cuprite were present

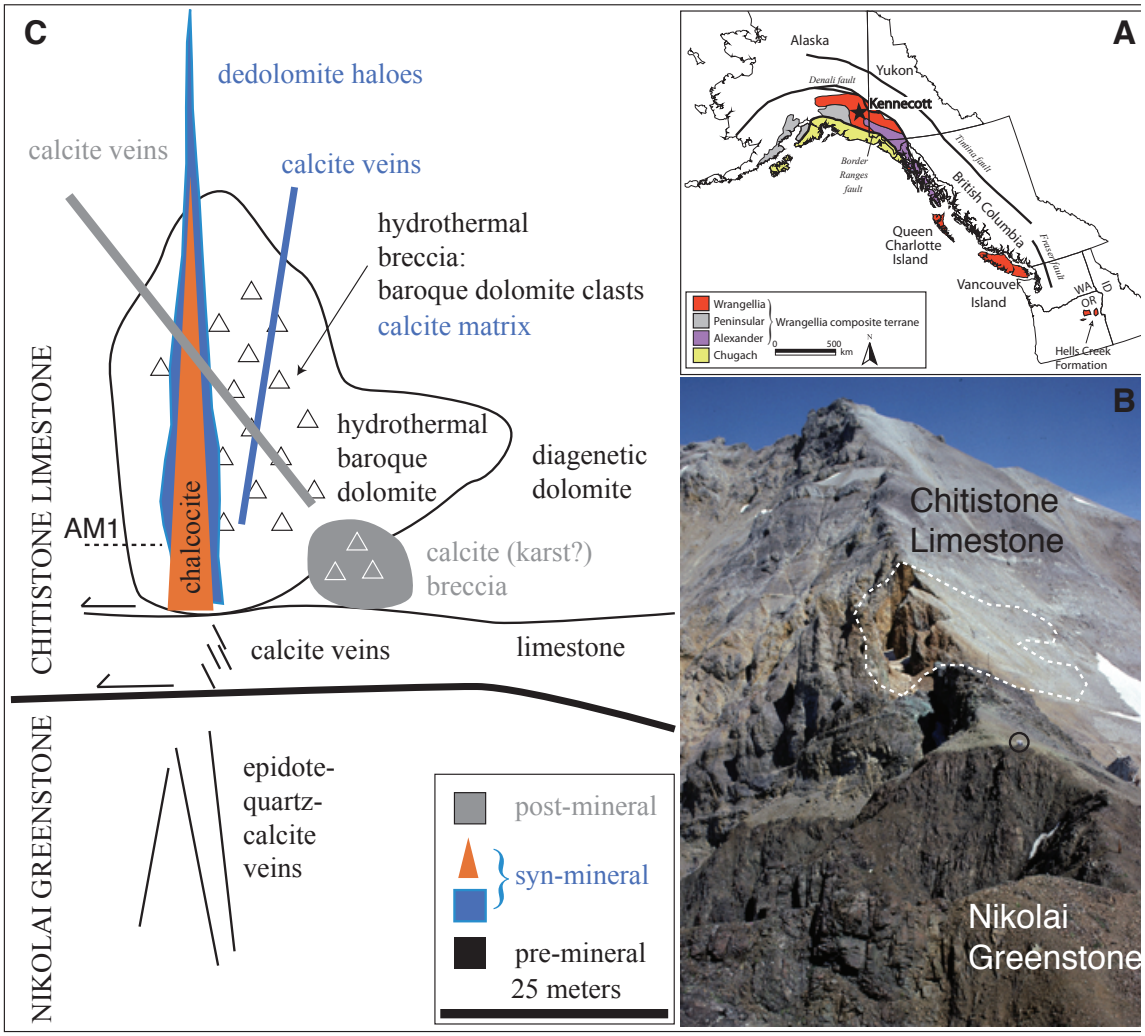

Fig. 3.1: A) Location map, B) outcrop view, and C) schematic illustration of the carbonate phases colored according to their paragenetic position with respect to the copper orebodies at Kennecott, Alaska. Dashed outline in 'B' indicates the surface trace of concentrated baroque dolomitization at Bonanza mine. Small black circle indicates a geologist (seated) for scale.

(Bateman and McLaughlin, 1920; MacKevett et al., 1997). Copper sulfide stabilities indicate that the main-stage assemblage of chalcocite-djurelite was deposited initially near 103.5°C (inversion temperature from hexagonal 'high' to pseudo-orthorhombic 'low' chalcocite) then below 93°C, which is the threshold for djurleite stability (Bateman and McLaughlin, 1920; Ramdohr, 1980; MacKevett et al., 1997).

3.3. Paleothermometry of Carbonate Phases

3.3.1. Motivation

The Kennecott copper deposits represent an ideal case study for applying the "clumped"

isotope paleothermometer (Ghosh et al., 2006; Huntington et al., 2009) to the question of the temperature of the ore fluids. There are ten phases of carbonate present at Kennecott that we consider here (Fig. 3.4, Table in Appendix 3). They include pre-, syn-, and postmineral calcite and premineral dolomite ("mineral" as used in this study refers specifically to the copper mineralization stage) in wallrock, tectonic and hydrothermal veins, and tectonic, hydrothermal, and karst breccias. Some of these phases have a clear paragenetic position relative to copper deposition, but others are uncertain. Temperatures for the mineralization event have been constrained between premineral prehnite-pumpellyite-native copper and epidote-quartz-native copper veins (~250°C, 2.5 kbar; Beiersdorfer and Day, 1995) in the greenstone immediately below the orebodies and main stage mineralization djurleite stability at < 93°C (Potter, 1977) and therefore fall into the measurable range for clumped isotope analysis (Eiler, 2011). The motivation to use the clumped isotope paleothermometer is: 1) to put carbonate phases of uncertain paragenetic position into their proper context, 2) to determine the temperatures of the carbonate phases in known paragenetic positions (including those reassigned from previously uncertain paragenetic positions) to compare to the theoretical sulfide stabilities, and 3) to document time-temperature changes during the evolution of the mineralizing system thereby testing the genetic models of MacKevett et al. (1997) and Price et al. (2014).

3.3.2. Methodology

Carbonate powders were drilled from rock samples using a small Dremel tool. Aliquots of carbonate powder weighing approximately 10 mg apiece were put into silver capsule-type boats and introduced into 100% H_3PO_4 heated to 90°C on the Autoline attached to a Thermo Finnegan MAT 253 gas-source isotope ratio mass spectrometer at Caltech. CO_2 gas was allowed to evolve for about nine minutes before being carried through a series of purification steps down the line: first through an ethanol-dry ice slurry to strip out water vapor, then through an LN2 bath to capture lighter, yet still condensable, phases, and finally through a GC column with Porapak filters to strip out any remaining organic contaminants. Purified CO_2 then entered the sample bellows on the MAT253. Analysis on the MAT253 involved switching back and forth from an aliquot of unknown sample gas to an aliquot from a working gas of known, standard composition. Switching between known and unknown seven times constitutes one measurement, and the mean of eight measurements yields one datum to plot. The entire process takes about three hours per sample. Unknown samples were standardized against Carrara Marble and internal lab standards TV01 (2012-early 2013) and TV03 (late 2013-2014). The reference line was established by gases (BOC and enriched BOC) heated to 1000°C for two hours to ensure a stochastic distribution of isotopologues. Beginning in 2013, 25°C water-equilibrated gases became widely incorporated into the sampling process in order to project Δ_{47} data into the absolute reference frame (Dennis et

al., 2011). Eight sessions were completed between June, 2012 and May, 2014. Session two, during August, 2012 had a problem with a falling heated gas line, but the reason for this was never discovered. Session four, during Nov-Dec, 2012, had a problem in that the reference gas tank ran out in the middle of the run and had to be replaced. Presumably as a result of this (although not for certain), the heated gas line dropped from the beginning to end of the session. To attempt to correct for this problem, the session was subdivided into "old reference tank" (Session 4) and "new reference tank" (Session 5). In both cases the heated gas line moved such that the standard residuals were more depleted with time (from ~0‰ to ~ -0.09‰). A least-squares linear best fit was calculated for the standard residuals and applied as a standard correction to the unknowns from these two sessions (Fig. 3.2).

All data reported here have been converted to the absolute reference frame. For sessions 1 and 3, where there were no problems with the heated gas line, the use of the Dennis et al. (2011) "secondary" conversion to the absolute reference frame (via standards of known composition) was used. For sessions 6, 8, 9, the Dennis et al. (2011) "primary" conversion was used (via 25°C equilibrated gases). For sessions 2, 4, 5 where there was a problem with heated gas line, a best fit line through TV01 standard (session 2) and Carrara marble standard (sessions 4, 5) was used to adjust sample D47 through the course of the sessions. The temperature-Δ_{47} calibration curve used here was projected from the Caltech reference frame (Stolper and Eiler, 2015) by M. Lloyd (unpublished data, 2016) and fits the form $\Delta_{47} = ax^2 + bx + c$, where,

$x = 10^6/T^2$ (in kelvin)

$a = 0.001083$

$b = 0.02854$

$c = 0.2587$

The total number of analyses, including heated gases, standards, and unknowns, was 329. Approximately 12 samples were discarded during the screening for Δ_{48} excess. After replicates are taken into account and averaged, total new data reported are 65 calcite and 23 dolomite measurements. A summary data table can be found in Appendix Three.

Fractionation factors used to convert from raw isotopic ratios are: $CO_{2(acid)}$-calcite (Kim et al., 2007), calcite-water $\delta^{18}O$ (Friedman and O'Neil, 1977), and dolomite-water $\delta^{18}O$ (Schmidt et al., 2005).

3.3.3. Data

Data are plotted in the absolute reference frame (Figs. 3.3, 3.4, 3.5). Calcites of 'unknown' paragenesis were first reassigned to a 'known' category based on their temperature (Fig. 3.3, which shows replicates). About half of the unknown calcites can be cleanly grouped with the syngenetic stage of mineralization based on their temperature. Two samples clearly belong to

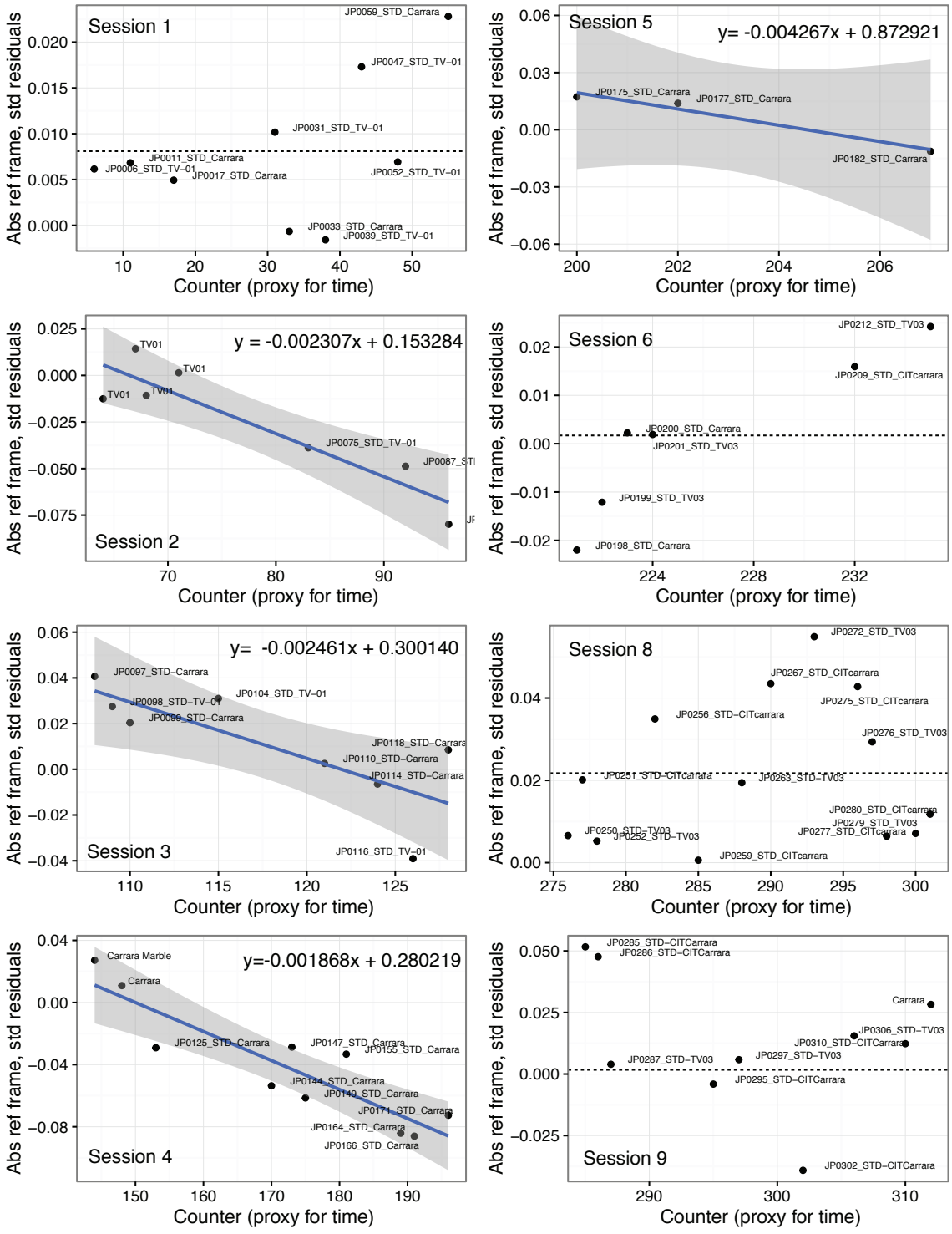

Fig. 3.2: Standard residuals through time for eight analytical sessions between June, 2012 and May, 2014. 'Counter' indicates position in the sample sequence. Each sample takes approximately three hours to run; thus, ten Counter units is approximately 30-32 hours in real time, which makes a convenient proxy for time in these plots. In sessions 2-5 (Aug, Sept, Nov, Dec, 2012), the heated gas line dropped during the run. A least-squares best fit line through the standards was used to correct Δ_{47} for these sessions. Otherwise, an average standard value was used (dotted line in sessions 1, 6, 8, 9).

a non-mineral stage. The remaining three samples (K-225, K-256, KEN-42) are cooler than the narrow threshold which defines the main-stage of copper mineralization, but have been tentatively placed into the syngenetic category.

When plotted against bulk stable isotopes ($\delta^{18}O$, $\delta^{13}C$; Figs. 3.3, 3.4) several trends in the data are apparent. Limestone (blue diamond in Fig. 3.4) and dolomite (orange X-box in Fig. 3.4) form overlapping clusters that are distinct from the various cross-cutting calcite phases in that they are higher temperature (mean limestone, 113.4°C, mean dolomite wallrock, 116.2°C) and are slightly enriched in both $\delta^{18}O_{mineral}$ (mean 19.2‰ for limestone and 18.1‰ for dolomite wallrock) and $\delta^{13}C$ (mean 4.16‰ for limestone and 3.66‰ for dolomite wallrock). However, the two vary with no overlap in their calculated $\delta^{18}O_{water}$ compositions (mean 3.3‰ for limestone versus -2.6‰ for dolomite wallrock; Fig. 3.5). It is noteworthy that, given the relatively restricted sampling area of c. 0.025 km^2 and 200 m of stratigraphy, the limestone varies over a several per mil range in both $\delta^{18}O_{mineral}$ and $\delta^{13}C$, which is in contrast to the relatively homogeneous dolomite sampled over that same area. Calcite found in greenstone veins (greenstone cal, upright blue triangle in Fig. 3.4) is depleted in $\delta^{18}O$ and overlaps the synmineral dedolomite phases, but in $\delta^{13}C$ space, it makes a markedly scattered yet clearly distinct population. Calculated $\delta^{18}O_{water}$ compositions cluster around -1‰ (mean -1.7‰). The hallmark dedolomite (downward-facing open triangles in Fig. 3.4) that forms selvages around chalcocite veins occurs in a relatively restricted range of 106-93°C, consistent with the thermal stability of chalcocite. In $\delta^{18}O_{mineral}$ composition, dedolomite scatters over about 5‰ (mean 15.7‰), but in $\delta^{13}C$ composition, it is buffered to <1‰ variation (mean 2.6‰), which is nevertheless depleted relative to the surrounding limestone wallrock. Calculated $\delta^{18}O_{water}$ composition for dedolomite is -1.8‰. Other synmineral calcite phases ('X' in Fig. 3.4) scatter markedly in all fields, ranging from 58-139°C, to 15.8-20.8‰ $\delta^{18}O_{mineral}$, to -8.2 to 4.4‰ $\delta^{13}C$. Despite such scatter in bulk stable isotopes and temperatures, calculated $\delta^{18}O_{water}$ composition (Fig. 3.5) is surprisingly restricted to -2 to +1‰ with a few outliers that extend up to +6‰. Fault steps (blue circles in Fig. 3.4) comprise calcite slickenfibers that grow on strike-slip faults in mesoscopic faults which underlie (but do not cut up into) the main ore horizon. They are invariably cooler than main-stage ore formation and scatter widely in $\delta^{18}O$ composition but less so in $\delta^{13}C$. There is one fault step outlier that is depleted in both $\delta^{18}O$ and $\delta^{13}C$. Calculated $\delta^{18}O_{water}$ composition for fault steps overlaps that of synmineral calcite and baroque dolomite with a mean of -1.3‰. Early and late calcite are invariably cool (<75°C) and are markedly scattered in both $\delta^{18}O_{mineral}$, $\delta^{18}O_{water}$, and $\delta^{13}C$ compositions. Baroque dolomite is a coarse-grained pre-mineral phase that ranges from c. 90-140°C with two outliers at >160°C and has bulk $\delta^{18}O_{mineral}$ ranging from 17.6-20.2‰ and bulk $\delta^{13}C$ ranging narrowly from 3.2 to 3.8‰. Calculated $\delta^{18}O_{water}$ compositions scatter over a range of -4.3 to 1.6‰ but exhibit a binned behavior rather than a smooth scatter.

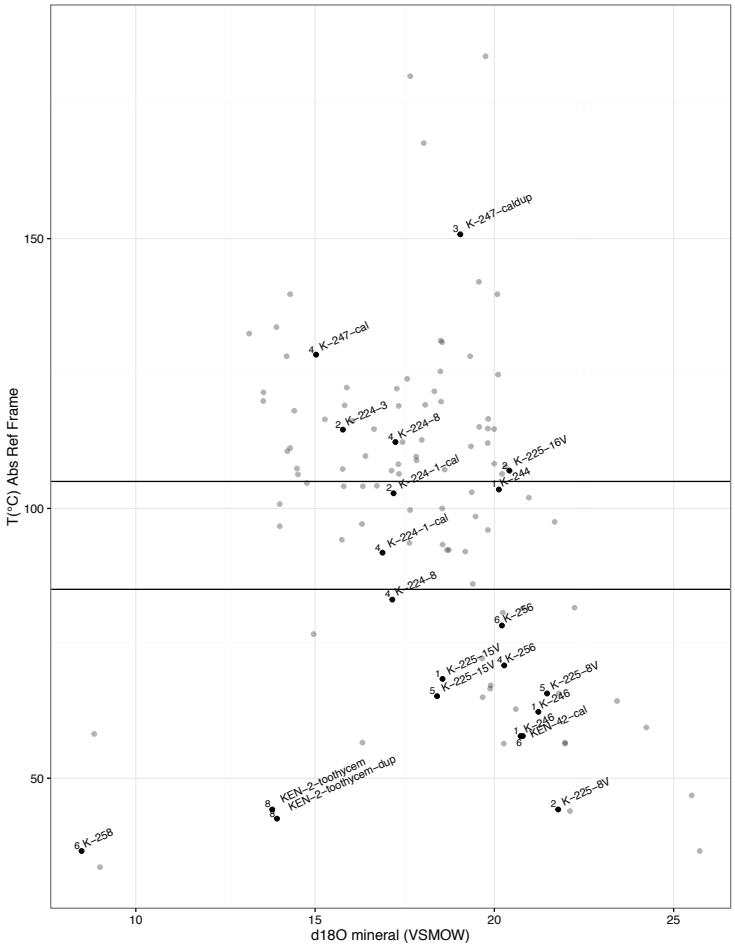

Fig. 3.3. Temperature vs. $\delta^{18}O_{mineral}$ for calcite phases of indeterminate paragenesis. Horizontal lines at 104°C and 90°C delineate the thermal range over which dedolomite is found. Temperature is useful discriminator of the phases. Replicates are included in this plot but are removed for subsequent plots.

We find that the hottest reliable temperatures for all phases are ≤ 140°C (Fig. 3.5). A 'hot' group consists of the phases dolomitized wallrock, baroque dolomite, greenstone calcite, limestone wallrock, and breccia matrix, whose range of medians is 117.2°C (greenstone calcite, maximum of the group as well as the entire study) to 110.2°C (breccia matrix, minimum of the group). Below this group is a smaller group of 'warm' synmineral calcite veins and dedolomite, whose range in medians is 101.6°C (synmineral calcite) to 95.4°C (dedolomite). Hotter outliers in the synmineral calcite population readily overlap the 'hot' group, but only a single outlier in the 'warm' group (a dedolomite) barely overlaps the bottom of the range for the 'hot' group. Remaining calcite phases are all 'cool' (≤ 61°C median), in particular early and late calcite and fault slickenfibers from the limestone. Lowest synmineral calcite temperatures overlap the 'cool' range.

When examined in terms of stratigraphy (Fig. 3.6), temperatures are hottest above the algal mat (AM1) and in the Nikolai Greenstone (Fig. 3.6A). The basal 32 m of the Chitistone Limestone host all the phases from the 'cool' group, but 'warm' and 'hot' phases can be found there as well. Intriguingly, $\delta^{18}O_{water}$ (Fig. 3.6C) varies only a few permil over the full stratigraphic range

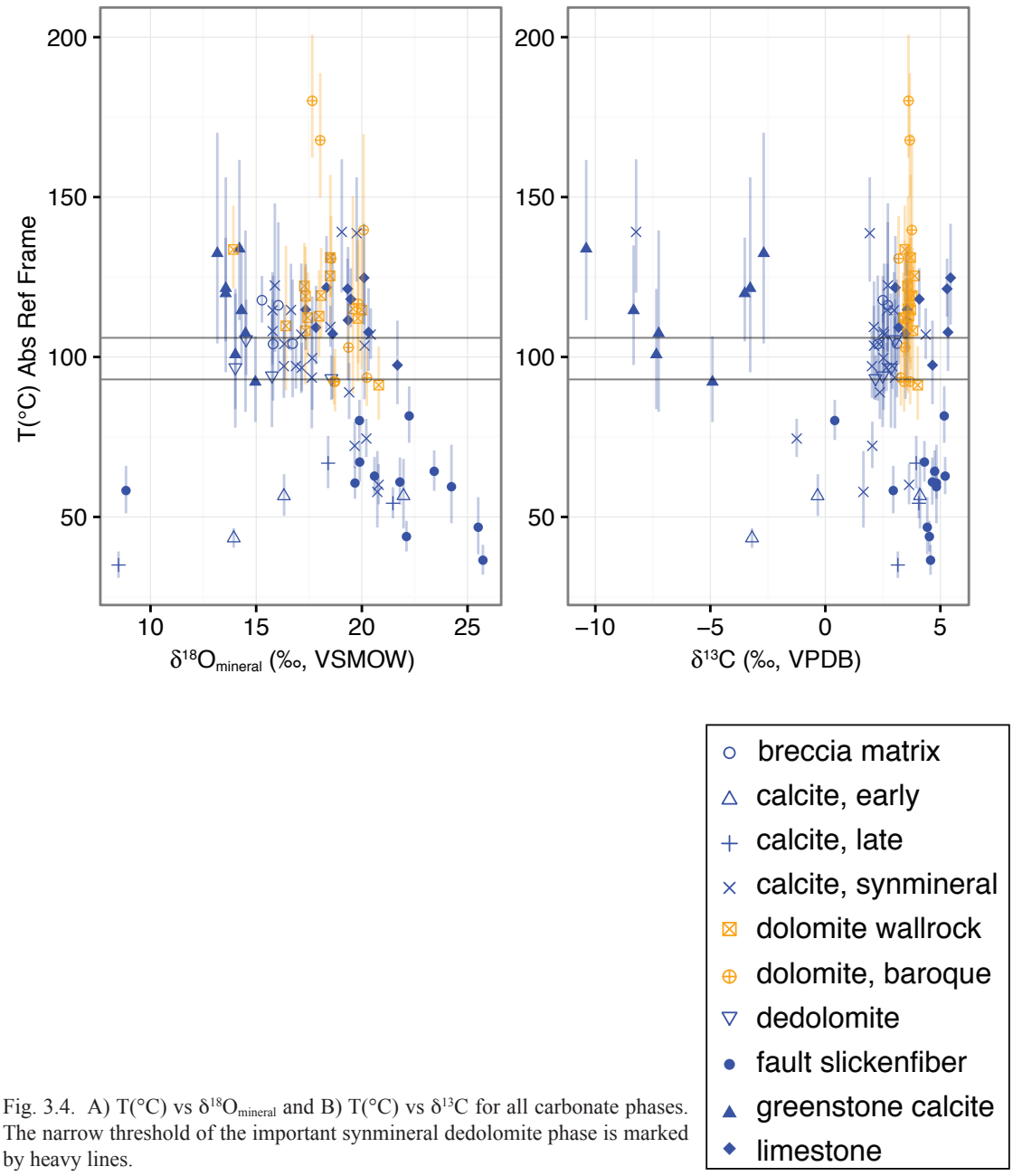

Fig. 3.4. A) T(°C) vs $\delta^{18}O_{mineral}$ and B) T(°C) vs $\delta^{13}C$ for all carbonate phases. The narrow threshold of the important synmineral dedolomite phase is marked by heavy lines.

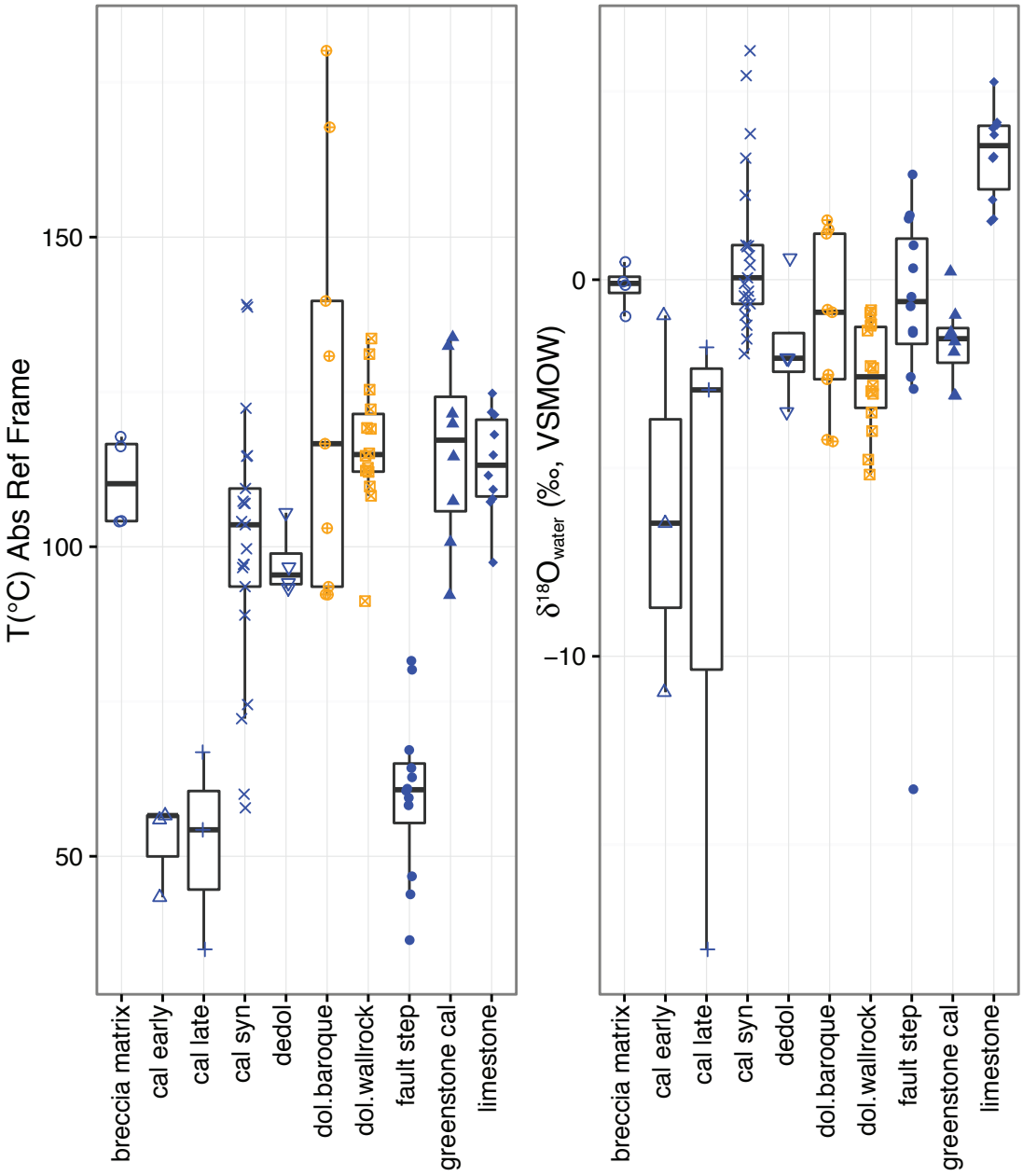

Fig. 3.5. Boxplots of carbonate phases showing the range of temperatures and $\delta^{18}O$ water compositions over which they occur. Whisker length extends to the highest or lowest value that falls within 1.5*interquartile range. Values outside of the whiskers are considered to be outliers following Tukey (1977).

from c. -20 m up to c. +70 m, and all of the depleted phases occur within the very narrow stratigraphic interval between the flat fault (FF) and the first algal mat horizon (AM1). It is possible that this latter point is the result of sampling bias, as the intial study was focused on hydrothermal, not stratigraphic, features. Bulk stable isotopes (Fig. 3.6B, D) indicate a reasonably tight buffering of d13C values in the Chitistone Limestone by the limestone wallrock and possibly the introduction of a hydrocarbon species in the Nikolai Greenstone to account for depleted d13C down to -10.4‰. 18O ratios in the Chistone Limestone are depleted moving upsection and reach a value of c. 14‰, which is equivalent to the mean value (14.03‰) measured in calcite veins in the Nikolai Greenstone.

3.4. Discussion

3.4.1. Utility of the clumped isotope tool for assignment of paragenesis

The orebodies at Kennecott are massive, structurally-controlled concentrations of copper which have very small footprints (<1 km^2). They are fringed with varible amounts of carbonate phases hosted in a carbonate unit. Single calcite veins or isolated pockets of breccia, particularly 100s of meters away from the ore zones cannot be assigned a paragenesis (relative to ore formation) in the field because such features could conceivably be related to early diagenesis, karsting, orogenic deformation, 'blind' mineralization, or even late, post-mineral volcanism (i.e., the hypabyssal Porphyry Mountain stock located only about 3 km south of the Bonanza mine or the more distant, but far more voluminous, Wrangell Mountains volcanic field). Economic geologists seek clues in outcrop that may guide drilling efforts to find buried mineralization, but foolish would be the geologist who drilled every local zone of calcite or carbonate breccia, even around productive districts like Kennecott, in hopes of finding more ore. Thus, the clumped isotope tool is capable of distinguishing between carbonate veins or breccias of higher temperature, and therefore potentially copper-mineralized, or lower temperature, and therefore most likely unmineralized. In addition, calculated $\delta^{18}O_{water}$ compositions strongly indicate the presence or absence of particular fluids associated with copper mineralization (i.e., marine vs. meteoric). At Kennecott specifically, the synmineral phases are all associated with a fluid broadly similar to standard mean ocean water (SMOW) in composition with temperatures in the range 140 to 80°C, whereas phases that are clearly unrelated to copper mineralization are depleted in $\delta^{18}O_{water}$ and are cooler (<75°C), which is a strong indication that meteoric fluids flooded the system after copper deposition. From an exploration standpoint, distinguishing between such phases, particularly when there is no copper mineralization in sight, is an extremely useful exploration criterion with wide applicability to carbonate terrain worldwide.

3.4.2. Retention of Δ_{47} signal through geological time

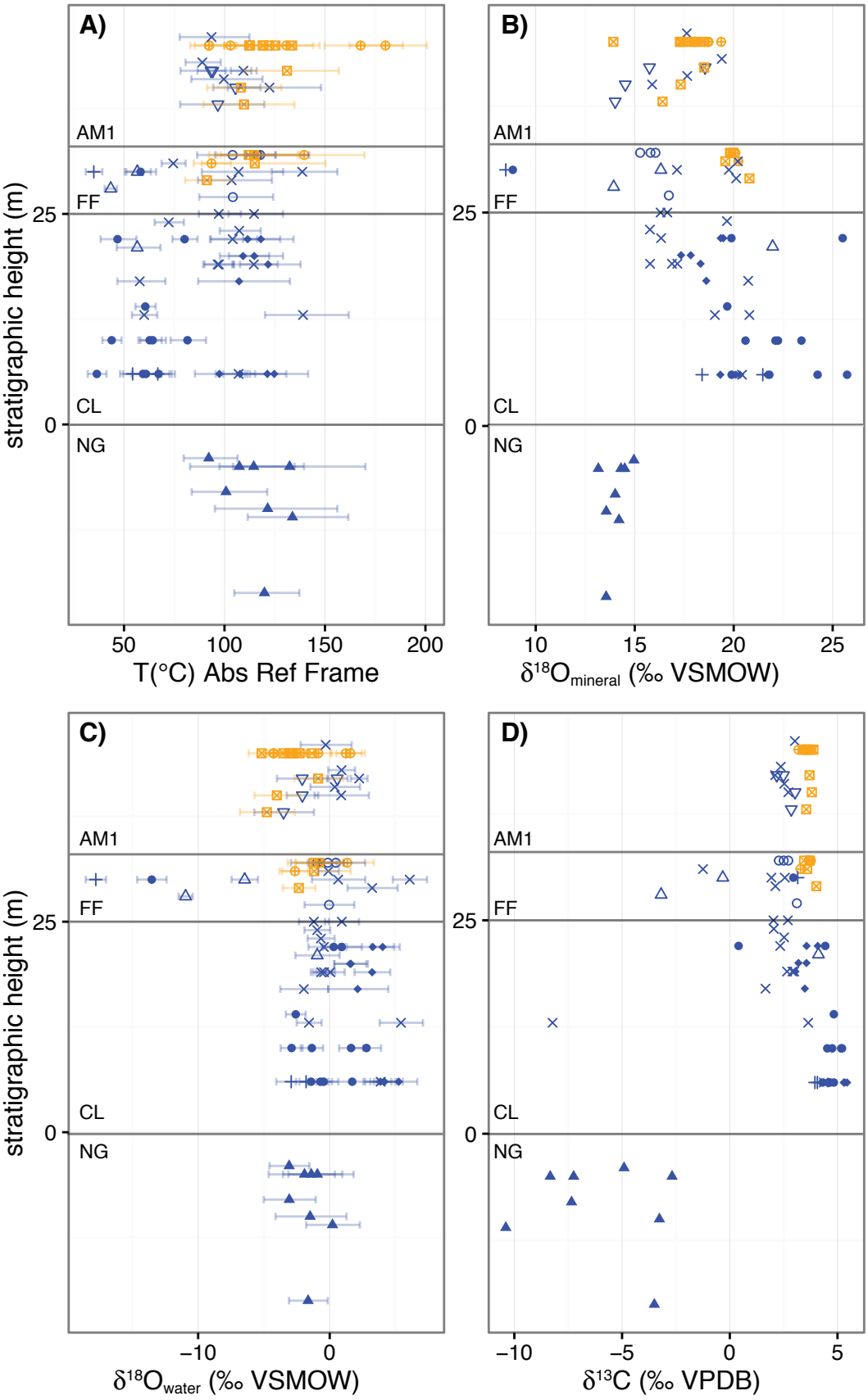
A)
B)
C)
D)
AM1
FF
CL
NG
stratigraphic height (m)
25
0
50
100
150
200
T(°C) Abs Ref Frame
10
15
20
25
δ18Omineral (‰ VSMOW)
−10
0
δ18Owater (‰ VSMOW)
−10
−5
0
5
δ13C (‰ VPDB)

Our analyses give an indication that the Δ_{47} double-substitution is stable over long periods of geologic time. The only two phases that are certain in their premineral paragenesis are baroque dolomite and limestone wallrock because chalcocite is observed to crosscut and replace those phases. Baroque dolomite and limestone wallrock present some of the highest temperatures recorded in this study (dolomite slightly higher than limestone). However, two additional calcite phases, while not observed to be cross-cut by the ore veins, have a high probability of being premineral (but not primary): a "toothy" calcite epitaxial cement which grows in an irregular hemispherical form at the stratigraphic level of the first algal horizon (AM1 in Fig. 3.1), and, occuring at the same stratigraphic horizon, an undolomitized pure-calcite polymictic breccia containing clasts of algal mat (AM1). Both of these phases yield temperatures in the c. 50°C range, which could reflect the temperature of recrystallization during diagenesis when the Triassic-Jurassic basin was forming. If true, their proximity to the main Bonanza orebody (m to 10s of m) would indicate that they were insensitive to peak diagenesis, orogeny, and mineralization. However, depleted $\delta^{18}O_{water}$ compositions favor an alternative hypothesis: these two phases were modified after mineralization by a meteoric fluid which permeated the tectonically and hydrothermally disrupted AM1 stratigraphic horizon, and thus, these two suspected early phases based on textural evidence have not preserved their early chemistry. Even so, high temperatures measured for premineral dolomite, much of the synmineral calcite, and greenstone calcite indicate that these have not been modified by subsequent meteoric fluids. While timing of the mineralization event is not tightly constrained, it is certainly post-Triassic (age of host rock) and pre-Miocene (age of nearby cross-cutting dikes) and likely occurred sometime during a poorly dated orogeny which occurred between c. 160-110 Ma based on unconformable stratigraphic relationships observed in the district (MacKevett et al., 1997).

3.4.3. Implications for model of ore formation

Bateman and McLaughlin (1920) presented a model of ore formation in which the ore bodies are structurally controlled along faults and formed in response to heating from a hypothetical pluton. MacKevett et al. (1997) presented a model of ore formation in which ground was prepared by karst collapse and brecciation some 100 m.y. prior to arrival of the ore-forming fluids which were sourced, not from a plutonic source, but from connate fluids which scavenged copper from the underlying Nikolai basalts. Price et al. (2014) presented a model in which the orebodies are controlled by structures as initially suggested by Bateman and McLaughlin (1920) and formed from connate fluids which scavenged copper from the Nikolai basalts similar to that suggested by MacKevett et al. (1997).

Fig. 3.6. Temperature, $\delta^{18}O_{water}$, $\delta^{18}O_{mineral}$, and $\delta^{13}C$ plotted against stratigraphic position. AM1: first algal mat horizon; CL: Chitistone Limestone; FF: flat fault (base of the orebody); NG: Nikolai Greenstone

MacKevett et al. (1997) placed temperature constraints on ore formation based on sulfide mineral stability of copper sulfide minerals in the Chitistone Limestone: 1) volumetrically minor chalcopyrite-bornite exsolution indicates T < 200°C, 2) volumetrically minor and anomalous bornite- and covellite-exsolution from chalcopyrite is only stable at T < 150°C, 3) Chalcocite inverts from the hexagonal 'high' to (pseudo) rhombohedral 'low' polymorph at 103.5±1.5°C, and 4) Djurleite is only stable at T <93±2°C. Using quartz-epidote $\delta^{18}O$ measurements, Silberman et al. (1980) estimated temperature and water composition of quartz-epidote-(native copper-calcite-copper sulfide) veins in the upper Nikolai Greenstone to be c. 200°C and 1‰ (using an unpublished calibration curve and tacitly assuming, but not demonstrating, that epidote and quartz are cogenetic, which may not be true as euhedral, terminated epidote everywhere forms vein margins, whereas anhedral quartz fills vein interiors). MacKevett et al. (1997) report a single fluid inclusion analysis of late-calcite collected from the nearby Jumbo mine dump, which yielded a pressure-corrected homogenization temperature of 93°C, a salinity of 15±3 wt % NaCl equivalent, and a calculated $\delta^{18}O$ water composition of -4‰. Combining all of these observations, MacKevett et al. (1997) state that there were four temperature stages for copper mineralization at Kennecott: Stage 1) c. 200°C for earliest sulfide-free vein formation, Stage 2) c. 200-150°C for first appearance of sulfides as volumetrically minor chalcopyrite-bornite, Stage 3) 100-80°C for main-stage djurleite-chalcocite mineralization, and Stage 4) 70-50°C late oxidation to form, among others, malachite, azurite, and blaubleibender covellite (i.e., yarrowite-spionkopite). Price et al. (2014) estimated temperatures of associated carbonate minerals by substituting a range of likely temperatures into the carbonate paleothermometer equation of Friedman and O'Neil (1977) and determined that the water compositions allowed by the assumed temperatures were too broad to place further constraints on the Silberman et al. (1980) and MacKevett et al. (1997) temperature models. No other paleothermometry techniques have proven useful on these rocks (e.g., illite crystallinity, fluid inclusions on main-stage phases, etc.; MacKevett et al., 1997; Price, 2004), except for clumped isotopes.

Our maximum reliable temperatures of c.140°C are slightly lower than the estimates made by MacKevett et al. (1997) for the early stage I and stage II mineralization and suggest that the formation of dolomite and greenstone calcite occurred at about the same temperature as the formation of early sulfides. The ages of the dolomitization and the formation of epidote-quartz-native copper-(calcite-copper sulfide) veins in the Nikolai Greenstone are unknown, but our results suggest that an isothermal period existed during their formation, which implies, but does not prove, a short duration between their formations. Our measured temperatures for breccia matrices, synmineral calcite, and dedolomite overlap those estimated for the main-stage mineralization event and show that in fact, volumetrically (sample count as a proxy), most of the calcite phases associated with mineralization precipitated at T ≤ 110°C. The important dedolomite selvages

record temperatures in the 93-105°C range, which is a little above the reported thermal stability field of djurleite and squarely in the range for 'low' chalcocite (Roseboom, 1966; Potter, 1977). MacKevett et al. (1997) report that strongly twinned djurleite was the first phase to form during main-stage mineralization, and it was overgrown by chalcocite and untwinned djurleite as the main-stage proceeded. If their observation is true, our measured temperatures suggest that early main-stage djurleite must have been highly metastable and, most likely, there was rapid cooling in order to quench twinned djurleite. Roseboom (1966) reports that a number of low-temperature (≤ 100°C) copper sulfides cannot be quenched even at room temperature because they so readily re-crystallize into another similar phase. The fact that our measured syngenetic temperatures dribble downward to c. 60°C more or less supports the observation from MacKevett et al. (1997) that Stage 4 oxidation occurred over a range of 70-50°C, although our data suggest that it be a little higher, c. 80-60°C. Importantly, calcite veins at this temperature indicates that fluid movement and mechanical deformation in the form of tensile fractures continued down to quite low crustal temperatures. Likewise, the low temperatures recorded by fault slickenfibers indicate on-going deformation at a high supracrustal position.

Calculated $\delta^{18}O$ water compositions indicate that phases associated with mineralization precipitated from fluids similar to SMOW. Two phases in particular, breccia matrices (median -0.1‰) and synmineral calcite veins (median 0.2‰) are essentially identical to SMOW. A more depleted group includes dedolomite (median -2.1‰), dolomitized wallrock (median -2.6‰), and greenstone calcite (median -1.6‰). Of note, limestone records the heaviest $\delta^{18}O_{water}$ of 3.6‰. Dedolomite is the product of a recrystallization reaction in the dolomite wallrock adjacent to a vein with enough activity to remove an Mg^{2+} ion in exchange for a Ca^{2+} ion. It can be seen in the $\delta^{18}O_{water}$ data that dedolomite falls on a mixing line between the two end members dolomitized wallrock and synmineral calcite veins.

MacKevett et al. (1997) state that because the late calcite vein from the Jumbo dump had a calculated $\delta^{18}O_{water}$ of -4‰ and they expected main-stage fluids to be hotter than those which precipitated that vein, they predicted that main stage $\delta^{18}O_{water}$ should be essentially 0‰ or maybe slightly enriched. Our data indicate that the median $\delta^{18}O_{water}$ compositions for both synmineral calcite and breccia matrices are close to SMOW in composition, and a few symineral calcite outliers have enriched $\delta^{18}O_{water}$ compositions. However, several of the early phases, particularly dolomite wallrock and greenstone calcite have $\delta^{18}O_{water}$ compositions that are c. 2 permil depleted relative to SMOW.

Thus, we find that our clumped isotope temperatures agree generally with the estimations for temperatures made by MacKevett et al. (1997), but our data have the capacity to refine the range in temperature responsible for ore formation. In particular, the data indicate that the maximum temperature which precipitated carbonate minerals was <160°C and that nearly all of the

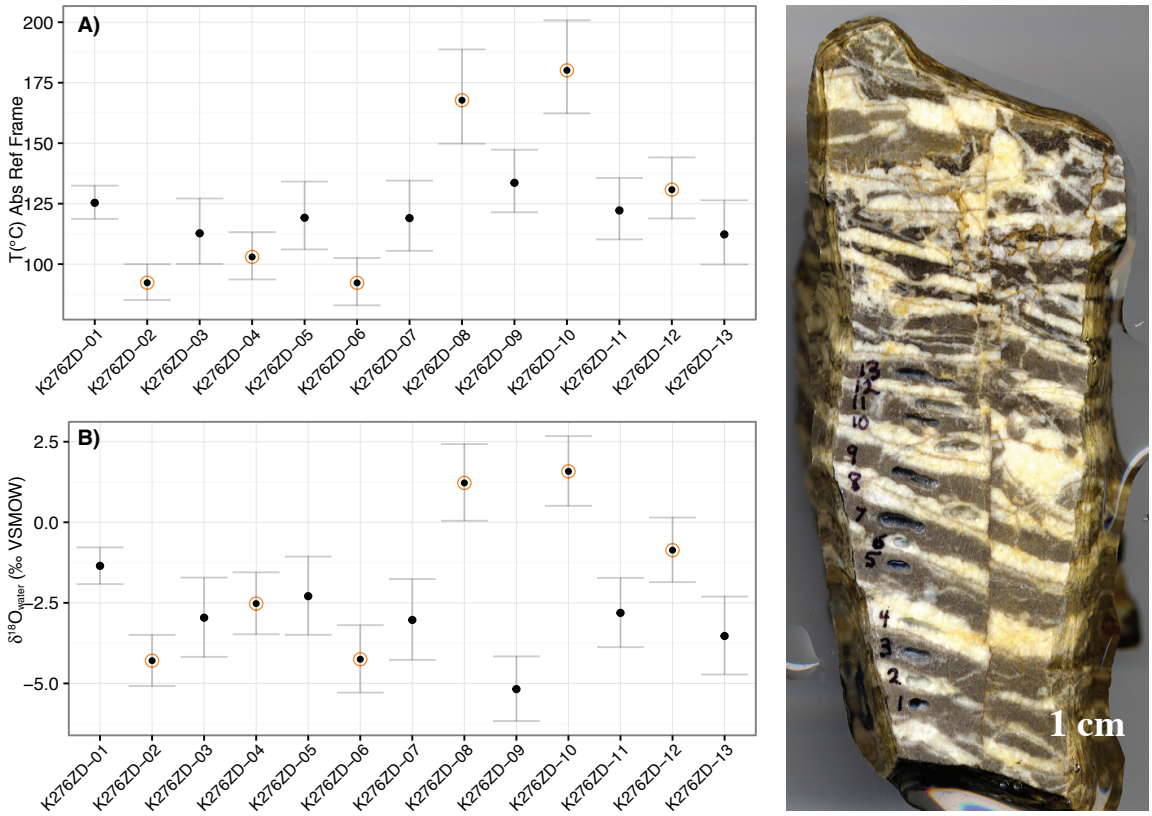

Fig.3.7: A) Temperature and B) $\delta^{18}O$ water composition of banded Zebra dolomite from Bonanza mine, collected near the horizon of the main orebody. Grey bands are earlier dolomitized wallrock and are represented by smaller circles in the plots. Yellow bands are later "cements" of baroque dolomite that replace and cross-cut the wallrock and are represented by larger orange bulls-eye circles in the plots. Dolomite powders were drilled out of the numbered slots on the left side of the photograph. Deliquescent edges are the result of scanning the sample, the sawn face of which was coated by a thin film of water.

carbonate phases that have an association with ore minerals precipitated below c. 110°C. Finally, if the main-stage mineralogy observed by MacKevett et al. (1997) is true, the clumped isotope temperatures indicate a rapid drop in temperature during ore formation (in order to quench twinned djurleite). Price et al. (2014) concluded that the limiting factor for ore formation was the availability of a reductant that could produce sulfide. These new data suggest that, in addition, falling temperatures also played a role in limiting the availability of sulfide.

3.4.4. Zebra Dolomite

Zebra dolomite (Fig. 3.7) is a distinctive carbonate texture in numerous carbonate-hosted ore deposits worldwide, i.e, Irish-type (Hitzman and Large, 1986), Mississippi Valley type (Leach et al., 2005), Carlin-type Au deposits in Nevada (Emsbo et al., 1999), and Kennecott, Alaska (Price et al., 2014); and in a variety of carbonate reservoir oil and gas fields, including the Western Canada, Michigan, and Appalachian basins (Davies and Smith, 2006). Zebra dolomite consists of rhythmic layers of dark grey, fine-grained replacement dolomite often with geopetal

filling, and coarse-grained white or yellow sparry baroque (saddle) dolomite (Diehl et al., 2010). The prevailing hypthothesis is that zebra dolomite is formed from deeply circulating, hot (up to 200°C), salty (up to 30 wt% NaCl equivalent) brines that may travel long distances, including from carbonate shelf to basin or vice versa (Diehl et al., 2010). Davies and Smith (2006) suggest that the coarse-grained bands of the zebra dolomite form during a pressure drop and release of CO_2 associated with fault slip. In mineral districts, zebra dolomite tends to host ore, but it is unclear how much older the zebra dolomite is compared to the ore it hosts.

Although Zebra dolomite at Kennecott is volumetrically small and, as in other global occurrences, predates ore formation, because of its distinctive rhythmic texture, it is of interest to examine with clumped isotopes to see if there is a regular pattern in either temperature or $\delta^{18}O_{water}$ that can be observed. In particular, no one has reported clumped isotope temperatures on zebra dolomite, and to date, the only way to determine temperature of formation is by measuring homogenization temperatures of fluid inclusions.

Preliminary results (Fig. 3.7) suggest that a slight variation in temperature can be observed between the layers. In particular, coarse-grained baroque dolomite (larger circles in Fig. 3.7) tend to be some 10-20°C cooler than the fine-grained dolomite wallrock (Fig. 3.7A), which is particularly evident for ZD-01, -02, -03, and -05, -06, -07, which we will call "well behaved." It is unknown why ZD-08 and ZD-10 spiked so high in temperature. ZD-08 and -10 excavation pits (cf. photo in Fig. 3.7) are close to the small fault offset, and maybe this is the cause of the high temperature. Calculated $\delta^{18}O_{water}$ compositions (Fig. 3.7B) indicate similar rhythmic fluctuations as found for temperature but variation of individual bands is not able to be discriminated within error. Nevertheless, the median water composition for the zebra population is -2.8‰.

Although these few data are preliminary, they offer an indication that, in fact, temperature and $\delta^{18}O_{water}$ do fluctuate between the formation of the fine-grained dolomite wallrock and the coarse-grained baroque dolomite 'stripes'. If, as postulated by Davies and Smith (2006), there is a pressure drop which is responsible for the formation of the coarse-grained zebra 'stripes', there is apparently also a concomitant drop in T, a dP/dT. Such a change in temperature contrasts with one model that calls for isothermal boiling to form saddle dolomites in MVT deposits in the Tri-State district (Leach et al., 1991). Since zebra dolomite predates ore minerals at Kennecott, this drop in temperature to form the 'stripes' may have been the beginning of falling temperatures that is observed in both sulfide mineralogy (MacKevett et al., 1997) and in the rest of the clumped isotope dataset, particularly for syngenetic calcite veins and breccia matrices.

3.5. Acknowledgements

I would like to thank Nami Kitchen, lab manager at Caltech for her help facilitating this study. I would also like to thank the past and present Eiler "clumptime" lab group and associates,

including Nithya Thiaragajan, Max Lloyd, Kristen Bergmann, Katie Snell, Sebastian Kopf, Alison Piasecki, and Renata Cummins for their help in the lab and with data processing.

3.6. References Cited

Bateman, A.M., and McLaughlin, D.H., 1920, Geology of the ore deposits of Kennecott, Alaska. Economic Geology, v. 15, p. 1-80.

Bateman, A.M., and Lasky, S.G., 1932, Covellite-chalcocite solid solution and exsolution. Economic Geology, v. 27, p. 52-86.

Beiersdorfer, R.E., and Day, H.W., 1995, Mineral paragenesis of pumpellyite, in: Schiffman, P., and Day, H.W., eds., Low-Grade Metamorphism of Mafic Rocks, Geological Society of America Special Paper 296, p. 5-27.

Davies, G.R., and Smith, L.B., Jr., 2006, Structurally controlled hydrothermal dolomite reservoir facies: An overview: AAPG Bulletin, v. 90, p. 1641–1690, doi: 10.1306/05220605164.

Diehl, S. F., Hofstra, A. H., Koenig, A. E., Emsbo, P., Christiansen, W., and Johnson, C., 2010, Hydrothermal zebra dolomite in the Great Basin, Nevada—attributes and relation to Paleozoic stratigraphy, tectonics, and ore deposits. Geosphere, v. 6, p. 663-690. doi: 10.1130/GES00530.1

Eiler, J.M., 2011, Paleoclimate reconstruction using carbonate clumped isotope thermometry, Quaternary Science Reviews, v. 30, p. 3575-3588.

Emsbo, P., Hofstra, A.H., Lauha, E.A., Griffin, G.L., and Hutchinson, R.W., 2003, Origin of high-grade gold ore, source of ore fluid components, and genesis of the Meikle and neighboring Carlin-type deposits, northern Carlin Trend, Nevada: Economic Geology, v. 98, p. 1069–1105.

Friedman, I., and O'Neil, J. R., 1977, Data of geochemistry: Compilation of stable isotope fractionation factors of geochemical interest. U.S. Geological Survey Professional Paper Vol. 440-K. US Government Printing Office.

Ghosh, P., Adkins, J., Affek, H., Balta, B., Guo, W., Schauble, E.A., Schrag, D., and Eiler, J.M., 2006, 13C-18O bonds in carbonate minerals: A new kind of paleothermometer, Geochimica et Cosmochimica Acta, v. 70, p. 1439-1456.

Hitzman, M. W., and Large, D., 1986, A review and classification of the Irish carbonate-hosted base metal deposits. Geology and genesis of mineral deposits in Ireland: Dublin, Irish Association for Economic Geology, p. 217-238.

Huntington, K.W., Eiler, J.M., Affek, H.P., Guo, W., Bonifacie, M., Yeung, L.Y., Thiagarajan, N., Passey, B., Tripati, A., Daëron, M., and Came, R., 2009, Methods and limitations of 'clumped' CO2 isotope (Δ47) analysis by gas-source isotope ratio mass spectrometry, Journal of Mass Spectrometry, v. 44, p. 1318-1329.

Kim, S.T., Mucci, A., and Taylor, B.E., 2007, Phosphoric acid fractionation factors for calcite and aragonite between 25 and 75°C: Revisited. Chemical Geology, v. 246, p. 135-146.

Kim, S.T, and O'Neil, J.R., 1997, Equilibrium and nonequilibrium oxygen isotope effects in synthetic carbonates: Geochimica et Cosmochimica Acta, v. 61, p. 3461-3475.

Leach, D. L., Plumlee, G. S., Hofstra, A. H., Landis, G. P., Rowan, E. L., and Viets, J. G., 1991, Origin of late dolomite cement by CO2-saturated deep basin brines: Evidence from the Ozark region, central United States. Geology, v. 19, p. 348-351.

Leach, D. L., Sangster, D. F., Kelley, K. D., Ross, R. L., Garven, G., and Allen, C. R., 2005, Sediment-hosted Pb-Zn deposits: A global perspective, *in*: Hedenquist, J.W., Thompson, J.F.H., Goldfarb, R.J., and Richards, J.P., eds. Economic Geology, 100th Anniversary Volume, p. 561-608.

MacKevett, E.M., Jr., 1970b, Geological map of the McCarthy C-5 quadrangle, Alaska: U.S. Geological Survey Geologic Quadrangle Map GQ-899, scale 1:63,360.

MacKevett, E.M., Jr., 1971, Stratigraphy and General Geology of the McCarthy C-5 Quadrangle, Alaska, U.S. Geological Survey Bulletin 1323, 35p.

MacKevett, E.M. Jr., Cox, D.P., Potter, R.W. II, and Silberman, M.L., 1997, Kennecott-type deposits in the Wrangell Mountains, Alaska: High-grade copper ores near a basalt-limestone contact: Economic Geology Monograph 9, p. 66-89.

McClelland, W.C., Gehrels, G.E., and Saleeby, J.B., 1992, Upper Jurassic-Lower Cretaceous basinal strata along the Cordilleran margin: Implications for the accretionary history of the Alexander-Wrangellia-Peninsular terrane, Tectonics, v. 11, p. 823-835.

Potter, R.W. II, 1977, An electrochemical investigation of the system copper-sulfur, Economic Geology, v. 72, p. 1524-1542.

Price, J.B., 2004, Structural controls and stable isotope geochemistry of mineralization and wallrock alteration at the Bonanza mine, Kennecott, Alaska, unpublished M.S. thesis, Colorado School of Mines, 222 p.

Price, J.B., Hitzman, M.W., Nelson, E.P., Humphrey, J.D., and Johnson, C.A., 2014, Wallrock Alteration, Sulfur Isotopic Variation of Sulfides, and Structural Control of the High-grade Copper Orebodies of the Kennecott District, Alaska: Economic Geology, v. 109, p. 581-620.

Ramdohr, P., 1980, The Ore Minerals and their Intergrowths, 2nd ed., Pergamon Press, New York, 1205 p.

Roseboom, E., 1966, An investigation of the system Cu-S and some natural copper sulfides between 25° and 700°C. Economic Geology, v. 61, p. 641-672.

Rosenbaum, J., and Sheppard, S.M.F., 1986, An isotopic study of siderites, dolomites, and ankerites at high temperatures, Geochimica et Cosmochimica Acta, v. 50, p. 1147-1150.

Schmidt, M., Xeflide, S., Botz, R., and Mann, S., 2005, Oxygen isotope fractionation during synthesis of CaMg-carbonate and implications for sedimentary dolomite formation: Geochimica et Cosmochimica Acta, v. 69, p. 4665-4674.

Silberman, M.L., MacKevett, E.M. Jr., Connor, C.L., Matthews, A., 1980, Metallogenic and tectonic significance of whole-rock potassium-argon ages of the Nikolai Greenstone, McCarthy quadrangle, Alaska, USGS Open-File Report 80-2019, p. 53-73.

Stolper, D.A. and Eiler, J.M., 2015, The kinetics of solid-state isotope-exchange reactions for clumped isotopes: A study of inorganic calcites and apatites from natural and experimental samples. American Journal of Science, v. 315, p. 363-411.

Swart, P.K., Burns, S.J., and Leder, J.J., 1991, Fractionation of the stable isotopes of oxygen and carbon in carbon dioxide during the reaction of calcite with phosphoric acid as a function of temperature and technique, Chemical Geology, v. 86, p. 89-96.

Trop, J.M., Ridgway, K.D., Manuszak, J.D., and Layer, P., 2002, Mesozoic sedimentary-basin development on the allocthonous Wrangellia composite terrane, Wrangell Mountains basin, Alaska: A long-term record of terrane migration and arc construction, Geological Society of America Bulletin, v. 114, p. 693-717.

Tukey, J.W., 1977, Exploratory Data Analysis (1st edition). Reading, Massachusetts, Addison-Wesley publishing company.

Winkler, G.R., MacKevett, E.M. Jr., Plafker, G., Richter, D.H., Rosenkrans, D.S., and Schmoll, H.R., 2000, A Geologic Guide to Wrangell-Saint Elias National Park and Preserve, Alaska, United States Geological Survey Professional Paper 1616, 166 p.

Appendix I.

Table of published thermochronological ages compiled for the Graubünden region

	system	sample	lon_WGS84	lat_WGS84	X_CH1903	Y_CH1903	Z_m	location	mineral	lithology	nappe	age	err	reference	relx	structZ_km	prof
1	AFT	AZ/BG/1	9.8711	47.0227	784804	210682	2254		apatite	Bilk-engrat gneis	Arosa	23.1	1.6	Knaus, 1990	22905.8	-0.50	1
2	AFT	AZ/G/1	9.8751	47.0285	785084	211332	2152		apatite	green-schist, ophiolite	Arosa	26.1	2.4	Knaus, 1990	23072.1	-0.53	1
3	AFT	AZ/PG/1	9.8891	47.0159	786194	209962	2091		apatite	Plaseg-gen granite	Arosa	23.0	1.9	Knaus, 1990	24397.1	-0.45	1
4	AFT	AZ/PG/2	9.8874	47.0125	786074	209582	2139		apatite	Plaseg-gen granite	Arosa	22.2	1.8	Knaus, 1990	24343.0	-0.44	1
5	AFT	KAW 0090	9.6965	46.4064	773505	141810	1819	Maloja Pass	apatite		Margna-Sella	15.0	1.5	Wagner et al., 1977	39850.2	1.12	5
6	AFT	KAW 0105	9.3691	46.3459	748508	134411	611	Truzzo	apatite		Tambo	10.2	1.0	Wagner et al., 1977	13956.0	-8.05	5
7	AFT	KAW 0145	9.2031	46.3348	735760	132881	696	Soazza	apatite		Adula	6.4	0.6	Wagner et al., 1977	1134.0	-12.00	5
8	AFT	KAW 0189	9.2275	46.3745	737540	137330	627	Soazza	apatite		Adula	7.1	0.7	Wagner et al., 1977	3649.1	-11.40	5
9	AFT	KAW 0224	9.8465	46.7196	783964	176946	1881	Sand	apatite	2-mica gneiss	Silvretta	14.4	1.4	Wagner et al., 1977	37756.0	1.60	3
10	AFT	KAW 0233	10.0935	46.7124	802861	176756	1553	Plattas	apatite		Silvretta	15.1	1.5	Wagner et al., 1977	56423.5	0.12	3
11	AFT	KAW 0328	9.7018	46.3838	773985	139310	1950	Lago di Cavloc	apatite		Margna-Sella	14.0	1.4	Wagner et al., 1977	39895.2	1.14	5
12	AFT	KAW 0775	9.7746	46.3783	779604	138860		Val Fex	apatite		Margna-Sella	14.7	1.5	Wagner et al. 1977	45354.3	3.35	5
13	AFT	KAW 0778	10.0001	46.4306	796752	145209	2168	Bernina	apatite		Err-Bernina	17.4	1.7	Wagner et al. 1977	72645.4	4.35	4
14	AFT	KAW 0778	10.0001	46.4306	796752	145209	2168	Bernina	apatite		Err-Bernina	17.4	1.7	Wagner et al. 1977	63335.7	8.78	5
15	AFT	KAW 1237	9.4253	46.5811	752168	160657	1130	Roffla	apatite		Suretta	14.0	0.4	Hunziker et al., 1992	25668.7	-6.60	4
16	AFT	KAW 1238	9.4237	46.5958	752008	162287	1022	Andeer	apatite		Suretta	12.4	0.6	Hunziker et al., 1992	25126.2	-6.90	4
17	AFT	KAW 1243	9.3567	46.4176	747359	142359	1755	Motta	apatite		Suretta	12.7	2.7	Hunziker et al., 1992	14183.7	-6.95	5
18	AFT	KAW 1246	9.3569	46.3857	747458	138810	1154	Prestone	apatite		Suretta	9.9	0.6	Hunziker et al., 1992	13674.6	-7.70	5
19	AFT	KAW 1247	9.3308	46.4032	745409	140710	1900	Prestone	apatite		Suretta	13.4	2.1	Hunziker et al., 1992	11980.3	-7.40	5
20	AFT	KAW 1379	9.4959	46.4179	758057	142660	1977	Val Madris	apatite		Suretta	14.6	3.2	Hunziker et al., 1992	24775.7	-3.50	5
21	AFT	KAW 1382	9.4397	46.4103	753758	141710	1966	Alpe Pian del Nido	apatite		Suretta	13.7	1.3	Hunziker et al., 1992	20377.2	-4.85	5
22	AFT	KAW 1383	9.3789	46.4029	749108	140760	1517	Fracisco	apatite		Suretta	11.4	1.6	Hunziker et al., 1992	15633.9	-6.72	5
23	AFT	KAW 2151	9.9592	46.9078	791903	198128	2457	Rot Büel	apatite	anatexite	Silvretta	25.3	2.1	Flisch, 1986	32021.1	1.25	1
24	AFT	KAW 2252	9.9650	46.7250	793003	177830	2871	Radünt	apatite	bt augen gneiss	Silvretta	28.9	2.4	Flisch, 1986	46523.0	2.00	3
25	AFT	KAW 2254	9.9717	46.7339	793483	178835	2683	Radünt	apatite	2-mica gneiss	Silvretta	25.6	1.7	Flisch, 1986	46829.7	1.90	3

26	AFT	KAW 2296	9.9712	46.8258	793113	189044	1814	Vereina	apatite	2-mica augen gneiss	Silvretta	17.1	1.4	Flisch, 1986	32685.5	1.10	2
27	AFT	KAW 2306	9.9521	46.8525	791558	191964	1339	Novai	apatite	2-mica augen gneiss	Silvretta	10.9	1.0	Flisch, 1986	30642.6	0.50	2
28	AFT	KAW 2413	9.9668	46.7628	793003	182035	3052	Flüela-Wiss-horn	apatite	2-mica augen gneiss	Silvretta	31.0	2.5	Flisch, 1986	33806.9	2.40	2
29	AFT	KAW 2415	10.1520	46.9554	806402	203903	1714	Vermunt	apatite	coarse granite gneiss	Silvretta	23.7	3.1	Flisch, 1986	45337.3	0.48	1
30	AFT	KAW 2466	10.1251	46.7139	805276	177006	2712	Munt Basel-gia	apatite	bt granite	Silvretta	31.1	2.1	Flisch 1986	58763.4	1.28	3
31	AFT	MR P 220	9.1798	46.6116	733285	163597	1303	Vals	apatite	sericite gneiss	Adula	8.6	1.4	Rahn, 2005	6628.2	-13.90	4
32	AFT	MR P 221	9.2004	46.5875	734920	160957	1670	Peil	apatite	ser chl orthog-neiss	Adula	5.0	1.6	Rahn, 2005	8843.0	-12.50	4
33	AFT	MR P 226	9.2045	46.4293	735630	143379	1217	Spina	apatite	fs-augen parag-neiss	Adula	6.8	2.0	Rahn, 2005	2803.0	-11.10	5
34	AFT	MR P 227	9.2368	46.4197	738140	142369	1307	Pian San Giacomo	apatite	ms-bt-chl parag-neiss	Tambo	5.3	0.9	Rahn, 2005	5102.6	-10.20	5
35	AFT	MR P 228	9.2332	46.3789	737970	137830	698	Castello Mesocco	apatite	two mica parag-neiss	Adula	4.6	1.0	Rahn, 2005	4158.3	-11.20	5
36	AFT	MR P 264	9.2132	46.3421	736520	133711	508	Soazza	apatite	light ms gneiss	Adula	5.8	1.0	Rahn, 2005	2024.7	-11.90	5
37	AFT	MR P 267	9.1776	46.3976	733640	139810	2073	Trescolmen	apatite	two-mica orthog-neiss	Adula	4.8	0.5	Rahn, 2005	231.5	-10.95	5
38	AFT	MU 10	9.7177	46.3700	775255	137810	2031	Plan Canin	apatite		Forno, Muretto	8.5	2.7	Ciancaleoni, 2005	40889.5	1.60	5
39	AFT	MW 237	9.8497	46.9172	783534	198903	2252		apatite	Verspala flysch	Arosa	12.8	2.2	Weh, 1998	23641.3	0.03	1
40	AFT	MW 319	9.8583	46.9775	783984	205632	2195		apatite	Ruchberg series	Grava	13.1	1.2	Weh, 1998	22949.5	-0.02	1
41	AFT	MW 320	9.8557	46.9926	783734	207302	1675		apatite	Bündner-schiefer	Grava	9.1	1.9	Weh, 1998	22421.5	-0.57	1
42	AFT	MW 322	9.7464	47.0349	775285	211751	2175		apatite	Ruchberg series	Grava	10.3	0.7	Weh, 1998	13342.9	-1.80	1
43	AFT	MW 96-1	9.8402	46.9781	782604	205652	1628		apatite	Bündner-schiefer	Grava	11.4	1.0	Weh, 1998	21586.1	-1.25	1

44	AFT	MW 96-4	9.5594	47.0087	761157	208432	796		apatite	Bündner-schiefer	Grava	5.6	0.8	Weh, 1998	-22.9	-4.80	1
45	AFT	MW 96-536	9.7656	46.8658	777305	193004	2427		apatite	Ruchberg series	Grava	5.9	0.7	Weh, 1998	16428.0	-0.25	2
46	AFT	MW 97-1	9.6029	47.0125	764457	208952	2345		apatite	Ruchberg series	Grava	6.7	1.1	Weh, 1998	3141.8	-2.90	1
47	AFT	MW 97-10	9.7350	46.8298	775085	188934	1730		apatite	Bündner-schiefer	Grava	8.5	0.8	Weh, 1998	14956.8	-1.25	2
48	AFT	MW 97-11	9.7257	46.8216	774405	188004	1463		apatite	Bündner-schiefer	Grava	6.3	0.5	Weh, 1998	14450.5	-1.55	2
49	AFT	MW 97-12	9.6751	46.8348	770506	189354	1348		apatite	Bündner-schiefer	Grava	3.7	0.5	Weh, 1998	10374.7	-2.70	2
50	AFT	MW 97-15	9.8227	46.9366	781414	201003	2290		apatite	Ruchberg series	Grava	12.1	0.7	Weh, 1998	21197.6	-0.62	1
51	AFT	MW 97-16	9.8248	46.9492	781534	202403	1805		apatite	Bündner-schiefer	Grava	6.6	1.4	Weh, 1998	21079.7	-1.10	1
52	AFT	MW 97-17	9.7832	46.9374	778405	201003	1305		apatite	Bündner-schiefer	Grava	4.3	0.5	Weh, 1998	18231.3	-1.95	1
53	AFT	MW 97-18	9.7691	46.9159	777405	198583	837		apatite	Bündner-schiefer	Grava	4.5	0.5	Weh, 1998	17653.9	-2.55	1
54	AFT	MW 97-2	9.6155	47.0130	765407	209032	2027		apatite	Ruchberg series	Grava	7.5	0.6	Weh, 1998	4064.6	-3.10	1
55	AFT	MW 97-3	9.6310	47.0079	766606	208502	1625		apatite	Ruchberg series	Grava	2.2	0.8	Weh, 1998	5336.6	-3.38	1
56	AFT	MW 97-5	9.7061	46.9546	772486	202733	703		apatite	Bündner-schiefer	Grava	3.4	0.5	Weh, 1998	12105.0	-3.40	1
57	AFT	MW 97-9	9.7235	46.8512	774145	191284	2462		apatite	Bündner-schiefer	Grava	6.8	1.3	Weh, 1998	13619.2	-0.85	2
58	AHe	08BP01	10.0277	46.4108	798944	143082	2332	Val Bernina	apatite		Bernina	26.8	1.6	Evans, 2011	75279.6	7.15	4,5
59	AHe	08BP03	9.9776	46.4436	794976	146600	2058	Val Bernina	apatite		Bernina	22.5	1.4	Evans, 2011	70590.1	6.70	4,5
60	AHe	08BP06	9.9238	46.4750	790734	149956	1838	Val Bernina	apatite		Bernina	16.9	1.0	Evans, 2011	65672.4	5.05	4,5
61	AHe	08BP10	9.9779	46.4632	794928	148778	2690	Val Bernina	apatite		Bernina	26.1	1.6	Evans, 2011	70026.8	6.75	4,5
62	AHe	08BP11	9.9796	46.4621	795063	148660	2578	Val Bernina	apatite		Bernina	26.5	1.6	Evans, 2011	70185.4	6.64	4,5
63	AHe	08ED01	9.7257	46.5459	775299	157371	2962	Jenatsch	apatite		Err	23.8	1.4	Evans, 2011	48918.2	2.06	4
64	AHe	08ED04	9.7252	46.5448	775264	157248	2881	Jenatsch	apatite		Err	24.4	1.5	Evans, 2011	48913.8	2.02	4
65	AHe	08ED06	9.7252	46.5454	775262	157314	2926	Jenatsch	apatite		Err	21.3	1.3	Evans, 2011	48896.0	2.04	4
66	AHe	08PN03	9.7914	46.5053	780470	153009	2840	Piz Nair	apatite		Err	24.5	1.5	Evans, 2011	54977.7	2.50	4
67	AHe	08PN04	9.7975	46.5047	780940	152957	2697	Piz Nair	apatite		Err	28.0	1.7	Evans, 2011	55446.7	2.42	4
68	AHe	08PN05	9.8044	46.5023	781478	152706	2620	Piz Nair	apatite		Err	21.8	1.3	Evans, 2011	56028.2	2.36	4
69	AHe	08TS04	10.2465	46.8227	814117	189415	2655	Engadine Window	apatite		Engadine Window	15.8	0.9	Evans, 2011	53298.5	-0.20	2
70	AHe	08TS05	10.2492	46.8230	814321	189456	2571	Engadine Window	apatite		Engadine Window	10.0	0.6	Evans, 2011	53492.8	-0.28	2
71	AHe	08TS08	10.2132	46.7723	811776	183726	1403	Engadine Window	apatite		Engadine Window	7.1	0.4	Evans, 2011	51992.0	-1.10	2
72	AHe	08TS09	10.2243	46.7861	812568	185289	1608	Engadine Window	apatite		Engadine Window	15.1	0.9	Evans, 2011	52498.0		2
73	AHe	08TS11	10.2398	46.7885	813742	185598	1614	Engadine Window	apatite		Engadine Window	8.1	0.5	Evans, 2011	53598.9	-1.20	2
74	AHe	10ED01	9.7453	46.5397	776821	156726	2430	Jenatsch	apatite		Err	16.1	1.0	Evans, 2011	50550.5	1.65	4

75	AHe	10ED03	9.7414	46.5421	776515	156984	2669	Jenatsch	apatite		Err	22.7	1.4	Evans, 2011	50191.3	1.88	4
76	AHe	10ED04	9.7426	46.5414	776609	156909	2618	Jenatsch	apatite		Err	26.2	1.6	Evans, 2011	50300.6	1.80	4
77	AHe	10ED05	9.7437	46.5395	776699	156700	2505	Jenatsch	apatite		Err	24.6	1.5	Evans, 2011	50438.2	1.75	4
78	AHe	10EN01	9.8246	46.4320	783265	144943	2699	Fuorcla Surlej	apatite		Corvatsch	20.5	1.2	Evans, 2011	59607.8	3.41	4,5
79	AHe	10EN03	9.8303	46.4408	783673	145934	2495	Fuorcla Surlej	apatite		Corvatsch	23.2	1.4	Evans, 2011	59768.8	3.35	4,5
80	AHe	10EN04	9.8273	46.4570	783388	147726	2392	Rosatsch	apatite		Corvatsch	23.5	1.4	Evans, 2011	59066.1	3.14	4,5
81	AHe	10EN08	9.8202	46.4626	782824	148332	2000	Rosatsch	apatite		Corvatsch	19.0	1.1	Evans, 2011	58374.5	2.85	4,5
82	AHe	10SL01	10.0608	46.9428	799511	202267	1620	Kromertal	apatite		Silvretta	15.6	0.9	Evans, 2011	38820.9	1.82	1
83	AHe	10SL02	10.0595	46.9350	799441	201398	1758	Kromertal	apatite		Silvretta	14.2	0.9	Evans, 2011	38898.8	2.05	1
84	AHe	10SL03	10.0626	46.9457	799637	202594	1527	Kromertal	apatite		Silvretta	16.7	1.0	Evans, 2011	38890.2	1.80	1
85	AHe	10SL04	10.0442	46.9214	798327	199848	2033	Kromertal	apatite		Silvretta	18.2	1.1	Evans, 2011	38062.2	2.38	1
86	AHe	10SL05	10.0401	46.9109	798053	198671	2141	Kromertal	apatite		Silvretta	14.8	0.9	Evans, 2011	37991.3	2.40	1
87	AHe	10SL06	10.0399	46.9042	798063	197926	2260	Kromertal	apatite		Silvretta	16.5	1.0	Evans, 2011	38126.3	2.42	1
88	AHe	10SL07	10.0414	46.9002	798192	197486	2353	Gross See-horn	apatite		Silvretta	13.1	0.8	Evans, 2011	38327.8	2.50	1
89	AHe	10SL08	10.0321	46.8944	797505	196818	2634	Gross See-horn	apatite		Silvretta	17.4	1.0	Evans, 2011	37763.4	2.73	1
90	AHe	10SL09	10.0308	46.8935	797409	196715	2706	Gross See-horn	apatite		Silvretta	19.4	1.2	Evans, 2011	37686.5	2.75	1
91	AHe	110825-03	9.8031	46.4125	781678	142728	2761	Furtschellas	apatite	S-C my-lonite	Corvatsch	21.8	3.3	Price, 2016	48059.9	4.50	5
92	AHe	110825-14	9.8164	46.4114	782701	142639	3221	PizCorvatsch	apatite	S-C myl, augen gneiss	Corvatsch	22.0	1.8	Price, 2016	49052.5	5.25	5
93	AHe	110826-08	9.7941	46.4073	781002	142123	2571	Alp Munt	apatite	orthog-neiss	Sella	34.3	7.2	Price, 2016	47290.3	4.00	5
94	AHe	110830-03	9.8801	46.3689	787744	138064	3366	Fuorcla da la Sella	apatite	quartz diorite	Bernina	19.1	2.3	Price, 2016	53238.1	6.60	5
95	AHe	110830-11	9.8832	46.3712	787975	138321	3721	Piz Roseg, Pt. 3719	apatite	monzo-diorite	Bernina	22.8	4.2	Price, 2016	53509.6	7.10	5
96	AHe	110831-02	9.8856	46.3742	788154	138663	3847	Piz Roseg near summit	apatite	monzo-diorite	Bernina	15.2	1.8	Price, 2016	53744.5	7.40	5
97	KArAm		9.7099	46.4256	774475	143975	2124	Grevasalvas	glauco-phane		Platta	59.4	7.4	Hunziker, 1992	41176.6	1.80	5
98	KArAm		9.7899	46.3860	780750	139750	2124	Val Fex	hbl		Margna-Sella	103.0	6.0	Hunziker, 1992	46635.8	3.45	5
99	KArAm		9.7225	46.4259	775443	144034	2020	Grevasalvas	richterite	Na-Ca-Mg am-phibole	Platta	62.3	0.5	Philipp, 1982	42140.4	2.00	5
100	KArAm		9.7256	46.4262	775682	144071	1975	Grevasalvas	rieb-Mg		Platta	80.5	1.3	Philipp, 1982	42382.2	2.03	5
101	KArAm		9.7256	46.4262	775682	144071	1975	Grevasalvas	rieb-Mg		Platta	84.3	1.3	Philipp, 1982	42382.2	2.03	5
102	KArAm		9.6634	46.4124	770944	142396	2660	Piz dal Sasc	rieb-Mg		Platta	108.3	1.9	Philipp, 1982	37427.3	1.10	5
103	KArAm		9.6634	46.4124	770944	142396	2660	Piz dal Sasc	rieb-Mg		Platta	111.7	2.0	Philipp, 1982	37427.3	1.10	5
104	KArAm		9.6704	46.4149	771477	142694	2562	Piz Lunghin	rie-beckite		Platta	90.2	1.9	Philipp, 1982	38003.6	1.25	5
105	KArAm		9.7145	46.4289	774820	144347	2162	Plaun Grand	rieb-Mg		Platta	70.8	1.2	Philipp, 1982	41580.2	1.90	5
106	KArAm		9.7145	46.4289	774820	144347	2162	Plaun Grand	rieb-Mg		Platta	66.5	1.1	Philipp, 1982	41580.2	1.90	5

107	KArAm	RT16	9.6625	46.4112	770970	142410	2661		rie-beckite	blue am-phibole schist	Platta	72.4	0.9	Handy et al., 1996	37455.4	1.10	5
108	KArAm	RT48	9.6625	46.4113	770970	142420	2661		rie-beckite	blue am-phibole schist	Platta	68.2	2.5	Handy et al., 1996	37457.1	1.11	5
109	KArBi		9.9511	46.4545	792900	147750	2070	Bernina	bi-chl		Bernina	258.0	20.0	Hunziker 1992	68300.6	5.77	4,5
110	KArBi		9.9513	46.4545	792920	147750	2077	Bernina	bi-chl		Bernina	254.0	13.0	Hunziker 1992	68320.1	5.78	4,5
111	KArBi		9.9524	46.4545	793000	147750	2105	Bernina	biotite		Bernina	236.0	12.0	Hunziker 1992	68397.8	5.86	4,5
112	KArBi		9.9706	46.4258	794500	144600	2596	Bernina	biotite		Bernina	237.0	16.0	Hunziker 1992	70602.8	6.65	4,5
113	KArBi		9.9708	46.4257	794520	144600	2585	Bernina	bi-chl		Bernina	223.0	13.0	Hunziker 1992	70622.3	6.64	4,5
114	KArBi		10.0008	46.4314	796800	145300	2201	Stretta	biotite		Bernina	257.0	13.0	Hunziker 1992	72670.8	6.59	4,5
115	KArBi		9.7634	46.3600	778800	136800	2506	Val Fedoz	biotite		Avers Bündnersch	29.8	2.0	Hunziker 1992	44209.7	3.13	5
116	KArBi		9.7099	46.4256	774475	143975	2124	Grevasalvas	stilp-nomeln		Platta	63.4	1.0	Hunziker, 1992	41176.6	1.80	5
117	KArBi		9.9053	46.7925	788203	185188	1975		biotite		Silvretta	330.0	50.0	loc from Hunziker et al., 1992	28528.0	1.00	2
118	KArBi		9.9447	46.9126	790784	198624	2626		biotite		Silvretta	190.0	50.0	loc from Hunziker et al., 1992	30833.9	1.10	1
119	KArBi		9.9396	46.7177	791086	176959	2548		biotite		Silvretta	330.0	50.0	loc from Hunziker et al., 1992	44777.7	1.75	3
120	KArBi		9.9516	46.8705	791461	193960	2043		biotite		Silvretta	190.0	50.0	loc from Hunziker et al., 1992	32288.3	0.90	1
121	KArBi		9.9567	46.8521	791912	191929	1370		biotite		Silvretta	260.0	20.0	loc from Hunziker et al., 1992	30997.2	0.50	2
122	KArBi		9.9713	46.7434	793415	179896	2230		biotite		Silvretta	330.0	50.0	loc from Hunziker et al., 1992	34587.9	1.65	2
123	KArBi		9.9768	46.8191	793567	188318	1887		biotite		Silvretta	260.0	20.0	loc from Hunziker et al., 1992	33260.1	1.25	2
124	KArBi		10.0195	46.7823	796952	184331	2939		biotite		Silvretta	330.0	50.0	loc from Hunziker et al., 1992	37292.3	2.60	2
125	KArBi		10.1440	46.9460	805829	202837	1756		biotite		Silvretta	190.0	50.0	loc from Hunziker et al., 1992	44952.7	0.58	1
126	KArBi		10.0655	46.7231	800690	177868	1661		biotite		Silvretta	175.0	5.0	loc from Thoni, 1978	42105.7	1.45	2
127	KArBi		10.0655	46.7231	800690	177868	1661		biotite		Silvretta	175.0	5.0	loc from Thoni, 1978	54097.3	0.40	3
128	KArBi		9.8208	46.8381	781606	190049	2537	Totalp	phlogo-pite	pyrox-enite	Arosa	160.0	8.0	Peters and Stettler, 1987	21181.1	0.47	2

129	KArBi		10.1155	46.7769	804301	183980	1749		bi-chl	parag-neiss	Silvretta	172.4	5.3	Thoni, 1978	44588.8	0.95	2
130	KArBi		10.2571	46.9590	814383	204585	2599		biotite	fine-grained parag-neiss	Silvretta	167.8	5.3	Thoni, 1978	53089.5	0.33	1
131	KArBi	KAW105	9.3598	46.3271	747843	132302	968	Truzzo	biotite	gneiss	Tambo	29.0	0.0	Armstrong et al., 1966	12939.5	-8.00	5
132	KArBi	KAW145	9.2045	46.3242	735897	131706	441	Soazza	biotite	gneiss	Adula	17.5	0.0	Armstrong et al., 1966	1067.9	-12.20	5
133	KArBi	KAW145repl	9.1992	46.3200	735500	131230	426	Soazza	biotite	gneiss	Adula	17.0	0.0	Armstrong et al., 1966	595.4	-12.40	5
134	KArBi	KAW153	9.1483	46.5873	730930	160847	1919	Zervreila	biotite	gneiss	Bündner-schiefer	335.0	0.0	Armstrong et al., 1966	4992.7	-13.80	4
135	KArBi	KAW153repl	9.1406	46.5871	730343	160805	1841	Zervreila	biotite	gneiss	Bündner-schiefer	345.0	0.0	Armstrong et al., 1966	4433.1	-14.20	4
136	KArWM		9.1828	46.6137	733513	163833	1338		white mica	mylonite	Adula	33.5	0.8	Augenstein, 2012	6793.3	-13.70	4
137	KArWM		9.3188	46.3610	744600	136000	2079	Baccino del Truzzo	musco-vite	pegma-tite	Tambo	173.0	9.0	Hanson et al., 1966	10377.4	-7.75	5
138	KArWM		9.3107	46.3882	743900	139000	2377	Motto Alto	musco-vite	pegma-tite	Tambo	297.0	15.0	Hanson et al., 1966	10201.2	-7.50	5
139	KArWM		10.2257	46.3460	814414	136406	2370	Val Grosina	musco-vite	pegma-tite	Grosina	217.0	11.0	Hanson et al., 1966	91892.9	5.40	4
140	KArWM		10.0008	46.4314	796800	145300	2201	Stretta	musco-vite		Bernina	286.0	13.0	Hunziker 1992	72670.8	4.38	4
141	KArWM		10.0008	46.4314	796800	145300	2201	Stretta	musco-vite		Bernina	286.0	13.0	Hunziker 1992	63398.9	8.80	5
142	KArWM		9.7564	46.3781	778200	138800	2077	Val Fedoz	phengite		Avers Bünd.	67.4	2.8	Hunziker 1992	43960.9	2.60	5
143	KArWM		9.6957	46.4080	773440	141980	1833	Maloja Pass	musco-vite		Margna	240.0	10.0	Hunziker, 1992	39815.4	1.10	5
144	KArWM		9.6957	46.4080	773440	141980	1833	Maloja Pass	phengite		Margna	105.0	5.0	Hunziker, 1992	39815.4	1.10	5
145	KArWM		9.6978	46.4077	773600	141950	1816	Maloja Pass	musco-vite		Margna	270.0	10.0	Hunziker, 1992	39968.0	1.10	5
146	KArWM		9.6978	46.4077	773600	141950	1816	Maloja Pass	ms-pheng		Margna	119.0	5.0	Hunziker, 1992	39968.0	1.10	5
147	KArWM		9.6978	46.4077	773600	141950	1816	Maloja Pass	phengite		Margna	77.8	3.2	Hunziker, 1992	39968.0	1.10	5
148	KArWM		9.7759	46.3795	779700	139000	2348	Val Fex	phengite		Margna	63.4	2.6	Hunziker, 1992	45473.0	3.35	5
149	KArWM		9.7762	46.3795	779720	139000	2345	Val Fex	phengite		Margna	63.5	2.7	Hunziker, 1992	45492.7	3.35	5
150	KArWM		9.7874	46.3739	780600	138400	2117	Val Fex	phengite		Margna	61.2	2.6	Hunziker, 1992	46257.0	3.35	5
151	KArWM		9.7978	46.7777	780053	183283	1840		musco-vite		Silvretta	330.0	50.0	loc from Hunziker et al., 1992	20839.4	0.73	2
152	KArWM		9.9002	46.8022	787779	186246	1876		musco-vite		Silvretta	330.0	50.0	loc from Hunziker et al., 1992	27925.4	0.85	2
153	KArWM		9.9363	46.9243	790107	199903	2260		musco-vite		Silvretta	330.0	50.0	loc from Hunziker et al., 1992	29950.9	0.65	1
154	KArWM		9.9677	46.7488	793124	180478	2558		musco-vite		Silvretta	330.0	50.0	loc from Hunziker et al., 1992	34199.2	1.95	2

155	KArWM		10.1361	46.9665	805152	205094	1991		musco-vite		Silvretta	190.0	50.0	loc from Hunziker et al., 1992	43904.7	1.00	1
156	KArWM		10.0581	46.7399	800055	179720	2438		white mica		Silvretta	275.0	5.0	loc from Thoni, 1978	41155.5	2.38	2
157	KArWM		9.4897	46.4787	757400	149400	1874	Grot-Avers	phengite	Triassic quartzite	Schams	38.4	1.6	Steinitz & Jager 1981	33424.1	-2.78	4
158	KArWM		9.4250	46.5971	752100	162430	1012	Andeer	phengite		Suretta	40.3	1.5	Steinitz and Jager, 1981	25181.8	-6.70	4
159	KArWM		9.4250	46.5971	752100	162430	1012	Andeer	phengite		Suretta	45.3	1.6	Steinitz and Jager, 1981	25181.8	-6.70	4
160	KArWM		9.4252	46.5971	752120	162430	1008	Andeer	phengite		Suretta	49.4	1.7	Steinitz and Jager, 1981	25201.2	-6.66	4
161	KArWM		9.3802	46.4041	749200	140900	1668	Frascicio	phengite		Suretta	40.7	1.4	Steinitz and Jager, 1981	15748.2	-6.45	5
162	KArWM		9.3804	46.4041	749220	140900	1684	Frascicio	phengite		Suretta	39.6	1.3	Steinitz and Jager, 1981	15767.9	-6.45	5
163	KArWM		9.4972	46.4191	758150	142800	1946	Madriser Tal	phengite		Suretta	165.1	5.6	Steinitz and Jager, 1981	24891.4	-3.58	5
164	KArWM		9.5063	46.4019	758900	140900	2043	Madriser Tal	phengite		Suretta	39.5	1.4	Steinitz and Jager, 1981	25305.2	-3.30	5
165	KArWM		9.4403	46.5691	753350	159350	1281	N Ausser Ferrera	phengite		Suretta	38.5	2.2	Steinitz and Jager, 1981	27127.4	-5.75	4
166	KArWM		9.4265	46.5824	752260	160800	1273	Roffla	phengite		Suretta	41.9	1.5	Steinitz and Jager, 1981	25724.3	-6.30	4
167	KArWM		9.4410	46.4125	753850	141950	2038	Val di Lei	phengite		Suretta	47.4	1.6	Steinitz and Jager, 1981	20509.3	-4.70	5
168	KArWM		10.1806	46.6556	809738	170672	1890		white mica	Eng-adiner dolomite	Scarl	89.4	2.9	Thoni, 1978	64214.0	3.55	3
169	KArWM		10.1893	46.6506	810426	170142	1826		white mica	Eng-adiner dolomite	Scarl	89.1	2.9	Thoni, 1978	64980.2	3.50	3
170	KArWM		10.2204	46.6503	812808	170195	2365		white mica	Eng-adiner dolomite	Scarl	85.0	2.7	Thoni, 1978	67319.8	4.05	3
171	KArWM		10.2644	46.6445	816194	169666	1995		white mica	Eng-adiner dolomite	Scarl	91.6	3.0	Thoni, 1978	70747.3	3.75	3
172	KArWM	110825-14	9.8164	46.4114	782701	142639	3221	Piz Corvatsch	white mica	S-C myl, augen gneiss	Corvatsch	50.0	0.6	Price, 2016	49052.5	5.25	5
173	KArWM	110830-03	9.8801	46.3689	787744	138064	3366	Fuorcla da la Sella	white mica	quartz diorite	Bernina	260.0	60.0	Price, 2016	53238.1	6.60	5
174	KArWM	130817-11	9.8663	46.9317	784845	200707	2720	Madrisa ridge	white mica	granitoid	Silvretta	250.0	20.0	Price, 2016	24628.9	0.23	1
175	KArWM	130818-04	9.7755	46.9281	777945	200099	902	Küblis, Schaniela-bach	white mica	Gyren-spitz, grey psam-mite	Prattigau	299.0	5.0	Price, 2016	17930.4	-2.45	1
176	KArWM	130819-07	9.6192	46.4063	767659	141773	2547	Val Turba, TMZ -45 m	white mica	meta-pelite	Avers	37.7	1.1	Price, 2016	34084.3	-0.04	5
177	KArWM	130819-08	9.6196	46.4079	767682	141942	2514	Val Turba, TMZ +98 m	white mica	spilite	Platta	61.9	1.7	Price, 2016	34135.9	0.10	5

178	KArWM	130819-08b	9.6196	46.4079	767682	141942	2514	Val Turba, TMZ +98 m	white mica	spilite	Platta	62.6	1.2	Price, 2016	34135.9	0.10	5
179	KArWM	130823-03	9.6759	46.4154	771989	142906	2446	Piz Lunghin	white mica	augen gneiss	Margna	87.0	6.0	Price, 2016	38544.3	1.26	5
180	KArWM	Alp0502	9.6872	46.4195	772749	143238	2438		white mica		Margna	71.0	5.0	Augenstein, 2012	39349.9	1.50	5
181	KArWM	Alp0504	9.6849	46.4070	772617	141849	1930		white mica		Margna	72.0	5.0	Augenstein, 2012	38981.9	0.93	5
182	KArWM	Alp0581	9.4755	46.4901	756279	150646	1666		white mica		Suretta	39.0	0.2	Augenstein, 2012	32039.0	-3.60	4
183	KArWM	AS5	9.6706	46.5335	771116	155873	2541		illite	Arlberg Fm	Carungas	89.3	0.7	Ferriero-Mahlmann, 2001	45210.7	1.45	4
184	KArWM	HM1c	9.6963	46.4583	773420	147710	2197		white mica	meta-radiolarite, S2	Err	70.3	0.5	Handy et al., 1996	49387.2	1.51	4,5
185	KArWM	J15	9.6798	46.5391	771804	156513	2607		illite	radiolarite	Platta	140.1	1.3	Ferriero-Mahlmann, 2001	45727.0	1.57	4
186	KArWM	J62a	9.6474	46.5065	769420	152817	2034		illite	radiolarite, F2 foliation	Platta	69.3	1.5	Ferriero-Mahlmann, 2001	44288.7	0.88	4
187	KArWM	KS100	9.6856	46.5432	772236	156977	3020		illite	Carungas Fm	Carungas	105.1	0.9	Ferriero-Mahlmann, 2001	46036.6	2.00	4
188	KArWM	Lep0937	9.6279	46.4113	768218	142207	2520		white mica		Platta	92.0	5.0	Augenstein, 2012	34709.7	0.13	5
189	KArWM	Lep0941	9.6201	46.4052	767641	141504	2474		white mica		Bündner-schiefer	34.0	2.0	Augenstein, 2012	34020.2	-0.09	5
190	KArWM	MH101	9.6860	46.4515	772650	146940	2272		white mica	meta-radiolarite, S2	Err	79.7	2.4	Handy et al., 1996	48822.1	1.46	4,5
191	KArWM	MH95	9.6960	46.4577	773400	147650	2250		white mica	meta-radiolarite, S1	Err	76.1	2.3	Handy et al., 1996	49382.1	1.57	4,5
192	KArWM	MH96	9.6932	46.4527	773200	147080	2266		white mica	meta-radiolarite, S1	Err	89.1	2.7	Handy et al., 1996	49323.1	1.54	4,5
193	KArWM	MH98	9.6894	46.4511	772910	146900	2238		white mica	meta-radiolarite, S2	Err	67.5	2.0	Handy et al., 1996	49084.2	1.44	4,5
194	KArWM	RS127	9.6809	46.5952	771708	162753	2540		illite	Raibler Fm, F2 foliation	Ela	98.2	2.2	Ferriero-Mahlmann, 2001	44152.0	1.32	4
195	RbSrBi	10c	9.9266	46.8670	789564	193513	1530		biotite	quartz mica schist	Austroalpine	175.0	28.0	Bachmann et al., 2009	28407.4	0.45	2
196	RbSrBi	KAW105	9.3598	46.3271	747843	132302	968	Truzzo	biotite	gneiss	Tambo	25.0	1.0	Armstrong et al., 1966	12939.5	-8.00	5
197	RbSrBi	KAW105repl	9.3598	46.3271	747843	132302	968	Truzzo	biotite	gneiss	Tambo	25.3	1.0	Armstrong et al., 1966	12939.5	-8.00	5
198	RbSrBi	KAW145	9.2045	46.3242	735897	131706	441	Soazza	biotite	gneiss	Tambo	18.5	1.6	Armstrong et al., 1966	1067.9	-12.20	5
199	RbSrBi	KAW145repl	9.1992	46.3200	735500	131230	426	Soazza	biotite	gneiss	Tambo	18.3	1.6	Armstrong et al., 1966	595.4	-12.40	5

200	RbSrBi	KAW153	9.1483	46.5873	730930	160847	1919	Zervreila	biotite	gneiss	Bündner-schiefer	175.0	7.0	Armstrong et al., 1966	4992.7	-13.80	4
201	RbSrWM		10.2243	46.3448	814312	136267	2365	Val Grosina	musco-vite		Grosina	252.0	25.0	Hanson et al., 1966	91827.3	5.40	4
202	RbSrWM		9.4237	46.5958	752008	162287	1022	Andeer	phengite		Suretta	38.0	4.8	Steinitz and Jager, 1981	25126.2	-6.90	4
203	RbSrWM		9.4240	46.5958	752028	162287	1023	Andeer	phengite		Suretta	37.3	4.5	Steinitz and Jager, 1981	25145.7	-6.80	4
204	RbSrWM		9.3789	46.4029	749108	140760	1518	Frascicio	phengite		Suretta	31.1	5.4	Steinitz and Jager, 1981	15634.0	-6.72	5
205	RbSrWM		9.3789	46.4029	749108	140760	1518	Frascicio	phengite		Suretta	30.7	9.7	Steinitz and Jager, 1981	15634.0	-6.72	5
206	RbSrWM		9.4884	46.4774	757307	149259	1751	Grot-Avers	phengite		Suretta	39.3	2.9	Steinitz and Jager, 1981	33367.6	-2.95	4
207	RbSrWM		9.4959	46.4179	758057	142659	1977	Madriser Tal	phengite		Suretta	39.3	11.4	Steinitz and Jager, 1981	24776.0	-3.50	5
208	RbSrWM		9.5050	46.4006	758807	140760	1995	Madriser Tal	phengite		Suretta	22.8	0.7	Steinitz and Jager, 1981	25189.7	-3.35	5
209	RbSrWM		9.4390	46.5678	753258	159207	1260	N Ausser Ferrera	phengite		Suretta	35.2	1.1	Steinitz and Jager, 1981	27071.6	-5.90	4
210	RbSrWM		9.4253	46.5811	752168	160657	1130	Roffla	phengite		Suretta	35.2	2.7	Steinitz and Jager, 1981	25668.9	-6.60	4
211	RbSrWM		9.4397	46.4113	753757	141810	1973	Val di Lei	phengite		Suretta	45.5	2.7	Steinitz and Jager, 1981	20394.1	-4.85	5
212	RbSrWM	4d	9.8746	46.9811	785214	206063	2211		white mica	mylonite	Austroal-pine	303.0	17.0	Bachmann et al., 2009	24089.0	0.20	1
213	RbSrWM	B11	9.8020	46.3955	781654	140830	2644		white mica	quartz mylonite	Austroal-pine	48.6	0.7	Bachmann et al., 2009	47711.0	4.30	5
214	RbSrWM	B13	9.7840	46.4091	780224	142300	2427		white mica	quartz mica schist	Platta	57.7	4.9	Bachmann et al., 2009	46554.0	3.80	5
215	RbSrWM	B14	9.7821	46.4127	780064	142700	2456		white mica	calcmy-lonite	Platta	54.2	1.3	Bachmann et al., 2009	46464.5	3.70	5
216	RbSrWM	B32	9.7901	46.4113	780684	142559	2707		white mica	calcsili-cate	Platta	47.1	0.4	Bachmann et al., 2009	47051.5	4.18	5
217	RbSrWM	B8	9.7901	46.4113	780684	142559	2707		white mica	sf-par-allel qz mobili-zate	Platta	49.2	8.6	Bachmann et al., 2009	47051.5	4.18	5
218	RbSrWM	C12	9.7292	46.4288	775945	144370	1920		white mica	quartz mica schist	Austroal-pine	59.9	3.4	Bachmann et al., 2009	42692.0	1.98	5
219	RbSrWM	C15	9.7203	46.4221	775284	143600	1895		white mica	quartz mica green-schist	Platta	53.9	0.6	Bachmann et al., 2009	41909.7	1.75	5
220	RbSrWM	C5	9.6874	46.4923	772535	151329	2597		white mica	Permian meta-volcanics	Austroal-pine	48.3	9.3	Bachmann et al., 2009	47668.4	1.76	4
221	RbSrWM	J91	10.1642	46.8714	807651	194604	2400		white mica	gneiss	Austroal-pine	192.0	30.0	Bachmann et al., 2009	48137.8	0.50	1
222	ZFT		9.6133	46.7707	765988	182103	2257		zircon		Arosa	111.0	0.0	loc from Weh, 1998	19174.3	0.90	3
223	ZFT		9.6401	46.7883	767978	184114	2529		zircon		Arosa	97.0	0.0	loc from Weh, 1998	8805.8	0.25	2
224	ZFT		9.6476	46.7752	768592	182674	2044		zircon		Arosa	174.0	0.0	loc from Weh, 1998	21647.0	0.60	3
225	ZFT		9.9000	46.8689	787536	193660	1371		zircon		Arosa	128.0	0.0	loc from Weh, 1998	26385.5	0.25	2

226	ZFT	110823-06	9.6771	46.4168	771981	142925	2454	Piz Lunghin	zircon	augen gneiss	Margna	74.6	10.2	Price, 2016	38539.7	1.28	5
227	ZFT	110826-08	9.7941	46.4073	781002	142123	2571	Alp Munt	zircon	orthog-neiss	Sella	58.0	11.4	Price, 2016	47290.3	4.00	5
228	ZFT	110831-02	9.8856	46.3742	788154	138663	3847	Piz Roseg near summit	zircon	monzo-diorite	Bernina	53.4	7.5	Price, 2016	53744.5	7.40	5
229	ZFT	130819-06	9.6194	46.4066	767676	141807	2538	Val Turba, TMZ -12 m	zircon	grey	Avers	35.5	11.7	Price, 2016	34106.8	-0.02	5
230	ZFT	KAW 0224	9.8465	46.7196	783964	176946	1881	Sand	zircon	2-mica gneiss	Silvretta	184.0	15.0	Flisch, 1986	37756.0	1.60	3
231	ZFT	KAW 0231	10.0955	46.7126	803016	176786	1650	Plattas	zircon	granitic 2-mica gneiss	Silvretta	60.2	3.9	Flisch, 1986	56571.3	0.22	3
232	ZFT	KAW 1237	9.4253	46.5811	752168	160657	1130	Roffla	zircon		Suretta	22.1	1.4	Hunziker et al., 1992	25668.7	-6.60	4
233	ZFT	KAW 1238	9.4237	46.5958	752008	162287	1022	Andeer	zircon		Suretta	21.8	0.2	Hunziker et al., 1992	25126.2	-6.90	4
234	ZFT	KAW 1243	9.3567	46.4176	747359	142359	1755	Motta	zircon		Suretta	21.3	1.5	Hunziker et al., 1992	14183.7	-6.95	5
235	ZFT	KAW 1247	9.3308	46.4032	745409	140710	1900	Prestone	zircon		Suretta	18.1	1.2	Hunziker et al., 1992	11980.3	-7.40	5
236	ZFT	KAW 2151	9.9592	46.9078	791903	198128	2457	Rot Büel	zircon	anatexite	Silvretta	105.0	8.0	Flisch, 1986	32021.1	1.25	1
237	ZFT	KAW 2154	9.9017	46.8281	787804	189134	1835	Münchalptal	zircon	anatexite, Rotbüel-granit	Silvretta	106.0	7.0	Flisch, 1986	27442.8	0.75	2
238	ZFT	KAW 2252	9.9650	46.7250	793003	177830	2871	Radünt	zircon	bt augen gneiss	Silvretta	161.0	12.0	Flisch, 1986	46523.0	2.00	3
239	ZFT	KAW 2254	9.9717	46.7339	793483	178835	2683	Radünt	zircon	2-mica gneiss	Silvretta	160.0	12.0	Flisch, 1986	46829.7	1.90	3
240	ZFT	KAW 2296	9.9712	46.8258	793113	189044	1814	Vereina	zircon	2-mica augen gneiss	Silvretta	78.0	5.0	Flisch, 1986	32685.5	1.10	2
241	ZFT	KAW 2305	10.1094	46.7620	803891	182305	1398	Lavin	zircon	2-mica granitic gneis	Silvretta	61.0	5.0	Flisch, 1986	44479.3	0.60	2
242	ZFT	KAW 2306	9.9521	46.8525	791558	191964	1339	Novai	zircon	2-mica augen gneiss	Silvretta	80.0	5.0	Flisch, 1986	30642.6	0.50	2
243	ZFT	KAW 2413	9.9668	46.7628	793003	182035	3052	Flüela-Wiss-horn	zircon	2-mica augen gneiss	Silvretta	156.0	12.0	Flisch, 1986	33806.9	2.40	2
244	ZFT	KAW 2415	10.1520	46.9554	806402	203903	1714	Vermunt	zircon	coarse granite gneiss	Silvretta	74.0	6.0	Flisch, 1986	45337.3	0.48	1
245	ZFT	KAW 2466	10.1251	46.7139	805276	177006	2712	Munt Basel-gia	zircon	bt granite	Silvretta	68.0	4.0	Flisch, 1986	58763.4	1.28	3
246	ZFT	KAW 2612	9.4338	46.7641	752308	181003	709	Rothenbrun-nen	zircon	marly schist	Bündner-schiefer	21.3	2.8	Michalski & Soom, 1990	5865.5	-3.50	3
247	ZFT	MU 10	9.7177	46.3700	775255	137810	2031	Plan Canin	zircon		Muretto Series	18.9	2.2	Ciancaleoni, 2005	40889.5	1.60	5

248	ZFT	MW 237	9.8497	46.9172	783534	198903	2252		zircon	Verspala flysch	Arosa	113.0	10.0	Weh 1998	23641.3	0.03	1
249	ZFT	MW 317	9.8757	46.9850	785279	206502	2067		zircon	Augeng-neiss	Silvretta	61.3	5.8	Weh, 1998	24079.1	0.01	1
250	ZFT	MW 318	9.8825	46.9831	785804	206302	2482		zircon	gneiss	Silvretta	74.2	3.9	Weh, 1998	24630.2	0.45	1
251	ZFT	MW 319	9.8583	46.9775	783984	205632	2195		zircon	Ruchberg series	Grava	119.0	23.0	Weh 1998	22949.5	-0.02	1
252	ZFT	MW 320	9.8557	46.9926	783734	207302	1675		zircon	Bündner-schiefer	Grava	91.8	9.0	Weh 1998	22421.5	-0.57	1
253	ZFT	MW 322	9.7464	47.0349	775285	211751	2175		zircon	Ruchberg	N Penninic	63.3	8.0	Weh, 1998	13342.9	-1.80	1
254	ZFT	MW 96-4	9.5594	47.0087	761157	208432	796		zircon	Bündner-schiefer	N Penninic	114.0	8.5	Weh, 1998	-22.9	-4.80	1
255	ZFT	MW 97-13	9.5871	46.8396	763782	189704	1107		zircon	Bündner-schiefer	N Penninic	24.9	5.8	Weh, 1998	3693.4	-4.45	2
256	ZFT	MW 97-7	9.6277	46.9502	766531	202078	1329		zircon	Bündner-schiefer	N Penninic	60.8	5.4	Weh, 1998	6346.6	-3.50	1
257	ZHe	08BP01	10.0277	46.4108	798944	143082	2332	Pso del Bernina	zircon		Bernina	32.5	2.6	Evans, 2011	75279.6	7.15	4,5
258	ZHe	08BP03	9.9776	46.4436	794976	146600	2058	Val Bernina	zircon		Bernina	34.8	2.8	Evans, 2011	70590.1	6.70	4,5
259	ZHe	08BP04	9.9897	46.4553	795863	147930	2180	Val Bernina	zircon		Bernina	33.4	2.7	Evans, 2011	71135.8	6.43	4,5
260	ZHe	08BP05	9.9884	46.4577	795754	148194	2227	Val Bernina	zircon		Bernina	36.3	2.9	Evans, 2011	70968.0	6.41	4,5
261	ZHe	08BP06	9.9238	46.4750	790734	149956	1838	Val Bernina	zircon		Bernina	39.7	3.2	Evans, 2011	65672.4	5.05	4,5
262	ZHe	08BP09	9.9774	46.4648	794884	148955	2752	Val Bernina	zircon		Bernina	35.0	2.8	Evans, 2011	69942.0	6.79	4,5
263	ZHe	08BP10	9.9779	46.4632	794928	148778	2690	Val Bernina	zircon		Bernina	33.9	2.7	Evans, 2011	70026.8	6.75	4,5
264	ZHe	08BP11	9.9796	46.4621	795063	148660	2578	Val Bernina	zircon		Bernina	36.0	2.9	Evans, 2011	70185.4	6.64	4,5
265	ZHe	08BP12	9.9858	46.4610	795543	148554	2360	Val Bernina	zircon		Bernina	34.9	2.8	Evans, 2011	70676.9	6.46	4,5
266	ZHe	08ED01	9.7257	46.5459	775394	157513	2979	Jenatsch	zircon		Err	31.9	2.6	Evans, 2011*	48977.1	2.20	4
267	ZHe	08ED02	9.7222	46.5455	775127	157461	2981	Jenatsch	zircon		Err	49.6	4.0	Evans, 2011	48730.1	2.10	4
268	ZHe	08ED04	9.7252	46.5454	775368	157482	2876	Jenatsch	zircon		Err	55.0	4.4	Evans, 2011	48959.2	2.05	4
269	ZHe	08ED06	9.7252	46.5454	775357	157456	2935	Jenatsch	zircon		Err	54.1	4.3	Evans, 2011	48954.7	2.11	4
270	ZHe	08FA05	9.6821	46.5629	771997	159305	2583	Val d'Err	zircon		Err	61.2	4.9	Evans, 2011	45251.8	1.40	4
271	ZHe	08FA06	9.6820	46.5635	771893	159230	2579	P. d'Err	zircon		Err	37.9	3.0	Evans, 2011	45168.5	1.49	4
272	ZHe	08FA07	9.6816	46.5660	771854	159507	2529	P. d'Err	zircon		Err	44.9	3.6	Evans, 2011	45065.2	1.40	4
273	ZHe	08FA17	9.7290	46.4727	775789	149246	2299	Julierpaß	zircon		Julier	37.8	3.0	Evans, 2011	51324.0	2.13	4,5
274	ZHe	08IGT01	10.2633	46.4082	817056	143418	2594	Val Grosina	zircon		Grosina	52.2	4.2	Evans, 2011	92794.7	5.60	4
275	ZHe	08IGT02	10.2534	46.3869	816381	141025	1918	Val Grosina	zircon		Grosina	46.6	3.7	Evans, 2011	92706.6	5.10	4
276	ZHe	08IGT03	10.2527	46.3858	816331	140901	1909		zircon		Campo	30.7	2.5	Evans, 2011	92688.1	5.10	4
277	ZHe	08IGT04	10.2494	46.3628	816169	138337	1513		zircon		Campo	35.6	2.9	Evans, 2011	93139.4	4.73	4
278	ZHe	08PN02	9.7871	46.5059	780234	153207	3025	Piz Nair	zircon		Err	77.7	6.2	Evans, 2011	54701.2	2.60	4
279	ZHe	08PN03	9.7914	46.5053	780566	153151	2850	Piz Nair	zircon		Err	55.8	4.5	Evans, 2011	55037.0	2.50	4
280	ZHe	08PN04	9.7975	46.5047	781036	153098	2697	Piz Nair	zircon		Err	73.5	5.2	Evans, 2011	55506.1	2.40	4
281	ZHe	08PN05	9.8044	46.5023	781573	152847	2620	Piz Nair	zircon		Err	74.8	6.0	Evans, 2011	56087.3	2.38	4
282	ZHe	08PN06	9.8114	46.5026	782110	152897	2523	Piz Nair	zircon		Err	53.6	4.3	Evans, 2011	56597.1	2.25	4
283	ZHe	08TS04	10.2465	46.8227	814117	189415	2655	Engadine Window	zircon		Engadine Window	28.0	2.2	Evans, 2011	53298.5	-0.20	2
284	ZHe	08TS05	10.2492	46.8230	814321	189456	2571	Engadine Window	zircon		Engadine Window	31.8	2.5	Evans, 2011	53492.8	-0.28	2

285	ZHe	08TS07	10.2144	46.7783	811844	184396	1523	Engadine Window	zircon		Engadine Window	33.1	2.6	Evans, 2011	51941.4		2
286	ZHe	08TS08	10.2132	46.7723	811776	183726	1403	Engadine Window	zircon		Engadine Window	35.4	2.8	Evans, 2011	51992.0	-1.10	2
287	ZHe	08TS09	10.2243	46.7861	812568	185289	1608	Engadine Window	zircon		Engadine Window	26.0	2.1	Evans, 2011	52498.0		2
288	ZHe	08TS11	10.2398	46.7885	813742	185598	1614	Engadine Window	zircon		Engadine Window	28.8	2.3	Evans, 2011	53598.9	-1.20	2
289	ZHe	08TS13	10.2469	46.8326	814108	190516	2727	Engadine Window	zircon		Engadine Window	29.1	2.3	Evans, 2011	55191.8	-0.80	1
290	ZHe	08TS14	10.2476	46.8321	814163	190463	2678	Engadine Window	zircon		Engadine Window	24.4	2.0	Evans, 2011	55255.4	-0.81	1
291	ZHe	09EN01	10.0726	46.6773	801399	172803	1555	Ental	zircon		Engadine line	31.8	1.9	Evans, 2011	55636.9	0.15	3
292	ZHe	09EN04	10.2776	46.7886	816625	185713	1233	Engadine Window	zircon		Engadine Window	28.1	2.2	Evans, 2011	56417.7	-1.80	2
293	ZHe	10ED01	9.7453	46.5397	776917	156868	2425	Jenatsch	zircon		Err	41.2	2.9	Evans, 2011	50609.7	1.68	4
294	ZHe	10ED02	9.7380	46.5434	776345	157263	2760	Jenatsch	zircon		Err	41.5	2.9	Evans, 2011	49960.3	2.00	4
295	ZHe	10ED03	9.7414	46.5241	776668	155126	2689	Jenatsch	zircon		Err	44.8	3.1	Evans, 2011	50781.5	1.95	4
296	ZHe	10ED04	9.7426	46.5414	776704	157051	2626	Jenatsch	zircon		Err	57.5	4.6	Evans, 2011	50359.4	1.80	4
297	ZHe	10ED05	9.7437	46.5395	776795	156842	2502	Jenatsch	zircon		Err	39.5	3.2	Evans, 2011	50497.4	1.72	4
298	ZHe	10EN01	9.8246	46.4320	783265	144943	2699	Fuorcla Surlej	zircon		Corvatsch	30.1	2.4	Evans, 2011	59607.8	3.41	4,5
299	ZHe	10EN02	9.8280	46.4361	783512	145406	2595	Fuorcla Surlej	zircon		Corvatsch	31.1	2.5	Evans, 2011	59738.0	3.38	4,5
300	ZHe	10EN03	9.8303	46.4408	783673	145934	2495	Fuorcla Surlej	zircon		Corvatsch	29.5	2.4	Evans, 2011	59768.8	3.35	4,5
301	ZHe	10EN04	9.8273	46.4570	783388	147726	2392	Rosatsch	zircon		Corvatsch	29.9	2.4	Evans, 2011	59066.1	3.14	4,5
302	ZHe	10EN05	9.8260	46.4594	783280	147990	2291	Rosatsch	zircon		Corvatsch	33.9	2.7	Evans, 2011	58898.7	3.08	4,5
303	ZHe	10EN06	9.8287	46.4658	783466	148707	2215	Rosatsch	zircon		Corvatsch	36.5	2.9	Evans, 2011	58908.7	3.09	4,5
304	ZHe	10EN07	9.8249	46.4640	783180	148498	2104	Rosatsch	zircon		Corvatsch	30.4	2.4	Evans, 2011	58680.7	2.93	4,5
305	ZHe	10EN08	9.8202	46.4626	782824	148332	2000	Rosatsch	zircon		Corvatsch	27.2	1.9	Evans, 2011	58374.5	2.85	4,5
306	ZHe	10IGT01	10.2497	46.3877	816093	141104	2092	Val Grosina	zircon		Grosina	33.5	2.0	Evans, 2011	92408.6	5.20	4
307	ZHe	10IGT02	10.2539	46.3877	816416	141115	1934	Val Grosina	zircon		Grosina	37.8	2.3	Evans, 2011	92719.4	5.10	4
308	ZHe	10IGT03	10.2471	46.3733	815951	139497	1679		zircon		Campo	37.8	2.6	Evans, 2011	92651.7	4.85	4
309	ZHe	10IGT04	10.2516	46.3555	816368	137532	1449		zircon		Campo	33.3	2.7	Evans, 2011	93523.2	4.60	4
310	ZHe	10SL01	10.0608	46.9428	799511	202267	1620	Kromertal	zircon		Silvretta	53.5	4.3	Evans, 2011	38820.9	1.82	1
311	ZHe	10SL02	10.0595	46.9350	799441	201398	1758	Kromertal	zircon		Silvretta	43.8	3.5	Evans, 2011	38898.8	2.05	1
312	ZHe	10SL03	10.0626	46.9457	799637	202594	1527	Kromertal	zircon		Silvretta	46.1	3.7	Evans, 2011	38890.2	1.80	1
313	ZHe	10SL04	10.0442	46.9214	798327	199848	2033	Kromertal	zircon		Silvretta	47.6	3.8	Evans, 2011	38062.2	2.38	1
314	ZHe	10SL05	10.0401	46.9109	798053	198671	2141	Kromertal	zircon		Silvretta	43.9	3.5	Evans, 2011	37991.3	2.40	1
315	ZHe	10SL06	10.0399	46.9042	798063	197926	2260	Kromertal	zircon		Silvretta	52.1	4.2	Evans, 2011	38126.3	2.42	1
316	ZHe	10SL07	10.0414	46.9002	798192	197486	2353	Gross See-horn	zircon		Silvretta	59.4	4.7	Evans, 2011	38327.8	2.50	1
317	ZHe	10SL08	10.0321	46.8944	797505	196818	2634	Gross See-horn	zircon		Silvretta	60.8	4.9	Evans, 2011	37763.4	2.73	1
318	ZHe	10SL09	10.0308	46.8935	797409	196715	2706	Gross See-horn	zircon		Silvretta	47.9	3.8	Evans, 2011	37686.5	2.75	1
319	ZHe	10SL11	10.0578	46.9220	799359	199949	1868	Kromertal	zircon		Silvretta	44.9	3.6	Evans, 2011	39063.1	2.10	1
320	ZHe	110823-06	9.6771	46.4168	771981	142925	2454	Piz Lunghin	zircon	augen gneiss	Margna	37.3	NA	Price, 2016	38539.7	1.28	5
321	ZHe	110824-01	9.6827	46.4019	772458	141274	1655	Casaccia	zircon	white mica schist	Margna	23.6	0.4	Price, 2016	38727.0	0.55	5

322	ZHe	110825-03	9.8031	46.4125	781678	142728	2761	Furtschellas	zircon	S-C my-lonite	Corvatsch	42.2	NA	Price, 2016	48059.9	4.50	5
323	ZHe	110825-14	9.8164	46.4114	782701	142639	3221	Piz Cor-vatsch	zircon	S-C myl, augen gneiss	Corvatsch	37.3	NA	Price, 2016	49052.5	5.25	5
324	ZHe	110830-03	9.8801	46.3689	787744	138064	3366	Fuorcla da la Sella	zircon	quartz diorite	Bernina	38.2	NA	Price, 2016	53238.1	6.60	5
325	ZHe	130816-18A	9.8663	46.9317	784842	200710	2704	Rätschenjoch	zircon	chlo-ritized felsite	Tschirpen	42.2	3.1	Price, 2016	24625.5	0.22	1
326	ZHe	130817-03	9.8610	46.9333	784435	200874	2633	Rätschenjoch	zircon	Mandel-schiefer flysch	Falknis	44.3	5.4	Price, 2016	24196.6	0.10	1
327	ZHe	130817-11	9.8663	46.9317	784845	200707	2720	Madrisa ridge	zircon	gneissose granitoid	Silvretta	49.5	3.7	Price, 2016	24628.9	0.23	1
328	ZHe	130817-12	9.8687	46.9320	785030	200749	2734	Madrisahorn	zircon	gneissose granitoid	Silvretta	41.8	3.2	Price, 2016	24804.2	0.26	1
329	ZHe	130818-04	9.7755	46.9281	777945	200099	902	Kublis, Schaniela-bach	zircon	Gyren-spitz psam-mite	Prattigau	19.4	1.8	Price, 2016	17930.4	-2.45	1
330	ZHe	130819-06	9.6194	46.4066	767676	141807	2538	Val Turba, TMZ -12 m	zircon	phyllite	Avers	21.4	0.7	Price, 2016	34106.8	-0.02	5
331	ZHe	130819-08	9.6196	46.4079	767682	141942	2514	Val Turba, TMZ +98 m	zircon	spilite	Platta	25.7	1.2	Price, 2016	34135.9	0.10	5
332	ZHe	130819-09	9.6364	46.4157	768950	142851	2311	Septimer pass	zircon	spilite	Platta	22.8	1.6	Price, 2016	35540.7	0.22	5
333	ZHe	130821-07	9.5859	46.4499	764967	146545	2397	Juf	zircon	Val Gronda phyllite	Arblatsch	26.8	1.8	Price, 2016	32248.8	-0.78	5
334	ZHe	130823-03	9.6759	46.4154	771989	142906	2446	Piz Lunghin	zircon	augen gneiss	Margna	22.3	0.5	Price, 2016	38544.3	1.27	5
335	ZHe	AD15-01	9.1826	46.6085	733598	163402	1469	Vals	zircon	ms-gt schist	Adula	11.7	0.6	Price, 2016	6978.1	-13.58	4
336	ZHe	AD15-03	9.1807	46.6125	733440	163840	1317	Vals	zircon	ms-gt schist	Adula	12.3	1.2	Price, 2016	6720.7	-13.70	4
337	ZHe	ARB15-01	9.5768	46.5218	764050	154510	2566	Sponda Mut-tariel	zircon	psam-mite	Arblatsch	29.1	1.1	Price, 2016	38670.6	-0.20	4
338	ZHe	BD15-03	9.6193	46.5906	767098	162243	1631	Tinizong-Senslas	zircon	psam-mite	Arblatsch	27.5	1.8	Price, 2016	39795.3	-0.55	4
339	ZHe	BD15-07	9.5074	46.6155	758449	164781	2589	Curvér-Ziteil	zircon	phyllite	Bündner-schiefer	23.8	1.6	Price, 2016	30791.0	-3.30	4
340	ZHe	BD15-08	9.6346	46.5991	768246	163222	2278	Tsant Son Martegn	zircon	metap-sammite	Err-Bernina	44.3	3.3	Price, 2016	40678.0	0.33	4
341	ZHe	BD15-15	9.5679	46.9004	762226	196570	718	Trimmis	zircon		Bündner-schiefer	6.6	0.4	Price, 2016	957.3	-5.85	2
342	ZHe	DL15-02	9.8053	46.8292	780549	189175	2608	Weissfluh	zircon	chlo-ritized granitoid	Tschirpen	47.7	7.0	Price, 2016*	20293.6	0.32	2
343	ZHe	DL15-04	9.6762	46.8345	770683	189469	1313	Peist	zircon	Pläti-grat, sand-stone	Prattigau	20.9	1.2	Price, 2016	10529.1	-3.20	2

344	ZHe	DL15-05	9.6581	46.8331	769309	189273	1259	St. Peter	zircon	Pfävi-grat, sand-stone	Prattigau	22.7	2.5	Price, 2016	9210.8	-3.48	2
345	ZHe	JUL15-01	9.7255	46.4727	775615	149373	2294	Julier pass	zircon	granite	Julier granite	29.2	2.0	Price, 2016	43223.7	2.55	5
346	ZHe	KK15-02	9.8245	46.9545	781586	203142	1866	Eggberg, Vordersäss	zircon	Eggberg, grit-cgl	Prattigau	33.2	3.5	Price, 2016*	21005.8	-1.10	1
347	ZHe	KK15-05	9.8338	46.9539	782294	203093	2191	Eggberg, pt. 2248	zircon	Ruch-berg, gritstone	Prattigau	48.8	7.9	Price, 2016	21711.9	-0.65	1
348	ZHe	KK15-11	9.6980	46.9381	772013	201037	768	Pragmartin quarry	zircon	Pfävi-grat, phyllite	Prattigau	11.0	1.2	Price, 2016	11925.2	-3.40	1
349	ZHe	LEN15-03	9.6008	46.7429	765216	179131	2805	Parpaner Rothorn	zircon	augen gneiss	Silvretta	56.5	9.4	Price, 2016	18905.3	1.10	3
350	ZHe	LEN15-05	9.5523	46.7354	761530	178203	1492	Hwy 3, Igl Lai Heidsee	zircon	Ruch-berg, sand-stone	Tomül	20.4	1.1	Price, 2016	15424.2	-0.65	3
351	ZHe	PL15-07	9.6223	46.6003	767297	163336	1967	Savognin, Funtanga	zircon	meta-diorite	Platta	48.7	7.2	Price, 2016	39729.1	0.05	4
352	ZHe	SUR15-01	9.4716	46.6224	755690	165478	2350	Alp Taspegn, Pt. 2357	zircon	quartz eye por-phyry	Suretta	24.5	1.4	Price, 2016	27945.4	-4.50	4
353	ZHe	SUR15-02	9.4791	46.5434	756490	156716	2483	Piz Grisch, Spunda da l'Iva	zircon	gneissose granitoid	Suretta	20.4	1.1	Price, 2016	30803.0	-3.22	4
354	ZHe	SUR15-03	9.5084	46.4913	758896	150985	2642	Hureli, Pt. 2654	zircon	gneissose granitoid	Suretta	18.6	1.2	Price, 2016	34501.0	-1.70	4
355	ZHe	SUR15-04	9.3527	46.5623	746747	158574	1432	Road 13, Sufnersee	zircon	orthog-neiss	Tambo-Aruea	14.6	0.6	Price, 2016	20897.5	-8.08	4
356	ZHe	TSC15-01	9.6260	46.5970	767593	162976	2017	Savognin, Funtanga	zircon	chlo-ritized granitoid	Tschirpen	40.8	2.7	Price, 2016	40102.1	0.06	4

[This page was intentionally left blank.]

Appendix II.

Table of new thermochronologic ages

Appendix 2.1. Table of $^{40}Ar/^{39}Ar$ ages

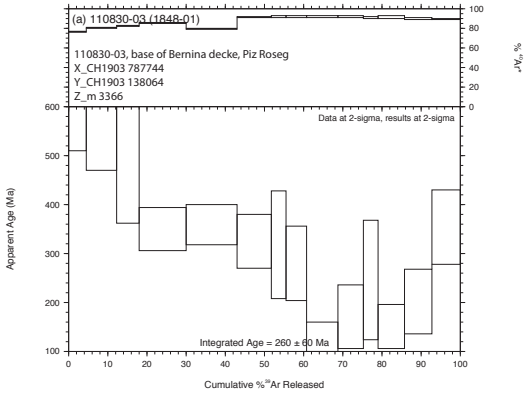

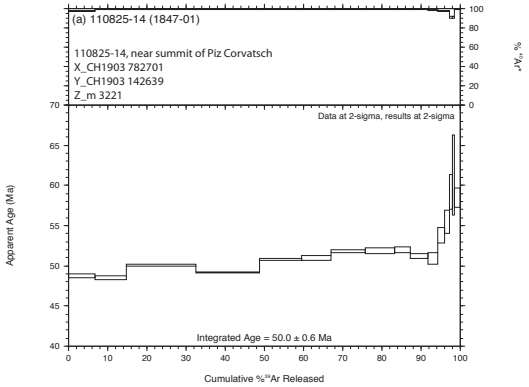

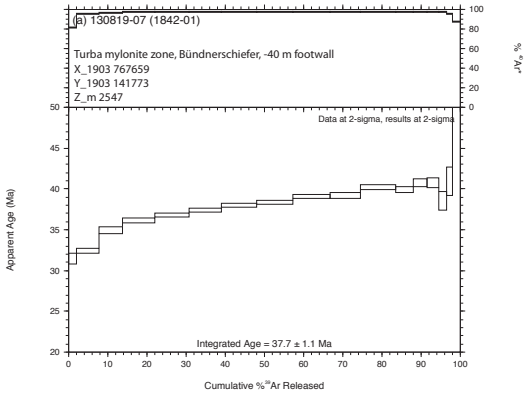

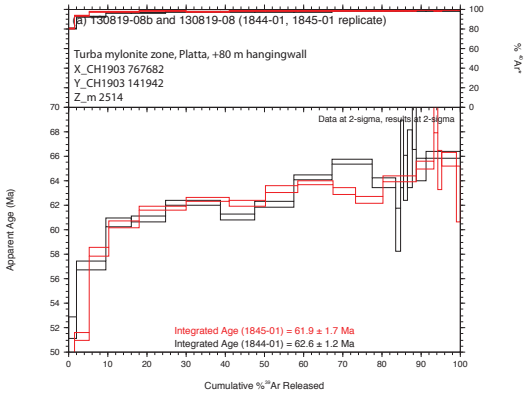

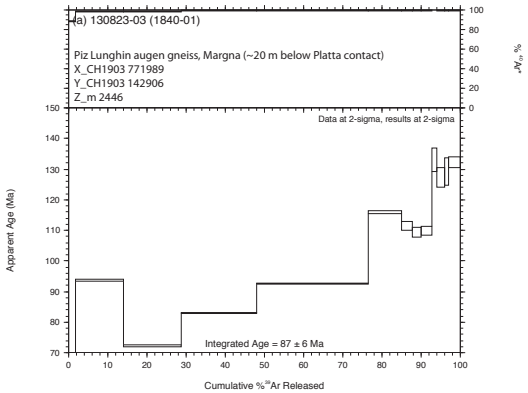

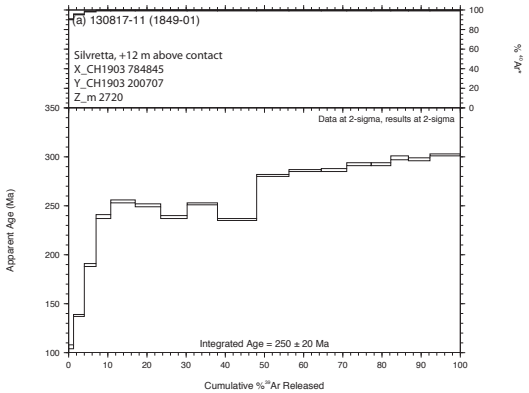

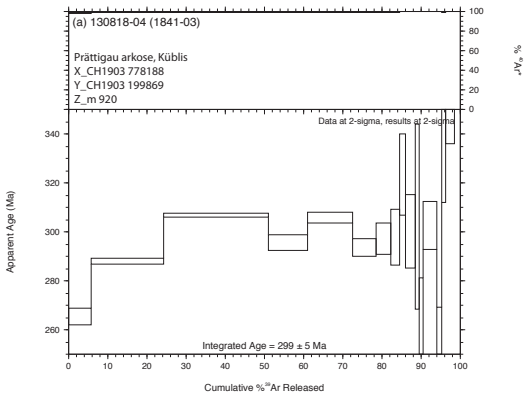

40/39 Argon analyses from Graubünden (Profiles 1, 4, 5 in Chapter 1). Measured at U.S. Geological Survey, Denver, Colorado with Mike Cosca.

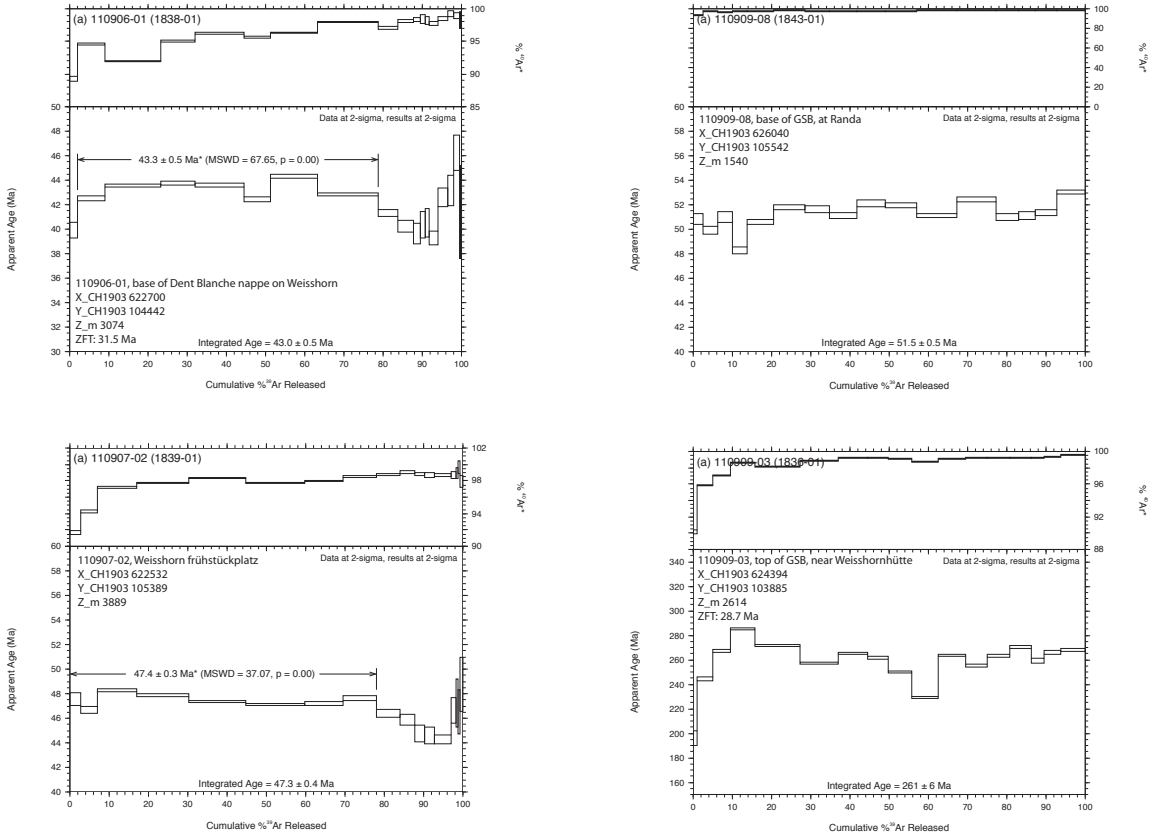

40/39 Argon analyses from Valais (Weisshorn traverse, unpublished). Measured at U.S. Geological Survey, Denver, Colorado with Mike Cosca.

						Relative Isotopic Abundances (fA)								Derived Results								Inverse Isochron Data					
Lab ID#	Sample	Material	Pwr_Achieved (W)	Irrad.	J x 10e-5	J_err (±1σ)	40Ar	40Ar_err (±1σ)	39Ar	39Ar_err (±1σ)	38Ar	38Ar_err (±1σ)	37Ar	37Ar_err (±1σ)	36Ar	36Ar_err (±1σ)	39Ar x 10e-18 (mol)	39Ar cum% of total	Ca/K	Ca/K_err (±1σ)	40Ar*/39Ar	40Ar*/39Ar_err (±1σ)	%40Ar*	Age (Ma)	Age_err (±1σ)	Age_err_tJ (±1σ)	isochron 36Ar/40Ar	pct isochron 36Ar/40Ar_err (±%1σ)	isochron 39Ar/40Ar	pct isochron 39Ar/40Ar_err (±%1σ)	Err_Corr_3 6Ar/39Ar
110825-14																															
1835-01A	110825-14	biotite	0.5	DT-31D	149.66	0.033103	-0.1470554	1.165373	-0.03666	0.1156685	-0.2762461	0.0888048	-0.1136261	0.0806073	-0.0000614	0.0008388	-1.954864	-0.763785596	36.66654	118.5773	5.431168	37.61777	132.3652	14.81594	102.205	102.205	-0.0010841	-954.3063	0.2437141	855.7512	0.7690198
1835-01B	110825-14	biotite	0.8	DT-31D	149.66	0.033103	16.71638	1.165552	0.0016889	0.1156685	-0.2019672	0.0903609	-0.0525791	0.0806073	0.0490647	0.0010182	0.09006149	0.035187057	-368.5447	25246.38	976.7719	54334.35	12.15891	1648.806	60451.94	60451.94	0.0029422	7.277599	0.0001245	5562.318	0.001201
1835-01C	110825-14	biotite	1	DT-31D	149.66	0.033103	38.1405	1.165552	0.0870302	0.1180043	-0.0291774	0.089709	-0.1424757	0.0799067	0.1145576	0.0012103	4.640816	1.81321367	-19.38727	28.44724	43.92181	60.44969	10.15065	116.5139	155.3605	155.3605	0.0030094	3.234478	0.0023111	133.9969	0.0215473
1835-01D	110825-14	biotite	1.2	DT-31D	149.66	0.033103	33.89611	1.164796	0.1495211	0.1159795	-0.1095885	0.0900301	0.0804441	0.0802517	0.089815	0.0011617	7.973093	3.111568096	6.373715	8.054349	47.71197	38.04505	20.97578	126.2291	97.26112	97.26113	0.0026468	3.674755	0.0043963	77.95561	0.0412217
1835-01E	110825-14	biotite	1.4	DT-31D	149.66	0.033103	50.21161	1.16492	0.4398205	0.1241788	0.1420298	0.0903609	0.268191	0.0802518	0.1375077	0.001268	23.45308	9.163354134	7.091703	2.947035	21.18332	6.627409	18.48447	57.12077	17.59479	17.5948	0.0027303	2.49918	0.008726	28.45525	0.0756878
1835-01F	110825-14	biotite	1.6	DT-31D	149.66	0.033103	45.63322	1.164713	0.3152362	0.1153651	0.0875323	0.0903609	0.074044	0.0806073	0.1031495	0.0012116	16.80972	6.567726917	2.784607	3.198141	47.23468	17.74577	32.59381	125.0085	45.39683	45.39684	0.0022577	2.812761	0.0069004	36.74971	0.0630219
1835-01G	110825-14	biotite	1.8	DT-31D	149.66	0.033103	31.20451	1.165552	0.5318182	0.1169584	-0.1149294	0.0900301	0.0281604	0.0802517	0.0668448	0.001117	28.35879	11.08006221	0.6281056	1.795305	21.1535	5.182959	36.06083	57.04162	13.76059	13.76059	0.0021416	4.096205	0.0170472	22.31594	0.1526279
1835-01H	110825-14	biotite	2	DT-31D	149.66	0.033103	36.00719	1.164768	0.5679815	0.1159795	0.0218584	0.0907013	0.0989551	0.0806073	0.0681744	0.0011036	30.28717	11.83349941	2.067359	1.736144	27.65559	6.044145	43.59563	74.22353	15.89706	15.89707	0.0018892	3.623341	0.0157638	20.7007	0.1395111
1835-01I	110825-14	biotite	2.2	DT-31D	149.66	0.033103	36.48137	1.164768	0.2897033	0.1265604	0.0596407	0.0890963	0.0336743	0.0802517	0.0646152	0.0010752	15.44821	6.035766709	1.379784	3.34306	59.40986	26.31067	47.16758	155.8927	66.18109	66.1811	0.0017696	3.606011	0.0079394	43.84097	0.0644811
1835-01J	110825-14	biotite	2.4	DT-31D	149.66	0.033103	30.24004	1.165373	0.2606933	0.1150696	0.0638936	0.0903301	0.1732945	0.0799067	0.0543668	0.0012848	13.90127	5.431363541	7.893611	5.038629	54.27811	24.53888	46.59021	142.9387	62.16281	62.16281	0.0017889	4.532422	0.0085836	44.52724	0.0735891
1835-01K	110825-14	biotite	2.6	DT-31D	149.66	0.033103	30.5992	1.165506	0.7549574	0.1166245	-0.031749	0.0914104	0.4507627	0.0799067	0.0401735	0.0010033	40.25753	15.7290122	7.092513	1.667695	25.00382	4.197537	61.45548	67.23563	11.08242	11.08243	0.001291	4.588343	0.0245784	15.97774	0.1978884
1835-01L	110825-14	biotite	2.8	DT-31D	149.66	0.033103	19.8587	1.165598	0.4737981	0.1166245	-0.1706138	0.0893977	0.3297519	0.0809734	0.0284261	0.0009591	25.26495	9.871253792	8.284972	2.880596	24.40503	6.554122	57.96121	65.65402	17.31928	17.31929	0.0014081	6.812481	0.0237497	25.4304	0.1988572
1835-01M	110825-14	biotite	3	DT-31D	149.66	0.033103	11.24283	1.165598	0.5123457	0.1153652	0.0101874	0.0903609	0.2490124	0.0802518	0.0170676	0.000899	27.32047	10.67436622	5.787743	2.275446	12.25367	3.627663	55.67408	33.25899	9.757302	9.757304	0.0014847	11.70604	0.0454346	24.86401	0.3692912
1835-01N	110825-14	biotite	3.45625	DT-31D	149.66	0.033103	27.07674	1.165694	0.3718654	0.1162982	-0.0477719	0.0893977	0.9870895	0.0809734	0.0520641	0.0010253	19.82946	7.747556902	31.62107	10.2238	32.83035	10.98645	44.2222	87.78361	28.68281	28.68282	0.0018682	4.764715	0.0134699	32.19695	0.1208169
1835-01O	110825-14	biotite	4	DT-31D	149.66	0.033103	8.329053	1.165331	0.1198156	0.1159795	-0.0973241	0.0907013	0.5037356	0.0795724	0.0092333	0.0008933	6.389083	2.49627467	50.10139	49.13884	49.8947	50.92155	69.56307	131.8006	129.7838	129.7838	0.0010195	17.56364	0.013942	100.9162	0.1104427
1835-01P	110825-14	biotite	4.5	DT-31D	149.66	0.033103	5.830252	1.165373	-0.0135115	0.1166245	0.0532117	0.0914104	0.2577756	0.0802518	0.0056125	0.0008661	-0.7204937	-0.281502703	-227.4319	1964.349	-276.62	2090.898	73.30237	-978.07	9772.876	9772.876	0.0008942	26.09656	-0.00265	-755.6233	0.0202616
1835-01Q	110825-14	biotite	5	DT-31D	149.66	0.033103	2.218515	1.165794	-0.0263276	0.1159795	-0.0235398	0.0903609	0.091275	0.0806073	0.0012268	0.0008388	-1.403904	-0.54851723	-41.35815	185.8175	-70.00627	303.8107	85.28905	-202.5552	929.5317	929.5317	0.0004927	93.68227	-0.012183	-432.5898	0.068139
110909-03																															
1836-01A	110909-03	muscovite	0.5	DT-31D	149.66	0.033103	-0.278749	1.165373	-0.0501715	0.1169583	-0.1465795	0.0921565	0.1200261	0.0795724	-0.000108	0.0008497	-2.675364	-0.010018197	-28.55542	69.20707	3.919943	25.01738	71.86484	10.70543	68.12344	68.12344	0.0009424	530.6306	0.1833314	476.6897	0.6910045
1836-01B	110909-03	muscovite	0.8	DT-31D	149.66	0.033103	423.6399	1.167326	4.906975	0.1237216	0.2152207	0.0903609	0.0703024	0.0802517	0.139261	0.0020953	261.6612	0.979820021	0.171073	0.1953311	77.82712	1.981043	90.19471	201.6423	4.860036	4.860219	0.0003284	1.533591	0.0115891	2.536653	0.019518
1836-01C	110909-03	muscovite	1	DT-31D	149.66	0.033103	1970.746	1.175242	19.56779	0.1169696	0.3777242	0.0903609	0.0031508	0.0813496	0.2773167	0.0017458	1043.44	3.907277376	0.0019234	0.0496584	96.42078	0.5801241	95.79904	246.6984	1.388592	1.38953	0.0001407	0.6339966	0.0099355	0.6007421	0.0093376
1836-01D	110909-03	muscovite	1.1	DT-31D	149.66	0.033103	2323.584	1.179701	21.46606	0.1169719	0.1409419	0.0893977	-0.0257973	0.0821324	0.233241	0.0022329	1144.664	4.286322093	-0.0143652	0.0457355	104.9309	0.5752723	97.00213	266.9557	1.361822	1.36293	0.0001004	0.9599228	0.0092444	0.5472782	0.0049068
1836-01E	110909-03	muscovite	1.2	DT-31D	149.66	0.033103	3391.006	1.183087	29.90372	0.1163247	0.4868181	0.089709	0.1250477	0.0802517	0.1549235	0.0014897	1594.597	5.971145879	0.050003	0.0320909	111.7841	0.4369147	98.63777	283.1077	1.025205	1.026845	0.0000456	0.9667863	0.008824	0.3905761	0.0032237
1836-01F	110909-03	muscovite	1.3	DT-31D	149.66	0.033103	6161.269	1.199873	56.74738	0.1266478	0.8620697	0.0900302	0.0571084	0.0799067	0.3956057	0.0034472	3026.019	11.33126194	0.012038	0.0168437	106.4249	0.2391531	98.08346	270.4892	0.5650468	0.5677775	0.0000642	0.8723833	0.0092162	0.2240304	0.0019406
1836-01G	110909-03	muscovite	1.4	DT-31D	149.66	0.033103	4784.052	1.190838	47.00914	0.1173644	0.606594	0.0910512	0.0414528	0.0799067	0.1824788	0.0016731	2506.733	9.386739595	0.0105518	0.0203402	100.5458	0.252534	98.86155	256.5455	0.6012249	0.6035518	0.0000381	0.9199837	0.0098325	0.2509056	0.0026843
1836-01H	110909-03	muscovite	1.5	DT-31D	149.66	0.033103	3761.64	1.188779	35.72398	0.1173361	0.7419195	0.0903301	0.0663619	0.0799067	0.3104218	0.0019004	1882.24	7.047334301	0.0225011	0.0313145	104.9115	0.3474271	97.15849	264.5411	0.8235142	0.8251144	0.0000282	1.825709	0.0095426	0.3339465	0.0016917
1836-01I	110909-03	muscovite	1.6	DT-31D	149.66	0.033103	2654.182	1.181353	25.71683	0.1176677	0.4711909	0.0903609	0.0774902	0.0799067	0.0734142	0.0021136	1371.335	5.135111734	0.0360947	0.0372207	102.2935	0.4705315	99.17577	260.7018	1.117685	1.118977	0.0000276	1.665364	0.0096952	0.4597271	0.0025876
1836-01J	110909-03	muscovite	1.7	DT-31D	149.66	0.033103	2848.754	1.179701	29.01365	0.1173243	0.1316446	0.0910512	0.0597669	0.0806073	0.0876094	0.0012267	1547.136	5.793417562	0.0246847	0.0332923	97.22433	0.3954705	99.08227	248.6208	0.9456094	0.9470064	0.0000307	1.408616	0.0101911	0.4065027	0.002995
1836-01K	110909-03	muscovite	1.8	DT-31D	149.66	0.033103	2991.559	1.179701	33.34013	0.12562	0.381087	0.0900301	-0.1448388	0.0802517	0.1305306	0.0014762	1777.843	6.657324903	-0.0520765	0.0288555	88.49745	0.3355766	98.69496	227.6341	0.8116514	0.813031	0.0000437	1.13352	0.0111523	0.3788334	0.0036215
1836-01L	110909-03	muscovite	1.9	DT-31D	149.66	0.033103	3524.262	1.184903	33.73743	0.1270855	0.6275622	0.0917789	-0.0272742	0.0809733	0.1156829	0.0013874	1799.029	6.736657382	-0.0096943	0.0287812	103.3703	0.391168	99.0199	263.2577	0.9278713	0.929455	0.0000328	1.204532	0.0095791	0.3781894	0.0024815
1836-01M	110909-03	muscovite	2	DT-31D	149.66	0.033103	2673.158	1.179701	26.5783	0.117669	0.3718887	0.0907013	0.0121109	0.0802517	0.0744308	0.0012367	1417.273	5.30712923	0.0054662	0.036221	99.6768	0.4437555	99.16893	254.4755	1.057675	1.058979	0.0000278	1.670847	0.009949	0.4449272	0.0026199
1836-01N	110909-03	muscovite	2.1	DT-31D	149.66	0.033103	2794.672	1.178132	26.96198	0.1176696	0.2634871	0.0907013	0.2214428	0.0799067	0.0738465	0.0017122	1437.733	5.383742081	0.098594	0.0355799	102.7781	0.4511184	99.21449	261.8524	1.070899	1.072258	0.0000263	2.335051	0.0096533	0.4384916	0.0017357
1836-01O	110909-03	muscovite	2.2	DT-31D	149.66	0.033103	2824.92	1.179701	26.97212	0.1183388	0.5805816	0.0903609	-0.1413926	0.0799067	0.0751042	0.0012522	1438.273	5.385696827	-0.0629517	0.0355777	105.6828	0.4661347	99.21823	268.7349	1.102392	1.103777	0.0000262	1.67196	0.0093883	0.4408325	0.0022846
1836-01P	110909-03	muscovite	2.3	DT-31D	149.66	0.033103	1666.675	1.175242	16.30923	0.1183754	0.0774438	0.0903609	-0.0447021	0.0806073	0.0454813	0.0010964	869.6806	3.256611268	-0.0329265	0.059374	101.2903	0.7389888	99.18358	258.3171	1.757659	1.758467	0.0000273	2.422102	0.009792	0.7292303	0.0028152
1836-01Q	110909-03	muscovite	2.5	DT-31D	149.66	0.033103	2086.666	1.176645	19.89515	0.11697	0.2636849	0.0903609	0.0083693	0.0806073	0.05421	0.0015327	1060.898	3.972644304	0.0050553	0.0486893	104.0029	0.6147729	99.22454	264.7576	1.457079	1.458099	0.000026	2.837927	0.0095406	0.59064	0.001897
1836-01R	110909-03	muscovite	3	DT-31D	149.66	0.033103	3172.204	1.181353	30.06239	0.1260967	0.4549702	0.0890963	0.1230785	0.0802517	0.0550611	0.0017079	1603.061	6.002828951	0.0492175	0.0320923	104.9112	0.4421537	99.48364	266.9092	1.046722	1.048162	0.0000173	3.121491	0.0094827	0.4211177	0.0010551
1836-01S	110909-03	muscovite	3.5	DT-31D	149.66	0.033103	1225.115	1.172687	12.65137	0.118009	0.1883181	0.089709	0.2416277	0.0802518	0.0158537	0.0009865	674.6279	2.526213322	0.2296804	0.0763138	96.42272	0.9046381	99.62272	246.7031	2.165348	2.16595	0.0000126	6.422671	0.0103319	0.9378209	0.0015212
1836-01T	110909-03	muscovite	4	DT-31D	149.66	0.033103	291.6389	1.16691	2.592229	0.1265606	-0.19267	0.0888048	0.1737868	0.0802518	0.0049245	0.0009076	138.2293	0.517613779	0.8065167	0.3745113	111.9478	5.488088	99.51869	283.4918	12.8749	12.87503	0.0000161	19.48763	0.0088897	4.901196	0.0016762
1836-01U	110909-03	muscovite	4.5	DT-31D	149.66	0.033103	235.8755	1.166284	2.122206	0.1153653	-0.0419364	0.0910512	0.0637054	0.0802517	0.00316	0.000879	113.1656	0.423760041	0.3612542	0.4555069	110.6671	6.043865	99.61068	280.4848	14.20206	14.20217	0.000013	28.86294	0.0090009	5.459844	0.0015514
110830-03																															
1837-01A	110830-03	amphibole	1	DT-31D	149.66	0.033103	1017.701	1.169485	0.3587513	0.1153651	0.1606243	0.0903609	0.3313273	0.0806074	0.3632047	0.0020742	19.13007	0.510106082	10.85583	4.377446	2550.703	825.8939	89.35972	2877.435	469.5786	469.5787	0.0003564	0.5842851	0.0003503	32.37861	0.000698
1837-01B	110830-03	amphibole	1.4	DT-31D	149.66	0.033103	1065.626	1.169485	1.333371	0.1187382	0.0654761	0.0914104	1.080334	0.0809735	0.4336853	0.0022302	71.10072	1.895911336	9.527143	1.108918	706.2219	63.28335	87.89423	1319.94	84.26838	84.26864	0.0004055	0.5284594	0.0012446	8.959458	0.0025439
1837-01C	110830-03	amphibole	1.5	DT-31D	149.66	0.033103	415.8059	1.167546	1.501867	0.1328611	0.0229463	0.0907013	1.132027	0.0802519	0.1596756	0.0014126	80.08567	2.135494676	8.866149	1.005109	246.667	21.96119	88.65566	575.0342	43.93354	43.93368	0.00038	0.9403111	0.0035941	8.900407	0.009421
1837-01D	110830-03	amphibole	1.6	DT-31D	149.66	0.033103	261.0679	1.166713	1.299393	0.1180044	-0.0713116	0.0890963	0.7895731	0.0813497	0.0889893	0.0016287	69.28896	1.847598245	7.162822	0.9837488	181.4348	16.5815	89.95578	439.6506	35.71827	35.71837	0.0003364	1.912703	0.004958	9.133563	0.0114327
1837-01E	110830-03	amphibole	1.7	DT-31D	149.66	0.033103	350.3155	1.166843	1.950133	0.1162983	0.0184955	0.0907013	1.136654	0.0806075	0.077755	0.0014543	103.9891	2.772881113	6.873073	0.6368489	168.6119	10.12064	93.51767	411.8181	22.13499	22.13514	0.0002171	1.947504	0.0055463	5.998776	0.0094969
1837-01F	110830-03	amphibole	1.8	DT-31D	149.66	0.033103	420.0615	1.166977	2.922964	0.1166248	-0.0799165	0.0903609	1.512192	0.0809736	0.0737924	0.0011337	155.8645	4.156143027	6.102725	0.4075263	136.8386	5.497888	94.91413	340.9727	12.4991	12.49929	0.0001703	1.61757	0.0069362	4.014963	0.0118842
1837-01G	110830-03	amphibole	1.9	DT-31D	149.66	0.033103	1368952	1.167472	2.982573	0.1169586	-0.0234409	0.0893977	2.516906	0.080608	0.0751306	0.0011063	159.0431	4.256144666	9.958129	0.5041847	140.1237	5.547669	95.12206	348.4246	12.56101	12.56121	0.0001634	1.582048	0.0067884	3.955146	0.0113122
1837-01H	110830-03	amphibole	2	DT-31D	149.66	0.033103	445.6954	1.167045	2.92197	0.1169586	-0.0203748	0.0914104	3.207721	0.0802528	0.0825518	0.0011095	155.8115	4.154729665	12.95916	0.6117106	145.6786	5.899188	94.79059	360.9602	13.26575	13.26595	0.0001745	1.458916	0.0065068	4.044085	0.0116215
1837-01I	110830-03	amphibole	3	DT-31D	149.66	0.033103	6685.536	1.197495	32.65521	0.1169897	0.9015334	0.0907013	46.08925	0.0819488	1.250727	0.0057218	1741.311	46.43222542	16.67301	0.0666843	195.852	0.8314481	94.72286	470.4462	1.761141	1.763529	0.0001768	0.4846699	0.0048365	0.3624929	0.0018262
1837-01J	110830-03	amphibole	4	DT-31D	149.66	0.033103	2758.905	1.183087	15.2283	0.1156754	0.3559647	0.0907013	21.14872	0.0810187	0.4272657	0.0021419	812.0362	21.65301826	16.41171	0.1396213	175.1062	1.398981	95.71914	425.9671	3.036165	3.037329	0.0001434	0.5440499	0.0054663	0.7687194	0.0043971
1837-01K	110830-03	amphibole	5	DT-31D	149.66	0.033103	1111.404	1.170468	6.187988	0.1166257	0.1270949	0.0903609	10.6713	0.0802634	0.1768746	0.0015039	329.9692	8.798658887	20.38654	0.4136938	173.9595	3.360234	95.67806	423.4767	7.302545	7.303024	0.0001448	0.9437012	0.0055	1.912061	0.0061469
1837-01L	110830-03	amphibole	6	DT-31D	149.66	0.033103	188.5823	1.166169	0.9862432	0.1162983	0.0415408	0.089709	2.522912	0.0799074	0.0375009	0.0010214	52.59059	1.402332632	30.25157	3.693714	184.3903	22.212	94.66211	446.0061	47.68108	47.68116	0.0001788	3.112674	0.0051338	12.03628	0.0102073
110906-01																															
1838-01A	110906-01	muscovite	0.5	DT-31D	149.66	0.033103	0.1658581	1.165289	0.1597541	0.1156685	0.1303589	0.0903609	0.0639024	0.0799067	-0.0002782	0.0009176	8.518814	0.046837286	4.824051	6.97048	1.789309	7.626416	171.9355	4.894401	20.83311	20.83311	-0.0024094	-739.7984	0.9609042	706.3255	0.9446635
1838-01B	110906-01	muscovite	0.8	DT-31D	149.66	0.033103	112.333	1.164796	7.027194	0.1162997	0.2340129	0.0903301	0.0108309	0.0802517	0.0409803	0.0009793	374.7219	2.060258217	0.0185945	0.1377767	14.23707	0.2910944	89.11928	38.58597	0.7806789	0.7807246	0.0003644	2.624744	0.0625966	1.953033	0.2097499
1838-01C	110906-01	muscovite	1	DT-31D	149.66	0.033103	395.0113	1.16691	24.01835	0.1173166	0.3023574	0.0900301	-0.1032875	0.0806073	0.0736335	0.0011264	1280.768	7.04178694	-0.0518992	0.0405038	15.51834	0.0911173	94.42234	42.01897	0.2439073	0.2440803	0.0001868	1.563897	0.0608456	0.5708222	0.09776
1838-01D	110906-01	muscovite	1.2	DT-31D	149.66	0.033103	851.9091	1.169485	48.73504	0.1307362	0.5230179	0.0914104	0.027865	0.0795724	0.2321638	0.0016258	2598.774	14.28831573	0.0069028	0.019712	16.0479	0.0502848	91.86411	43.43596	0.1345008	0.1348355	0.0002725	0.7156282	0.0572437	0.3013477	0.08739
1838-01E	110906-01	muscovite	1.3	DT-31D	149.66	0.033103	500.129	1.167697	29.54159	0.1166503	0.4524976	0.0903609	0.0673485	0.0806073	0.0848139	0.0011522	1575.293	8.66111047	0.0275334	0.032954	16.06349	0.0756452	94.94366	43.47767	0.2023296	0.2025527	0.0001694	1.388089	0.0591052	0.4587404	0.0856104
1838-01F	110906-01	muscovite	1.4	DT-31D	149.66	0.033103	706.5583	1.168251	42.22059	0.1286198	0.568515	0.0910512	0.0858596	0.0806073	0.0908055	0.001297	2251.395	12.37838566	0.0245774	0.0230741	16.08355	0.0570164	96.16857	43.53131	0.1524983	0.1527948	0.0001283	1.446479	0.0597931	0.3466232	0.0545282
1838-01G	110906-01	muscovite	1.5	DT-31D	149.66	0.033103	374.4212	1.167326	22.73923	0.1166398	0.3453817	0.089709	-0.0897981	0.0802517	0.0552238	0.00102	1212.56	6.666769901	-0.0477438	0.0426689	15.72841	0.096562	95.58615	42.5812	0.2584026	0.2585703	0.0001478	1.882304	0.0607729	0.6002529	0.0860309
1838-01H	110906-01	muscovite	1.6	DT-31D	149.66	0.033103	292.1201	1.167329	16.71375	0.1175635	0.5048191	0.0910512	0.1117553	0.0806073	0.0888853	0.0011897	717.1044	3.778645615	0.0331976	0.0239451	16.341	0.0586685	96.19247	44.21976	0.1568581	0.1571555	0.0001275	1.365841	0.0588657	0.1517067	0.0592827
1838-01I	110906-01	muscovite	1.7	DT-31D	149.66	0.033103	852.1469	1.168587	52.76436	0.1261479	0.6653445	0.089709	0.1816638	0.0813496	0.060988	0.0011219	2813.638	15.46964638	0.0416545	0.0186533	15.8031	0.0442562	97.87364	42.78106	0.1184118	0.1187868	0.0000712	1.86448	0.0619332	0.2755965	0.0365704
1838-01J	110906-01	muscovite	1.8	DT-31D	149.66	0.033103	269.7136	1.16691	17.0317	0.1166331	0.1876258	0.0900301	-0.0128986	0.0799067	0.0274511	0.0009646	908.2084	4.99341556	-0.0091659	0.0567824	15.34425	0.1265824	96.95834	41.5529	0.3389283	0.3390501	0.0001019	3.565584	0.0631887	0.8100263	0.0648118
1838-01K	110906-01	muscovite	1.9	DT-31D	149.66	0.033103	198.2022	1.166343	13.00118	0.1280652	0.1624046	0.0907013	0.1346971	0.0802517	0.0134291	0.0008985	693.283	3.811733093	0.1254347	0.0747435	14.93274	0.1735458	98.00803	40.45071	0.4649543	0.4650385	0.0000667	6.8847	0.065633	1.147493	0.0438345
1838-01L	110906-01	muscovite	2	DT-31D	149.66	0.033103	93.93111	1.165794	6.191962	0.124644	0.1425244	0.0914104	-0.0552376	0.0806073	0.0046374	0.0008538	330.184	1.81538187	-0.1080825	0.157738	14.93199	0.3570581	98.50269	40.44872	0.9566112	0.9566522	0.0000502	18.36016	0.0659676	2.364757	0.0354795
1838-01M	110906-01	muscovite	2.1	DT-31D	149.66	0.033103	61.25114	1.164796	3.850193	0.1173001	0.0933678	0.0900301	0.0048247	0.081736	0.0026462	0.0009675	205.3101	1.128813544	0.0151876	0.2572976	15.69454	0.5708184	98.71766	42.49054	1.527601	1.52763	0.000043	37.14029	0.0628994	3.59146	0.0271126
1838-01N	110906-01	muscovite	2.2	DT-31D	149.66	0.033103	54.77066	1.164796	3.433819	0.1162986	0.0372878	0.089709	0.0235326	0.0792488	0.0027251	0.0008537	183.1072	1.006739505	0.0830906	0.2798317	15.70706	0.6353462	98.53348	42.52405	1.700257	1.700283	0.0000491	32.13067	0.062732	3.999385	0.0351971
1838-01O	110906-01	muscovite	2.3	DT-31D	149.66	0.033103	118.8952	1.165598	7.388213	0.1170567	0.1305567	0.0893977	0.0443802	0.0806073	0.0082955	0.0008621	396.5691	2.180432486	0.1316761	0.1460491	14.98097	0.2850969	97.81088	40.57994	0.7637616	0.7638134	0.0000733	10.4736	0.0652901	1.875925	0.1052268
1838-01P	110906-01	muscovite	2.4	DT-31D	149.66	0.033103	134.0709	1.16595	8.353709	0.1290912	0.1300621	0.0907013	-0.0286527	0.0806073	0.0062338	0.0009796	445.4586	2.449170694	-0.0416154	0.1170765	15.81434	0.2836097	98.60287	42.81112	0.7588552	0.7589097

Lab ID#	Sample	Material	Pwr_Achieved (W)	Irrad.	J x 10e-5	J_err (±1σ)	40Ar	40Ar_err (±1σ)	39Ar	39Ar_err (±1σ)	38Ar	38Ar_err (±1σ)	37Ar	37Ar_err (±1σ)	36Ar	36Ar_err (±1σ)	39Ar x 10e-18 (mol)	39Ar cum% of total	Ca/K	Ca/K_err (±1σ)	40Ar*/39Ar	40Ar*/39Ar_err (±1σ)	%40Ar*	Age (Ma)	Age_err (±1σ)	Age_err_tJ (±1σ)	isochron 36Ar/40Ar	pct isochron 36Ar/40Ar_err (±%1σ)	isochron 39Ar/40Ar	pct isochron 39Ar/40Ar_err (±%1σ)	Err_Corr_36Ar/39Ar
130823-03																															
1840-01A	130823-03	muscovite	0.5	DT-31D	149.66	0.033103	-0.2509877	1.165331	-0.17565	0.1255896	0.0542997	0.0903609	0.0831026	0.0802517	0.000037	0.0008387	-9.366537	-0.057456516	-5.843984	7.022004	1.24721	6.81837	87.66174	3.412947	18.64085	18.64085	0.0004133	940.429	0.7028629	469.7315	0.4880109
1840-01B	130823-03	muscovite	0.8	DT-31D	149.66	0.033103	140.9988	1.165694	5.471777	0.1173005	0.0386725	0.0893977	0.1095891	0.0799067	0.0560444	0.0010264	291.7825	1.789861907	0.2474774	0.1805258	22.70794	0.5344385	88.16745	61.16394	1.415724	1.415787	0.0003963	2.026998	0.0388267	2.29797	0.1467418
1840-01C	130823-03	muscovite	1	DT-31D	149.66	0.033103	1328.994	1.171535	37.56854	0.1328976	0.4884006	0.0903001	-0.0446036	0.0802517	0.0664223	0.0011449	2003.343	12.28896913	-0.0146756	0.0264048	34.82356	0.1274041	98.50621	92.98	0.3316762	0.3322818	0.00005	1.734669	0.0282872	0.3645657	0.0122882
1840-01D	130823-03	muscovite	1.2	DT-31D	149.66	0.033103	1196.862	1.170468	44.05915	0.129141	0.4864225	0.089709	0.1541927	0.0809733	0.0538778	0.0014476	2349.455	14.41209944	0.0432746	0.0227258	26.78444	0.0834663	98.6616	71.93084	0.2198048	0.2203578	0.0000448	2.710491	0.0368354	0.3090031	0.0114192
1840-01E	130823-03	muscovite	1.4	DT-31D	149.66	0.033103	1814.468	1.173923	58.32366	0.1271466	0.7514921	0.089709	0.2542309	0.081736	0.0497664	0.0013639	3110.11	19.07813446	0.0539192	0.0173356	30.83838	0.0705301	99.18765	82.57568	0.1846608	0.1855223	0.0000272	2.775754	0.0321637	0.2274093	0.0066314
1840-01F	130823-03	muscovite	1.6	DT-31D	149.66	0.033103	2973.294	1.183087	85.41487	0.1324958	1.059784	0.0907013	0.252754	0.0806073	0.0596352	0.0015339	4555.819	27.94642753	0.0366729	0.0116957	34.57289	0.0556396	99.40506	92.32729	0.1449006	0.1462628	0.0000199	2.598228	0.0287523	0.1601123	0.003806
1840-01G	130823-03	muscovite	1.8	DT-31D	149.66	0.033103	1121.62	1.170468	25.5231	0.1180233	0.4251993	0.0903001	0.0589792	0.0809733	0.0180939	0.0009747	1361.021	8.348809619	0.0286551	0.0393412	43.70693	0.2075754	99.52129	115.9615	0.5336463	0.5342248	0.0000316	5.468011	0.0227701	0.4740461	0.0042013
1840-01H	130823-03	muscovite	2	DT-31D	149.66	0.033103	358.7733	1.16691	8.529161	0.1169605	0.2479588	0.0903609	0.0803456	0.0799067	0.0095283	0.000875	454.8181	2.789956604	0.1168549	0.1162275	41.71171	0.5890033	99.21972	110.8249	1.518498	1.518684	0.0000261	9.434689	0.023787	1.409462	0.0079555
1840-01I	130823-03	muscovite	2.1	DT-31D	149.66	0.033103	287.7194	1.166524	6.953874	0.116626	0.0503434	0.0903001	0.1964333	0.0802518	0.0077243	0.0008748	370.8159	2.274667659	0.3505364	0.1433304	41.03873	0.7096204	99.22972	109.0891	1.831195	1.831344	0.0000258	11.91625	0.0241795	1.725829	0.0079933
1840-01J	130823-03	muscovite	2.2	DT-31D	149.66	0.033103	328.2929	1.166524	8.03132	0.1163001	-0.0824881	0.089709	0.1233739	0.0799067	0.0087643	0.000898	428.2708	2.627108841	0.1906934	0.123539	40.53484	0.6057125	99.21739	107.7883	1.564169	1.56434	0.0000262	10.54532	0.0244771	1.491229	0.0080293
1840-01K	130823-03	muscovite	2.3	DT-31D	149.66	0.033103	189.9989	1.165845	3.729185	0.1169588	0.1088961	0.0903001	0.0902904	0.0802517	0.0018503	0.0009675	198.8592	1.219846163	0.3007698	0.2674961	50.78947	1.625546	99.73336	134.0797	4.137874	4.137973	8.9309E-06	57.51348	0.0196366	3.196395	0.0020482
1840-01L	130823-03	muscovite	2.4	DT-31D	149.66	0.033103	295.6644	1.166343	6.109899	0.129613	0.1451948	0.0907013	0.0230403	0.0806073	0.0033612	0.0008537	325.811	1.998596704	0.0468614	0.1639495	48.19885	1.041057	99.6655	127.4733	2.659623	2.659763	0.0000112	26.06415	0.020678	2.157813	0.002767
1840-01M	130823-03	muscovite	2.5	DT-31D	149.66	0.033103	157.0816	1.165794	3.289365	0.1180047	-0.1268971	0.0907013	0.1314478	0.0795724	0.0025041	0.0008498	175.4058	1.075977532	-0.4967725	0.3012504	47.45934	1.740347	99.47862	125.5831	4.450718	4.450799	0.0000175	31.33055	0.0209608	3.662377	0.0048004
1840-01N	130823-03	muscovite	2.6	DT-31D	149.66	0.033103	431.8447	1.167546	8.623741	0.1176505	-0.0115721	0.0910512	-0.0031508	0.0802517	0.0079014	0.0008793	459.862	2.820894476	-0.0045436	0.1157256	49.76878	0.6930482	99.45177	131.4797	1.766683	1.766906	0.0000184	11.20786	0.0199828	1.39081	0.0046894
1840-01O	130823-03	muscovite	2.7	DT-31D	149.66	0.033103	41.16007	1.164713	0.8982195	0.1169584	0.0643882	0.0907013	0.037022	0.0813496	0.0020971	0.0008576	47.89767	0.293814764	0.5127458	1.128649	45.12641	6.026397	98.51074	119.6072	15.46216	15.46218	0.0000499	42.33988	0.02183	13.32934	0.0141887
1840-01P	130823-03	muscovite	2.8	DT-31D	149.66	0.033103	8.998082	1.16474	0.1954206	0.1153651	0.1103797	0.0903609	0.1186477	0.0806073	0.0007793	0.0008388	10.42083	0.063923637	7.55823	6.80269	45.35642	27.59364	98.10266	120.1972	70.77525	70.77526	0.0000635	148.9555	0.0216293	60.71244	0.0185285
1840-01Q	130823-03	muscovite	2.9	DT-31D	149.66	0.033103	4.689935	1.165598	-0.0146044	0.1169583	0.0130557	0.0903001	0.0525791	0.0806073	0.0013742	0.000832	-0.778781	-0.004777216	-44.83483	365.5768	-286.5287	2233.281	91.79534	-1024.98	10709.39	10709.39	0.0002748	69.88784	-0.003204	-779.3373	0.011341
1840-01R	130823-03	muscovite	3	DT-31D	149.66	0.033103	21.93409	1.165506	0.2963598	0.1159795	-0.1211605	0.0910512	-0.0004923	0.0802517	0.000657	0.000832	15.80343	0.096941655	-0.0206949	3.373469	73.27604	28.95783	99.07264	190.4431	71.47749	71.4775	0.0000311	123.6661	0.0135205	39.49386	0.0057813
1840-01S	130823-03	muscovite	3.2	DT-31D	149.66	0.033103	40.07592	1.164661	0.6918704	0.1159795	-0.0979175	0.0903609	0.1651221	0.0806073	0.0015528	0.0008498	36.8941	0.226316327	2.974231	1.535143	57.42714	9.798391	99.02242	150.8986	24.71393	24.71395	0.0000327	65.55977	0.0172431	17.04436	0.0075584
1840-01T	130823-03	muscovite	3.4	DT-31D	149.66	0.033103	53.84386	1.165794	0.9669894	0.1172897	0.072657	0.0907013	0.1611836	0.0802517	0.001708	0.0008353	51.5638	0.316303405	-2.078052	1.964908	54.97282	6.772929	99.01838	144.6977	17.14095	17.14098	0.0000362	43.37853	0.0179941	12.30665	0.0038605
1840-01U	130823-03	muscovite	3.6	DT-31D	149.66	0.033103	53.525	1.164888	1.00512	0.1160721	-0.0830815	0.0903001	-0.0519884	0.0799067	0.0020152	0.0008354	53.59818	0.328782877	-0.645274	0.9950906	123.5686	6.696944	98.81996	338.6026	17.00519	17.00522	0.0000395	40.00369	0.0187983	12.72555	0.0093043
1840-01V	130823-03	muscovite	3.8	DT-31D	149.66	0.033103	8.070219	1.165416	0.1358109	0.1156685	-0.1971208	0.089709	-0.0673485	0.0795724	0.0008188	0.000828	7.242139	0.044424829	-6.188762	9.013771	57.04649	49.18297	96.43797	149.9383	124.1165	124.1165	0.0001193	88.26879	0.0169052	86.0608	0.0274533
1840-01W	130823-03	muscovite	4	DT-31D	149.66	0.033103	3.754833	1.164768	0.0723265	0.1159795	-0.1225452	0.0903609	-0.0878288	0.0802517	0.0000763	0.000888	3.856824	0.023658575	-15.16018	27.97984	50.41728	81.74374	98.10357	133.1321	208.1889	208.1889	0.0000635	377.4602	0.0194583	161.8474	0.015752
1840-01X	130823-03	muscovite	4.5	DT-31D	149.66	0.033103	6.232439	1.165373	-0.0291094	0.1166245	0.1584483	0.0903001	0.116383	0.0813496	0.000972	0.0008353	-1.552266	-0.009521917	-49.93156	203.0684	-199.9296	777.6833	96.36913	-650.7204	3039.575	3039.575	0.0001216	113.0922	-0.00482	-388.9258	0.0079493
1840-01Y	130823-03	muscovite	5	DT-31D	149.66	0.033103	3.196039	1.165416	0.0190751	0.1166245	-0.0961372	0.0903001	0.0662655	0.0809733	0.0012207	0.0008423	1.017185	0.006239617	43.40038	270.596	153.8928	969.3974	89.40642	379.3393	2158.143	2158.143	0.0003548	83.52957	0.0058097	629.579	0.0252848
130818-04																															
1841-03A	130818-04	muscovite	0.5	DT-31D	149.66	0.033103	0.3219691	1.165373	0.208336	0.1251132	-0.0361009	0.089709	0.1317432	0.0789363	0.000453	0.000887	11.10957	0.163315185	7.914836	6.714305	1.190261	5.79393	76.6862	3.257247	15.84147	15.84147	0.0007809	494.8101	0.6442806	366.9493	0.7215465
1841-03B	130818-04	muscovite	0.8	DT-31D	149.66	0.033103	801.9996	1.169485	7.559807	0.1166262	0.0587505	0.0903609	0.3617523	0.0813496	0.0562928	0.0011132	403.1286	5.926154269	0.5991466	0.1350508	103.8568	1.610952	97.92541	264.4114	3.818855	3.819243	0.0000695	2.016555	0.0094289	1.550191	0.0068024
1841-03C	130818-04	muscovite	1	DT-31D	149.66	0.033103	2725.783	1.183087	23.84151	0.1173163	0.1857465	0.0907013	0.4600182	0.0799067	0.0735234	0.0012438	1271.355	18.68942769	0.2416731	0.0419963	113.3596	0.5603405	99.2024	286.8008	1.312169	1.313482	0.0000267	1.717675	0.0087511	0.4940593	0.00222
1841-03D	130818-04	muscovite	1.1	DT-31D	149.66	0.033103	4220.101	1.192977	34.73052	0.1160153	0.6729603	0.0903609	0.0472621	0.0809733	0.0126861	0.0013584	1852.014	27.22535369	0.0170507	0.0292128	121.3228	0.4069108	99.91108	305.3542	0.943266	0.945315	2.9784E-06	10.85697	0.0082351	0.3352467	0.0002196
1841-03E	130818-04	muscovite	1.2	DT-31D	149.66	0.033103	1500.67	1.172687	12.89071	0.1260766	-0.0156272	0.089709	0.0151633	0.0806073	0.0052462	0.0011112	687.4004	10.10506434	0.0147439	0.0783781	116.2173	1.140625	99.89542	293.4805	2.66131	2.661986	3.5029E-06	21.2826	0.0085956	0.9811807	0.0002924
1841-03F	130818-04	muscovite	1.3	DT-31D	149.66	0.033103	1800.966	1.175242	14.76364	0.1191221	0.2675423	0.0903609	0.1877685	0.0799067	0.0051173	0.0011473	787.2755	11.5732595	0.1595265	0.0679002	121.8209	0.9865503	99.92035	306.5085	2.285495	2.286347	2.6677E-06	24.02997	0.0082022	0.8095871	0.0002189
1841-03G	130818-04	muscovite	1.4	DT-31D	149.66	0.033103	909.525	1.168587	7.75334	0.1159813	0.0692346	0.0903001	-0.0948197	0.0806073	0.0027573	0.0010165	413.4491	6.07786534	-0.1534504	0.1304702	117.1065	1.758584	99.90434	295.554	4.098447	4.098932	3.2039E-06	35.16556	0.0085311	1.501275	0.0003127
1841-03H	130818-04	muscovite	1.5	DT-31D	149.66	0.033103	558.0311	1.167773	4.673442	0.116959	0.1522172	0.0907013	0.0811333	0.0799067	0.0027562	0.0008745	247.2663	3.634912059	0.2196243	0.2163741	120.1136	3.041155	99.86037	302.5489	7.060581	7.060831	4.6768E-06	33.86726	0.0083138	2.531379	0.0053108
1841-03I	130818-04	muscovite	1.6	DT-31D	149.66	0.033103	335.9809	1.167045	2.719893	0.1187383	-0.0221551	0.0903001	-0.179853	0.0799067	0.0020799	0.0008576	145.0391	2.132113188	-0.8122916	0.3705919	123.1226	5.390347	99.78933	309.5216	12.46702	12.46718	7.0562E-06	36.57975	0.0081049	4.377193	0.0007536
1841-03J	130818-04	muscovite	1.7	DT-31D	149.66	0.033103	255.3868	1.166843	2.085347	0.1176485	0.2022639	0.0903001	-0.0943274	0.0809733	0.0002643	0.0008497	111.2018	1.634709461	-0.5681732	0.4887886	122.288	6.920585	99.95542	307.5903	16.02312	16.02324	1.4931E-06	225.4359	0.0081738	5.658221	0.0001637
1841-03K	130818-04	muscovite	1.8	DT-31D	149.66	0.033103	399.6034	1.167255	2.901206	0.1280608	-0.0435189	0.0903609	0.1313494	0.0802517	0.0009654	0.000846	154.7078	2.274263658	0.569086	0.348606	137.6155	6.090709	99.94235	342.7382	13.83349	13.83366	1.9308E-06	110.9158	0.0072624	4.425337	0.0001738
1841-03L	130818-04	muscovite	1.9	DT-31D	149.66	0.033103	138.4082	1.166058	0.9008026	0.1172997	-0.0501456	0.0903001	-0.089995	0.0802517	-0.0002906	0.0009335	48.03559	0.706141727	-1.256239	1.132113	153.472	20.01374	100.0292	378.4022	44.57888	44.57894	-9.794E-07	-695.2347	0.0065178	13.03886	0.0000783
1841-03M	130818-04	muscovite	2	DT-31D	149.66	0.033103	153.5476	1.165897	1.093342	0.1169584	0.190593	0.089709	0.0057108	0.0799067	0.0004437	0.000846	58.30283	0.857073912	0.0657024	0.9193422	140.2447	15.04315	99.92392	348.6999	34.05555	34.05562	2.5481E-06	218.707	0.007125	10.72484	0.0002458
1841-03N	130818-04	muscovite	2.1	DT-31D	149.66	0.033103	514.5755	1.167697	3.957292	0.1162987	-0.0054399	0.0890963	0.0923581	0.0795724	0.0002816	0.0010101	211.024	3.102132486	0.2936763	0.2531679	129.9591	3.83227	99.99158	325.2653	8.787516	8.787763	2.8186E-07	702.0091	0.0076941	2.948176	0.0002249
1841-03O	130818-04	muscovite	2.2	DT-31D	149.66	0.033103	154.6316	1.165694	1.309924	0.1169584	0.0312545	0.0889977	0.0095687	0.0795724	0.0004666	0.0008423	69.85216	1.02685316	1.927361	0.7837774	118.078	10.59521	99.97221	297.8168	24.66224	24.66234	9.3072E-07	592.0036	0.0084666	8.971309	0.0003107
1841-03P	130818-04	muscovite	2.3	DT-31D	149.66	0.033103	173.4969	1.166169	1.321151	0.1172797	-0.0235529	0.0903001	0.0518899	0.0802517	0.0002938	0.0008497	70.45083	1.035654037	0.4947475	0.7695102	131.2346	11.69078	99.96827	328.1878	26.76455	26.76463	1.0629E-06	466.1414	0.0076175	8.906887	0.0001088
1841-03Q	130818-04	muscovite	2.5	DT-31D	149.66	0.033103	424.0356	1.167472	3.149977	0.1241791	0.0386725	0.0910512	0.0770964	0.0795724	-0.0001893	0.0009501	167.9737	2.469275955	0.3084137	0.3185507	134.5817	5.320389	100.022	335.8347	12.12957	12.12976	-7.359E-07	-307.2405	0.0074321	3.952636	0.0000624
1841-03R	130818-04	muscovite	3	DT-31D	149.66	0.033103	293.462	1.16691	1.743088	0.1265605	-0.0552888	0.0910512	0.0221541	0.0799067	-0.0003788	0.0009281	92.95083	1.366411655	0.1602125	0.5779803	168.3311	12.24292	100.0406	411.204	26.78563	26.78576	-1.361E-06	-234.588	0.0059431	7.272405	0.0000927
130819-07																															
1842-01A	130819-07	phengite	0.5	DT-31D	149.66	0.033103	-0.3092456	1.165373	-0.0381502	0.1241788	-0.0236387	0.0907013	-0.1887532	0.0809733	-0.0002422	0.0008319	-2.034376	-0.015553131	62.38968	204.8342	8.949955	44.45347	106.1595	24.35137	120.1495	120.1495	-0.0002063	-1372.631	0.1186145	506.7287	0.2041776
1842-01B	130819-07	phengite	0.8	DT-31D	149.66	0.033103	76.09859	1.164856	5.42697	0.1159804	0.0049453	0.0907013	-0.0141786	0.0799067	0.0465674	0.0009926	289.3953	2.212475329	-0.032957	0.1857373	11.45057	0.3300694	81.71567	31.09763	0.8888345	0.8888606	0.0006124	2.63744	0.0713638	2.628744	0.3379645
1842-01C	130819-07	phengite	1	DT-31D	149.66	0.033103	179.5503	1.165448	14.25001	0.1163042	0.3753304	0.0903609	0.0079755	0.0795724	0.0294469	0.001172	759.8874	5.809465607	0.0070651	0.0704896	11.97616	0.1298399	95.11149	32.51243	0.349372	0.3494447	0.0001637	4.062843	0.0794173	1.043133	0.0995693
1842-01D	130819-07	phengite	1.1	DT-31D	149.66	0.033103	99.0852	1.166058	15.03546	0.1172272	0.0568494	0.0903609	-0.0260928	0.0802517	0.0021709	0.0009248	801.7723	6.129677905	-0.0219146	0.0674017	12.7997	0.1320913	96.73238	34.72705	0.3550001	0.3550816	0.0001094	4.325954	0.075574	1.01006	0.0785142
1842-01E	130819-07	phengite	1.2	DT-31D	149.66	0.033103	275.8259	1.16595	20.19379	0.1166366	0.1416342	0.0903609	0.1093922	0.0809733	0.0245111	0.0009414	1076.842	8.232634818	0.0684313	0.0506552	13.29053	0.0970696	97.36328	36.04571	0.2606901	0.2608096	0.0000883	3.924754	0.0732576	0.7157724	0.0636089
1842-01F	130819-07	phengite	1.3	DT-31D	149.66	0.033103	296.7735	1.166713	21.21888	0.1169716	0.2478599	0.089709	0.0777856	0.0799067	0.0233706	0.0009304	1131.506	8.650545058	0.0463252	0.0475892	13.65045	0.0941225	97.66082	37.01205	0.252642	0.252772	0.0000783	4.058983	0.071544	0.6771037	0.0562369
1842-01G	130819-07	phengite	1.4	DT-31D	149.66	0.033103	290.1233	1.166649	20.45439	0.1173119	0.1795154	0.0903001	0.0575023	0.081736	0.0229928	0.000925	1090.739	8.33887662	0.0355381	0.0505156	13.84051	0.0986849	97.6416	37.52213	0.2648145	0.2649419	0.000079	4.097246	0.0705477	0.7004732	0.056344
1842-01H	130819-07	phengite	1.5	DT-31D	149.66	0.033103	320.4923	1.166843	22.12833	0.1176626	0.2694215	0.0903609	0.0524807	0.0809733	0.0238697	0.0009697	1180.004	9.021311008	0.0300448	0.0463569	14.15322	0.0928278	97.78386	38.36109	0.2489833	0.2491249	0.0000742	4.12933	0.0690895	0.6444436	0.0498128
1842-01I	130819-07	phengite	1.6	DT-31D	149.66	0.033103	326.5931	1.166778	22.3007	0.1173142	0.3116546	0.0914104	-0.0224495	0.0802517	0.025103	0.0009361	1189.195	9.09158307	-0.0127574	0.0456047	14.29883	0.0924862	97.70221	38.75159	0.2480141	0.248159	0.000077	3.776928	0.0683288	0.6359023	0.0531433
1842-01J	130819-07	phengite	1.7	DT-31D	149.66	0.033103	283.0627	1.166977	23.2068	0.1163144	0.3488435	0.0903609	0.1789069	0.0806073	0.0260233	0.0009062	1246.783	9.531850564	-0.0970059	0.0437091	14.5833	0.0888695	97.75003	39.51173	0.2382162	0.2383731	0.0000754	3.60957	0.0670299	0.5993611	0.0514642
1842-01K	130819-07	phengite	1.8	DT-31D	149.66	0.033103	283.5099	1.166713	18.90046	0.1174091	0.4344091	0.0914104	-0.0958043	0.0809733	0.0210649	0.0008963	1007.876	7.705366589	-0.0642828	0.0543332	14.66882	0.1159469	97.3016	39.7433	0.3107556	0.3108283	0.0000717	4.491881	0.066713	0.7794786	0.0483698
1842-01L	130819-07	phengite	1.9	DT-31D	149.66	0.033103	331.7896	1.166778	21.60893	0.1232824	0.3576462	0.0903001	0.0221541	0.0809733	0.0255593	0.0009416	1152.307	8.809561231	0.0130064	0.0475385	14.99196	0.1019915	97.70452	40.60938	0.2732262	0.2733706	0.0000769	3.743519	0.0651713	0.6702007	0.0492926
1842-01M	130819-07	phengite	2	DT-31D	149.66	0.033103	168.9911	1.166113	11.26952	0.1166283	0.1600308	0.0903609	0.0865488	0.0809733	0.0146022	0.0010633	600.9529	4.594374941	0.0974986	0.0912233	14.60347	0.1853408	97.4452	39.56836	0.4967943	0.4968698	0.0000856	7.441612	0.0667274	1.243922	0.0514409
1842-01N	130819-07	phengite	2.1	DT-31D	149.66	0.033103	138.256	1.166169	8.791145	0.1166268	0.1495467	0.089709	-0.1275093	0.0809733	0.0118825	0.0008796	468.7924	3.583987276	-0.1842019	0.1170008	15.30447	0.2443548	97.39109	41.44637	0.6543058	0.6543686	0.0000874	7.409925	0.0636357	1.571969	0.0610819
1842-01O	130819-07	phengite	2.2	DT-31D	149.66	0.033103	115.5478	1.165794	7.339251	0.1166261	0.111171	0.0903001	0.0124063	0.0809733	0.0113868	0.0008795	391.3694	2.992076937	0.0214755	0.1401663	15.27154	0.292268	97.06367	41.3582	0.78264	0.7826923	0.0000983	7.890748	0.0635585	1.882349	0.0685358
1842-01P	130819-07	phengite	2.3	DT-31D	149.66	0.033103	71.19546	1.164888	4.790934	0.1251139	-0.2072093	0.0903001	0.1545866	0.0799067	0.0073659	0.0009677	255.4791	1.953175212	0.41007	0.2122379	14.40784	0.452175	96.99392	39.0439	1.212374	1.212404	0.0001007	13.7196	0.0673202	3.082299	0.0633086
1842-01Q	130819-07	phengite	2.5	DT-31D	149.66	0.033103	54.18776	1.165744	3.237206	0.1260723	0.147173	0.0903609	0.0680378	0.0806073	0.0094645	0.0008794	172.6258	1.319749033	0.2672028	0.3167378	15.87017	0.720079	94.85659	42.96051	1.926552	1.926575	0.0001723	9.764175	0.0597704	4.449782	0.1065233
1842-01R	130819-07	phengite	3	DT-31D	149.66	0.033103	109.2164	1.166058	5.001059	0.1169591	0.0697291	0.0907013	-0.1144138	0.081736	0.0485041	0.0010115	266.6842	2.038839289	-0.2910614	0.2080427	18.91586	0.5036539	86.69001	51.09109	1.341539	1.341586	0.0004458	2.351649	0.0458293	2.57051	0.1885753
110909-08																															
1843-01A	110909-08	muscovite	0.5	DT-31D	149.66	0.033103	-0.0481864	1.165552	0.1022307	0.1159795	0.0495522	0.0893977	-0.1502542	0.0809733	-0.000621	0.000888	5.45151	0.02147737	-18.70544	23.49366	0.6533809	11.57874	-140.3398	1.788748	31.6834	31.6834	0.0080499	2429.886	-2.147902	-2421.437	0.9943863
1843-01B	110909-08	muscovite	0.8	DT-31D	149.66	0.033103	39.566	1.165331	1.70623	0.1290894	-0.1230398	0.0903001	0.0293419	0.0795724	0.0047807	0.0010238	90.58565	0.35845723	0.2189426	0.5939817	14.81141	1.324778	63.90601	40.12562	3.549902	3.549913	0.0012089	3.650984	0.0431465	8.119893	0.2926168
1843-01C	110909-08	muscovite	1	DT-31D	149.66	0.033103	253.4887	1.166402	12.45695	0.1187426	0.0133524	0.0903609	-0.052973	0.0799067	0.057052	0.0010656	664.2738	2.617046819	-0.0541598	0.0816985	18.96572	0.2052001	93.26677	51.22389	0.546534	0.5466482	0.0002255	1.933408	0.0491765	1.058456	0.1034661
1843-01D	110909-08	muscovite	1.1	DT-31D	149.66	0.033103	343.031	1.16691	17.95743	0.1173091	0.1797132	0.0903609	0.0694163	0.0806073	0.0352983	0.0012569	957.5906	3.772627735	0.0492498	0.0571907	18.50548	0.1388446	96.93656	49.99766	0.3700494	0.3702102	0.0001026	3.606662	0.0523826	0.736553	0.0435626
1843-01E	110909-08	muscovite	1.2	DT-31D	149.66	0.033103	341.9872	1.167472	17.4179	0.1270629	0.1903951	0.089709	0.0770964	0.0795724	0.0420423	0.0010159	928.6539	3.65862997	0.0564312	0.0582572	18.90701	0.1543802	96.33981	51.06752	0.4112144	0.4113653	0.0001226	2.466678

Lab ID#	Sample	Material	Pwr_Ach ieved (W)	Irrad.	J x 10e-5	J_err (±1σ)	40Ar	40Ar_err (±1σ)	39Ar	39Ar_err (±1σ)	38Ar	38Ar_err (±1σ)	37Ar	37Ar_err (±1σ)	36Ar	36Ar_err (±1σ)	39Ar x 10e-18 (mol)	39Ar cum% of total	Ca/K	Ca/K_err (±1σ)	40Ar*/39Ar	40Ar*/39Ar_err (±1σ)	%40Ar*	Age (Ma)	Age_err (±1σ)	Age_err_sl (±1σ)	isochron 36Ar/40Ar	pct isochron 36Ar/40Ar_e rr (±%1σ)	isochron 39Ar/40Ar	pct isochron 39Ar/40Ar_e rr (±%1σ)	Err_Corr_3 6Ar/39Ar
1844-01L	130819-08b	muscovite	1.9	DT-31D	149.66	0.033103	106.61	1.165416	4.737385	0.1166252	0.0438156	0.0900301	-0.0955089	0.0813496	0.0070221	0.0008747	252.6249	1.125867252	-0.260158	0.2216819	22.03295	0.5980923	97.98873	59.37503	1.585892	1.585945	0.0000674	12.3707	0.0444737	2.693269	0.0358681
1844-01M	130819-08b	muscovite	2	DT-31D	149.66	0.033103	86.43814	1.165598	3.519757	0.118368	-0.1546899	0.0900301	0.1196323	0.0799067	0.0061534	0.0008578	187.6939	0.836490837	0.4387553	0.2934317	24.03982	0.8769866	97.92885	64.68868	2.318662	2.318705	0.0000694	14.53692	0.0407361	3.624149	0.0345163
1844-01N	130819-08b	muscovite	2.1	DT-31D	149.66	0.033103	114.2332	1.165897	4.82521	0.1150703	0.1277873	0.0900301	0.0644931	0.0795724	0.0076546	0.0008748	257.3083	1.146739377	0.172599	0.2129944	23.19482	0.6061547	98.03019	62.45323	1.604569	1.604627	0.000066	11.7814	0.0422638	2.59427	0.0340831
1844-01O	130819-08b	muscovite	2.2	DT-31D	149.66	0.033103	114.3596	1.165694	4.73202	0.1255902	0.0379801	0.0907013	0.1726053	0.0806073	0.0061388	0.000866	252.339	1.124592229	0.4711978	0.2204063	23.78844	0.6801718	98.46989	64.02394	1.798957	1.799011	0.0000512	14.98532	0.041394	2.84383	0.0243821
1844-01P	130819-08b	muscovite	2.3	DT-31D	149.66	0.033103	111.5636	1.16595	4.360751	0.1180049	0.1468763	0.0903609	-0.0609485	0.0806073	0.0073391	0.0008747	232.5407	1.036357979	-0.1806143	0.2389212	25.05575	0.7312763	98.01383	67.37274	1.930586	1.930641	0.0000665	11.96796	0.0391183	2.900621	0.0314644
1844-01Q	130819-08b	muscovite	2.5	DT-31D	149.66	0.033103	263.8183	1.166843	10.63776	0.129615	0.1811968	0.0914104	0.3171486	0.0809734	0.0112904	0.001043	567.2675	2.52812588	0.3855416	0.0985472	24.48757	0.3193406	98.78201	65.87212	0.8437579	0.8438793	0.0000408	9.780593	0.0403396	1.296527	0.0154271
1844-01R	130819-08b	muscovite	3	DT-31D	149.66	0.033103	892.4495	1.168587	35.94716	0.1270896	0.5336999	0.0910512	1.576192	0.0806076	0.0359434	0.0010401	1916.913	8.543052814	0.5672279	0.0290777	24.54196	0.0931212	98.8844	66.01582	0.2460243	0.2464419	0.0000374	3.147316	0.040292	0.3771373	0.0144454
130819-08																															
1845-01A	130819-08	phengite	0.5	DT-31D	149.66	0.033103	0.0036356	1.165552	-0.0565299	0.1156685	0.1717018	0.0903609	-0.0563207	0.0813496	0.0000761	0.0008256	-3.014507	-0.012512544	12.8931	32.29201	0.655095	21.28731	-1011.053	1.793439	58.24924	58.24924	0.0372141	32065.58	-15.43368	-32060.28	0.9997934
1845-01B	130819-08	phengite	0.8	DT-31D	149.66	0.033103	139.1308	1.165897	7.170058	0.1150711	0.1115666	0.0903609	0.0062032	0.0809733	0.0929086	0.0011275	382.3497	1.587048078	0.0111998	0.146198	15.52581	0.3012457	80.06505	42.03896	0.8063807	0.8064331	0.0000677	1.481936	0.051569	1.810523	0.2617283
1845-01C	130819-08	phengite	1	DT-31D	149.66	0.033103	345.0131	1.166778	17.01461	0.1150783	0.1145338	0.0903609	0.0969858	0.0806073	0.0704759	0.0010904	907.3191	3.766078893	0.0738181	0.0613541	19.03126	0.1471152	93.91311	51.39845	0.3917923	0.3919527	0.0002039	1.598007	0.0493468	0.7562238	0.0946436
1845-01D	130819-08	phengite	1.1	DT-31D	149.66	0.033103	498.1205	1.167472	22.59338	0.1256036	0.1290731	0.0893977	0.1921009	0.0806073	0.0464812	0.001363	1204.813	5.000905196	0.1109439	0.0463054	21.42374	0.1310908	97.231	57.75894	0.3479054	0.3481326	0.0000927	2.973948	0.0453847	0.6033592	0.0306147
1845-01E	130819-08	phengite	1.2	DT-31D	149.66	0.033103	811.5428	1.169485	35.45528	0.1307069	0.4666412	0.0910512	0.2758927	0.0799067	0.0608512	0.0010734	1890.686	7.847807365	0.1010216	0.0292612	22.36694	0.0892809	97.77801	60.26041	0.2366213	0.2369843	0.0000744	1.796664	0.0437154	0.3958435	0.0292006
1845-01F	130819-08	phengite	1.3	DT-31D	149.66	0.033103	1242.734	1.170468	53.22743	0.1291647	0.7021377	0.0893977	0.0677424	0.0813496	0.0828574	0.0011582	2838.403	11.78156306	0.0165285	0.0198486	22.86831	0.0600495	98.01207	61.58872	0.1590339	0.1595971	0.0000666	1.412353	0.0428593	0.2603078	0.0241295
1845-01G	130819-08	phengite	1.4	DT-31D	149.66	0.033103	1190.158	1.171535	49.85312	0.1247114	0.6435851	0.0910512	0.1553743	0.0795724	0.1010173	0.0012174	2658.465	11.03468037	0.0404903	0.0207367	23.25473	0.0631693	97.47223	62.61181	0.1672029	0.1677563	0.0000847	1.219279	0.041915	0.2688369	0.0295614
1845-01H	130819-08	phengite	1.5	DT-31D	149.66	0.033103	965.9181	1.169485	41.1031	0.1286173	0.616089	0.0910512	0.1926917	0.0795724	0.0595063	0.0011002	2191.862	9.097917458	0.0609266	0.0251605	23.05538	0.0779712	98.17094	62.08409	0.2064414	0.2068824	0.0000613	1.876617	0.0425805	0.3355357	0.0232814
1845-01I	130819-08	phengite	1.6	DT-31D	149.66	0.033103	909.9838	1.169485	38.32598	0.1296509	0.3781198	0.0907013	0.1776269	0.0806073	0.0451237	0.0010105	2043.77	8.483219089	0.0602674	0.0273502	23.37894	0.0851447	98.52833	62.94057	0.2253289	0.2257441	0.0000493	2.276158	0.0421441	0.3618906	0.020052
1845-01J	130819-08	phengite	1.7	DT-31D	149.66	0.033103	957.5961	1.168587	39.80172	0.1180505	0.4877083	0.0903014	0.2121873	0.0792488	0.0477426	0.0009929	2122.466	8.809865029	0.0693489	0.0259016	23.68865	0.0765208	98.52217	63.76	0.2024158	0.2028897	0.0000495	2.116607	0.0415905	0.3207364	0.0219374
1845-01K	130819-08	phengite	1.8	DT-31D	149.66	0.033103	619.6884	1.168501	26.19957	0.1173198	0.3225343	0.089709	0.030425	0.0806073	0.0345469	0.0010017	1397.118	5.799113091	0.0151117	0.0403066	23.24398	0.1138228	98.33777	62.58336	0.3012823	0.3015895	0.0000557	2.935414	0.0423068	0.485885	0.0249301
1845-01L	130819-08	phengite	1.9	DT-31D	149.66	0.033103	746.0864	1.168587	31.81879	0.1265879	0.4159021	0.0910512	0.1321371	0.081736	0.0398276	0.0010217	1696.768	7.042892751	0.0540595	0.0334403	23.06153	0.0993016	98.41493	62.10036	0.2629148	0.2632614	0.0000531	2.606849	0.0426749	0.4275799	0.0220103
1845-01M	130819-08	phengite	2	DT-31D	149.66	0.033103	911.7414	1.169485	38.09053	0.1280995	0.497599	0.0903014	0.047656	0.0806073	0.0390119	0.0011961	2031.215	8.431103685	0.0162924	0.0275578	23.61529	0.0856692	98.72508	63.56595	0.2266396	0.2270605	0.0000427	3.094309	0.0418056	0.3599416	0.0147729
1845-01N	130819-08	phengite	2.1	DT-31D	149.66	0.033103	511.3725	1.168008	20.95173	0.1159926	0.2884116	0.0903609	0.1718176	0.0809733	0.0179781	0.0009296	1117.272	4.637536102	0.106866	0.0503667	24.14038	0.1454345	98.96709	64.95454	0.384458	0.384717	0.0000346	5.314335	0.0409965	0.598927	0.0163912
1845-01O	130819-08	phengite	2.2	DT-31D	149.66	0.033103	104.9895	1.164953	4.242028	0.1176489	0.0949503	0.0903014	-0.0339697	0.0813496	0.0063562	0.0008619	226.2104	0.938946712	-0.1043911	0.2500098	24.28105	0.7298021	98.17865	65.32637	1.928849	1.928902	0.000061	13.66775	0.0404343	2.987011	0.0301583
1845-01P	130819-08	phengite	2.3	DT-31D	149.66	0.033103	106.7256	1.166003	4.628299	0.118005	0.24875	0.0903014	0.1560635	0.0809733	0.0068739	0.0008703	246.8088	1.024445413	0.4397243	0.2284257	22.62588	0.6322231	98.15935	60.94655	1.674954	1.675007	0.0000617	13.43068	0.0433837	2.774539	0.0320324
1845-01Q	130819-08	phengite	2.5	DT-31D	149.66	0.033103	431.4393	1.167472	17.51205	0.1173086	0.2220452	0.0903609	0.8003056	0.0799068	0.0149551	0.0009455	933.8481	3.876184167	0.5961754	0.0596592	24.39691	0.1773319	99.05655	65.63257	0.4686055	0.4688224	0.0000316	7.009527	0.0406021	0.7227066	0.014455
1845-01R	130819-08	phengite	3	DT-31D	149.66	0.033103	88.86786	1.165552	3.854664	0.1251136	-0.072993	0.0907013	0.0807395	0.0806073	0.002815	0.0009229	205.5539	0.853206082	0.273344	0.2730408	22.83358	0.8038288	99.09115	61.49674	2.12895	2.128992	0.0000304	34.50233	0.0433971	3.501304	0.01424
110825-14 2																															
1847-01A	110825-14	muscovite	0.5	DT-31D	148.73	0.07529	-0.0691583	1.165331	-0.1473354	0.1162982	-0.0589483	0.0907013	0.0168371	0.0799067	-0.0001049	0.0008287	-7.856815	-0.043513888	-1.492379	7.179916	0.222416	8.079117	47.46015	0.6053159	21.98407	21.98407	0.0017598	1820.707	2.133846	1686.864	0.9244681
1847-01B	110825-14	muscovite	0.8	DT-31D	148.73	0.07529	80.94767	1.164888	2.749499	0.1280608	0.0091983	0.089709	-0.1371587	0.0806073	0.0453307	0.0010043	146.62	0.812034259	-0.6516906	0.3841956	24.4666	1.22025	83.19442	65.41495	3.204985	3.20506	0.0005629	2.648952	0.0340033	4.873092	0.1604323
1847-01C	110825-14	muscovite	1	DT-31D	148.73	0.07529	430.8333	1.167697	23.7061	0.1173161	0.0364965	0.0907013	-0.0788687	0.0802517	0.0399319	0.0010345	1264.153	7.001335643	-0.0434782	0.0442411	17.65628	0.1011537	97.22003	47.44017	0.2682948	0.2693402	0.0000931	2.614481	0.0550626	0.5642308	0.0497984
1847-01D	110825-14	muscovite	1.1	DT-31D	148.73	0.07529	474.1515	1.167851	26.41328	0.1180247	0.4367714	0.0903014	0.2229198	0.0802518	0.0176055	0.0009687	1408.516	7.800871452	0.1103337	0.0397235	17.74585	0.0914624	98.91581	47.67772	0.2425586	0.2437257	0.0000363	5.685255	0.0557402	0.5102586	0.020913
1847-01E	110825-14	muscovite	1.2	DT-31D	148.73	0.07529	1121.965	1.170468	60.27201	0.1271529	0.7837357	0.0910512	0.1678791	0.0806073	0.0327844	0.0009772	3214.07	17.80067459	0.0364264	0.0174904	18.44194	0.0437569	99.13499	49.52281	0.1159266	0.1185357	0.000029	3.036391	0.0537552	0.2353567	0.0152297
1847-01F	110825-14	muscovite	1.3	DT-31D	148.73	0.07529	995.5351	1.170468	54.34362	0.1192009	0.7271611	0.0907013	0.1118537	0.0809733	0.0287031	0.0009883	2897.933	16.04978987	0.0269367	0.0195002	18.15063	0.045595	99.14488	48.75088	0.1208473	0.1232766	0.0000286	3.500542	0.0546234	0.2488758	0.0158673
1847-01G	110825-14	muscovite	1.4	DT-31D	148.73	0.07529	681.5296	1.168169	35.96146	0.1169964	0.4261884	0.0903014	0.0989551	0.0795724	0.0147443	0.0010908	1917.684	10.62082129	0.0360245	0.0289684	18.81823	0.0699038	99.36094	50.51947	0.1850974	0.1868082	0.0000214	7.535037	0.0528004	0.3677395	0.0106031
1847-01H	110825-14	muscovite	1.5	DT-31D	148.73	0.07529	471.8477	1.164888	24.92611	0.1323226	0.1485457	0.0903014	0.0128557	0.0802517	0.0115604	0.0009288	1397.118	7.916532483	0.0148509	0.0421219	18.7772	0.1107257	99.80494	50.41189	0.2704849	0.2710247	0.0000247	8.070559	0.0528629	0.5857899	0.0123744
1847-01I	110825-14	muscovite	1.6	DT-31D	148.73	0.07529	564.6596	1.168008	29.27156	0.1176734	0.5848345	0.0907013	0.0896996	0.0809733	0.0135189	0.0009134	1560.939	8.645032982	0.0401468	0.0362415	19.14193	0.0871919	99.29516	51.37638	0.2307665	0.2321872	0.0000236	6.930021	0.0518731	0.4521168	0.0136568
1847-01J	110825-14	muscovite	1.7	DT-31D	148.73	0.07529	477.7246	1.167255	24.86501	0.131229	0.4590254	0.0900301	-0.076801	0.081736	0.007952	0.0010232	1325.954	7.343606953	-0.0404798	0.0430815	19.1026	0.1118943	99.49671	51.27228	0.2961617	0.2972656	0.0000169	12.82112	0.0520854	0.5815753	0.0080068
1847-01K	110825-14	muscovite	1.8	DT-31D	148.73	0.07529	274.8031	1.166586	14.18444	0.1176542	0.1744712	0.089709	0.0513976	0.0806073	0.0059501	0.0008978	756.4014	4.189218191	0.0475832	0.0746263	19.23761	0.1805312	99.36264	51.62961	0.4777367	0.4784312	0.0000213	15.48252	0.0516502	0.9318163	0.0124921
1847-01L	110825-14	muscovite	1.9	DT-31D	148.73	0.07529	286.5438	1.166713	14.91972	0.1145088	0.1451948	0.0910512	0.2924345	0.0799067	0.0077948	0.0010104	795.6115	4.406375044	0.2574815	0.0703837	19.04943	0.1670763	99.23757	51.13155	0.4422514	0.4429874	0.0000255	13.93586	0.0520948	0.8689364	0.0136912
1847-01M	110825-14	muscovite	2	DT-31D	148.73	0.07529	151.0815	1.165552	7.888157	0.1166264	0.0750701	0.0907013	0.0626223	0.0806073	0.0083483	0.0010232	420.6452	2.329680326	0.1043244	0.134295	18.82917	0.3175941	98.36977	50.54844	0.8409404	0.8413191	0.0000546	12.53535	0.0522433	1.667779	0.0284696
1847-01N	110825-14	muscovite	2.1	DT-31D	148.73	0.07529	124.496	1.165744	6.008861	0.1169594	0.0375845	0.0917789	-0.0496252	0.0806073	0.0118886	0.0010364	320.4296	1.774650942	-0.1085668	0.17636	20.1085	0.4398812	97.12714	53.93278	1.162586	1.162897	0.0000962	8.77582	0.0483015	2.159875	0.0462588
1847-01O	110825-14	muscovite	2.2	DT-31D	148.73	0.07529	88.68766	1.164888	4.122808	0.1162987	0.0220078	0.0908609	-0.1512388	0.0806073	0.0076883	0.0009856	219.8536	1.217625953	-0.4820403	0.2574719	20.91471	0.6578818	97.32134	56.06232	1.736756	1.736981	0.0000897	12.57278	0.0465325	3.110935	0.0441098
1847-01P	110825-14	muscovite	2.3	DT-31D	148.73	0.07529	66.16068	1.165744	2.857393	0.1166248	0.1235343	0.0903609	-0.0283573	0.0802517	0.0206669	0.0009143	152.3739	0.843899564	-0.1306	0.3696392	20.97556	0.9531704	90.65965	56.22294	2.516036	2.516192	0.0003128	4.800292	0.0432216	4.445349	0.1454945
1847-01Q	110825-14	muscovite	2.5	DT-31D	148.73	0.07529	32.74968	1.165461	1.40212	0.1180044	0.0240343	0.0907013	0.2164212	0.0802518	0.0100711	0.0008794	74.76976	0.414100705	2.03197	0.7726438	21.30252	1.987748	91.14859	57.08579	5.244486	5.244563	0.0002965	9.830486	0.0427877	9.147617	0.1408354
1847-01R	110825-14	muscovite	3	DT-31D	148.73	0.07529	103.1061	1.165646	4.849153	0.1159802	-0.0734876	0.0907013	0.0597669	0.0806073	0.0040994	0.0008499	258.5869	1.432143952	0.1623126	0.2189446	21.00267	0.5594519	98.83413	56.29451	1.476699	1.476966	0.000039	21.40579	0.0470579	2.645748	0.0225684
110830-03 2																															
1848-01A	110830-03	muscovite	0.5	DT-31D	148.73	0.07529	-0.1024301	1.165461	-0.0956736	0.1159795	0.1995935	0.0893977	-0.1281986	0.0802517	0.0000348	0.0008319	-5.101913	-1.467092567	17.65236	24.08366	1.743587	12.77406	161.1632	4.739898	34.68103	34.68103	-0.0020486	-1206.625	0.9243196	1144.395	0.9375479
1848-01B	110830-03	muscovite	0.8	DT-31D	148.73	0.07529	28.36595	1.165373	0.1928375	0.1159795	0.0033628	0.0907013	0.2247905	0.0799067	0.0444294	0.0010292	10.2833	2.957037917	15.36219	10.73251	79.60278	48.75476	53.63035	204.7823	118.6617	118.6617	0.0015531	4.73599	0.0067372	60.86886	0.0585509
1848-01C	110830-03	muscovite	1	DT-31D	148.73	0.07529	62.4787	0.0603075	0.297552	0.0592041	0.1371884	0.0450146	0.2451723	0.0445585	0.0860881	0.0010636	15.86733	4.567296819	10.86629	2.928261	124.6752	25.03282	59.01134	311.3202	2.941178	57.41197	0.0013729	1.246849	0.0047332	20.03429	0.300373
1848-01D	110830-03	muscovite	1	DT-31D	148.73	0.07529	31.09565	1.165331	0.0182803	0.1156685	-0.1724931	0.0907013	0.2648649	0.0802518	0.0328472	0.0009485	0.9748209	0.280316537	191.2239	1211.353	1330.041	9563.896	68.85426	1997.272	8741.242	8741.242	0.0010432	4.771627	0.0005177	719.0484	0.0040934
1848-01E	110830-03	muscovite	1.1	DT-31D	148.73	0.07529	130.6177	1.16595	0.7332992	0.1145021	-0.0552888	0.0907013	0.4593289	0.0795724	0.1174943	0.0012631	39.1041	11.24466735	8.269872	1.928716	131.184	20.66041	73.31549	326.2045	47.05644	47.05668	0.0008938	1.407393	0.0055888	15.72172	0.0360122
1848-01F	110830-03	muscovite	1.2	DT-31D	148.73	0.07529	132.4111	1.165744	0.332225	0.1153651	-0.0673554	0.0907013	0.2569879	0.0792488	0.1086454	0.0011847	17.71632	5.094454772	10.21624	4.744541	303.0307	105.9741	75.59564	680.9015	198.8432	198.8434	0.0008174	1.410197	0.0024947	34.96071	0.015722
1848-01G	110830-03	muscovite	1.3	DT-31D	148.73	0.07529	160.4212	1.166113	0.5444356	0.1166245	-0.1287764	0.0900301	0.3985774	0.0799067	0.1107414	0.0012748	29.03272	8.348566605	9.672341	2.837787	235.5466	50.81781	79.50844	549.685	102.4388	102.4391	0.0006863	1.372568	0.0033755	21.56459	0.0178523
1848-01H	110830-03	muscovite	1.4	DT-31D	148.73	0.07529	97.38292	1.16595	0.5726509	0.1176483	-0.008506	0.0914104	0.4309716	0.0802518	0.0600972	0.0010533	30.53734	8.78122992	9.946701	2.757988	139.8758	28.99661	81.79488	345.8949	65.33635	65.33654	0.0006098	2.152268	0.0058477	20.70852	0.0321632
1848-01I	110830-03	muscovite	1.5	DT-31D	148.73	0.07529	134.9982	1.166402	0.7598255	0.1180044	0.1209627	0.0907013	0.4090144	0.0799067	0.069863	0.0015363	40.51867	11.65143094	7.119193	1.776758	151.0678	23.62616	84.70502	370.941	52.51184	52.51212	0.0005123	2.391579	0.0056071	15.6243	0.0199788
1848-01J	110830-03	muscovite	1.7	DT-31D	148.73	0.07529	267.7563	1.166169	1.025288	0.1159584	0.0814001	0.0910512	0.4197469	0.0802518	0.0099402	0.0012218	54.67479	15.7221261	5.416294	1.209804	264.8155	122.3917	14.06103	79.32831	306.0688	32.73802	0.0006924	1.346616	0.0064815	11.47031	0.0353787
1848-01K	110830-03	muscovite	1.7	DT-31D	148.73	0.07529	81.93298	1.165506	0.5803008	0.1169584	0.0488598	0.0893977	0.3347735	0.0809734	0.0244755	0.0010989	30.9453	8.898536172	7.635071	2.403836	129.4229	26.29548	91.28843	322.1892	60.0225	60.02268	0.0002918	4.845961	0.0070535	20.30204	0.0205687
1848-01L	110830-03	muscovite	1.8	DT-31D	148.73	0.07529	36.18368	1.165461	0.0106304	0.1153651	0.2146273	0.0910512	0.4083252	0.0806074	0.0108585	0.0008795	0.5668802	0.163010285	508.541	5519.791	4577.98	72968.96	91.63977	3761.448	25435.49	25435.49	0.00028	9.356006	0.0002002	1593.88	0.0006957
1848-01M	110830-03	muscovite	1.9	DT-31D	148.73	0.07529	41.21408	1.16474	0.519797	0.1153652	-0.0127589	0.0900301	0.4342209	0.0799067	0.0121614	0.0008935	27.71886	7.970749664	11.06373	3.189792	73.17824	16.51912	91.71499	189.0787	40.55147	40.55158	0.0002775	8.391704	0.0125331	22.52777	0.0422486
1848-01N	110830-03	muscovite	2	DT-31D	148.73	0.07529	27.91436	1.165248	0.2415188	0.1237209	0.1065224	0.0900301	0.5272682	0.0795724	0.0089133	0.0008748	12.87931	3.70353406	28.93424	15.45174	107.56	56.34688	91.43503	271.5916	132.2238	132.2238	0.0002869	11.81598	0.0085008	52.34096	0.0281763
1848-01O	110830-03	muscovite	2.1	DT-31D	148.73	0.07529	30.55934	1.164826	0.1369037	0.1265604	0.0791253	0.0903609	0.6975104	0.0802518	0.0102293	0.0008839	7.300573	2.099323994	67.54931	62.92762	212.3601	205.2223	91.16543	502.3384	424.5299	424.53	0.0002959	10.59966	0.042093	96.61332	0.0141879
1848-01P	110830-03	muscovite	2.2	DT-31D	148.73	0.07529	26.59591	1.164713	-0.0666636	0.1159795	-0.0227485	0.0910512	0.4405225	0.0802518	0.0092568	0.0008621	-3.554824	-1.022243044	-87.64343	153.3134	-341.7539	563.8517	90.43449	-1299.172	3121.363	3121.364	0.0003204	11.1399	-0.002646	-164.9689	0.0104361
1848-01Q	110830-03	muscovite	2.3	DT-31D	148.73	0.07529	27.67258	1.164888	0.0911036	0.1166245	0.050838	0.089709	0.4288055	0.0799068	0.0092514	0.0008705	0.83822	1.397014583	6.214806	0.8077053	286.8772	382.4786	90.80654	650.3383	729.7444	729.7445	0.0003079	11.16389	0.0031653	133.3027	0.0119101
1848-01R	110830-03	muscovite	2.5	DT-31D	148.73	0.07529	40.23904	1.165598	0.2163834	0.1241788	-0.2941481	0.089709	0.9928003	0.0813497	0.0159492	0.0010567	11.53894	3.318099013	60.89565	35.30143	172.6634	103.2015	89.36181	418.321	223.5152	223.5153	0.0003563	7.977419	0.0051755	59.73955	0.0176073
1848-01S	110830-03	muscovite	3	DT-31D	148.73	0.07529	76.91609	1.166003	0.4106118	0.1180044	0.0245288	0.089709	1.822448	0.0802521	0.0309946	0.0009709	21.89645	6.29646548	59.0345	17.16374	173.3264	51.83716	89.16242	419.7564	112.1816	112.1817	0.000363	3.824899	0.0051442	29.88318	0.0201063
130817-11																															
1849-01A	130817-11	muscovite	0.5	DT-31D	148.73	0.07529	-0.1738926	1.165416	-0.2455921	0.1223854	-0.0648827	0.0903609	-0.0424375	0.0802517	0.0001125	0.0008287	-13.09655	-0.057327567	2.299174	4.496301	0.9472174	4.8807	133.6757	2.57651	13.26657	13.26657	-0.0011279	-795.3096	1.411246	672.0486	0.8403644
1849-01B	130817-11	muscovite	0.8	DT-31D	148.73	0.07529	245.41	1.166284	5.589506	0.1166254	0.0954448	0.0893977	0.0990536	0.0809733	0.0771736	0.0010998	298.0683	1.304735687	0.2358787	0.1928866	39.77105	0.8578625	90.63178	105.1759	2.20469	2.205297	0.0003138	1.515837	0.0227884	2.14028	0.069617
1849-01C	130817-11	muscovite	1	DT-31D	148.73	0.07529	669.2296	1.168587	12.23699	0.1166289	0.2512227	0.089709	0.0616377	0.0792488	0.1112507	0.0011861	652.5546	2.856430882	0.0670684	0.0862336	51.94435	0.5050818	95.0421	136.1966	1.276234	1.277963	0.0001661	1.088312	0.0182969	0.9690041	0.028914
1849-01D	130817-11	muscovite	1.1	DT-31D	148.73	0.07529	920.8215	1.170468	12.22924	0.1169628	0.289005	0.0907013	-0.1188446	0.0809733	0.0500859	0.0010905	652.1415	2.854621831	-0.1294435	0.0882035	74.01303	0.7147913	98.37032	191.1268	1.752722

Lab ID#	Sample	Material	Pwr_Achieved (W)	Irrad.	J x 10e-5	J_err (±1σ)	40Ar	40Ar_err (±1σ)	39Ar	39Ar_err (±1σ)	38Ar	38Ar_err (±1σ)	37Ar	37Ar_err (±1σ)	36Ar	36Ar_err (±1σ)	39Ar x 10e-18 (mol)	39Ar cum% of total	Ca/K	Ca/K_err (±1σ)	40Ar*/39Ar	40Ar*/39Ar_err (±1σ)	%40Ar*	Age (Ma)	Age_err (±1σ)	Age_err_tJ (±1σ)	isochron 36Ar/40Ar	pct isochron 36Ar/40Ar_err (±%1σ)	isochron 39Ar/40Ar	pct isochron 39Ar/40Ar_err (±%1σ)	Err_Corr_36Ar/39Ar
1846-04A	FCT-D13	sanidine	13	DT-31D	148.73	0.07529	2436.939	1.178132	229.5565	0.132584	2.994396	0.0907015	0.3402874	0.0809734	0.0259648	0.0015285	12240.4	6.831176254	0.0155849	0.0037085	10.57645	0.0082222	99.6875	28.56499	0.0220343	0.0262939	0.0000105	6.007981	0.0942542	0.0753203	0.005165
1846-05A	FCT-D13	sanidine	13	DT-31D	148.73	0.07529	5477.506	1.199873	523.8435	0.1544464	6.816344	0.090362	0.6989873	0.0817361	0.0404271	0.0018863	27932.35	15.58861229	0.0140337	0.001641	10.42772	0.0039818	99.78477	28.16637	0.0106729	0.0177232	7.209E-06	4.78531	0.0956919	0.0367306	0.0027301
1846-06A	FCT-D13	sanidine	13	DT-31D	148.73	0.07529	2020.777	1.175242	177.5027	0.1376703	2.41787	0.0893978	0.3072039	0.0806073	0.5639072	0.0026283	9464.79	5.282151581	0.0182151	0.0047795	10.43055	0.0113495	91.67465	28.17398	0.0304213	0.0335524	0.0002789	0.4704462	0.0878905	0.0969436	0.0741657
1846-07A	FCT-D13	sanidine	13	DT-31D	148.73	0.07529	3736.366	1.184903	356.3679	0.1479177	4.889545	0.0900307	0.4828615	0.0802518	0.0251138	0.0017038	19002.23	10.60484864	0.0142655	0.0023709	10.45794	0.0056511	99.80486	28.24738	0.0151466	0.0207549	6.536E-06	6.991257	0.0954345	0.0522358	0.002754
1846-08A	FCT-D13	sanidine	13	DT-31D	148.73	0.07529	3348.97	1.183087	318.2582	0.1376783	4.158032	0.0914108	0.391685	0.0795724	0.0629533	0.0017997	16970.15	9.470774553	0.0129621	0.0026333	10.45806	0.0060939	99.44349	28.24771	0.0163335	0.0216363	0.0000186	2.888494	0.0950879	0.0558522	0.0077359
1846-09A	FCT-D13	sanidine	13	DT-31D	148.73	0.07529	3123.034	1.181353	251.9507	0.1378828	3.677544	0.0890966	0.5090526	0.0806074	1.637303	0.0051058	13434.51	7.497586168	0.0212873	0.0033708	10.44992	0.0095531	84.35418	28.2259	0.0256054	0.0292691	0.000524	0.3143435	0.0807223	0.0665279	0.0684245
1846-10A	FCT-D13	sanidine	13	DT-31D	148.73	0.07529	3925.642	1.184903	374.9934	0.1469762	4.74168	0.0907018	0.5017664	0.0806074	0.0329766	0.0015294	19995.39	11.15910902	0.0141028	0.0022656	10.43666	0.0053104	99.75416	28.19034	0.0142339	0.0200784	8.2342E-06	4.743679	0.0955805	0.0494702	0.0038824

Appendix 2.2. Table of zircon fission track ages

Field.no	total spots	accepted spots	sumNs	sumRho	sumRho (1σ)	Dpar.m	Dper.m	[U] ppm	[Th] ppm	[Sm] ppm	eU.ppm
110826-08	16	8	459	15.40	1.33	0	0	176.86	104.31	0.00	201.37
110825-03	1	0	-	-	-	-	-	-	-	-	-
110831-02	20	20	538	19.63	1.09	0	0	163.03	169.21	0.00	202.79
110823-06	20	18	1089	36.26	2.19	0	0	162.82	67.17	0.00	178.61
110909-04	21	20	1265	59.60	3.90	0	0	164.66	155.21	0.00	201.13
110909-03	21	16	530	36.01	2.50	0	0	148.17	135.06	0.00	179.91
110906-01	8	8	437	27.03	2.26	0	0	597.00	559.57	0.00	728.50
130819-06	5	5	40	7.41	0.09	0	0	134.05	192.90	0.12	179.38

Field.no	wm pz:sz UCa	wm pz:unk Ca	relerr pz:sz	relerr analyst	relerr deficit	relerr Ca apfu	pZeta	pZeta (1σ)	$\chi 2$	Q($\chi 2$)
110826-08	0.9563	1.0002	2.22E-02	0.203	0.000	0	1955899	12225.72	11.62	0.11
110825-03	-	-	-	-	-	-	-	-	-	-
110831-02	1.0033	1.0068	2.22E-02	0.203	0.173	0	1955899	12225.72	39.74	0.00
110823-06	0.9187	0.9901	7.87E-02	0.203	0.147	0	2496646	30158.46	35.70	0.01
110909-04	1.1017	1.0008	2.22E-02	0.203	0.454	0	1955899	12225.72	127.64	0.00
110909-03	0.9713	0.9993	2.22E-02	0.203	0.397	0	1955899	12225.72	77.23	0.00
110906-01	0.9472	0.9888	2.22E-02	0.203	0.000	0	1955899	12225.72	10.37	0.17
130819-06	0.9737	1.0010	-	0	0.211	0	6658103	206438.00	15.32	0.00

Field.no	**pooled age**	95%-CI	95%+CI	avgerror	geologic position
110826-08	**58.02**	10.32	12.54	11.43	Sella, Alp Munt
110825-03	**-**	-		-	base of Corvatsch teildecke
110831-02	**53.38**	7.00	8.05	7.53	Bernina nappe, near summit of Piz Roseg
110823-06	**74.55**	9.52	10.91	10.21	Margna augen gneiss Piz Lunghin
110909-04	**41.38**	5.50	6.34	5.92	Berhard nappe midway up hill
110909-03	**28.72**	4.35	5.12	4.73	Berhard nappe near Weisshornhütte
110906-01	**31.54**	5.52	6.69	6.11	augen gneiss base of Dente Blanche, Weisshorn
130819-06	**35.50**	9.82	13.57	11.70	Turba mylonite footwall

Fission track ages measured by Ray Donelick at A to Z, Inc.

Appendix 2.3. Table of zircon U-Th/He ages

Full Sample Name	lithology	nappe	CorrectDate.Ma	Full Unc. (Ma)	Lavg.µm	Wavg.µm	Dim Mass.µg	rs.µm	4He.ncc	±	U.ng	±	Th.ng	±	Sm.ng	±	RawDate.Ma	±	Ft	Analytic Unc. (Ma)
110823-06_zr1	augengneiss	Margna	32.11		141.25	53.15	1.57	57.93	3.771	0.004	1.391	0.023	0.490	0.012	-	-	20.70	0.20	0.64	0.20
110823-06_zr2	augengneiss	Margna	37.39		81.1	41.2	0.51	40.98	0.586	0.001	0.234	0.006	0.032	0.001	-	-	20.08	0.23	0.54	0.23
110823-06_zr3	augengneiss	Margna	42.45		124.75	49.9	1.21	53.46	1.075	0.002	0.313	0.006	0.100	0.002	-	-	26.37	0.20	0.62	0.20
110823-06_zr4	augengneiss	Margna	6129.41		196.15	45.7	1.72	55.60	2.908	0.008	0.004	0.001	0.000	0.000	-	-	3775.31	0.44	0.62	0.44
1108240 1z1	S-C mylonite, orthogneiss	Margna	24.11	1.70	261.18	99.3175	8.56	60.52	9.436	0.009	3.749	0.037	0.988	0.021	0.000	0.000	19.59	0.18	0.81	0.18
1108240 1z2	S-C mylonite, orthogneiss	Margna	24.48	1.75	246.735	95.01	7.69	59.65	6.147	0.004	2.493	0.029	0.283	0.019	0.005	0.006	19.85	0.22	0.81	0.22
1108240 1z3	S-C mylonite, orthogneiss	Margna	23.26	1.67	197.35	88.78	6.15	54.06	7.195	0.008	3.133	0.048	0.382	0.015	0.021	0.045	18.46	0.27	0.79	0.27
1108240 1z4	S-C mylonite, orthogneiss	Margna	22.96	1.64	223.495	110.275	8.48	64.85	3.887	0.003	1.605	0.023	0.388	0.004	0.000	0.000	18.94	0.25	0.82	0.25
1108240 1z5	S-C mylonite, orthogneiss	Margna	24.51	1.77	266.695	90.565	7.73	57.53	6.597	0.010	2.662	0.049	0.446	0.010	0.026	0.059	19.71	0.34	0.80	0.34
1108240 1z6	S-C mylonite, orthogneiss	Margna	22.45	1.60	207.95	92.68	5.83	56.11	13.576	0.013	5.982	0.084	1.163	0.020	0.000	0.000	17.94	0.24	0.80	0.24
110825-03_zr1	S-C mylonite, orthogneiss	Corvatsch	38.98		144.3	59.95	2.01	63.53	5.836	0.006	1.700	0.036	0.555	0.010	-	-	26.35	0.20	0.68	0.20
110825-03_zr2	S-C mylonite, orthogneiss	Corvatsch	52.03		136.9	84.5	3.50	78.37	5.761	0.005	0.976	0.018	1.067	0.014	-	-	38.75	0.18	0.74	0.18
110825-03_zr3	S-C mylonite, orthogneiss	Corvatsch	80.26		157.7	55.6	1.94	61.66	4.593	0.009	0.653	0.009	0.254	0.007	-	-	53.09	0.20	0.66	0.20
110825-03_zr4	S-C mylonite, orthogneiss	Corvatsch	35.62		146.15	71.05	2.78	71.71	14.622	0.008	4.335	0.100	1.754	0.056	-	-	25.46	0.24	0.71	0.24
110825-14_zr1	S-C mylonite, orthogneiss	Corvatsch	35.65		154.235	63.605	2.42	67.55	5.257	0.005	1.681	0.026	0.334	0.004	-	-	24.71	0.17	0.69	0.17
110825-14_zr2	S-C mylonite, orthogneiss	Corvatsch	30.45		244.355	98.87	9.30	105.58	24.571	0.010	6.385	0.089	8.447	0.157	-	-	24.24	0.18	0.80	0.18
110825-14_zr3	S-C mylonite, orthogneiss	Corvatsch	29.03		238.345	92.945	8.06	100.30	16.797	0.010	5.270	0.063	3.482	0.038	-	-	22.80	0.15	0.79	0.15
110825-14_zr4	S-C mylonite, orthogneiss	Corvatsch	31.26		249.6	122.17	14.01	123.03	115.501	0.095	31.138	0.625	24.426	0.249	-	-	25.87	0.18	0.83	0.18
110825-14_zr5	S-C mylonite, orthogneiss	Corvatsch	37.24		247.555	104.9	10.52	110.52	37.639	0.018	9.586	0.122	3.302	0.067	-	-	30.01	0.18	0.81	0.18
110825-14_zr6	S-C mylonite, orthogneiss	Corvatsch	51.11		280.775	136.16	19.61	137.54	32.283	0.037	5.688	0.079	2.050	0.043	-	-	43.17	0.19	0.84	0.19
110825-14_zr7	S-C mylonite, orthogneiss	Corvatsch	46.63		181.6	94	5.97	92.91	13.625	0.017	2.920	0.035	0.789	0.016	-	-	36.23	0.18	0.78	0.18
110830-03_zr1	monzodiorite	Bernina	43.68		164.825	82.345	4.19	82.37	5.655	0.005	1.084	0.012	1.455	0.028	-	-	32.74	0.18	0.75	0.18
110830-03_zr2	monzodiorite	Bernina	39.84		132.05	79.01	2.97	74.15	5.524	0.004	1.289	0.017	1.184	0.021	-	-	29.10	0.18	0.73	0.18
110830-03_zr3	monzodiorite	Bernina	32.12		147.57	79.87	3.47	77.73	2.063	0.003	0.587	0.008	0.562	0.010	-	-	23.71	0.18	0.74	0.18
110830-03_zr4	monzodiorite	Bernina	37.08		215.415	120.62	11.46	115.99	16.556	0.019	3.575	0.061	3.893	0.033	-	-	30.44	0.16	0.82	0.16
110906-01_zr1	orthogneiss	Dent Blanche	104.80		98.595	58.37	1.21	55.00	0.010	0.000	0.001	0.001	0.000	0.000	-	-	67.78	0.73	0.65	0.73
110906-01_zr2	orthogneiss	Dent Blanche	30.18		80.92	49.065	0.70	45.82	1.960	0.006	0.804	0.010	0.470	0.007	-	-	17.72	0.18	0.59	0.18
110907-02_zr1	S-C mylonite, augengneiss	Dent Blanche	33.83		406.77	166.385	43.75	177.13	59.404	0.032	15.151	0.187	6.019	0.074	-	-	29.62	0.16	0.88	0.16
110907-02_zr2	S-C mylonite, augengneiss	Dent Blanche	29.44		272.795	148.49	22.13	144.23	24.768	0.013	7.469	0.138	2.865	0.051	-	-	25.14	0.19	0.85	0.19
110907-02_zr3	S-C mylonite, augengneiss	Dent Blanche	23.11		337.26	128.715	21.96	139.74	46.408	0.021	18.485	0.289	5.199	0.124	-	-	19.47	0.20	0.84	0.20
110907-02_zr4	S-C mylonite, augengneiss	Dent Blanche	27.99		349.325	100.015	14.31	116.63	21.555	0.010	7.239	0.138	2.739	0.025	-	-	22.61	0.17	0.81	0.17
110907-02_zr5	S-C mylonite, augengneiss	Dent Blanche	25.54		284.97	107.655	13.00	117.21	18.206	0.011	6.578	0.107	2.828	0.041	-	-	20.78	0.18	0.81	0.18
110909-08_zr1	mylonitic orthogneiss	Bernhard	19.03		97.795	47.515	0.83	47.97	1.188	0.002	0.822	0.018	0.214	0.005	-	-	11.27	0.21	0.59	0.21
110909-08_zr2	mylonitic orthogneiss	Bernhard	35.66		115.675	50.615	1.14	52.81	0.449	0.001	0.147	0.003	0.089	0.001	-	-	22.13	0.20	0.62	0.20
110909-08_zr3	mylonitic orthogneiss	Bernhard	20.05		137.185	60.94	1.95	63.29	5.511	0.004	3.164	0.054	0.824	0.009	-	-	13.58	0.17	0.68	0.17
110909-08_zr4	mylonitic orthogneiss	Bernhard	30.17		175.94	84.735	4.76	85.79	0.913	0.006	0.297	0.006	0.140	0.004	-	-	22.86	0.24	0.76	0.24
13081618Az1	metafelsite	Tschirpen	43.75	3.07	165.775	99.085	4.51	53.83	5.902	0.006	1.359	0.014	0.202	0.001	0.017	0.056	34.65	0.34	0.79	0.34
13081618Az2	metafelsite	Tschirpen	56.17	3.96	165.695	89.53	3.95	51.03	6.055	0.006	1.065	0.012	0.319	0.004	0.000	0.000	43.82	0.46	0.78	0.46
13081618Az3	metafelsite	Tschirpen	33.79	2.36	130.91	87.39	2.57	45.10	3.819	0.005	1.203	0.016	0.149	0.002	0.014	0.042	25.49	0.31	0.75	0.31
13081618Az4	metafelsite	Tschirpen	37.13	2.63	153.965	82.205	3.08	46.63	2.198	0.002	0.618	0.009	0.102	0.002	0.000	0.000	28.27	0.38	0.76	0.38
13081618Az5	metafelsite	Tschirpen	33.41	2.34	144.895	84.8	2.94	46.68	2.366	0.002	0.726	0.007	0.182	0.002	0.000	0.000	25.43	0.21	0.76	0.21
13081618Az6	metafelsite	Tschirpen	47.03	3.36	145.41	68.275	2.14	40.42	4.269	0.004	1.002	0.017	0.117	0.001	0.000	0.000	34.22	0.54	0.73	0.54
13081618Az7	metafelsite	Tschirpen	43.91	3.13	128.16	69.305	1.83	39.48	1.635	0.002	0.407	0.007	0.083	0.001	0.002	0.012	31.66	0.49	0.72	0.49
1308170 3z1	phyllitic tectonite	Falknis Mandelschiefer	27.94	1.90	125.33	90.025	2.44	48.76	2.328	0.005	0.819	0.008	0.379	0.003	0.017	0.042	21.17	0.19	0.76	0.19
1308170 3z2	phyllitic tectonite	Falknis Mandelschiefer	44.90	3.20	144.515	55.82	1.55	34.99	1.470	0.005	0.365	0.005	0.122	0.002	0.000	0.000	30.80	0.37	0.68	0.37
1308170 3z3	phyllitic tectonite	Falknis Mandelschiefer	32.96	2.34	124.645	59.43	1.72	35.72	2.761	0.004	0.856	0.010	0.611	0.006	0.000	0.000	22.80	0.22	0.69	0.22
1308170 3z4	phyllitic tectonite	Falknis Mandelschiefer	57.09	4.04	115.785	66.79	1.94	38.11	3.802	0.005	0.728	0.007	0.175	0.002	0.007	0.027	40.79	0.37	0.71	0.37
1308170 3z5	phyllitic tectonite	Falknis Mandelschiefer	61.61	4.32	148.22	52.565	1.40	32.60	3.431	0.005	0.660	0.007	0.126	0.002	0.000	0.000	41.05	0.42	0.66	0.42
1308170 3z6	phyllitic tectonite	Falknis Mandelschiefer	41.04	2.86	113.69	64.63	1.36	35.87	1.240	0.003	0.330	0.004	0.128	0.002	0.000	0.000	28.45	0.30	0.69	0.30
1308171 1z1	greenschist granitoid	Silvretta	58.77	4.17	331.42	131.2	19.22	80.95	43.576	0.033	6.711	0.072	1.728	0.024	0.006	0.009	50.47	0.50	0.86	0.50
1308171 1z2	greenschist granitoid	Silvretta	50.68	3.63	231.68	96.38	7.21	59.36	11.467	0.011	2.148	0.031	0.672	0.006	0.000	0.000	41.02	0.54	0.81	0.54
1308171 1z3	greenschist granitoid	Silvretta	43.20	3.06	217.55	120.3	9.23	67.91	10.677	0.014	2.283	0.027	0.710	0.057	0.000	0.000	35.96	0.43	0.83	0.43
1308171 1z4	greenschist granitoid	Silvretta	40.14	2.86	249.8	98.16	8.23	61.23	15.996	0.035	3.883	0.049	0.644	0.005	0.000	0.000	32.74	0.39	0.81	0.39
1308171 1z5	greenschist granitoid	Silvretta	42.33	3.01	206.28	90.425	5.54	55.00	7.298	0.011	1.718	0.020	0.299	0.005	0.000	0.000	33.69	0.37	0.79	0.37
1308171 1z6	greenschist granitoid	Silvretta	61.91	4.39	215.58	91.24	5.95	55.78	8.550	0.015	1.368	0.013	0.244	0.005	0.000	0.000	49.45	0.46	0.80	0.46
1308171 2z1	greenschist granitoid	Silvretta	44.29	4.20	241.13	115.53	10.00	67.67	9.195	0.123	1.873	0.133	0.799	0.042	0.000	0.000	36.80	2.36	0.83	2.36
1308171 2z2	greenschist granitoid	Silvretta	46.42	3.97	261.185	154.03	17.36	84.32	29.419	0.032	5.809	0.310	1.016	0.042	0.000	0.000	40.14	1.99	0.86	1.99
1308171 2z3	greenschist granitoid	Silvretta	33.51	3.21	210.115	127.4	9.14	67.61	7.343	0.007	2.086	0.150	0.379	0.021	0.000	0.000	27.89	1.86	0.83	1.86
1308171 2z4	greenschist granitoid	Silvretta	30.57	3.30	207.205	156.795	12.27	83.98	9.895	0.007	2.994	0.264	0.487	0.054	0.000	0.000	26.30	2.16	0.86	2.16

Full Sample Name	lithology	nappe	CorrectDate.Ma	Full Unc. (Ma)	Lavg.µm	Wavg.µm	Dim Mass.µg	rs.µm	4He.ncc	±	U.ng	±	Th.ng	±	Sm.ng	±	RawDate.Ma	±	Ft	Analytic Unc. (Ma)
13081712z5	greenschist granitoid	Silvretta	48.27	3.71	215.34	101.605	7.04	60.35	13.830	0.013	2.852	0.094	0.228	0.019	0.028	0.059	39.29	1.23	0.81	1.23
13081712z6	greenschist granitoid	Silvretta	47.87	4.39	210.75	116.085	10.73	66.99	10.658	0.012	2.112	0.134	0.411	0.018	0.000	0.000	39.82	2.33	0.83	2.33
130818-04_zr1	sandstone	Grava	14.91	1.06	240.405	93.225	7.18	58.35	4.485	0.005	2.902	0.035	0.790	0.006	-	-	12.01	0.13	0.81	0.13
130818-04_zr2	sandstone	Grava	77.85	5.55	237.215	95.36	7.31	59.11	23.140	0.016	2.771	0.035	1.090	0.013	-	-	62.92	0.72	0.81	0.72
130818-04_zr3	sandstone	Grava	17.38	1.30	207.655	88.24	6.37	53.88	4.298	0.004	2.369	0.033	0.915	0.008	-	-	13.75	0.17	0.79	0.17
130818-04_zr4	sandstone	Grava	18.15	1.27	186.92	95.225	5.19	55.33	5.116	0.004	2.704	0.037	0.961	0.010	-	-	14.44	0.18	0.79	0.18
130818-04_zr5	sandstone	Grava	17.27	1.34	133.225	85.675	2.60	45.20	1.516	0.003	0.857	0.008	0.460	0.006	-	-	12.97	0.10	0.75	0.10
130818-04_zr6	sandstone	Grava	15.98	1.09	130.945	104.45	3.09	47.70	5.598	0.006	3.453	0.038	1.424	0.020	-	-	12.22	0.12	0.76	0.12
130818-04_zr7	sandstone	Grava	21.72	1.75	143.34	83.78	2.68	44.17	6.036	0.006	2.746	0.032	1.428	0.015	-	-	16.19	0.16	0.74	0.16
130818-04_zr8	sandstone	Grava	31.28	2.49	153.965	86.575	3.35	48.57	3.667	0.005	1.189	0.013	0.296	0.003	0.000	0.000	24.07	0.25	0.77	0.25
130818-04_zr9	sandstone	Grava	18.42	1.38	101.27	72.4	1.19	34.00	2.686	0.006	1.631	0.016	0.633	0.005	0.023	0.078	12.48	0.11	0.68	0.11
130819-06_zr1	metapelite	Turba MZ -12 m	16.83	91.61	139.05	60.205	1.62	36.01	0.001	0.000	0.000	0.003	0.002	0.000	0.000	0.000	10.90	58.12	0.73	58.12
130819-06_zr2	metapelite	Turba MZ -12 m	21.40	1.65	179.08	80.625	3.52	46.04	4.745	0.008	2.194	0.023	0.987	0.012	0.000	0.000	16.16	0.16	0.75	0.16
130819-06_zr3	metapelite	Turba MZ -12 m	22.38	1.80	246	75.96	5.23	49.65	3.186	0.005	1.413	0.021	0.465	0.003	0.000	0.000	17.30	0.23	0.77	0.23
130819-06_zr4	metapelite	Turba MZ -12 m	20.09	1.55	145.645	88.115	3.12	47.74	3.730	0.006	1.945	0.025	0.240	0.004	0.000	0.000	15.41	0.19	0.77	0.19
130819-06_zr5	metapelite	Turba MZ -12 m	24.98	2.06	148.42	61.275	1.87	37.81	1.561	0.003	0.656	0.009	0.322	0.004	0.000	0.000	17.63	0.21	0.71	0.21
130819-06_zr6	metapelite	Turba MZ -12 m	19.15	1.51	133.215	70.59	1.97	40.13	1.739	0.003	0.955	0.009	0.355	0.005	0.000	0.000	13.85	0.11	0.72	0.11
130819-06_zr7	metapelite	Turba MZ -12 m	22.21	1.88	180.72	61.15	2.41	39.14	1.956	0.003	0.946	0.011	0.293	0.002	0.032	0.030	15.92	0.17	0.72	0.17
130819-06_zr8	metapelite	Turba MZ -12 m	18.42	1.55	123.735	60.7	1.42	35.73	2.381	0.005	1.480	0.013	0.267	0.007	0.000	0.000	12.77	0.11	0.69	0.11
130819-06_zr9	metapelite	Turba MZ -12 m	22.26	1.89	186.12	58.515	2.31	37.77	1.639	0.004	0.826	0.008	0.144	0.002	0.000	0.000	15.77	0.15	0.71	0.15
130819-08_zr1	spilite	Turba MZ +98 m	24.41	1.74	274.695	104.215	10.34	65.59	4.000	0.002	1.576	0.018	0.263	0.001	-	-	20.19	0.21	0.83	0.21
130819-08_zr2	spilite	Turba MZ +98 m	29.03	2.78	162.325	79.25	3.20	46.78	1.515	0.002	0.528	0.005	0.165	0.003	-	-	22.08	0.20	0.76	0.20
130819-08_zr3	spilite	Turba MZ +98 m	22.78	2.88	117.58	71.34	1.66	38.74	0.683	0.001	0.336	0.004	0.042	0.000	-	-	16.32	0.18	0.72	0.18
130819-08_zr4	spilite	Turba MZ +98 m	31.48	2.09	112.75	102.825	2.17	41.23	3.809	0.003	1.256	0.019	0.471	0.005	-	-	23.02	0.31	0.73	0.31
130819-08_zr5	spilite	Turba MZ +98 m	23.52	2.48	156.6	76.825	2.88	45.20	3.964	0.004	1.823	0.032	0.099	0.002	-	-	17.76	0.30	0.75	0.30
130819-08_zr6	spilite	Turba MZ +98 m	24.48	2.96	151.275	72.47	3.08	43.21	1.703	0.002	0.717	0.008	0.236	0.003	-	-	18.22	0.19	0.74	0.19
130819-08_zr7	spilite	Turba MZ +98 m	24.16	2.12	137.725	81.305	3.39	46.05	2.398	0.003	0.971	0.013	0.474	0.008	-	-	18.31	0.22	0.76	0.22
13081909z1	spilite	Platta	21.87	1.52	103.205	61.245	1.09	33.60	0.616	0.002	0.322	0.004	0.099	0.001	0.000	0.000	14.76	0.18	0.67	0.18
13081909z2	spilite	Platta	20.66	1.44	111.215	61.835	1.24	34.83	0.848	0.001	0.453	0.006	0.183	0.003	0.000	0.000	14.14	0.16	0.68	0.16
13081909z3	spilite	Platta	21.05	1.49	121.44	61.96	1.41	35.72	0.689	0.001	0.377	0.005	0.056	0.001	0.001	0.014	14.61	0.20	0.69	0.20
13081909z4	spilite	Platta	27.56	1.93	99.755	52.615	0.83	30.22	0.590	0.001	0.267	0.003	0.033	0.001	0.000	0.000	17.75	0.21	0.64	0.21
13082107z1	metapsammite	Arblatsch (Val Gronda)	28.92	2.05	205.28	117.34	8.13	65.38	6.376	0.009	2.077	0.028	0.543	0.006	0.009	0.029	23.90	0.29	0.83	0.29
13082107z2	metapsammite	Arblatsch (Val Gronda)	28.29	1.99	191.445	87.11	4.63	51.88	2.736	0.003	0.924	0.009	0.416	0.005	0.000	0.000	22.12	0.19	0.78	0.19
13082107z3	metapsammite	Arblatsch (Val Gronda)	24.71	1.75	169.195	80.52	3.41	47.15	3.598	0.003	1.493	0.021	0.363	0.002	0.013	0.021	18.85	0.25	0.76	0.25
13082107z4	metapsammite	Arblatsch (Val Gronda)	21.38	1.52	173.765	75.69	3.28	46.17	2.208	0.003	1.077	0.012	0.209	0.003	0.017	0.045	16.22	0.17	0.76	0.17
13082107z5	metapsammite	Arblatsch (Val Gronda)	24.02	1.64	149.845	86.48	3.18	47.79	4.465	0.006	1.832	0.017	0.753	0.009	0.004	0.025	18.37	0.15	0.76	0.15
13082107z6	metapsammite	Arblatsch (Val Gronda)	33.71	2.32	146.94	95.52	3.26	53.41	0.822	0.002	0.189	0.003	0.304	0.002	0.000	0.000	26.02	0.34	0.77	0.34
13082303z1	augengneiss	Margna	21.38	1.55	263.445	123.41	15.73	74.43	66.330	0.093	28.669	0.520	6.760	0.087	0.560	0.046	18.12	0.30	0.85	0.30
13082303z2	augengneiss	Margna	24.24	1.72	233.27	117.365	9.92	68.58	24.915	0.028	9.625	0.125	2.392	0.025	0.001	0.002	20.21	0.24	0.83	0.24
13082303z3	augengneiss	Margna	22.51	1.58	254.585	121.34	11.71	71.35	32.018	0.023	13.313	0.107	2.900	0.018	0.006	0.008	18.91	0.14	0.84	0.14
13082303z4	augengneiss	Margna	20.41	1.45	282.105	126.99	14.81	76.78	40.151	0.035	18.070	0.181	4.406	0.036	0.072	0.005	17.37	0.16	0.85	0.16
13082303z5	augengneiss	Margna	23.10	1.64	394.17	164.27	35.72	101.34	90.551	0.099	34.154	0.393	10.203	0.178	0.580	0.051	20.47	0.22	0.89	0.22
13082303z6	augengneiss	Margna	22.38	1.59	211.595	81.715	4.81	50.79	10.500	0.010	4.736	0.059	1.037	0.002	0.020	0.002	17.43	0.20	0.78	0.20
AD15-01_z1	muscovite-garnet schist	Adula	11.08	0.78	138.3486465	59.7936605	1.62	36.28	0.813	0.001	0.761	0.008	0.488	0.004	0.009	0.049	7.68	0.07	0.69	0.07
AD15-01_z2	muscovite-garnet schist	Adula	89.42	58.30	140.9602643	74.6117528	3.09	45.37	0.007	0.001	0.000	0.000	0.001	0.000	0.008	0.048	67.06	43.59	0.73	43.59
AD15-01_z3	muscovite-garnet schist	Adula	12.88	0.90	154.6015802	57.4297851	2.07	36.30	0.940	0.002	0.829	0.010	0.143	0.004	0.008	0.036	9.02	0.10	0.70	0.10
AD15-01_z4	muscovite-garnet schist	Adula	10.98	0.79	210.9371697	62.7510854	3.35	39.87	1.299	0.002	1.325	0.022	0.102	0.003	0.067	0.148	7.96	0.13	0.72	0.13
AD1503z1	quartzite	Adula	10.41	0.75	226.81	90.16	6.30	56.24	7.306	0.008	6.796	0.104	2.019	0.017	0.000	0.000	8.31	0.12	0.80	0.12
AD1503z2	quartzite	Adula	14.85	1.05	205.665	81.3	4.65	50.74	4.185	0.004	2.468	0.032	2.301	0.024	0.000	0.000	11.49	0.12	0.77	0.12
AD1503z3	quartzite	Adula	9.10	0.65	201.75	75.18	3.98	47.50	2.887	0.004	2.571	0.039	3.800	0.048	0.004	0.015	6.88	0.08	0.76	0.08
AD1503z4	quartzite	Adula	13.29	0.94	277.265	98.395	10.84	61.98	10.962	0.012	6.884	0.057	6.327	0.085	0.013	0.026	10.82	0.08	0.81	0.08
AD1503z5	quartzite	Adula	16.08	1.15	190.505	78.41	4.69	48.58	4.334	0.008	2.129	0.037	3.349	0.031	0.009	0.032	12.27	0.16	0.76	0.16
AD1503z6	quartzite	Adula	9.91	0.70	197.925	82.92	4.49	50.51	4.776	0.006	4.340	0.049	3.439	0.016	0.010	0.032	7.67	0.07	0.77	0.07
ARB15-01_z01	metapsammite	Arblatsch flysch	27.94	1.99	126.275	95.805	5.38	52.03	4.087	0.004	1.429	0.014	0.456	0.004	0.000	0.000	21.98	0.20	0.79	0.20
ARB15-01_z02	metapsammite	Arblatsch flysch	33.49	3.93	184.27	73.705	4.54	45.10	1.203	0.003	0.325	0.003	0.298	0.004	0.008	0.019	25.14	0.21	0.75	0.21
ARB15-01_z03	metapsammite	Arblatsch flysch	24.61	2.23	194.975	81.465	5.17	50.36	1.352	0.003	0.547	0.009	0.153	0.002	0.008	0.025	19.16	0.30	0.78	0.30
ARB15-01_z04	metapsammite	Arblatsch flysch	29.39	2.09	196.435	94.67	6.87	56.76	9.405	0.010	2.933	0.034	1.567	0.033	0.000	0.000	23.53	0.24	0.80	0.24
ARB15-01_z05	metapsammite	Arblatsch flysch	25.25	1.82	175.675	62.065	2.40	39.61	0.916	0.003	0.392	0.007	0.103	0.002	0.002	0.011	18.19	0.29	0.72	0.29
ARB15-01_z06	metapsammite	Arblatsch flysch	29.02	2.03	180.145	95.345	3.99	55.34	3.562	0.004	1.177	0.022	0.476	0.006	0.027	0.054	22.83	0.38	0.79	0.38

Full Sample Name	lithology	nappe	CorrectDate.Ma	Full Unc. (Ma)	Lavg.µm	Wavg.µm	Dim Mass.µg	rs.µm	4He.ncc	±	U.ng	±	Th.ng	±	Sm.ng	±	RawDate.Ma	±	Ft	Analytic Unc. (Ma)
ARB15-01_z07	metapsammite	Arblatsch flysch	31.21	2.23	225.65	106.115	8.09	63.27	11.463	0.011	3.519	0.044	0.753	0.009	0.000	0.000	25.62	0.30	0.82	0.30
ARB15-01_z08	metapsammite	Arblatsch flysch	26.79	1.93	210.705	78.11	4.49	49.36	5.759	0.006	2.223	0.038	0.315	0.003	0.000	0.000	20.73	0.33	0.77	0.33
ARB15-01_z09	metapsammite	Arblatsch flysch	33.95	2.44	205.46	72.835	4.47	46.43	1.528	0.005	0.418	0.007	0.310	0.004	0.000	0.000	25.71	0.35	0.76	0.35
BD15-16_z1	metapsammite	Bündnerschiefer	9.98	1.20	161.8532067	73.2078792	2.82	44.20	0.691	0.001	0.724	0.011	0.179	0.004	0.003	0.031	7.46	0.11	0.75	0.11
BD15-16_z2	metapsammite	Bündnerschiefer	11.68	1.34	172.1861293	74.7407853	4.40	45.45	0.392	0.002	0.326	0.007	0.175	0.002	0.022	0.040	8.82	0.18	0.75	0.18
BD15-16_z3	metapsammite	Bündnerschiefer	8.60	0.73	159.4790087	83.0091879	3.33	47.93	0.676	0.001	0.744	0.008	0.457	0.004	0.016	0.045	6.57	0.06	0.76	0.06
BD15-16_z4	metapsammite	Bündnerschiefer	8.61	0.62	99.871155	98.9885727	4.55	49.64	0.518	0.001	0.608	0.007	0.137	0.003	0.000	0.000	6.69	0.07	0.78	0.07
BD15-16_z5	metapsammite	Bündnerschiefer	9.03	1.57	137.3370317	63.3188284	1.76	37.82	0.374	0.001	0.438	0.006	0.203	0.002	0.031	0.095	6.38	0.08	0.71	0.08
BD15-16_z6	metapsammite	Bündnerschiefer	8.05	1.14	144.7899489	68.6659352	2.17	40.83	0.131	0.001	0.156	0.003	0.127	0.002	0.000	0.000	5.83	0.09	0.72	0.09
BD15-16_z7	metapsammite	Bündnerschiefer	45.59	7.61	127.2105611	64.6504438	2.05	38.18	2.097	0.004	0.472	0.007	0.261	0.003	0.053	0.108	32.45	0.45	0.71	0.45
BD15-16_z8	metapsammite	Bündnerschiefer	4.35	1.95	144.4183353	73.3678795	3.61	43.83	0.379	0.001	0.739	0.394	0.982	0.716	0.000	0.000	3.23	1.39	0.74	1.39
BD15-16_z9	metapsammite	Bündnerschiefer	10.09	1.02	204.800384	78.0027269	4.32	49.11	0.641	0.001	0.618	0.006	0.272	0.004	0.011	0.034	7.77	0.07	0.77	0.07
BD1503z1	metapsammite	Arblatsch	22.81	1.94	184.96	143.525	9.28	77.24	15.644	0.009	6.531	0.335	0.657	0.060	0.000	0.000	19.35	0.94	0.85	0.94
BD1503z2	metapsammite	Arblatsch	27.42	2.60	193.965	96.755	7.01	57.31	7.349	0.007	2.620	0.180	0.566	0.037	0.007	0.035	22.06	1.40	0.80	1.40
BD1503z3	metapsammite	Arblatsch	26.62	2.82	224.935	102.015	7.59	61.53	3.880	0.004	1.413	0.121	0.268	0.034	0.000	0.000	21.73	1.72	0.82	1.72
BD1503z4	metapsammite	Arblatsch	31.32	2.50	236.28	90.73	6.70	56.84	7.146	0.009	2.233	0.090	0.504	0.029	0.045	0.100	25.11	0.94	0.80	0.94
BD1503z5	metapsammite	Arblatsch	34.08	3.49	321.16	87.035	9.26	58.07	16.340	0.019	4.367	0.374	2.380	0.174	0.000	0.000	27.38	2.02	0.80	2.02
BD1503z6	metapsammite	Arblatsch	22.87	1.91	238.11	162.335	15.27	89.99	35.064	0.036	13.938	0.684	2.737	0.160	0.056	0.059	19.88	0.90	0.87	0.90
BD1507z1	metapelite	Bundnersf/Platta s.l.	19.86	1.41	147.575	79.78	2.79	45.44	7.476	0.013	3.980	0.053	0.602	0.003	0.004	0.002	15.00	0.19	0.75	0.19
BD1507z2	metapelite	Bundnersf/Platta s.l.	27.46	1.83	111.65	57.3	0.87	32.44	1.934	0.004	0.858	0.007	0.205	0.003	0.000	0.000	17.65	0.14	0.64	0.14
BD1507z3	metapelite	Bundnersf/Platta s.l.	23.49	1.63	103.505	46.22	0.70	27.38	0.584	0.002	0.314	0.004	0.108	0.001	0.000	0.000	14.25	0.16	0.61	0.16
BD1507z4	metapelite	Bundnersf/Platta s.l.	24.30	1.72	107.79	49.69	0.85	29.71	0.669	0.002	0.279	0.005	0.358	0.004	0.000	0.000	15.21	0.23	0.63	0.23
BD1508z1	sandstone	Err cover	43.98	4.64	178.63	93.485	4.71	53.82	2.022	0.004	0.425	0.039	0.239	0.022	0.000	0.000	34.70	2.75	0.79	2.75
BD1508z2	sandstone	Err cover	37.45	2.95	140.29	99.89	3.40	54.78	3.668	0.004	0.891	0.038	0.605	0.052	0.006	0.040	29.31	1.09	0.78	1.09
BD1508z3	sandstone	Err cover	37.56	2.93	188.565	95.47	5.29	55.69	6.977	0.009	1.766	0.068	0.674	0.035	0.000	0.000	29.93	1.03	0.80	1.03
BD1508z4	sandstone	Err cover	44.74	4.92	174.87	73.92	3.82	45.63	5.202	0.006	1.218	0.109	0.206	0.025	0.020	0.052	33.92	2.84	0.76	2.84
BD1508z5	sandstone	Err cover	59.59	5.90	153.48	81.725	3.07	46.83	4.416	0.007	0.667	0.055	0.591	0.087	0.000	0.000	45.13	3.18	0.76	3.18
BD1508z6	sandstone	Err cover	42.55	3.45	185.38	89.57	3.61	52.56	9.480	0.006	2.090	0.102	1.205	0.116	0.023	0.052	32.96	1.42	0.77	1.42
BD1515z1	metapelite	Bdsf	39.83	3.66	109.865	55.095	0.95	30.30	0.010	0.001	0.001	0.000	0.009	0.000	0.000	0.000	24.29	1.65	0.61	1.65
BD1515z2	metapelite	Bdsf	5.34	0.37	106.51	54.53	0.96	31.39	0.584	0.001	1.298	0.015	0.370	0.008	0.000	0.000	3.49	0.04	0.65	0.04
BD1515z3	metapelite	Bdsf	6.52	0.46	139.57	44.445	1.01	28.90	0.373	0.001	0.675	0.007	0.359	0.004	0.009	0.029	4.06	0.04	0.62	0.04
BD1515z4	metapelite	Bdsf	7.01	0.49	109.135	59.145	1.13	33.68	0.087	0.001	0.141	0.002	0.050	0.000	0.000	0.000	4.73	0.06	0.67	0.06
BD1515z5	metapelite	Bdsf	7.40	0.52	120.02	64.255	1.48	36.72	0.334	0.001	0.493	0.006	0.172	0.004	0.000	0.000	5.18	0.06	0.70	0.06
BD1515z6	metapelite	Bdsf	6.57	0.46	105.575	52.435	0.90	30.78	0.221	0.001	0.377	0.003	0.233	0.004	0.000	0.000	4.23	0.04	0.64	0.04
DL15-04_z1	sandstone	Prättigau	20.47	1.45	231.0146267	114.219569	9.38	67.09	8.668	0.007	3.866	0.039	1.500	0.022	0.030	0.073	16.98	0.15	0.83	0.15
DL15-04_z10	sandstone	Prättigau	19.06	1.36	196.4184328	132.4028289	15.80	73.54	1.021	0.003	0.431	0.007	0.396	0.007	0.061	0.109	16.07	0.21	0.84	0.21
DL15-04_z2	sandstone	Prättigau	25.73	1.83	249.8120813	122.7924883	14.64	73.27	17.337	0.012	6.270	0.072	1.356	0.009	0.006	0.018	21.75	0.23	0.84	0.23
DL15-04_z3	sandstone	Prättigau	21.14	1.49	216.7281483	117.0686066	8.83	66.71	9.772	0.012	4.262	0.050	1.476	0.016	0.005	0.006	17.53	0.18	0.83	0.18
DL15-04_z4	sandstone	Prättigau	15.07	1.09	189.9719691	122.2557131	12.93	68.28	0.558	0.004	0.322	0.006	0.195	0.003	0.041	0.086	12.55	0.21	0.83	0.21
DL15-04_z5	sandstone	Prättigau	19.56	1.40	204.9397391	106.2247153	7.00	61.21	7.432	0.011	3.569	0.060	1.231	0.017	0.000	0.000	15.92	0.24	0.81	0.24
DL15-04_z6	sandstone	Prättigau	18.19	1.30	215.5049202	120.2789352	14.03	68.73	1.188	0.008	0.564	0.008	0.356	0.005	0.009	0.025	15.16	0.21	0.83	0.21
DL15-04_z7	sandstone	Prättigau	25.76	1.83	172.5061299	90.5137181	4.27	52.11	1.893	0.004	0.716	0.009	0.250	0.005	0.000	0.000	20.19	0.24	0.78	0.24
DL15-04_z8	sandstone	Prättigau	22.93	1.63	221.5178347	116.7640899	13.72	68.04	6.128	0.007	2.336	0.033	1.343	0.008	0.036	0.072	19.09	0.23	0.83	0.23
DL15-04_z9	sandstone	Prättigau	0.00	0.00	161.6673999	129.5228235	12.23	67.86	0.000	0.003	0.000	0.000	0.000	0.000	0.051	0.100	0.00	0.00	0.83	-35.70
DL1502z1	greenschist granitoid	Tschirpen	50.11	3.54	170.785	99.655	6.31	56.47	4.098	0.005	0.827	0.007	0.057	0.001	0.000	0.000	40.25	0.34	0.80	0.34
DL1502z2	greenschist granitoid	Tschirpen	35.86	2.53	178.845	91.655	4.60	53.24	7.167	0.007	1.789	0.022	1.319	0.012	0.003	0.009	28.17	0.29	0.78	0.29
DL1502z3	greenschist granitoid	Tschirpen	70.73	4.95	161.61	98.82	4.34	53.41	13.742	0.012	1.869	0.016	0.673	0.007	0.027	0.074	55.83	0.42	0.79	0.42
DL1502z4	greenschist granitoid	Tschirpen	51.20	3.59	179.66	118.195	8.96	64.03	5.627	0.009	0.864	0.007	1.025	0.007	0.000	0.000	41.96	0.27	0.82	0.27
DL1502z5	greenschist granitoid	Tschirpen	30.70	2.17	169.38	93.44	4.34	52.77	2.322	0.003	0.731	0.009	0.271	0.003	0.000	0.000	24.14	0.27	0.79	0.27
DL1502z6	greenschist granitoid	Tschirpen	120.87	8.49	140.735	77.15	2.47	43.74	15.196	0.014	1.235	0.013	0.639	0.007	0.000	0.002	90.05	0.82	0.74	0.82
DL1505z1	sandstone	Prättigau	22.54	2.07	279.91	114.92	12.42	70.87	7.118	0.009	2.987	0.188	0.526	0.037	0.000	0.000	18.92	1.11	0.84	1.11
DL1505z2	sandstone	Prättigau	21.55	2.00	270.02	128.24	14.08	76.22	11.869	0.015	5.200	0.337	0.654	0.046	0.011	0.032	18.33	1.12	0.85	1.12
DL1505z3	sandstone	Prättigau	15.05	1.17	292.465	126.05	15.32	76.81	11.430	0.011	7.007	0.248	1.595	0.140	0.022	0.043	12.81	0.42	0.85	0.42
DL1505z4	sandstone	Prättigau	30.52	2.90	360.465	110.245	16.21	72.26	21.784	0.024	6.495	0.457	2.170	0.084	0.000	0.000	25.69	1.63	0.84	1.63
DL1505z5	sandstone	Prättigau	23.93	3.27	190.575	127.48	7.54	70.92	3.925	0.004	1.488	0.198	0.594	0.042	0.000	0.000	19.93	2.35	0.83	2.35
DLV1z1	purple Sernifite	Verrucano	15.22	1.11	225.93	116.885	9.38	67.56	4.231	0.007	2.613	0.059	0.628	0.035	0.605	0.057	12.66	0.27	0.83	0.27
DLV1z2	purple Sernifite	Verrucano	15.95	1.12	244.655	96.13	7.53	58.77	4.183	0.005	2.461	0.019	0.973	0.008	0.000	0.000	12.86	0.09	0.81	0.09
DLV1z3	purple Sernifite	Verrucano	26.63	1.90	373.56	94.925	14.33	63.49	6.977	0.009	2.472	0.027	0.695	0.007	0.010	0.016	21.88	0.22	0.82	0.22
DLV1z4	purple Sernifite	Verrucano	42.81	3.74	289.135	93.32	9.15	60.48	14.003	0.708	3.214	0.030	0.447	0.007	0.000	0.000	34.83	1.79	0.81	1.79

Full Sample Name	lithology	nappe	CorrectDate.Ma	Full Unc. (Ma)	Lavg.µm	Wavg.µm	Dim Mass.µg	rs.µm	4He.ncc	±	U.ng	±	Th.ng	±	Sm.ng	±	RawDate.Ma	±	Ft	Analytic Unc. (Ma)
DLV1z5	purple Sernifite	Verrucano	29.79	2.11	244.76	85.14	6.31	54.40	5.028	0.006	1.611	0.014	0.638	0.005	0.000	0.000	23.59	0.18	0.79	0.18
DLV1z6	purple Sernifite	Verrucano	27.32	1.92	219.76	96.345	6.60	57.94	9.689	0.008	3.447	0.029	0.826	0.002	0.000	0.000	21.99	0.17	0.80	0.17
DLV4z1	red Sernifite	Verrucano	13.72	0.97	176.51	101.29	5.20	56.38	7.850	0.006	5.383	0.062	2.299	0.011	0.000	0.010	10.96	0.11	0.80	0.11
DLV4z2	red Sernifite	Verrucano	58.57	4.15	213.69	83.37	5.11	52.23	8.116	0.007	1.239	0.012	0.944	0.006	0.032	0.075	45.78	0.37	0.78	0.37
IL15-01_z1	metavolcaniclastic	Ilanzer Verrucano	9.71	0.70	343.381289	115.3086033	16.47	74.42	5.039	0.004	4.679	0.070	1.702	0.021	0.000	0.000	8.21	0.11	0.85	0.11
IL15-01_z2	metavolcaniclastic	Ilanzer Verrucano	9.58	0.69	373.6471522	133.4763793	23.55	85.10	7.643	0.006	7.406	0.107	0.945	0.008	0.000	0.000	8.29	0.11	0.87	0.11
IL15-01_z3	metavolcaniclastic	Ilanzer Verrucano	7.85	0.56	233.0739854	84.2375773	5.77	53.17	1.378	0.002	1.759	0.027	0.350	0.006	0.102	0.237	6.19	0.09	0.79	0.09
IL15-01_z4	metavolcaniclastic	Ilanzer Verrucano	9.52	0.68	256.9708044	99.6234126	8.79	62.50	1.585	0.002	1.608	0.020	0.318	0.005	0.000	0.000	7.79	0.09	0.82	0.09
IL15-01_z5	metavolcaniclastic	Ilanzer Verrucano	7.63	0.54	398.3594566	128.8002415	24.08	83.65	14.167	0.015	16.592	0.221	5.232	0.072	0.006	0.006	6.58	0.08	0.86	0.08
IL15-01_z6	metavolcaniclastic	Ilanzer Verrucano	11.04	0.79	341.4664467	140.2789727	26.95	87.06	5.120	0.003	4.189	0.051	0.976	0.008	0.024	0.065	9.59	0.11	0.87	0.11
IL15-01_z7	metavolcaniclastic	Ilanzer Verrucano	8.40	0.60	402.9788201	142.709945	29.14	91.20	19.676	0.024	20.843	0.195	5.731	0.053	0.062	0.112	7.34	0.06	0.87	0.06
IL15-01_z8	metavolcaniclastic	Ilanzer Verrucano	13.77	0.99	217.8481504	108.6195585	6.25	63.58	3.814	0.005	2.727	0.063	0.356	0.004	0.000	0.000	11.23	0.25	0.82	0.25
IL15-01_z9	metavolcaniclastic	Ilanzer Verrucano	7.99	0.57	416.3465871	147.6028574	32.19	94.30	11.234	0.013	12.887	0.120	1.574	0.013	0.000	0.006	7.01	0.06	0.88	0.06
IL1502z1	metavolcaniclastic	Ilanzer Verrucano	12.06	0.90	361.895	96.3	12.78	64.20	5.991	0.005	4.509	0.129	2.097	0.134	0.004	0.045	9.90	0.26	0.82	0.26
IL1502z2	metavolcaniclastic	Ilanzer Verrucano	9.52	0.75	264.28	83.34	6.62	53.60	1.936	0.003	1.959	0.077	0.747	0.080	0.005	0.029	7.50	0.27	0.79	0.27
IL1502z3	metavolcaniclastic	Ilanzer Verrucano	9.20	0.78	237.45	121.11	13.44	71.60	1.117	0.001	1.060	0.057	0.575	0.035	0.029	0.099	7.73	0.36	0.84	0.36
IL1502z4	metavolcaniclastic	Ilanzer Verrucano	11.07	1.19	252.59	108.385	9.55	64.80	2.673	0.002	2.264	0.203	0.685	0.059	0.000	0.000	9.12	0.74	0.82	0.74
IL1502z5	metavolcaniclastic	Ilanzer Verrucano	11.17	1.44	199.515	113.85	9.74	65.27	2.852	0.004	2.308	0.286	1.067	0.081	0.001	0.020	9.22	1.00	0.83	1.00
IL1502z6	metavolcaniclastic	Ilanzer Verrucano	7.53	0.59	221.33	99.735	7.04	59.48	19.733	0.013	25.342	0.963	6.161	0.443	0.035	0.036	6.10	0.21	0.81	0.21
JUL1501z1	granite	Julier granite	27.51	2.59	319.8	171.63	35.34	98.81	70.041	0.099	22.356	1.540	6.137	0.420	0.000	0.000	24.32	1.53	0.88	1.53
JUL1501z2	granite	Julier granite	24.70	2.66	348.1	152.79	26.41	92.17	76.780	0.042	27.233	2.468	9.043	0.523	0.029	0.038	21.61	1.76	0.87	1.76
JUL1501z3	granite	Julier granite	27.15	2.95	319.545	131.375	22.02	81.23	54.441	0.045	17.994	1.631	5.466	0.656	0.002	0.018	23.33	1.92	0.86	1.92
JUL1501z4	granite	Julier granite	27.75	2.28	346.25	128.04	19.89	81.14	30.419	0.027	9.723	0.459	3.516	0.265	0.000	0.000	23.82	1.01	0.86	1.01
JUL1501z5	granite	Julier granite	29.65	2.51	321.27	138.115	24.41	84.96	47.500	0.038	14.522	0.736	3.273	0.274	0.000	0.000	25.66	1.20	0.87	1.20
JUL1501z6	granite	Julier granite	38.39	3.10	290.555	109.105	12.00	68.69	27.498	0.031	6.505	0.287	2.502	0.164	0.000	0.000	32.00	1.27	0.83	1.27
KK15-02_z1	gritstone	Prättigau	0.00	0.00	274.6379343	108.7589136	11.12	67.91	0.001	0.001	8.134	0.084	1.727	0.022	0.007	0.004	0.00	0.00	0.83	0.00
KK15-02_z2	gritstone	Prättigau	106.54	11.22	248.1449814	77.0375638	5.39	50.09	13.923	0.018	1.324	0.023	0.247	0.004	0.000	0.000	82.83	1.35	0.78	1.35
KK15-02_z3	gritstone	Prättigau	33.63	2.36	235.4481834	117.6724787	7.93	68.86	2.586	0.003	0.664	0.008	0.442	0.005	0.000	0.000	27.80	0.30	0.83	0.30
KK15-02_z4	gritstone	Prättigau	49.20	4.35	216.103631	81.7240242	4.73	49.22	6.783	0.006	1.388	0.023	0.364	0.005	0.001	0.027	37.98	0.57	0.77	0.57
KK15-02_z5	gritstone	Prättigau	36.20	2.55	195.4377858	94.9937265	5.50	55.85	8.244	0.008	2.172	0.022	0.791	0.008	0.001	0.014	28.87	0.26	0.80	0.26
KK15-02_z6	gritstone	Prättigau	22.97	1.63	242.9785201	108.593752	11.24	65.81	8.386	0.005	3.413	0.036	0.990	0.007	0.006	0.012	19.01	0.18	0.83	0.18
KK15-02_z7	gritstone	Prättigau	37.31	2.65	276.7437447	102.038901	10.11	64.71	8.680	0.008	1.991	0.023	1.469	0.029	0.039	0.067	30.66	0.31	0.82	0.31
KK15-02_z8	gritstone	Prättigau	31.48	2.22	211.3449124	132.026054	8.97	74.50	4.026	0.003	1.100	0.014	0.668	0.008	0.022	0.036	26.44	0.30	0.84	0.30
KK15-02_z9	gritstone	Prättigau	21.54	2.14	188.1706754	78.2814371	3.87	48.32	3.828	0.004	1.632	0.020	1.226	0.017	0.009	0.041	16.47	0.17	0.76	0.17
KK15-11_z1	metapelite	Prättigau	14.28	0.99	138.775	83.445	2.60	44.45	1.176	0.003	0.872	0.009	0.153	0.001	0.079	0.169	10.71	0.10	0.75	0.10
KK15-11_z2	metapelite	Prättigau	9.34	0.65	142.63	69.865	2.05	39.37	0.786	0.002	0.887	0.009	0.353	0.004	0.019	0.040	6.70	0.06	0.72	0.06
KK15-11_z3	metapelite	Prättigau	14.96	1.04	105.395	97.695	4.64	49.77	0.215	0.001	0.131	0.002	0.095	0.002	0.000	0.000	11.58	0.17	0.77	0.17
KK15-11_z4	metapelite	Prättigau	9.73	0.69	152.46	60.535	1.88	37.36	1.087	0.002	1.280	0.014	0.120	0.003	0.008	0.018	6.88	0.07	0.71	0.07
KK1505z1	sandstone	Prättigau	27.01	2.07	230.175	106.535	8.38	63.83	23.912	0.019	8.042	0.275	3.686	0.299	0.013	0.008	22.17	0.69	0.82	0.69
KK1505z2	sandstone	Prättigau	41.53	4.20	262.52	133.415	18.04	78.94	17.182	0.021	3.659	0.298	1.418	0.063	0.000	0.000	35.51	2.57	0.85	2.57
KK1505z3	sandstone	Prättigau	71.35	5.52	270.26	126.13	13.73	75.33	41.962	0.040	5.435	0.190	1.148	0.117	0.015	0.038	60.58	1.97	0.85	1.97
KK1505z4	sandstone	Prättigau	27.33	2.63	238.475	132.54	12.26	74.72	25.807	0.030	8.169	0.623	4.471	0.383	0.034	0.012	23.12	1.53	0.85	1.53
KK1505z5	sandstone	Prättigau	63.15	5.25	240.48	104.6775	8.67	63.72	16.168	0.018	2.113	0.114	1.967	0.136	0.047	0.039	51.69	2.31	0.82	2.31
KK1505z6	sandstone	Prättigau	62.23	6.19	307.23	120.8125	18.10	75.60	22.123	0.012	3.251	0.248	0.835	0.055	0.008	0.040	52.88	3.69	0.85	3.69
KK1511z5	metapelite	Prättigau	7.71	0.58	133.78	71.815	2.05	40.84	2.743	0.003	3.706	0.125	1.454	0.076	0.004	0.041	5.61	0.17	0.73	0.17
KK1511z6	metapelite	Prättigau	9.70	1.19	149.455	53.94	1.54	34.35	0.747	0.001	0.901	0.097	0.147	0.023	0.002	0.014	6.61	0.67	0.68	0.67
LEN15-03_z1	quartz monzonite porphyry	Silvretta	44.96	3.19	371.2058573	158.090619	36.55	96.48	101.981	0.062	20.131	0.234	4.706	0.055	0.020	0.036	39.62	0.42	0.88	0.42
LEN15-03_z2	quartz monzonite porphyry	Silvretta	87.19	6.20	286.3902144	138.1628397	17.10	81.35	56.574	0.028	5.266	0.079	4.063	0.059	0.000	0.000	74.76	0.94	0.86	0.94
LEN15-03_z3	quartz monzonite porphyry	Silvretta	77.10	5.45	274.7772894	122.9370047	16.11	73.84	38.314	0.029	4.382	0.044	1.935	0.032	0.008	0.026	65.20	0.58	0.84	0.58
LEN15-03_z4	quartz monzonite porphyry	Silvretta	42.66	3.03	199.9023103	102.2143852	6.35	59.09	11.224	0.011	2.610	0.033	0.312	0.005	0.000	0.000	34.54	0.41	0.81	0.41
LEN15-03_z5	quartz monzonite porphyry	Silvretta	32.83	2.32	252.6404737	159.5202991	23.45	88.26	8.235	0.009	2.136	0.023	1.047	0.010	0.005	0.011	28.55	0.27	0.87	0.27
LEN15-03_z6	quartz monzonite porphyry	Silvretta	42.98	3.04	193.0481039	115.6905395	7.03	62.03	24.488	0.024	5.348	0.081	1.731	0.016	0.026	0.072	35.12	0.48	0.82	0.48
LEN15-03_z7	quartz monzonite porphyry	Silvretta	27.28	1.91	267.045662	198.0132745	35.62	101.78	29.329	0.028	9.015	0.082	4.267	0.048	0.025	0.038	24.18	0.19	0.89	0.19
LEN15-03_z8	quartz monzonite porphyry	Silvretta	97.04	6.93	283.6185963	105.703424	11.06	66.82	29.327	0.018	2.527	0.038	2.012	0.013	0.006	0.017	80.31	0.99	0.83	0.99
LEN15-05_z1	sandstone	Prättigau	18.39	1.30	436.5272701	122.2041001	23.62	78.34	17.864	0.009	8.685	0.086	3.093	0.030	0.004	0.018	15.69	0.14	0.85	0.14
LEN15-05_z2	sandstone	Prättigau	19.46	1.38	433.6162969	155.3293235	36.92	98.83	53.678	0.113	23.834	0.250	8.464	0.058	0.092	0.077	17.18	0.17	0.88	0.17
LEN15-05_z3	sandstone	Prättigau	22.80	1.64	398.7568767	132.0105701	24.88	84.61	6.499	0.007	2.554	0.044	0.737	0.011	0.000	0.000	19.70	0.31	0.86	0.31
LEN15-05_z4	sandstone	Prättigau	22.72	1.62	278.3282638	118.6376418	13.04	72.78	7.588	0.005	2.873	0.040	1.727	0.018	0.000	0.000	19.12	0.23	0.84	0.23
LEN15-05_z5	sandstone	Prättigau	20.17	1.43	266.9217908	115.8557011	14.02	70.21	28.590	0.030	12.916	0.133	4.561	0.041	0.025	0.024	16.90	0.16	0.84	0.16

Full Sample Name	lithology	nappe	CorrectDate.Ma	Full Unc. (Ma)	Lavg.µm	Wavg.µm	Dim Mass.µg	rs.µm	4He.ncc	±	U.ng	±	Th.ng	±	Sm.ng	±	RawDate.Ma	±	Ft	Analytic Unc. (Ma)
LEN15-05_z6	sandstone	Prättigau	14.30	1.03	241.497227	156.6867454	27.00	87.35	33.648	0.035	20.452	0.347	8.245	0.093	0.015	0.004	12.43	0.19	0.87	0.19
LEN15-05_z7	sandstone	Prättigau	25.58	1.90	228.335912	88.9601668	6.21	55.70	5.963	0.006	2.297	0.031	0.505	0.007	0.025	0.059	20.40	0.26	0.80	0.26
LEN15-05_z8	sandstone	Prättigau	18.71	1.34	214.1010466	104.9343903	9.15	62.53	9.490	0.008	4.705	0.071	1.774	0.017	0.004	0.027	15.32	0.21	0.82	0.21
LEN15-05_z9	sandstone	Prättigau	21.08	1.51	219.1023463	149.0996344	11.77	82.08	13.126	0.009	5.718	0.125	1.243	0.009	0.000	0.000	18.06	0.36	0.86	0.36
Lochseitz1	arkosic conglermerate	Verrucano	9.60	0.68	303.31	114.87	13.86	72.24	14.168	0.017	13.352	0.103	4.953	0.030	0.016	0.039	8.07	0.06	0.84	0.06
Lochseitz2	arkosic conglermerate	Verrucano	85.11	6.12	323.62	90.82	10.09	60.32	16.371	0.028	1.639	0.028	1.340	0.015	0.000	0.011	68.89	0.97	0.81	0.97
Lochseitz3	arkosic conglermerate	Verrucano	5.96	0.42	215.4	97.88	6.69	59.01	8.236	0.013	12.279	0.124	8.139	0.065	0.039	0.012	4.80	0.04	0.81	0.04
Lochseitz5	arkosic conglermerate	Verrucano	120.37	20.70	339.375	166.14	36.38	99.08	62.546	9.860	4.309	0.051	2.174	0.014	0.010	0.005	106.41	16.81	0.88	16.81
Lochseitz6	arkosic conglermerate	Verrucano	146.09	10.39	267.935	97.045	8.88	61.66	87.782	0.178	5.892	0.054	0.510	0.005	0.000	0.000	119.62	1.06	0.82	1.06
PL15-07_z1	spilite	Err cover	39.40	2.81	197.125	75.925	3.93	47.69	5.597	0.008	1.406	0.018	0.545	0.009	0.000	0.000	30.12	0.34	0.76	0.34
PL15-07_z2	spilite	Err cover	45.84	3.22	150.3	77.165	2.73	44.75	1.983	0.004	0.403	0.004	0.318	0.007	0.000	0.000	34.25	0.34	0.75	0.34
PL15-07_z3	spilite	Err cover	81.09	5.67	149.105	79.135	2.72	44.34	13.674	0.017	1.694	0.019	0.688	0.005	0.007	0.046	60.68	0.60	0.75	0.60
PL15-07_z4	spilite	Err cover	55.69	3.94	155.08	74.075	2.66	43.54	5.607	0.007	1.009	0.014	0.457	0.005	0.037	0.071	41.39	0.51	0.74	0.51
PL15-07_z5	spilite	Err cover	35.04	2.45	161.87	92.53	3.97	51.38	2.148	0.004	0.539	0.006	0.477	0.006	0.009	0.036	27.24	0.25	0.78	0.25
PL15-07_z6	spilite	Err cover	35.08	2.42	106.61	70.585	1.38	36.61	0.678	0.002	0.204	0.002	0.107	0.002	0.000	0.000	24.48	0.26	0.70	0.26
SUR15-02_z1	gneissose granitoid	Suretta	28.97	2.05	436.5272701	122.2041001	23.62	78.34	31.807	0.035	10.162	0.122	1.955	0.012	0.014	0.005	24.75	0.28	0.85	0.28
SUR15-02_z2	gneissose granitoid	Suretta	21.04	1.49	433.6162969	155.3293235	36.92	98.83	65.404	0.080	28.066	0.230	4.324	0.052	0.020	0.007	18.60	0.14	0.88	0.14
SUR15-02_z3	gneissose granitoid	Suretta	19.87	1.41	398.7568767	132.0105701	24.88	84.61	34.463	0.022	15.915	0.148	2.844	0.037	0.094	0.166	17.18	0.15	0.86	0.15
SUR15-02_z4	gneissose granitoid	Suretta	18.79	1.34	278.3282638	118.6376418	13.04	72.78	18.472	0.016	9.474	0.122	0.683	0.007	0.072	0.157	15.86	0.20	0.84	0.20
SUR15-02_z5	gneissose granitoid	Suretta	20.38	1.45	266.9217908	115.8557011	14.02	70.21	5.394	0.007	2.435	0.040	0.750	0.012	0.021	0.048	17.08	0.25	0.84	0.25
SUR15-02_z6	gneissose granitoid	Suretta	19.27	1.34	241.497227	156.6867454	14.14	85.89	18.452	0.014	8.544	0.097	2.699	0.028	0.047	0.074	16.62	0.17	0.86	0.17
SUR15-02_z7	gneissose granitoid	Suretta	17.94	1.33	228.335912	88.9601668	6.21	55.70	3.697	0.003	2.037	0.023	0.424	0.004	0.000	0.000	14.31	0.15	0.80	0.15
SUR15-02_z8	gneissose granitoid	Suretta	17.21	1.44	271.535993	83.5872535	6.79	53.35	6.470	0.008	3.787	0.049	0.654	0.005	0.000	0.000	13.58	0.17	0.79	0.17
SUR15-02_z9	gneissose granitoid	Suretta	20.37	1.45	297.5799128	101.4918032	11.01	65.32	21.869	0.013	10.025	0.110	3.080	0.034	0.027	0.065	16.82	0.17	0.83	0.17
SUR1501_z1	bx'd hypabyssal porphyry	Suretta	23.99	1.72	404.89	75.645	9.40	52.38	4.491	0.004	1.887	0.026	0.356	0.003	0.000	0.000	18.84	0.24	0.78	0.24
SUR1501_z2	bx'd hypabyssal porphyry	Suretta	24.20	1.72	351.65	98.895	12.85	65.07	11.198	0.010	4.449	0.046	0.782	0.010	0.000	0.000	19.98	0.20	0.83	0.20
SUR1501_z3	bx'd hypabyssal porphyry	Suretta	2.07	2.29	252.66	112.215	10.19	66.99	0.001	0.001	0.003	0.000	0.011	0.000	0.000	0.000	1.70	1.89	0.82	1.89
SUR1501_z4	bx'd hypabyssal porphyry	Suretta	23.32	1.65	490.17	123.94	28.77	82.64	22.542	0.020	8.714	0.084	2.393	0.009	0.060	0.102	20.08	0.18	0.86	0.18
SUR1501_z5	bx'd hypabyssal porphyry	Suretta	29.59	2.08	323.485	158.555	25.13	92.59	48.772	0.051	11.659	0.116	16.749	0.175	0.002	0.003	25.79	0.20	0.87	0.20
SUR1501_z6	bx'd hypabyssal porphyry	Suretta	21.40	1.52	330.01	173.39	29.67	99.11	7.633	0.008	3.085	0.039	1.073	0.011	0.015	0.040	18.90	0.21	0.88	0.21
SUR1503z1	orthogneiss	Suretta	14.37	1.12	379.885	194.49	52.73	110.58	95.390	0.074	57.768	2.172	15.049	0.461	0.158	0.036	12.87	0.44	0.90	0.44
SUR1503z2	orthogneiss	Suretta	16.97	1.30	363.24	118.24	18.40	76.47	42.302	0.055	22.401	0.737	7.896	0.521	0.014	0.016	14.42	0.43	0.85	0.43
SUR1503z3	orthogneiss	Suretta	17.24	1.35	282.305	133.27	15.77	78.70	60.575	0.049	27.272	1.189	29.042	1.527	0.119	0.016	14.67	0.52	0.85	0.52
SUR1503z4	orthogneiss	Suretta	21.05	2.20	280.15	103.14	10.36	64.94	28.488	0.039	12.273	1.074	5.562	0.438	0.011	0.063	17.34	1.33	0.82	1.33
SUR1503z5	orthogneiss	Suretta	22.03	1.63	268.655	124.565	13.36	74.54	29.821	0.017	11.941	0.314	5.483	0.423	0.023	0.040	18.63	0.45	0.85	0.45
SUR1503z6	orthogneiss	Suretta	19.65	1.87	285.86	93.755	9.13	60.78	21.409	0.015	10.588	0.724	2.059	0.133	0.000	0.000	15.99	1.01	0.81	1.01
SUR1504z1	orthogneiss	Aruea slice	14.40	1.02	282.235	100.175	11.37	62.81	17.043	0.017	10.582	0.096	5.863	0.019	0.009	0.005	11.78	0.09	0.82	0.09
SUR1504z2	orthogneiss	Aruea slice	17.15	1.21	238.73	91.89	6.97	57.74	3.606	0.006	1.962	0.014	0.862	0.008	0.000	0.000	13.77	0.09	0.80	0.09
SUR1504z3	orthogneiss	Aruea slice	14.74	1.02	163.055	123.945	6.09	66.98	5.152	0.004	3.264	0.038	1.046	0.013	0.000	0.000	12.14	0.13	0.82	0.13
SUR1504z4	orthogneiss	Aruea slice	13.98	0.99	261.915	97.02	8.63	61.46	10.187	0.016	6.733	0.071	2.828	0.022	0.006	0.009	11.39	0.11	0.81	0.11
SUR1504z5	orthogneiss	Aruea slice	12.79	0.90	216.035	91.525	6.01	56.06	12.534	0.010	8.960	0.086	5.152	0.040	0.000	0.000	10.19	0.08	0.80	0.08
SUR1504z6	orthogneiss	Aruea slice	14.49	1.00	199.495	120.895	7.03	67.92	5.170	0.004	3.362	0.025	0.891	0.010	0.010	0.027	11.97	0.08	0.83	0.08
TSC1501z1	greenschist granitoid	Tschirpen	254.36	19.13	138.83	63.39	2.19	38.40	0.104	0.001	0.001	0.000	0.017	0.000	0.000	0.000	173.35	5.12	0.68	5.12
TSC1501z2	greenschist granitoid	Tschirpen	39.26	2.75	149.675	75.945	2.58	43.31	1.177	0.002	0.295	0.004	0.167	0.001	0.000	0.000	29.08	0.31	0.74	0.31
TSC1501z3	greenschist granitoid	Tschirpen	50.25	3.52	190.38	100.495	5.62	56.49	3.933	0.007	0.599	0.008	0.906	0.018	0.001	0.002	39.87	0.43	0.79	0.43
TSC1501z4	greenschist granitoid	Tschirpen	34.40	2.41	155.275	78.12	2.91	45.50	1.928	0.002	0.536	0.004	0.336	0.005	0.000	0.000	25.86	0.18	0.75	0.18
TSC1501z5	greenschist granitoid	Tschirpen	47.23	3.32	140.17	85.06	3.68	47.17	2.331	0.003	0.482	0.005	0.219	0.004	0.011	0.016	36.07	0.33	0.76	0.33
TSC1501z6	greenschist granitoid	Tschirpen	39.13	2.74	128.755	101.425	3.17	53.54	3.211	0.003	0.755	0.010	0.492	0.003	0.000	0.000	30.44	0.34	0.78	0.34
TSC1501z7	greenschist granitoid	Tschirpen	34.63	2.39	142.95	82.38	2.68	44.66	0.714	0.001	0.200	0.004	0.116	0.002	0.002	0.025	25.91	0.41	0.75	0.41
VE1501z1	quartz-eye porphyry	Verrucano	11.02	1.14	217.805	118.685	9.08	67.41	1.985	0.003	1.706	0.142	0.369	0.027	0.015	0.032	9.16	0.71	0.83	0.71
VE1501z2	quartz-eye porphyry	Verrucano	9.82	0.73	231.94	106.29	6.31	62.13	1.812	0.002	1.786	0.052	0.417	0.035	0.011	0.031	7.96	0.22	0.81	0.22
VE1501z3	quartz-eye porphyry	Verrucano	7.70	0.75	222.44	96.265	6.77	58.50	1.239	0.001	1.568	0.114	0.349	0.024	0.009	0.030	6.21	0.42	0.81	0.42
VE1501z4	quartz-eye porphyry	Verrucano	10.29	1.05	213.995	80.76	4.83	50.75	1.478	0.002	1.476	0.116	0.210	0.024	0.014	0.034	8.02	0.59	0.78	0.59
VE1501z5	quartz-eye porphyry	Verrucano	8.35	1.13	232.89	74.165	4.69	48.31	1.360	0.001	1.713	0.209	0.173	0.019	0.000	0.000	6.42	0.74	0.77	0.74
VE1501z6	quartz-eye porphyry	Verrucano	8.53	0.84	198.57	88.05	5.04	53.41	0.664	0.001	0.767	0.058	0.209	0.029	0.006	0.028	6.73	0.46	0.79	0.46
VE1502z1	phyllite	Verrucano	8.34	0.59	325.07	94.77	10.85	62.18	1.368	0.002	1.465	0.020	0.846	0.007	0.000	0.000	6.80	0.08	0.81	0.08
VE1502z2	phyllite	Verrucano	13.70	0.98	304.32	129.54	16.98	79.41	4.657	0.007	3.008	0.039	1.192	0.016	0.001	0.006	11.71	0.14	0.85	0.14
VE1502z3	phyllite	Verrucano	13.41	0.95	328.345	146.35	22.82	88.26	4.280	0.005	2.675	0.027	1.543	0.016	0.005	0.015	11.65	0.10	0.87	0.10
VE1502z4	phyllite	Verrucano	7.11	0.50	430.68	167.65	41.62	104.97	8.148	0.005	9.730	0.090	3.946	0.030	0.043	0.077	6.32	0.05	0.89	0.05

Full Sample Name	lithology	nappe	CorrectDate.Ma	Full Unc. (Ma)	Lavg.µm	Wavg.µm	Dim Mass.µg	rs.µm	4He.ncc	±	U.ng	±	Th.ng	±	Sm.ng	±	RawDate.Ma	±	Ft	Analytic Unc. (Ma)
VE1502z5	phyllite	Verrucano	7.31	0.52	279.555	105.97	10.61	65.39	1.985	0.002	2.503	0.025	0.934	0.004	0.012	0.035	6.03	0.05	0.82	0.05
VE1502z6	phyllite	Verrucano	7.80	0.55	245.545	139.735	13.38	76.19	2.233	0.002	2.379	0.032	1.757	0.014	0.010	0.009	6.61	0.07	0.85	0.07
VE1503z1	arkosic conglomerate	Verrucano	22.17	2.46	262.145	113.8	11.22	69.48	5.469	0.005	2.161	0.212	1.197	0.178	0.074	0.133	18.50	1.59	0.83	1.59
VE1503z2	arkosic conglomerate	Verrucano	15.85	1.45	236.3	99.66	7.84	61.29	7.360	0.010	3.993	0.286	3.120	0.102	0.007	0.013	12.87	0.76	0.81	0.76
VE1503z3	arkosic conglomerate	Verrucano	28.81	2.27	232.22	102.105	7.95	62.11	11.688	0.009	3.393	0.136	3.071	0.289	0.000	0.000	23.44	0.84	0.81	0.84
VE1503z4	arkosic conglomerate	Verrucano	14.38	1.59	192.755	93.435	5.30	55.28	6.522	0.007	4.160	0.418	2.405	0.115	0.005	0.033	11.41	0.98	0.79	0.98
VE1503z5	arkosic conglomerate	Verrucano	33.97	2.77	276.205	212.765	42.54	108.69	31.651	0.034	7.505	0.367	4.702	0.376	0.022	0.032	30.34	1.29	0.89	1.29
VE1503z6	arkosic conglomerate	Verrucano	19.19	1.73	223.855	154.8	19.18	83.33	10.617	0.008	4.567	0.311	3.153	0.077	0.020	0.029	16.53	0.94	0.86	0.94

Appendix 2.4. Table of apatite U-Th/He ages

Ref #	SplName	elevation(m)	Corr Age Ma	+/- 1s Ma	U ppm	+/- 1s ppm	Th ppm	+/- 1s ppm	eU ppm	Sm ppm	He nmol/g	He+/-nmol/g	mass (ug)	Ft, alphas retained	r um	l um	RE	Raw Age (Ma	Dim Mass(ug)
09PKB	110830-03	3366	14.50	0.42	155.01	1.84	454.93	4.35	261.921858	104.292031	14.249	0.010645	1.661	0.69	52	111	0	10.00	2.417
09PKC	110830-03	3366	21.94	0.79	166.45	3.11	553.25	6.56	296.461762	142.086417	21.531	0.006764	0.694	0.61	37.5	104	0	13.34	1.178
09PKE	110830-03	3366	23.78	0.70	86.95	1.29	276.37	2.89	151.899343	92.107533	13.709	0.012866	2.089	0.70	51	130	0	16.57	2.723
09PKI	110830-03	3366	16.99	0.53	65.91	1.26	239.78	2.81	122.258889	106.142355	7.748	0.005835	1.659	0.68	54	99	0	11.64	2.325
09PKK	110830-03	3366	19.98	0.44	124.57	0.44	385.14	2.02	215.076169	88.435568	18.857	0.066032	7.816	0.81	82	215	0	16.10	11.643
09PKM	110830-03	3366	17.48	0.65	146.92	2.78	444.33	5.46	251.335357	126.497203	14.356	0.005022	0.767	0.60	36.5	102	0	10.49	1.094
09PKN	110830-03	3366	18.94	0.59	131.81	2.04	409.33	4.40	228.000977	140.262992	15.799	0.009139	1.284	0.67	51	96	0	12.73	2.011
09PKD	110831-02	3847	7.57	4.09	-4.18	-0.60	-17.54	-5.56	-8.2972485	-83.485917	-0.207	0.000197	-0.101	0.59	33.5	138	1	4.53	1.247
09PKF	110831-02	3847	12.89	8.86	0.10	21.75	284.20	73.90	66.8832617	1002.29367	3.127	0.000226	0.008	0.65	39	283	1	8.43	3.467
09PKA	110831-02	3847	15.80	0.62	20.98	0.68	96.07	1.69	43.5578298	174.954318	2.573	0.001609	1.141	0.68	50	119	0	10.81	2.396
09PKJ	110831-02	3847	15.11	0.52	41.72	0.99	128.52	1.86	71.9226554	150.362185	3.997	0.002936	1.555	0.67	42	184	0	10.19	2.614
09PKL	110831-02	3847	15.29	0.58	50.25	1.30	156.32	2.44	86.9887096	152.341776	4.632	0.002262	0.993	0.64	39	137	0	9.77	1.678
09PKP	110831-02	3847	14.90	0.56	54.15	1.35	163.82	2.49	92.6507551	153.516663	4.784	0.002415	1.040	0.63	37	164	0	9.47	1.808
09PKH	110831-02	3847	14.97	0.53	64.44	1.52	189.29	2.77	108.921068	144.902368	5.809	0.00281	1.018	0.65	40.5	149	0	9.79	1.968
09PJZ	110831-02	3847	10.18	0.52	68.15	2.42	254.70	5.47	128.004406	254.575607	4.907	0.001056	0.252	0.69	44.5	203	1	7.03	3.238
09PKO	110831-02	3847	15.47	0.51	92.77	2.03	278.45	3.81	158.200172	245.410489	9.109	0.003616	0.856	0.68	47.5	132	0	10.57	2.399
09PKG	110831-03	3906	20.06	0.59	89.00	1.26	297.00	2.98	158.795249	129.489153	12.101	0.01199	2.205	0.70	53	119	0	13.99	2.692

[This page was intentionally left blank.]

Appendix III.

Clumped isotope data for Kennecott, Alaska

(no Δ_{48} excess in any of these samples)

Sample.ID	dup	MS	Session	Comment	Date	mass.spec.room	Sample.ID.orig.data	mineral	min.type	carb.code1	carb.code2	reltime
1-CAL-GST	B	P.Leia	4		12/3/12	NM01	JP0159_1-CAL-GST	cal	greenstone vein	gst_cal	gst_cal	1.5
2-CAL-GST	B	P.Leia	4		12/3/12	NM01	JP0154_2-CAL-GST	cal	greenstone vein	gst_cal	gst_cal	1.5
4-CAL-GST		P.Leia	1		6/15/12	NM01	JP0023_4-CAL-GST	cal	greenstone vein	gst_cal	gst_cal	1.5
6-CAL-GST	B	P.Leia	4		12/3/12	NM01	JP0160_6-CAL-GST	cal	greenstone vein	gst_cal	gst_cal	1.5
K-203		P.Leia	4		12/3/12	NM01	JP0156_K-203	cal	greenstone vein	gst_cal	gst_cal	1.5
K-204		P.Leia	1		6/14/12	NM01	JP0013_K-204	cal	calcite_vein_dd	cal_syn	cal_syn	2
K-204-DD	B	P.Leia	4		12/4/12	NM01	JP0162_K-204-DD	cal	dedolomite	dedol	dedol	2
K-204-dolwr		P.Leia	1		6/16/12	NM01	JP0027_K-204-DOLWR	dol	dolzd wallrock	dolzd_wallrock	dol.wallrock	1.8
K-206		P.Leia	4		11/30/12	NM01	JP0132_K-206	cal	calcite_vein_contactminzn	cal_syn	cal_syn	2
K-209		P.Leia	1		6/20/12	NM01	JP0057_K-209	cal	calcite_vein_contactminzn	cal_syn	cal_syn	2
K-212		P.Leia	1		6/20/12	NM01	JP0054_K-212	cal	calcite_vein_contactminzn	cal_syn	cal_syn	2
K-213		P.Leia	4		11/30/12	NM01	JP0136_K-213	cal	calcite_vein_contactminzn	cal_syn	cal_syn	2
K-224-1-cal	B	P.Leia	4		12/4/12	NM01	JP0167_K-224-1-cal	cal	calcite_vein	cal_unknown	cal_syn	2
K-224-1-LS		P.Leia	4		12/1/12	NM01	JP0143_K-224-1-LS	cal	limestone	limestone	limestone	0.5
K-224-14F		P.Leia	5		12/7/12	NM01	JP0180_K-224-14F	cal	fault step	fault_step	fault_step	0
K-224-3		Adm.Ackbar	2		8/26/12	NM01	JP0089_K-224-3	cal	calcite_vein	cal_unknown	cal_syn	2
K-224-4	B	P.Leia	4		12/5/12	NM01	JP0168_K-224-4	cal	fault step	fault_step	fault_step	0
K-224-8	B	P.Leia	4		12/5/12	NM01	JP0169_K-224-8	cal	calcite_vein	cal_unknown	cal_syn	2
K-225-10F		P.Leia	1		6/13/12	NM01	JP0009_K-225-10F	cal	fault step	fault_step	fault_step	0
K-225-11F		Adm.Ackbar	2		8/23/12	NM01	JP0072_K-225-11F	cal	fault step	fault_step	fault_step	0
K-225-14F		Adm.Ackbar	2		8/24/12	NM01	JP0081_K-225-14F	cal	fault step	fault_step	fault_step	0
K-225-15-LS		Adm.Ackbar	9	double clean	5/23/14	NM07	JP0294_K-225-15-LS-dblcln	cal	limestone	limestone	limestone	0.5
K-225-15V	B	P.Leia	5		12/7/12	NM01	JP0184_K-225-15V	cal	calcite_vein	cal_unknown	cal_late	2.2
K-225-16V		Adm.Ackbar	2		8/24/12	NM01	JP0080_K-225-16V	cal	calcite_vein	cal_unknown	cal_syn	2
K-225-8V	B	P.Leia	5		12/7/12	NM01	JP0183_K-225-8V	cal	calcite_vein	cal_unknown	cal_late	2.2
K-225-9F	B	P.Leia	5		12/7/12	NM01	JP0181_K-225-9F	cal	fault step	fault_step	fault_step	0
K-225-9F-LS		P.Leia	4		12/1/12	NM01	JP0145_K-225-9F-LS	cal	limestone	limestone	limestone	0.5
K-244		P.Leia	1		6/18/12	NM01	JP0048_K-244	cal	calcite_vein_nodd	cal_unknown	cal_syn	2
K-244-dolwr	B	P.Leia	4		11/28/12	NM01	JP0123_K-244-dolwr	dol	dolzd wallrock	dolzd_wallrock	dol.wallrock	1.8
K-245	B	P.Leia	5		12/8/12	NM01	JP0190_K-245	cal	calcite_vein_dd	cal_syn	cal_syn	2
K-246	B	Adm.Ackbar	6		10/15/13	NM07	JP0203_K-246	cal	calcite_vein	cal_unknown	cal_syn	2.2
K-247-cal	B	Adm.Ackbar	3		9/12/12	NM07	JP0101_K-247dup	cal	calcite_vein_dark	cal_unknown	cal_syn	2
K-249	B	Adm.Ackbar	6		10/15/13	NM07	JP0204_K-249	cal	fault step	fault_step	fault_step	0
K-256	B	Adm.Ackbar	6		10/16/13	NM07	JP0205_K-256	cal	calcite_vein	cal_unknown	cal_syn	2.2
K-257		Adm.Ackbar	6		10/16/13	NM07	JP0206_K-257	cal	fault step	fault_step	fault_step	0
K-258	B	Adm.Ackbar	6		10/16/13	NM07	JP0210_K-258	cal	calcite_vein	cal_unknown	cal_late	0
K-276-ZD-1	Z	Adm.Ackbar	8		3/6/14	NM07	JP0260_K-276ZD-1	dol	dolzd wallrock	dolzd_wallrock	dol.wallrock	1.8
K-276-ZD-2	Z	Adm.Ackbar	8	acq 7-8 <14V, P balance OK	3/6/14	NM07	JP0261_K-276ZD-2	dol	baroque dol	baroque_dol	dol.baroque	1.8
K-276-ZD-3	Z	Adm.Ackbar	9		5/23/14	NM07	JP0296_K-276-ZD-3	dol	dolzd wallrock	dolzd_wallrock	dol.wallrock	1.8
K-276-ZD-4	Z	Adm.Ackbar	9		5/23/14	NM07	JP0298_K-276-ZD-4	dol	baroque dol	baroque_dol	dol.baroque	1.8
K-276-ZD-5	Z	Adm.Ackbar	8		3/8/14	NM07	JP0274_K-274ZD-5	dol	dolzd wallrock	dolzd_wallrock	dol.wallrock	1.8
K-276-ZD-6	Z	Adm.Ackbar	9		5/22/14	NM07	JP0292_K-276-ZD-6	dol	baroque dol	baroque_dol	dol.baroque	1.8
K-276-ZD-7	Z	Adm.Ackbar	9		5/23/14	NM07	JP0300_K-276-ZD-7	dol	dolzd wallrock	dolzd_wallrock	dol.wallrock	1.8
K-276-ZD-8	Z	Adm.Ackbar	9		5/24/14	NM07	JP0301_K-276-ZD-8	dol	baroque dol	baroque_dol	dol.baroque	1.8
K-276-ZD-9	Z	Adm.Ackbar	9	rejected 1 acq.	5/24/14	NM07	JP0303_K-276-ZD-9	dol	dolzd wallrock	dolzd_wallrock	dol.wallrock	1.8
K-276-ZD-10	Z	Adm.Ackbar	9		5/24/14	NM07	JP0304_K-276-ZD-10	dol	baroque dol	baroque_dol	dol.baroque	1.8
K-276-ZD-11	Z	Adm.Ackbar	9		5/24/14	NM07	JP0307_K-276-ZD-11	dol	dolzd wallrock	dolzd_wallrock	dol.wallrock	1.8

Sample.ID	ARF.Δ_{47}err.dup	ARF.T.final (°C)	ARF.T.err.u (°C)	ARF.T.err.d (°C)	δ^{18}O.min.SMOW (‰)	δ^{18}O.water.SMOW (‰)	δ^{18}O.water.err.u (‰)	δ^{18}O.water.err.d (‰)
K-276-ZD-12	0.0159	130.8	13.3	11.9	18.5440	-0.8647	1.0127	0.9919
K-276-ZD-13	0.0199	112.3	14.1	12.4	17.4396	-3.5280	1.2246	1.1950
K-300	0.0126	93.3	7.2	6.7	18.5564	0.5751	0.7932	0.7818
K-301	0.0182	97.1	11.0	9.9	16.3095	-1.2080	1.1527	1.1285
K-302	0.0104	117.8	7.6	7.1	15.2729	-0.1444	0.6833	0.6744
K-302-bdol	0.0167	93.5	9.7	8.8	20.2351	-2.6426	0.9891	0.9704
K-303-DD	0.0363	96.7	23.1	18.8	14.0131	-3.5108	2.3171	2.2212
K-303-dolwr	0.0345	109.7	25.1	20.2	16.4051	-4.7772	2.1285	2.0410
K-304	0.0187	104.1	12.2	10.9	16.3325	-0.4461	1.2016	1.1750
K-305-1	0.0156	64.3	6.6	6.1	23.4223	1.6246	0.9233	0.9088
K-305-3	0.0150	43.9	4.9	4.6	22.1102	-2.9001	0.8361	0.8246
K-305-5	0.0146	62.8	6.0	5.6	20.5966	-1.3592	0.8550	0.8425
K-305-6	0.0180	81.6	9.2	8.4	22.2378	2.7946	1.1095	1.0878
K-307B-LS	0.0312	111.5	22.9	18.8	19.3481	3.2710	2.0574	1.9800
K-308-CAL	0.0226	119.9	17.4	15.0	13.5557	-1.6421	1.4951	1.4531
KEN-1	0.0293	56.6	11.6	10.2	21.9688	-0.9490	1.7052	1.6569
Ken-1-LS-dblcln	0.0131	118.1	9.6	8.8	19.4742	4.0244	0.8665	0.8523
KEN-14A-LS	0.0197	114.8	14.3	12.6	17.3409	1.6129	1.2954	1.2641
KEN-14B-LS	0.0190	109.2	13.0	11.6	17.8295	1.5508	1.2349	1.2067
KEN-2-toothycem	0.0097	43.4	3.1	3.0	13.9381	-10.9547	0.5332	0.5285
KEN-20	0.0176	56.6	6.8	6.3	16.3207	-6.4656	1.0108	0.9936
KEN-22	0.0402	132.4	37.7	28.2	13.1624	-0.9352	2.7538	2.6119
KEN-23	0.0161	107.3	10.7	9.7	15.7697	-0.6660	1.0379	1.0179
KEN-26A-LS	0.0210	124.8	16.9	14.6	20.1040	5.2505	1.4072	1.3699
KEN-26B-LS	0.0125	121.3	9.4	8.7	19.3257	4.1744	0.8295	0.8165
KEN-30	0.0099	109.4	6.6	6.2	18.5140	2.2408	0.6409	0.6332
KEN-302-dolwr	0.0442	115.1	35.2	26.4	19.5778	-1.1793	2.7824	2.6340
KEN-35	0.0297	104.2	20.1	16.8	16.7235	-0.0517	1.9227	1.8556
KEN-4-DD	0.0314	94.2	19.2	16.1	15.7464	-2.0890	1.9917	1.9208
KEN-4-dolwr	0.0293	131.1	25.9	21.0	18.5069	-0.8756	1.8772	1.8069
KEN-40-CAL-GST	0.0438	107.4	32.2	24.5	14.4946	-1.9163	2.8749	2.7262
KEN-42-cal	0.0317	57.8	12.8	11.1	20.7319	-1.9671	1.8499	1.7930
KEN-42-LS	0.0356	107.2	25.3	20.3	18.6155	2.1238	2.3329	2.2345
KEN-4B	0.0166	89.0	9.1	8.4	19.3967	0.8994	1.0333	1.0141
KEN-5	0.0299	99.7	19.3	16.2	17.6519	0.3866	1.9193	1.8530
KEN-7A-bdol	0.0310	139.7	30.0	23.7	20.0832	1.3345	2.0232	1.9409
KEN-7A-CAL	0.0335	116.2	25.9	20.8	16.0480	0.4706	2.2231	2.1321
KEN-7A-dolwr	0.0300	114.7	22.5	18.6	19.9931	-0.8088	1.8682	1.8003
KEN-7B-bdol	0.0294	116.6	22.5	18.6	19.8286	-0.7951	1.8365	1.7706
KEN-7B-CAL	0.0315	104.1	21.4	17.7	15.7980	-0.9738	2.0411	1.9656
KEN-7B-dolwr	0.0329	112.1	24.4	19.8	19.8137	-1.2218	2.0451	1.9642

Sample.ID	dup	MS	Session	Comment	Date	mass.spec.room	Sample.ID.orig.data	mineral	min.type	carb.code1	carb.code2	reltime
K-276-ZD-12	Z	Adm.Ackbar	9	rejected 1 acq.	5/24/14	NM07	JP0308_K-276-ZD-12	dol	baroque dol	baroque_dol	dol.baroque	1.8
K-276-ZD-13	Z	Adm.Ackbar	9		5/24/14	NM07	JP0309_K-276-ZD-13	dol	dolzd wallrock	dolzd_wallrock	dol.wallrock	1.8
K-300		Adm.Ackbar	2		8/26/12	NM01	JP0090_K-300	cal	dedolomite	dedol	dedol	2
K-301		Adm.Ackbar	6		10/17/13	NM07	JP0211_K-301	cal	calcite_vein_contactminzn	cal_syn	cal_syn	2
K-302	B	Adm.Ackbar	6		10/17/13	NM07	JP0213_K-302	cal	cal bx matrix	bx_matrix	bx_matrix	1.9
K-302-bdol	B	Adm.Ackbar	6	acq 2-8 <14V, P balance OK	10/17/13	NM07	JP0214_K-302BDOL	dol	baroque dol	baroque_dol	dol.baroque	1.8
K-303-DD		Adm.Ackbar	3		9/13/12	NM07	JP0107_K-303-DD	cal	dedolomite	dedol	dedol	2
K-303-dolwr		Adm.Ackbar	3		9/13/12	NM07	JP0105_K-303-dolwr	dol	dolzd wallrock	dolzd_wallrock	dol.wallrock	1.8
K-304		P.Leia	4		11/29/12	NM01	JP0129_K-304	cal	calcite_vein_contactminzn	cal_syn	cal_syn	2
K-305-1		P.Leia	4		11/30/12	NM01	JP0133_K-305-1	cal	fault step	fault_step	fault_step	0
K-305-3		Adm.Ackbar	2		8/23/12	NM01	JP0077_K-305-3	cal	fault step	fault_step	fault_step	0
K-305-5		Adm.Ackbar	2		8/29/12	NM01	JP0094_K-305-5	cal	fault step	fault_step	fault_step	0
K-305-6		P.Leia	4		11/30/12	NM01	JP0134_K-305-6	cal	fault step	fault_step	fault_step	0
K-307B-LS		P.Leia	1		6/17/12	NM01	JP0035_K-307B-LS	cal	limestone	limestone	limestone	0.5
K-308-CAL		Adm.Ackbar	2		8/24/12	NM01	JP0082_K-308-CAL	cal	greenstone vein	gst_cal	gst_cal	1.5
KEN-1		P.Leia	1		6/19/12	NM01	JP0050_KEN-1	cal	calcite_vein_early	cal_early	cal_early	1.9
Ken-1-LS-dblcln	B	Adm.Ackbar	9		5/21/14	NM07	JP0289_Ken-1-LS-dblcln	cal	limestone	limestone	limestone	0.5
KEN-14A-LS	B	P.Leia	4		11/28/12	NM01	JP0122_KEN-14A-LS	cal	limestone	limestone	limestone	0.5
KEN-14B-LS	B	P.Leia	4		11/28/12	NM01	JP0126_KEN-14B-LS	cal	limestone	limestone	limestone	0.5
KEN-2-toothycem	B	Adm.Ackbar	8		3/7/14	NM07	JP0266_KEN-2B-toothycem-dup	cal	toothycem	cal_unknown	cal_early	0.5
KEN-20		Adm.Ackbar	2		8/22/12	NM01	JP0069_KEN-20	cal	cal bx matrix type 2	cal_unknown	cal_early	2.5
KEN-22		P.Leia	1		6/20/12	NM01	JP0056_KEN-22	cal	greenstone vein	gst_cal	gst_cal	1.5
KEN-23		Adm.Ackbar	2		8/26/12	NM01	JP0093_KEN-23	cal	calcite_vein	cal_early	cal_syn	1.9
KEN-26A-LS		P.Leia	4	sm spl, P balance OK	11/30/12	NM01	JP0139_KEN-26A-LS	cal	limestone	limestone	limestone	0.5
KEN-26B-LS	B	Adm.Ackbar	9	oven thermal fault, runaway LN2	5/21/14	NM07	JP0290_Ken26B-LS	cal	limestone	limestone	limestone	0.5
KEN-30	B	Adm.Ackbar	2		8/25/12	NM01	JP0088_KEN-30-dup	cal	calcite_vein_dd	cal_syn	cal_syn	2
KEN-302-dolwr		Adm.Ackbar	3		9/12/12	NM07	JP0102_KEN-302-dolwr	dol	dolzd wallrock	dolzd_wallrock	dol.wallrock	1.8
KEN-35		P.Leia	1		6/20/12	NM01	JP0061_KEN-35	cal	cal bx matrix	bx_matrix	bx_matrix	1.8
KEN-4-DD		P.Leia	1		6/13/12	NM01	JP0007_KEN-4-DD	cal	dedolomite	dedol	dedol	2
KEN-4-dolwr		P.Leia	1		6/16/12	NM01	JP0030_KEN-4-DOLWR	dol	dolzd wallrock	dolzd_wallrock	dol.wallrock	1.8
KEN-40-CAL-GST		P.Leia	1		6/19/12	NM01	JP0049_KEN-40-CAL-GST	cal	greenstone vein	gst_cal	gst_cal	1.5
KEN-42-cal		P.Leia	1		6/20/12	NM01	JP0060_KEN-42	cal	calcite_vein	cal_unknown	cal_syn	2.2
KEN-42-LS		Adm.Ackbar	3		9/14/12	NM07	JP0109_KEN-42-LS	cal	limestone	limestone	limestone	0.5
KEN-4B	B	Adm.Ackbar	2		8/22/12	NM01	JP0070_KEN-4B_dup	cal	calcite_vein_dd	cal_syn	cal_syn	2
KEN-5		P.Leia	1		6/20/12	NM01	JP0055_KEN-5	cal	calcite_vein_dd	cal_syn	cal_syn	2
KEN-7A-bdol		P.Leia	1		6/14/12	NM01	JP0018_KEN-7A-BDOL	dol	baroque dol	baroque_dol	dol.baroque	1.8
KEN-7A-CAL		P.Leia	1		6/12/12	NM01	JP0004_KEN-7A-CAL	cal	cal bx matrix	bx_matrix	bx_matrix	1.8
KEN-7A-dolwr		P.Leia	1		6/16/12	NM01	JP0028_KEN-7A-DOLWR	dol	dolzd wallrock	dolzd_wallrock	dol.wallrock	1.8
KEN-7B-bdol		P.Leia	1		6/15/12	NM01	JP0019_KEN-7B-BDOL	dol	baroque dol	baroque_dol	dol.baroque	1.8
KEN-7B-CAL		P.Leia	1		6/12/12	NM01	JP0005_KEN-7B-CAL	cal	cal bx matrix	bx_matrix	bx_matrix	1.8
KEN-7B-dolwr		P.Leia	1		6/16/12	NM01	JP0029_KEN-7B-DOLWR	dol	dolzd wallrock	dolzd_wallrock	dol.wallrock	1.8

Sample.ID	strat.height_m	notes	spec.num	num.acq	$\delta^{13}C$ (‰)	$\delta^{13}C$.stdev (‰)	$\delta^{13}C$.sterr (‰)	$\delta^{18}O$.gas (‰)	$\delta^{18}O$.gas.stdev (‰)	$\delta^{18}O$.gas.sterr (‰)	δ^{47} (‰)
1-CAL-GST	-5	epi-cal vn	164	8	-8.3350	0.0073	0.0026	22.5491	0.0114	0.0040	-7.7351
2-CAL-GST	-4	epi-cal vn	124	8	-4.9071	0.0058	0.0020	23.2114	0.0115	0.0041	-3.6139
4-CAL-GST	-10	epi-cal vn	717	8	-3.2660	0.0080	0.0028	21.8000	0.0160	0.0057	-3.4620
6-CAL-GST	-11	epi-cal vn	172	8	-10.3965	0.0044	0.0016	22.4510	0.0124	0.0044	-9.8907
K-203	-8	epi-cal vn	140	8	-7.3455	0.0046	0.0016	22.2565	0.0103	0.0036	-7.0341
K-204	40	has dedolomite halo	637	8	2.7180	0.0060	0.0021	24.1400	0.0110	0.0039	4.8030
K-204-DD	40	unit 4	188	8	3.0308	0.0079	0.0028	22.7700	0.0170	0.0060	3.6937
K-204-dolwr	40	unit 4	751	8	3.8090	0.0080	0.0028	26.8010	0.0180	0.0064	8.6160
K-206	25	synmineral	1616	8	2.6939	0.0038	0.0013	24.9086	0.0070	0.0025	5.5899
K-209	46	synmineral	996	8	3.0230	0.0060	0.0021	25.9030	0.0090	0.0032	6.9470
K-212	30	synmineral	972	8	2.5560	0.0200	0.0071	25.4020	0.0480	0.0170	5.9530
K-213	24	synmineral	1648	8	2.0419	0.0064	0.0023	27.9479	0.0118	0.0042	8.1228
K-224-1-cal	19	unit 4	238	8	2.9070	0.0059	0.0021	25.1471	0.0132	0.0047	6.0204
K-224-1-LS	19	unit 4, next to Glory Hole	32	8	3.0446	0.0174	0.0062	26.6045	0.0449	0.0159	7.6426
K-224-14F	22	unit 4	363	8	4.4310	0.0020	0.0007	33.8400	0.0060	0.0021	16.6540
K-224-3	19	unit 4	1430	8	2.9869	0.0026	0.0009	24.0326	0.0037	0.0013	4.9361
K-224-4	22	unit 4	246	8	0.4085	0.0043	0.0015	28.1743	0.0127	0.0045	6.6917
K-224-8	19	unit 4	254	8	2.6598	0.0036	0.0013	25.4233	0.0120	0.0042	6.0716
K-225-10F	6	unit 2	604	8	4.8300	0.0100	0.0035	32.5640	0.0190	0.0067	15.6190
K-225-11F	6	unit 2	1719	8	4.3080	0.0020	0.0007	28.1870	0.0040	0.0014	10.6070
K-225-14F	6	unit 2	1371	8	4.5741	0.0030	0.0011	34.0653	0.0027	0.0009	16.9547
K-225-15-LS	6	unit 2	1052	8	4.6573	0.0035	0.0013	29.9874	0.0045	0.0016	12.6694
K-225-15V	6	unit 2	395	8	3.9510	0.0010	0.0004	26.6810	0.0030	0.0011	8.7900
K-225-16V	6	unit 2	1363	8	4.3646	0.0018	0.0006	28.7149	0.0025	0.0009	11.1100
K-225-8V	6	unit 2	387	8	4.0650	0.0010	0.0004	29.7730	0.0030	0.0011	12.0650
K-225-9F	6	unit 2	371	8	4.6520	0.0030	0.0011	30.1060	0.0040	0.0014	12.9970
K-225-9F-LS	6	unit 2	48	8	5.3321	0.0074	0.0026	28.6093	0.0171	0.0060	11.9797
K-244	29	no dedolomite halo	923	8	2.1160	0.0090	0.0032	28.4170	0.0180	0.0064	8.5990
K-244-dolwr	29	unit 4, cal vein no dedol halo	1526	8	4.0174	0.0039	0.0014	30.3069	0.0070	0.0025	12.5000
K-245	30	has dedolomite halo	444	8	1.9313	0.0018	0.0006	28.0436	0.0042	0.0015	8.0008
K-246	13	N of chute off Glory Hole	862	8	3.6404	0.0037	0.0013	29.0910	0.0088	0.0031	10.8041
K-247-cal	13	organic C	432	8	-8.2259	0.0017	0.0006	27.3336	0.0072	0.0026	-2.7233
K-249	14	near slip adit (unit 3)	871	8	4.8283	0.0046	0.0016	27.9625	0.0077	0.0027	10.8104
K-256	31	big calcite vein on 1st hoodoo	880	8	-1.2445	0.0033	0.0012	28.5030	0.0082	0.0029	5.3651
K-257	30	SW side of 1st hoodoo	889	8	2.9524	0.0029	0.0010	17.0411	0.0067	0.0024	-2.0892
K-258	30	void-fill, late, SW side of 1st hoodoo	929	8	3.1528	0.0027	0.0010	16.6853	0.0053	0.0019	-2.2006
K-276-ZD-1	45	zebra dolomite	128	8	3.8820	0.0030	0.0011	27.9840	0.0050	0.0018	9.8260
K-276-ZD-2	45	zebra dolomite	137	8	3.6860	0.0040	0.0014	28.1700	0.0080	0.0028	9.8670
K-276-ZD-3	45	zebra dolomite	1071	8	3.6274	0.0041	0.0014	27.4588	0.0054	0.0019	9.0736
K-276-ZD-4	45	zebra dolomite	1090	8	3.4638	0.0035	0.0012	28.8648	0.0057	0.0020	10.3504
K-276-ZD-5	45	zebra dolomite	254	8	3.7760	0.0050	0.0018	27.5560	0.0100	0.0035	9.2960
K-276-ZD-6	45	zebra dolomite	1031	8	3.4235	0.0020	0.0007	28.2218	0.0031	0.0011	9.6744
K-276-ZD-7	45	zebra dolomite	1109	8	3.6524	0.0034	0.0012	26.8099	0.0072	0.0025	8.4326
K-276-ZD-8	45	zebra dolomite	1118	8	3.6688	0.0039	0.0014	27.5148	0.0089	0.0031	9.1178
K-276-ZD-9	45	zebra dolomite	1136	7	3.4556	0.0040	0.0015	23.3673	0.0059	0.0022	8.1184
K-276-ZD-10	45	zebra dolomite	1145	8	3.6166	0.0047	0.0017	27.1346	0.0102	0.0036	8.6729
K-276-ZD-11	45	zebra dolomite	1173	8	3.5743	0.0048	0.0017	26.7560	0.0090	0.0032	8.2978

Sample.ID	strat.height_m	notes	spec.num	num.acq	$\delta^{13}C$ (‰)	$\delta^{13}C$.stdev (‰)	$\delta^{13}C$.sterr (‰)	$\delta^{18}O$.gas (‰)	$\delta^{18}O$.gas.stdev (‰)	$\delta^{18}O$.gas.sterr (‰)	δ^{47} (‰)
K-276-ZD-12	45	zebra dolomite	1182	7	3.1846	0.0044	0.0017	28.0324	0.0116	0.0044	9.2000
K-276-ZD-13	45	zebra dolomite	1191	8	3.3896	0.0029	0.0010	26.9178	0.0058	0.0021	8.2923
K-300	42	Bonanza cirque	1438	8	2.1791	0.0025	0.0009	26.8359	0.0040	0.0014	7.0329
K-301	25	synmineral	938	8	2.0259	0.0034	0.0012	24.5706	0.0097	0.0034	4.5657
K-302	32	NE end of Glory Hole	956	8	2.5023	0.0037	0.0013	23.5256	0.0077	0.0027	3.9472
K-302-bdol	31	NE end of Glory Hole	965	7	3.2833	0.0025	0.0009	29.7393	0.0085	0.0032	11.0652
K-303-DD	38	NE end of Glory Hole	507	8	2.8531	0.0034	0.0012	22.2556	0.0081	0.0029	3.0468
K-303-dolwr	38	NE end of Glory Hole	489	8	3.5495	0.0063	0.0022	25.8736	0.0123	0.0044	7.3738
K-304	22	azurite	1585	8	2.3395	0.0064	0.0023	24.5939	0.0124	0.0044	4.9398
K-305-1	10	unit 2	1624	8	4.7521	0.0053	0.0019	31.7413	0.0120	0.0043	14.7232
K-305-3	10	unit 2	1339	8	4.5238	0.0019	0.0007	30.4185	0.0027	0.0009	13.1557
K-305-5	10	unit 2	1615	8	5.2090	0.0021	0.0008	28.8926	0.0054	0.0019	12.2786
K-305-6	10	unit 2	1632	8	5.1683	0.0065	0.0023	30.5471	0.0135	0.0048	13.8708
K-307B-LS	22	unit 4, fresh rock	815	8	3.5630	0.0100	0.0035	27.6340	0.0200	0.0071	9.2180
K-308-CAL	-20	epi-cal vn	1379	8	-3.5025	0.0026	0.0009	21.7945	0.0040	0.0014	-3.7321
KEN-1	21	cut by stylolites	939	8	4.1150	0.0050	0.0018	30.2760	0.0110	0.0039	12.5760
Ken-1-LS-dblcln	22	unit 4	1003	8	4.0826	0.0037	0.0013	27.7611	0.0059	0.0021	9.8516
KEN-14A-LS	20	unit 4	1518	8	3.5574	0.0063	0.0022	25.6105	0.0114	0.0040	7.1908
KEN-14B-LS	20	unit 4	1552	8	3.1861	0.0048	0.0017	26.1030	0.0082	0.0029	7.3163
KEN-2-toothycem	28	1st algal mat	180	8	-3.1870	0.0040	0.0014	22.1800	0.0050	0.0018	-2.8160
KEN-20	30	void fill type 2 bx	1695	8	-0.3260	0.0020	0.0007	24.5820	0.0040	0.0014	2.3780
KEN-22	-5	epi-cal-Cu vn	988	8	-2.6790	0.0060	0.0021	21.3980	0.0160	0.0057	-3.3090
KEN-23	23	pre-chalcocite	1465	8	2.5195	0.0033	0.0011	24.0265	0.0026	0.0009	4.4732
KEN-26A-LS	6	unit 2, fresh	1672	8	5.4435	0.0177	0.0063	28.3960	0.0313	0.0111	11.8557
KEN-26B-LS	6	unit 2, fresh	1012	8	5.2913	0.0033	0.0012	27.6114	0.0042	0.0015	10.8428
KEN-30	42	has dedolomite halo	1421	8	2.1094	0.0032	0.0011	26.7931	0.0045	0.0016	6.8840
KEN-302-dolwr	31	NE end of Glory Hole	441	8	3.5939	0.0099	0.0035	29.0759	0.0183	0.0065	10.6593
KEN-35	27	Glory Hole	1028	8	3.1120	0.0060	0.0021	24.9880	0.0120	0.0042	6.0820
KEN-4-DD	42	prominent dedolomite halo	588	8	2.4910	0.0080	0.0028	24.0030	0.0140	0.0049	4.4840
KEN-4-dolwr	42	prominent dedolomite halo	775	8	3.7040	0.0080	0.0028	27.9950	0.0180	0.0064	9.6980
KEN-40-CAL-GST	-5	epi-cal vn	931	8	-7.2460	0.0060	0.0021	22.7410	0.0160	0.0057	-6.4000
KEN-42-cal	17	unit 3	1020	8	1.6560	0.0040	0.0014	29.0290	0.0080	0.0028	8.8640
KEN-42-LS	17	unit 3	526	8	3.4829	0.0032	0.0011	26.8954	0.0045	0.0016	8.3377
KEN-4B	43	has dedolomite halo	1703	8	2.3680	0.0030	0.0011	27.6830	0.0040	0.0014	8.1360
KEN-5	41	has dedolomite halo	980	8	2.5270	0.0050	0.0018	25.9240	0.0070	0.0025	6.4680
KEN-7A-bdol	32	NE end of Glory Hole	677	8	3.7620	0.0070	0.0025	29.5860	0.0140	0.0049	11.3710
KEN-7A-CAL	32	NE end of Glory Hole	562	8	2.7150	0.0070	0.0025	24.3070	0.0130	0.0046	4.9780
KEN-7A-dolwr	32	NE end of Glory Hole	759	8	3.7140	0.0050	0.0018	29.4950	0.0150	0.0053	11.2630
KEN-7B-bdol	32	NE end of Glory Hole	685	8	3.6730	0.0070	0.0025	29.3290	0.0150	0.0053	11.0510
KEN-7B-CAL	32	NE end of Glory Hole	570	8	2.2780	0.0070	0.0025	24.0550	0.0160	0.0057	4.3110
KEN-7B-dolwr	32	NE end of Glory Hole	767	8	3.4490	0.0080	0.0028	29.3140	0.0190	0.0067	10.8200

Sample.ID	δ^{47}.stdev (‰)	δ^{47}.sterr (‰)	Δ_{47} (‰)	Δ_{47}.stdev (‰)	Δ_{47}.sterr (‰)	δ^{48} (‰)	δ^{48}.stdev (‰)	δ^{48}.sterr (‰)	Δ_{48} (‰)	Δ_{48}.stdev (‰)	Δ_{48}.sterr (‰)	Δ_{47}.extvar (‰)^2	Δ_{47}.extsterr (‰)	HGcorrΔ_{47} (‰)
1-CAL-GST	0.0280	0.0099	-0.7280	0.0257	0.0091	-9.3127	0.1663	0.0588	-4.5034	0.1790	0.0633	0.0010	0.0319	0.3048
2-CAL-GST	0.0307	0.0109	-0.5659	0.0211	0.0075	-7.3176	0.3702	0.1309	-3.8030	0.3867	0.1367	0.0007	0.0267	0.3752
4-CAL-GST	0.0360	0.0127	-0.5940	0.0400	0.0141	-10.9800	0.2260	0.0799	-4.7460	0.2470	0.0873	0.0017	0.0412	0.3308
6-CAL-GST	0.0346	0.0122	-0.8013	0.0408	0.0144	-9.6970	0.4360	0.1542	-4.6897	0.4376	0.1547	0.0013	0.0363	0.2795
K-203	0.0230	0.0081	-0.6906	0.0281	0.0099	-10.5540	0.3392	0.1199	-5.1867	0.3595	0.1271	0.0010	0.0314	0.3266
K-204	0.0330	0.0117	-0.4310	0.0300	0.0106	-2.8990	0.2770	0.0979	-1.2140	0.2740	0.0969	0.0010	0.0314	0.3296
K-204-DD	0.0386	0.0137	-0.4716	0.0349	0.0123	-8.7088	0.2998	0.1060	-4.3762	0.3096	0.1094	0.0005	0.0217	0.3068
K-204-dolwr	0.0250	0.0088	-0.3350	0.0160	0.0057	5.2260	0.4100	0.1450	1.7120	0.4190	0.1481	0.0008	0.0286	0.3498
K-206	0.0334	0.0118	-0.3894	0.0318	0.0113	-0.1217	0.1308	0.0462	0.0674	0.1335	0.0472	0.0004	0.0199	0.3468
K-209	0.0350	0.0124	-0.3440	0.0360	0.0127	2.4370	0.3960	0.1400	0.6850	0.4080	0.1442	0.0010	0.0312	0.3740
K-212	0.0910	0.0322	-0.3860	0.0370	0.0131	0.6070	0.2120	0.0750	-0.1630	0.2280	0.0806	0.0010	0.0318	0.3517
K-213	0.0273	0.0097	-0.2643	0.0206	0.0073	9.9489	0.2500	0.0884	4.1849	0.2594	0.0917	0.0003	0.0164	0.4156
K-224-1-cal	0.0295	0.0104	-0.4029	0.0286	0.0101	-0.1166	0.3378	0.1194	-0.3930	0.3456	0.1222	0.0004	0.0190	0.3238
K-224-1-LS	0.0928	0.0328	-0.3717	0.0401	0.0142	5.3328	0.3444	0.1218	2.2055	0.3950	0.1397	0.0004	0.0207	0.3189
K-224-14F	0.0390	0.0138	-0.0456	0.0412	0.0146	29.6921	0.7780	0.2751	12.0020	0.7740	0.2737	0.0007	0.0270	0.4904
K-224-3	0.0337	0.0119	-0.4496	0.0314	0.0111	-4.8430	0.7449	0.2634	-2.9538	0.7418	0.2623	0.0003	0.0166	0.2933
K-224-4	0.0308	0.0109	-0.3377	0.0318	0.0112	10.7169	0.3070	0.1085	4.5140	0.3214	0.1136	0.0004	0.0192	0.3740
K-224-8	0.0290	0.0103	-0.3889	0.0261	0.0092	0.7899	0.3427	0.1212	-0.0237	0.3413	0.1207	0.0003	0.0185	0.3366
K-225-10F	0.0300	0.0106	-0.0990	0.0240	0.0085	24.2350	0.1510	0.0534	9.3020	0.1850	0.0654	0.0010	0.0320	0.4467
K-225-11F	0.0320	0.0113	-0.2160	0.0300	0.0106	10.6040	0.5580	0.1973	4.3590	0.5500	0.1945	0.0002	0.0152	0.4072
K-225-14F	0.0317	0.0112	-0.0187	0.0299	0.0106	30.3649	0.7110	0.2514	12.4005	0.6987	0.2470	0.0003	0.0161	0.4706
K-225-15-LS	0.0515	0.0182	-0.2563	0.0507	0.0179	11.9290	0.5230	0.1849	2.1468	0.5108	0.1806	0.0005	0.0226	0.3326
K-225-15V	0.0330	0.0117	-0.2694	0.0335	0.0118	5.6168	0.8841	0.3126	2.1600	0.8850	0.3129	0.0007	0.0264	0.4249
K-225-16V	0.0177	0.0063	-0.2955	0.0176	0.0062	12.2257	0.5221	0.1846	4.9398	0.5164	0.1826	0.0002	0.0125	0.3172
K-225-8V	0.0150	0.0053	-0.2005	0.0156	0.0055	16.0763	0.2539	0.0898	6.5180	0.2510	0.0887	0.0005	0.0231	0.4279
K-225-9F	0.0230	0.0081	-0.1734	0.0246	0.0087	16.6727	0.3160	0.1117	6.4550	0.3150	0.1114	0.0006	0.0240	0.4363
K-225-9F-LS	0.0451	0.0160	-0.2586	0.0420	0.0149	12.4537	0.2674	0.0946	5.3682	0.2907	0.1028	0.0004	0.0202	0.3354
K-244	0.0380	0.0134	-0.3280	0.0290	0.0103	10.9160	0.3390	0.1199	4.2310	0.3680	0.1301	0.0009	0.0299	0.3572
K-244-dolwr	0.0228	0.0080	-0.1646	0.0241	0.0085	18.6384	0.2104	0.0744	8.1883	0.2121	0.0750	0.0003	0.0161	0.4179
K-245	0.0205	0.0072	-0.4633	0.0215	0.0076	9.2029	0.4996	0.1766	3.0810	0.5016	0.1773	0.0006	0.0252	0.2468
K-246	0.0337	0.0119	-0.2375	0.0303	0.0107	10.1994	0.7977	0.2820	2.1797	0.7764	0.2745	0.0002	0.0158	0.4046
K-247-cal	0.0465	0.0164	-0.5151	0.0394	0.0139	6.5186	0.9090	0.3214	1.9958	0.8947	0.3163	0.0017	0.0414	0.2826
K-249	0.0525	0.0186	-0.2526	0.0437	0.0155	6.8144	0.9448	0.3341	1.0083	0.9283	0.3282	0.0004	0.0193	0.3894
K-256	0.0441	0.0156	-0.3512	0.0362	0.0128	9.3236	0.8388	0.2965	2.4764	0.8226	0.2908	0.0003	0.0177	0.3646
K-257	0.0321	0.0113	-0.4132	0.0329	0.0116	-25.0391	0.7111	0.2514	-9.7460	0.7101	0.2511	0.0004	0.0196	0.4036
K-258	0.0491	0.0174	-0.3607	0.0436	0.0154	-25.8261	0.6399	0.2262	-9.8541	0.6428	0.2273	0.0005	0.0221	0.4576
K-276-ZD-1	0.0270	0.0095	-0.3400	0.0220	0.0078	7.6270	0.2730	0.0965	1.7790	0.2650	0.0937	0.0001	0.0091	0.3153
K-276-ZD-2	0.0440	0.0156	-0.2970	0.0360	0.0127	8.2700	0.5310	0.1877	2.0560	0.5180	0.1831	0.0002	0.0136	0.3577
K-276-ZD-3	0.0441	0.0156	-0.3213	0.0419	0.0148	5.7568	0.4301	0.1521	0.9417	0.4183	0.1479	0.0004	0.0202	0.3129
K-276-ZD-4	0.0225	0.0080	-0.2930	0.0237	0.0084	10.3954	0.2937	0.1038	2.8154	0.2865	0.1013	0.0003	0.0161	0.3251
K-276-ZD-5	0.0670	0.0237	-0.3400	0.0540	0.0191	6.2010	0.8390	0.2966	1.1940	0.8170	0.2889	0.0004	0.0197	0.3222
K-276-ZD-6	0.0329	0.0116	-0.2867	0.0327	0.0115	9.1952	0.2952	0.1044	2.8759	0.2899	0.1025	0.0003	0.0179	0.3399
K-276-ZD-7	0.0411	0.0145	-0.3367	0.0423	0.0150	4.0980	0.5856	0.2070	0.5530	0.5799	0.2050	0.0004	0.0204	0.3057
K-276-ZD-8	0.0423	0.0150	-0.3723	0.0325	0.0115	6.3051	0.5177	0.1830	1.3784	0.5021	0.1775	0.0003	0.0179	0.2614
K-276-ZD-9	0.0161	0.0061	-0.3560	0.0210	0.0079	4.6612	0.2711	0.1025	1.3182	0.2697	0.1020	0.0003	0.0160	0.2904
K-276-ZD-10	0.0336	0.0119	-0.3866	0.0233	0.0082	6.1036	1.1115	0.3930	1.9179	1.0936	0.3867	0.0003	0.0160	0.2527
K-276-ZD-11	0.0351	0.0124	-0.3419	0.0298	0.0105	4.2684	0.5886	0.2081	0.8280	0.5711	0.2019	0.0003	0.0174	0.3022

Sample.ID	δ^{47}.stdev (‰)	δ^{47}.sterr (‰)	Δ_{47} (‰)	Δ_{47}.stdev (‰)	Δ_{47}.sterr (‰)	δ^{48} (‰)	δ^{48}.stdev (‰)	δ^{48}.sterr (‰)	Δ_{48} (‰)	Δ_{48}.stdev (‰)	Δ_{48}.sterr (‰)	Δ_{47}.extvar (‰)^2	Δ_{47}.extsterr (‰)	HGcorrΔ_{47} (‰)
K-276-ZD-12	0.0290	0.0110	-0.3395	0.0213	0.0081	7.6590	0.7091	0.2680	1.7191	0.6832	0.2582	0.0003	0.0159	0.2932
K-276-ZD-13	0.0459	0.0162	-0.3306	0.0405	0.0143	4.5279	0.6511	0.2302	0.7724	0.6469	0.2287	0.0004	0.0199	0.3135
K-300	0.0173	0.0061	-0.3749	0.0145	0.0051	4.7567	0.5540	0.1959	1.1840	0.5500	0.1944	0.0002	0.0126	0.3238
K-301	0.0416	0.0147	-0.3919	0.0376	0.0133	-2.6770	0.4658	0.1647	-1.8471	0.4474	0.1582	0.0003	0.0182	0.3348
K-302	0.0309	0.0109	-0.4255	0.0262	0.0092	-6.1152	0.6316	0.2233	-3.2598	0.6226	0.2201	0.0002	0.0157	0.3095
K-302-bdol	0.0316	0.0119	-0.2782	0.0351	0.0132	13.2447	0.4309	0.1629	3.9384	0.4287	0.1620	0.0003	0.0176	0.3603
K-303-DD	0.0549	0.0194	-0.3949	0.0463	0.0164	-7.5705	0.7890	0.2789	-2.2493	0.7808	0.2761	0.0013	0.0363	0.3354
K-303-dolwr	0.0369	0.0130	-0.3590	0.0270	0.0096	2.2339	0.8855	0.3131	0.5176	0.8614	0.3046	0.0012	0.0345	0.3207
K-304	0.0247	0.0087	-0.3824	0.0229	0.0081	-2.1666	0.2938	0.1039	-1.3633	0.3104	0.1097	0.0004	0.0187	0.3683
K-305-1	0.0212	0.0075	-0.0935	0.0190	0.0067	24.0075	0.1941	0.0686	10.6859	0.1840	0.0651	0.0002	0.0156	0.4395
K-305-3	0.0321	0.0113	-0.1130	0.0290	0.0102	18.5082	0.5765	0.2038	7.8391	0.5681	0.2009	0.0002	0.0150	0.4564
K-305-5	0.0249	0.0088	-0.1260	0.0275	0.0097	13.2487	0.6139	0.2170	5.6047	0.6174	0.2183	0.0002	0.0146	0.4620
K-305-6	0.0319	0.0113	-0.1524	0.0325	0.0115	19.5959	0.2010	0.0711	8.6611	0.2151	0.0761	0.0003	0.0180	0.3996
K-307B-LS	0.0430	0.0152	-0.3280	0.0390	0.0138	8.6740	0.5900	0.2086	3.5240	0.6130	0.2167	0.0010	0.0312	0.3449
K-308-CAL	0.0418	0.0148	-0.6308	0.0393	0.0139	-11.9102	0.5243	0.1854	-5.6692	0.5279	0.1866	0.0005	0.0226	0.2949
KEN-1	0.0250	0.0088	-0.1520	0.0160	0.0057	17.0250	0.2200	0.0778	6.6520	0.2270	0.0803	0.0009	0.0293	0.4542
Ken-1-LS-dblcln	0.0372	0.0132	-0.2869	0.0300	0.0106	6.5249	0.5411	0.1913	1.1155	0.5280	0.1867	0.0003	0.0173	0.3376
KEN-14A-LS	0.0264	0.0093	-0.3249	0.0261	0.0092	1.5404	0.3719	0.1315	0.3575	0.3749	0.1325	0.0003	0.0178	0.3757
KEN-14B-LS	0.0369	0.0130	-0.3332	0.0326	0.0115	3.2988	0.2975	0.1052	1.1543	0.3029	0.1071	0.0004	0.0190	0.3646
KEN-2-toothycem	0.0400	0.0141	-0.3640	0.0330	0.0117	-9.7490	0.4790	0.1694	-4.2660	0.4750	0.1679	0.0002	0.0140	0.4571
KEN-20	0.0310	0.0110	-0.3580	0.0310	0.0110	-2.3390	0.3620	0.1280	-1.5010	0.3670	0.1298	0.0003	0.0176	0.4389
KEN-22	0.0450	0.0159	-0.6050	0.0330	0.0117	-12.3930	0.3810	0.1347	-5.3870	0.4070	0.1439	0.0016	0.0402	0.3167
KEN-23	0.0278	0.0098	-0.4554	0.0284	0.0100	-3.4612	0.4821	0.1705	-1.5555	0.4835	0.1709	0.0003	0.0161	0.2972
KEN-26A-LS	0.0495	0.0175	-0.2765	0.0449	0.0159	10.9670	0.4420	0.1563	4.3073	0.4357	0.1540	0.0004	0.0210	0.3203
KEN-26B-LS	0.0396	0.0140	-0.3161	0.0418	0.0148	5.6020	0.6015	0.2127	0.4837	0.5920	0.2093	0.0004	0.0202	0.2958
KEN-30	0.0312	0.0110	-0.4133	0.0252	0.0089	5.1821	0.7769	0.2747	1.6918	0.7704	0.2724	0.0002	0.0146	0.2885
KEN-302-dolwr	0.0946	0.0334	-0.3213	0.0687	0.0243	10.5539	2.8245	0.9986	2.5609	2.7716	0.9799	0.0020	0.0442	0.3201
KEN-35	0.0180	0.0064	-0.3790	0.0200	0.0071	-0.5010	0.3140	0.1110	-0.4670	0.3310	0.1170	0.0009	0.0297	0.3562
KEN-4-DD	0.0170	0.0060	-0.3940	0.0280	0.0099	-3.6500	0.4060	0.1435	-1.7000	0.4100	0.1450	0.0010	0.0314	0.3729
KEN-4-dolwr	0.0340	0.0120	-0.3450	0.0240	0.0085	9.4130	0.3220	0.1138	3.5530	0.3500	0.1237	0.0009	0.0293	0.3183
KEN-40-CAL-GST	0.0300	0.0106	-0.6320	0.0220	0.0078	-7.9400	0.3920	0.1386	-3.5020	0.4170	0.1474	0.0019	0.0438	0.3511
KEN-42-cal	0.0480	0.0170	-0.2290	0.0420	0.0148	13.0160	0.3050	0.1078	5.1240	0.3060	0.1082	0.0010	0.0317	0.4509
KEN-42-LS	0.0319	0.0113	-0.3530	0.0305	0.0108	4.2672	0.6820	0.2411	0.5557	0.6757	0.2389	0.0013	0.0356	0.3154
KEN-4B	0.0330	0.0117	-0.3020	0.0330	0.0117	8.5110	0.4360	0.1541	3.2710	0.4290	0.1517	0.0003	0.0162	0.3734
KEN-5	0.0210	0.0074	-0.3640	0.0240	0.0085	2.7690	0.2210	0.0781	0.9790	0.2240	0.0792	0.0009	0.0299	0.3635
KEN-7A-bdol	0.0350	0.0124	-0.3220	0.0360	0.0127	14.5440	0.1730	0.0612	5.5420	0.1800	0.0636	0.0010	0.0310	0.3081
KEN-7A-CAL	0.0470	0.0166	-0.4190	0.0450	0.0159	-2.4020	0.2620	0.0926	-1.0410	0.2580	0.0912	0.0011	0.0335	0.3381
KEN-7A-dolwr	0.0370	0.0131	-0.2920	0.0280	0.0099	14.1530	0.1640	0.0580	5.3330	0.1660	0.0587	0.0009	0.0300	0.3402
KEN-7B-bdol	0.0170	0.0060	-0.2990	0.0230	0.0081	13.9500	0.3870	0.1368	5.4550	0.3920	0.1386	0.0009	0.0294	0.3374
KEN-7B-CAL	0.0410	0.0145	-0.4140	0.0280	0.0099	-2.9310	0.2080	0.0735	-1.0800	0.2140	0.0757	0.0010	0.0315	0.3563
KEN-7B-dolwr	0.0380	0.0134	-0.2970	0.0480	0.0170	13.7080	0.2330	0.0824	5.2460	0.2380	0.0841	0.0011	0.0329	0.3440

Sample.ID	Stretch.corrΔ_{47} (‰)	CIT.Acid.corrΔ_{47} (‰)	CIT.Δ_{47}stdcorr.allstds (‰)	ARF.ghosh.temp.sec.allstds (°C)	ARF.std.corr.toapply (‰)	ARF.whichstdcorr	ARF.stdcorrΔ_{47}.dup.mean (‰)
1-CAL-GST	0.2994	0.3804	0.4182	89.1	-0.0639	primary, best fit resid Carrara	0.4965
2-CAL-GST	0.3685	0.4495	0.4873	66.6	-0.0546	primary, best fit resid Carrara	0.5333
4-CAL-GST	0.3266	0.4076	0.4309	86.6	0.0081	secondary, mean resid all	0.4866
6-CAL-GST	0.2745	0.3555	0.3933	98.4	-0.0658	primary, best fit resid Carrara	0.4705
K-203	0.3207	0.4017	0.4395	81.7	-0.0583	primary, best fit resid Carrara	0.5182
K-204	0.3255	0.4065	0.4298	87.1	0.0081	secondary, mean resid all	0.4854
K-204-DD	0.3013	0.3823	0.4201	88.4	-0.0695	primary, best fit resid Carrara	0.5105
K-204-dolwr	0.3455	0.4265	0.4498	79.7	0.0081	secondary, mean resid all	0.5061
K-206	0.3407	0.4217	0.4595	75.2	-0.0156	primary, best fit resid Carrara	0.4963
K-209	0.3693	0.4503	0.4736	71.5	0.0081	secondary, mean resid all	0.5308
K-212	0.3473	0.4283	0.4516	79.0	0.0081	secondary, mean resid all	0.5081
K-213	0.4082	0.4892	0.5270	55.4	-0.0231	primary, best fit resid Carrara	0.5741
K-224-1-cal	0.3180	0.3990	0.4368	82.6	-0.0769	primary, best fit resid Carrara	0.5244
K-224-1-LS	0.3132	0.3942	0.4320	84.3	-0.0342	primary, best fit resid Carrara	0.4863
K-224-14F	0.4759	0.5569	0.5697	42.7	-0.0018	secondary, best fit resid Carrara	0.6409
K-224-3	0.2927	0.3737	0.3970	103.8	-0.0636	primary, best fit resid TV01	0.4964
K-224-4	0.3673	0.4483	0.4861	66.9	-0.0788	primary, best fit resid Carrara	0.5569
K-224-8	0.3306	0.4116	0.4494	78.4	-0.0806	primary, best fit resid Carrara	0.5253
K-225-10F	0.4411	0.5221	0.5454	49.8	0.0081	secondary, mean resid all	0.6052
K-225-11F	0.4064	0.4874	0.5107	60.3	-0.0313	primary, best fit resid TV01	0.5859
K-225-14F	0.4696	0.5506	0.5739	41.7	-0.052	primary, best fit resid TV01	0.6742
K-225-15-LS	0.3754	0.4564	0.4608	73.7	0.0136	primary, mean resid all	0.5239
K-225-15V	0.4123	0.4933	0.5061	60.8	-0.0189	secondary, best fit resid Carrara	0.5867
K-225-16V	0.3165	0.3975	0.4208	93.3	-0.0497	primary, best fit resid TV01	0.5080
K-225-8V	0.4152	0.4962	0.5090	59.9	-0.0146	secondary, best fit resid Carrara	0.6191
K-225-9F	0.4233	0.5043	0.5171	57.4	-0.0061	secondary, best fit resid Carrara	0.6014
K-225-9F-LS	0.3294	0.4104	0.4482	78.8	-0.0379	primary, best fit resid Carrara	0.5069
K-244	0.3527	0.4337	0.4570	77.1	0.0081	secondary, mean resid all	0.5136
K-244-dolwr	0.4104	0.4914	0.5292	54.8	-8.00E-04	primary, best fit resid Carrara	0.5351
K-245	0.2395	0.3205	0.3333	132.2	-0.0317	secondary, best fit resid Carrara	0.4646
K-246	0.4337	0.5147	0.5264	51.5	0.0017	primary, mean resid all	0.6037
K-247-cal	0.3119	0.3929	0.4101	94.4	0.0245	secondary, best fit resid all	0.4641
K-249	0.4174	0.4984	0.5101	56.7	0.0017	primary, mean resid all	0.6022
K-256	0.3908	0.4718	0.4835	65.8	0.0017	primary, mean resid all	0.5690
K-257	0.4327	0.5137	0.5254	51.8	0.0017	primary, mean resid all	0.6084
K-258	0.4906	0.5716	0.5833	35.0	0.0017	primary, mean resid all	0.6795
K-276-ZD-1	0.3399	0.4209	0.4238	88.5	0.0218	primary, mean resid all	0.4814
K-276-ZD-2	0.3856	0.4666	0.4695	70.7	0.0218	primary, mean resid all	0.5331
K-276-ZD-3	0.3532	0.4342	0.4386	82.1	0.0136	primary, mean resid all	0.4992
K-276-ZD-4	0.3670	0.4480	0.4524	76.8	0.0136	primary, mean resid all	0.5145
K-276-ZD-5	0.3474	0.4284	0.4313	85.4	0.0218	primary, mean resid all	0.4898
K-276-ZD-6	0.3837	0.4647	0.4691	70.7	0.0136	primary, mean resid all	0.5332
K-276-ZD-7	0.3450	0.4260	0.4304	85.3	0.0136	primary, mean resid all	0.4900
K-276-ZD-8	0.2950	0.3760	0.3804	107.3	0.0136	primary, mean resid all	0.4342
K-276-ZD-9	0.3277	0.4087	0.4131	92.5	0.0136	primary, mean resid all	0.4707
K-276-ZD-10	0.2852	0.3662	0.3706	112.1	0.0136	primary, mean resid all	0.4233
K-276-ZD-11	0.3411	0.4221	0.4265	86.9	0.0136	primary, mean resid all	0.4856

Sample.ID	Stretch.corrΔ_{47} (‰)	CIT.Acid.corrΔ_{47} (‰)	CIT.Δ_{47}stdcorr.allstds (‰)	ARF.ghosh.temp.sec.allstds (°C)	ARF.std.corr.toapply (‰)	ARF.whichstdcorr	ARF.stdcorrΔ_{47}.dup.mean (‰)
K-276-ZD-12	0.3309	0.4119	0.4163	91.1	0.0136	primary, mean resid all	0.4743
K-276-ZD-13	0.3539	0.4349	0.4393	81.8	0.0136	primary, mean resid all	0.4999
K-300	0.3231	0.4041	0.4274	90.5	-0.0659	primary, best fit resid TV01	0.5313
K-301	0.3589	0.4399	0.4516	77.8	0.0017	primary, mean resid all	0.5245
K-302	0.3318	0.4128	0.4245	89.0	0.0017	primary, mean resid all	0.4918
K-302-bdol	0.3863	0.4673	0.4790	67.4	0.0017	primary, mean resid all	0.5308
K-303-DD	0.3701	0.4511	0.4683	73.2	0.0097	secondary, best fit resid all	0.5252
K-303-dolwr	0.3540	0.4350	0.4522	78.7	0.0147	secondary, best fit resid all	0.5038
K-304	0.3618	0.4428	0.4806	68.6	-0.0101	primary, best fit resid Carrara	0.5128
K-305-1	0.4317	0.5127	0.5505	49.3	-0.0175	primary, best fit resid Carrara	0.5929
K-305-3	0.4555	0.5365	0.5598	45.6	-0.0428	primary, best fit resid TV01	0.6499
K-305-5	0.4611	0.5421	0.5654	44.1	0.0164	primary, mean resid all	0.5967
K-305-6	0.3925	0.4735	0.5113	59.7	-0.0193	primary, best fit resid Carrara	0.5539
K-307B-LS	0.3406	0.4216	0.4449	81.5	0.0081	secondary, mean resid all	0.5010
K-308-CAL	0.2943	0.3753	0.3986	103.1	-0.0543	primary, best fit resid TV01	0.4889
KEN-1	0.4485	0.5295	0.5528	47.8	0.0081	secondary, mean resid all	0.6128
Ken-1-LS-dblcln	0.3810	0.4620	0.4664	71.7	0.0218	primary, mean resid all	0.4914
KEN-14A-LS	0.3690	0.4500	0.4878	66.4	0.0011	primary, best fit resid Carrara	0.4961
KEN-14B-LS	0.3581	0.4391	0.4769	69.7	-0.0063	primary, best fit resid Carrara	0.5045
KEN-2-toothycem	0.4927	0.5737	0.5766	37.6	0.0218	primary, mean resid all	0.6514
KEN-20	0.4380	0.5190	0.5423	50.6	-0.0244	primary, best fit resid TV01	0.6128
KEN-22	0.3128	0.3938	0.4171	92.0	0.0081	secondary, mean resid all	0.4723
KEN-23	0.2966	0.3776	0.4009	102.0	-0.0705	primary, best fit resid TV01	0.5075
KEN-26A-LS	0.3146	0.3956	0.4334	83.8	-0.0286	primary, best fit resid Carrara	0.4822
KEN-26B-LS	0.3339	0.4149	0.4193	89.9	0.0136	primary, mean resid all	0.4868
KEN-30	0.2879	0.3689	0.3922	106.1	-0.0613	primary, best fit resid TV01	0.5043
KEN-302-dolwr	0.3533	0.4343	0.4515	79.0	0.022	secondary, best fit resid all	0.4957
KEN-35	0.3517	0.4327	0.4560	77.5	0.0081	secondary, mean resid all	0.5126
KEN-4-DD	0.3683	0.4493	0.4726	71.8	0.0081	secondary, mean resid all	0.5297
KEN-4-dolwr	0.3144	0.3954	0.4187	91.4	0.0081	secondary, mean resid all	0.4739
KEN-40-CAL-GST	0.3467	0.4277	0.4510	79.2	0.0081	secondary, mean resid all	0.5074
KEN-42-cal	0.4453	0.5263	0.5496	48.6	0.0081	secondary, mean resid all	0.6095
KEN-42-LS	0.3481	0.4291	0.4463	80.8	0.0048	secondary, best fit resid all	0.5077
KEN-4B	0.3726	0.4536	0.4769	71.6	-0.0267	primary, best fit resid TV01	0.5394
KEN-5	0.3590	0.4400	0.4633	75.0	0.0081	secondary, mean resid all	0.5201
KEN-7A-bdol	0.3042	0.3852	0.4085	95.4	0.0081	secondary, mean resid all	0.4634
KEN-7A-CAL	0.3339	0.4149	0.4382	83.9	0.0081	secondary, mean resid all	0.4941
KEN-7A-dolwr	0.3360	0.4170	0.4403	83.1	0.0081	secondary, mean resid all	0.4963
KEN-7B-bdol	0.3332	0.4142	0.4375	84.2	0.0081	secondary, mean resid all	0.4935
KEN-7B-CAL	0.3519	0.4329	0.4562	77.4	0.0081	secondary, mean resid all	0.5128
KEN-7B-dolwr	0.3397	0.4207	0.4440	81.8	0.0081	secondary, mean resid all	0.5002

Sample.ID	ARF.Δ_{47}err.dup	ARF.T.final (°C)	ARF.T.err.u (°C)	ARF.T.err.d (°C)	δ^{18}O.min.SMOW (‰)	δ^{18}O.water.SMOW (‰)	δ^{18}O.water.err.u (‰)	δ^{18}O.water.err.d (‰)
1-CAL-GST	0.0273	114.6	20.3	17.0	14.3043	-1.4006	1.7945	1.7348
2-CAL-GST	0.0245	92.2	14.3	12.5	14.9612	-3.0834	1.5386	1.4961
4-CAL-GST	0.0412	121.5	34.7	26.3	13.5612	-1.4898	2.7685	2.6273
6-CAL-GST	0.0305	133.8	27.8	22.3	14.2069	0.2124	2.0800	1.9980
K-203	0.0314	100.8	20.5	17.1	14.0140	-3.0729	2.0115	1.9383
K-204	0.0314	122.4	25.7	20.8	15.8823	0.8767	2.1072	2.0246
K-204-DD	0.0188	105.5	12.4	11.1	14.5233	-2.0800	1.2117	1.1846
K-204-dolwr	0.0286	108.2	20.1	16.8	17.3239	-4.0184	1.7579	1.6980
K-206	0.0199	114.7	14.4	12.7	16.6447	0.9183	1.3045	1.2728
K-209	0.0312	93.6	18.9	15.8	17.6311	-0.3056	1.9770	1.9074
K-212	0.0318	107.0	22.2	18.3	17.1341	0.6414	2.0698	1.9919
K-213	0.0164	72.2	7.6	7.0	19.6595	-0.9462	0.9861	0.9692
K-224-1-cal	0.0128	97.2	7.6	7.1	16.8813	-0.6418	0.8097	0.7977
K-224-1-LS	0.0207	121.7	16.1	14.0	18.3269	3.2262	1.3760	1.3404
K-224-14F	0.0270	46.8	9.4	8.4	25.5041	0.9137	1.5302	1.4922
K-224-3	0.0166	114.6	11.9	10.7	15.7758	0.0517	1.0883	1.0661
K-224-4	0.0131	80.1	6.5	6.1	19.8840	0.3047	0.7964	0.7852
K-224-8	0.0132	96.6	7.8	7.3	17.1552	-0.4313	0.8349	0.8222
K-225-10F	0.0320	59.4	13.1	11.4	24.2384	1.7091	1.8800	1.8212
K-225-11F	0.0152	67.2	6.6	6.1	19.8967	-1.4117	0.8997	0.8857
K-225-14F	0.0161	36.5	4.8	4.5	25.7275	-0.7064	0.8804	0.8679
K-225-15-LS	0.0226	97.5	13.9	12.2	21.6825	4.1082	1.4444	1.4068
K-225-15V	0.0196	66.8	8.5	7.8	18.4028	-2.9250	1.1625	1.1393
K-225-16V	0.0125	107.0	8.2	7.6	20.4203	3.8764	0.8080	0.7959
K-225-8V	0.0135	54.3	5.0	4.7	21.4699	-1.7958	0.7755	0.7654
K-225-9F	0.0189	60.9	7.7	7.1	21.8002	-0.4550	1.1074	1.0866
K-225-9F-LS	0.0202	107.7	13.7	12.1	20.3155	3.8473	1.3144	1.2826
K-244	0.0299	103.5	20.1	16.8	20.1248	3.2285	1.9384	1.8705
K-244-dolwr	0.0211	91.2	12.1	10.8	20.7974	-2.3430	1.2524	1.2226
K-245	0.0192	138.7	17.5	15.2	19.7544	6.0810	1.3162	1.2829
K-246	0.0163	60.0	6.5	6.1	20.7934	-1.5727	0.9519	0.9365
K-247-cal	0.0243	139.1	22.7	18.9	19.0502	5.4175	1.6743	1.6206
K-249	0.0130	60.6	5.2	4.9	19.6740	-2.5827	0.7589	0.7491
K-256	0.0132	74.5	6.2	5.8	20.2101	-0.1029	0.7957	0.7846
K-257	0.0196	58.2	7.7	7.1	8.8407	-13.5296	1.1267	1.1051
K-258	0.0145	35.0	4.2	4.0	8.4877	-17.7813	0.7754	0.7656
K-276-ZD-1	0.0091	125.4	7.1	6.7	18.4960	-1.3527	0.5731	0.5665
K-276-ZD-2	0.0136	92.3	7.7	7.1	18.6803	-4.2942	0.8002	0.7879
K-276-ZD-3	0.0202	112.7	14.4	12.7	17.9756	-2.9611	1.2450	1.2145
K-276-ZD-4	0.0161	103.0	10.2	9.3	19.3686	-2.5228	0.9698	0.9515
K-276-ZD-5	0.0197	119.2	14.9	13.1	18.0719	-2.2928	1.2288	1.1988
K-276-ZD-6	0.0179	92.3	10.3	9.3	18.7316	-4.2493	1.0576	1.0362
K-276-ZD-7	0.0204	119.0	15.5	13.5	17.3327	-3.0306	1.2711	1.2390
K-276-ZD-8	0.0179	167.7	21.0	18.0	18.0311	1.2215	1.2049	1.1742
K-276-ZD-9	0.0160	133.6	13.7	12.2	13.9219	-5.1756	1.0135	0.9925
K-276-ZD-10	0.0160	180.1	20.7	17.8	17.6545	1.5801	1.0945	1.0687
K-276-ZD-11	0.0174	122.2	13.4	12.0	17.2793	-2.8115	1.0865	1.0629

NAME	EXPLANATION
Sample.ID	abbreviated sample ID
dup	B: There was a duplicate measurement made in a separate session, Z: zebra dolomite
MS	name of the mass spectrometer, P. Leia is the original MAT253, A. Akbar is the second MAT253.
Session	sequential order; session 7 analyzed samples from other projects and is not included here
Comment	comment about the run, including pressure drops
Date	date of run
mass.spec.room	location of the mass spectrometer in North Mudd building at Caltech
Sample.ID.orig.data	sample ID used during the run
mineral	cal: calcite; dol: dolomite
min.type	specific geological designation based on paragenesis or host rock
carb.code1	original carbonate designation, including "unknown" for ambiguous paragenetic position
carb.code2	updated carbonate designation, assigning "unknowns" a paragenetic position based on clumped measurements
reltime	paragenetic position relative to copper mineralization where '2' is coeval with copper
strat.height_m	stratigraphic height in meters above the Nikolai Greestone-Chitistone Limestone contact
notes	additional notes about geologic locations or relationships
spec.num	assigned by the data management program on the mass spec
num.acq	number of acquisitions, used to computer standard error
$\delta^{13}C$ (‰)	13C permil relative to VPDB
$\delta^{13}C$.stdev (‰)	13C standard deviation
$\delta^{13}C$.sterr (‰)	13C standard error
$\delta^{18}O$.gas (‰)	18O of O2 gas liberated during the run, relative to VSMOW
$\delta^{18}O$.gas.stdev (‰)	18O gas standard deviation
$\delta^{18}O$.gas.sterr (‰)	18O gas standard error
δ^{47} (‰)	mass 47 relative to working gas
δ^{47}.stdev (‰)	mass 47 standard deviation
δ^{47}.sterr (‰)	mass 47 standard error
Δ_{47} (‰)	proportion of mass 47 to all isotopologues of CO2
Δ_{47}.stdev (‰)	proportion of mass 47 to all isotopologues of CO2, standard deviation

Δ_{47}.sterr (‰)	proportion of mass 47 to all isotopologues of CO2, standard error
δ^{48} (‰)	mass 48 relative to working gas
δ^{48}.stdev (‰)	mass 48 standard deviation
δ^{48}.sterr (‰)	mass 48 standard error
Δ_{48} (‰)	proportion of mass 48 to all isotopologues of CO2
Δ_{48}.stdev (‰)	proportion of mass 48 to all isotopologues of CO2, standard deviation
Δ_{48}.sterr (‰)	proportion of mass 48 to all isotopologues of CO2, standard error
Δ_{47}.extvar (‰)^2	D47 external variance (σ^2)
Δ_{47}.extsterr (‰)	D47 external standard error (1σ)
HGcorrΔ_{47} (‰)	heated gas corrected D47
Stretch.corrΔ_{47} (‰)	stretch corrected D47
CIT.Acid.corrΔ_{47} (‰)	Caltech reference frame, acid corrected D47
CIT.Δ_{47}stdcorr.allstds (‰)	Caltech reference frame, Standard corrected D47, considered to be "final" D47 used to compute Temperature and d18O water until the beginning of 2013.
ARF.ghosh.temp.sec.allstds (°C)	Absolute reference frame, Ghosh et al. (2006) calibration curve, using the secondary method of Huntington et al. (2009) to convert CIT to ARF
ARF.std.corr.toapply (‰)	Absolute reference frame, value of the standard correction applied to the D47 in this data set
ARF.whichstdcorr	Absolute reference frame, tells which standard correction was applied based on the standard residuals plotted in Fig. 3.2.
ARF.stdcorrΔ_{47}.dup.mean (‰)	Absolute reference frame, standard corrected, and including duplicate measurements of unknowns; considered to be "final" for this study
ARF.Δ_{47}err.dup	Absolute reference frame, error in standard corrected D47
ARF.T.final (°C)	final temperatuer in the absolute reference frame
ARF.T.err.u (°C)	final temperature, upper error bar value (1σ)
ARF.T.err.d (°C)	final temperature, lower error bar value (1σ)
δ^{18}O.min.SMOW (‰)	calculated d18O of the mineral relative to SMOW, CO2-calcite fractionation from Kim et al. (2007)
δ^{18}O.water.SMOW (‰)	calculated d18O of the water of formation relative to SMOW, calcite-water fractionation from Freidman and ONeil (1977), dolomite-water from Schmidt et al. (2005)
δ^{18}O.water.err.u (‰)	calculated d18O of the water of formation relative to SMOW, upper error bar (1σ)
δ^{18}O.water.err.d (‰)	calculated d18O of the water of formation relative to SMOW, lower error bar (1σ)